An Investigation of a Frequency Diverse Array

By

Paul Antonik

A thesis submitted for the degree of Doctor of Philosophy of
University College London

Faculty of Engineering Sciences
Department of Electronic and Electrical Engineering
University College London

United Kingdom

April 2009

I, Paul Antonik, confirm that the work presented in this thesis is my own. Where information has been derived from other sources, I confirm that this has been indicated in the thesis.

_____

The views expressed in this thesis are those of the author and do not necessarily reflect the official policy or position of the U.S. Air Force, the U.S. Department of Defense, or the U.S. Government.

Abstract

This thesis presents a novel concept for focusing an antenna beam pattern as a function of range, time, and angle. In conventional phased arrays, beam steering is achieved by applying a linear phase progression across the aperture. This thesis shows that by applying an additional linear frequency shift across the elements, a new term is generated which results in a scan angle that varies with range in the far-field. Moreover, the antenna pattern is shown to scan in range and angle as a function of time. These properties result in more flexible beam scan options for phased array antennas than traditional phase shifter implementations. The thesis subsequently goes on to investigate this phenomenon via full scale experimentation, and explores a number of aspects of applying frequency diversity spatially across array antennas. This new form of frequency diverse array may have applications to multipath mitigation, where a radio signal takes two or more routes between the transmitter and receiver due to scattering from natural and man-made objects. Since the interfering signals arrive from more than one direction, the range-dependent and auto-scanning properties of the frequency diverse array beam may be useful to isolate and suppress the interference. The frequency diverse array may also have applications to wideband array steering, in lieu of true time delay solutions which are often used to compensate for linear phase progression with frequency across an array, and to sonar, where the speed of propagation results in large percentage bandwidth, creating similar wideband array effects. The frequency diverse array is also a stepping stone to more sophisticated joint antenna and waveform design for the creation of new radar modes, such as simultaneous multi-mode operation, for example, enabling joint synthetic aperture radar and ground moving target indication.

Acknowledgements

The U.S. Air Force Office of Scientific Research generously sponsored this work. In particular, thanks go to Dr. Jon Sjogren for his vision and support.

I also owe a debt of gratitude to U.S Air Force Research Laboratory management, including Mr. Gerard Genello, Mr. William Baldygo, Mr. William Moore, Mr. Tracy Johnston, Mr. Joseph Sciabica, and Dr. David Jerome, who allowed me to start, continue, and complete this programme.

I would also like to thank my advisors, Prof. Hugh Griffiths and Prof. Chris Baker, for their guidance and many helpful comments. Particular thanks go to my external advisor, Dr. Michael Wicks, one of the most creative people I have ever known.

Special thanks go to Cathy and Anna, whom I like better than my friends at work, who have provided much support and understanding over long absences.

Finally, I would like to acknowledge the memory and influence of my father, Frank Antonik, a radar technician turned radar engineer from The Greatest Generation.

Ad majorem Dei gloriam.

Novel Research Contributions

The novel research contributions of this work are:

1. The development of an array antenna with a beam that focuses in different directions as a function of range. [See Section 4.1]
2. The development of an array antenna that scans in range as a function of time [See Section 4.4]
3. The development of an array antenna with an auto-scanning property; that is, the antenna scans in angle as a function of time without mechanical steering or electronic phase shifters [See Section 4.4]
4. The development of new approaches for the simultaneous transmission and reception of spatial-temporal signals for target detection and imaging at the same time. [See Section 8.2]

Publications Arising from the Research Described in this Thesis

The following papers were published as a result of this Ph.D. research programme:

P. Antonik, M. C. Wicks, H. D. Griffiths, C. J. Baker, “Frequency diverse array radars”, Proc. 2006 IEEE Radar Conf., Verona, NY, pp. 215-217, 24-27 April 2006.

P. Antonik, M. C. Wicks, H. D. Griffiths, C. J. Baker, “Multi-mission, multi-mode waveform diversity”, Proc. 2006 IEEE Radar Conf., Verona, NY, pp. 580-582, 24-27 April 2006.

In addition, the following patents related to this research have been awarded or are pending:

Michael C. Wicks and Paul Antonik, “Frequency diverse array with independent modulation of frequency, amplitude, and phase”, U.S. Patent No, 7,319,427, January 15, 2008.

Michael C. Wicks and Paul Antonik, “Method and apparatus for a frequency diverse array”, U.S. Patent No. 7,511,665 B2, March 31, 2009.

Paul Antonik and Michael C. Wicks, “Method and apparatus for simultaneous synthetic aperture radar and moving target indication”, U.S. Patent Application 20080129584, June 5, 2008.

Table of Contents

List of Tables

List of Figures

List of Principal Symbols

Nomenclature for all equations is defined in the main body of the document; however, a list of some of the more commonly used symbols is given here.

Symbol	Quantity
α	Attenuation constant
β	Phase constant, $\beta = 2\pi/\lambda$
c	Speed of propagation
d	Spacing between array elements
δ	Dirac delta function
Δf	Frequency shift from element-to-element
∇	Gradient operator
ε	Permittivity of free space, $\varepsilon_0 \approx 8.854 \times 10^{-12}$ F/m
E	Electric field
f_i	Frequency of the i^{th} element
γ	Propagation constant
H	Magnetic field
j	The imaginary unit, $\sqrt{-1}$
λ	Wavelength
μ_0	Permeability of free space, $\mu_0 \approx 4\pi \times 10^{-7}$ N-A^{-2}
N	Number of elements
v_p	Phase velocity
R_i	Range from the i^{th} element to a point in space
rep	Woodward repetition function
θ	Angle with respect to antenna boresight

List of Abbreviations

BLAST	Bell-laboratories layered space-time (architecture)
FDA	Frequency diverse array
GMTI	Ground moving target indication
InSAR	Interferometric synthetic aperture radar
LFM	Linear frequency modulation
MIMO	Multiple input – multiple output
MTI	Moving target indication
PAM	Pulse amplitude modulation
RCS	Radar cross section
SAR	Synthetic aperture radar
STAP	Space time adaptive processing
TEM	Transverse electromagnetic
UWB	Ultra-wideband

Chapter 1

Introduction

1.1 Background

In this thesis a novel concept using frequency diversity, specifically in an array antenna, is explored. This has been done both mathematically and experimentally. It is demonstrated that this offers a new dimension of design freedom that results in novel beam formation and control.

This research evolved out of a study exploring waveform diversity to support simultaneous synthetic aperture radar and moving target indication. Traditional waveform design techniques focus on single-mode waveforms. Even for modern multi-mode radars, waveforms are typically designed separately for each mode, and waveforms for different missions are transmitted sequentially, or perhaps interleaved in time. However, new digital programmable waveform generators permit much greater flexibility in waveform synthesis. Moreover, different signals can be radiated from different portions of the antenna, providing spatial diversity as well. In this manner, a full spectrum of dimensionality can be exploited (space, time, frequency, code, and polarization) in order to construct new radar modes.

A first step in this new approach to joint aperture-waveform design is the frequency diverse array. In its simplest configuration, a simple continuous wave signal is radiated from each spatial channel. A small (few Hertz) frequency shift is applied from channel-to-channel. This small frequency shift results in a beam pattern for which the beam focus direction changes as a function of range, angle, and time. This is significantly different than the conventional phased array, where the beam pointing direction is independent of range and time in the far-field.

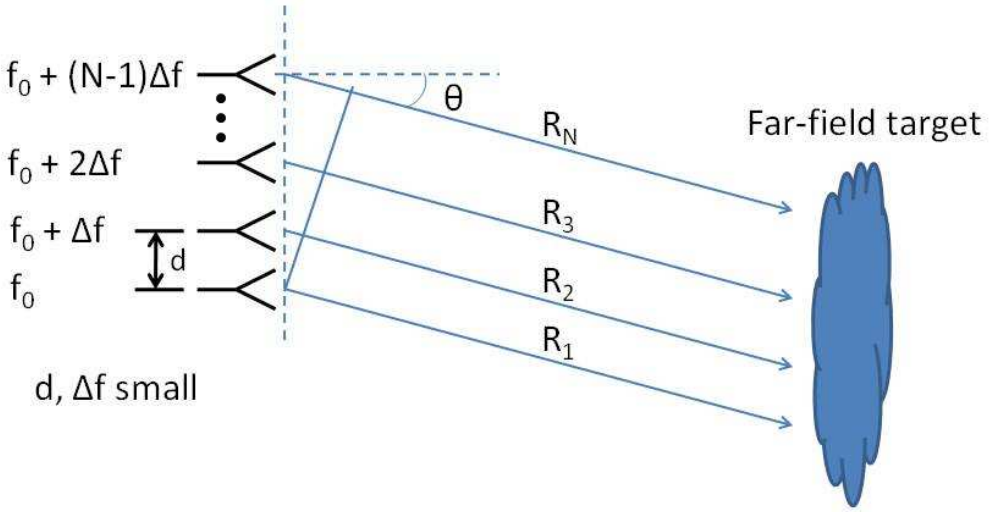

Fig. 1-1: Concept of frequency diverse array

The frequency diverse array is also significantly different than multiple input-multiple output (MIMO) schemes. MIMO has long been in use for communications applications, where multiple channels provide multiple independent paths to reduce fading due (primarily) to multipath [1] – [9]. MIMO has more recently been applied to radar [10] – [13]. The first MIMO radar concepts, similar to communications applications, proposed multiple independent paths to reduce fading due to target radar cross section fluctuations. Such statistical MIMO schemes were typically considered for distributed sensor geometries. More recent developments have considered coherent

MIMO approaches for closely spaced spatial channels. These approaches generally use large frequency separations between spatial channels, resulting in no significant spectral overlap of the signals across spatial channels. Spatial channel separation distances are also much larger than in the frequency diverse array. By contrast, the frequency diverse array utilizes very small changes in frequencies between channels resulting in significant signal overlap. Moreover, the frequency diverse array results in very different beam properties than MIMO in range, angle, and time. These new beam properties result in new capabilities, such as range-dependent beamforming and auto-scanning in angle without the need for phase shifters or mechanical beam steering.

1.2 Research Aims

The principal aims of this research programme are as follows:

To explore frequency diverse spatial arrays. This includes:

1. Development of frequency diverse array theory and signal processing algorithms
2. Conduct of experiments investigating the impact of varying frequency shift on antenna pattern as functions of range, angle, and time
3. Understand and describe beam forming and radiation control using frequency diverse arrays.

1.3 Motivation

In part, this work is motivated by curiosity to examine the properties of array antennas that use frequency diversity in a spatial sense. This is a new design freedom hitherto unexplored. Frequency diversity and its benefits when applied temporally have been the subject of much research. However, the benefits of frequency diversity applied spatially are unknown. An antenna pattern which changes direction of focus with range

can provide more flexible beam scan options for a phased array radar. Since the direction and amount of focus can be determined analytically, multiple targets at different angles can be illuminated simultaneously. In addition, the time variation of the pattern with range and angle results in an auto-scanning capability without the introduction of phase shifters.

Another potential application for the range-dependent beam pattern is multipath mitigation. Multipath is caused when signals are reflected off of nearby scatterers and are summed in the receiver, causing dispersion or time-spreading of the received signal. Multipath occurs because the signals reflected from scatterers at different ranges have varying round-trip delays. The signals add coherently in the receiver, producing a resultant sum signal which has a longer duration than the direct path signal alone. By applying an antenna pattern which focuses in different directions as a function of range, the phase coherency of the multipath components can be disturbed, such that the resultant sum is less dispersive.

Other potential applications include a method for true time delay for wideband radio-frequency arrays and also for sonar.

Beyond the basic range-dependent beamforming described in this thesis, more sophisticated adaptive transmit waveforms may enable the development of modes that support SAR and MTI at the same time through a single aperture. Traditional approaches to achieving “simultaneous” SAR and MTI include interleaving of SAR and MTI functions on a dwell-to-dwell or sortie-to-sortie basis. This approach is limited due to conflicting requirements on waveform parameters (bandwidth) and timing (dwell time) parameters. Alternatively, simultaneous SAR/MTI has been implemented via image change detection schemes.

1.4 Layout of the Thesis

The Literature Review discusses research on array antennas in general, including phase and frequency scanned arrays and multiple input – multiple output concepts. This is followed by a review of array antenna fundamentals in Chapter 3. Chapter 4 describes the principles of a frequency diverse array in detail. Chapter 5 presents the results of simulations of the frequency diverse array, and Chapter 6 describes experimental measurements taken to verify the simulations. An analysis of the simulated and measured results is presented in Chapter 7, and summary of the results, conclusions of the research, and areas of potential future work are finally presented in Chapter 8.

Chapter 2

Context of the Work

2.1 Literature Review

This section provides a critical review of the prior art in the joint design of waveforms and multi-channel array antennas. It is not intended to cite all work performed in the related areas, but the important accomplishments relevant to the development of the frequency diverse array are summarized. Prior work in the development of phased array antennas, waveform diversity, and multiple input – multiple output systems is of particular interest.

The review begins with a history of the phased array antenna. The phased array was fundamentally derived from the interferometer, which was first introduced in the 1800s. A key feature of the phased array antenna is the ability to scan the antenna beam electronically, without mechanical rotation. Traditionally, electronic beam steering has been achieved through both phase and frequency scanned arrays. In frequency scanned arrays, beam steering is achieved by the variation of frequency as a function of time, and the same signal is applied simultaneously to all spatial channels. In the frequency

diverse array, separate signals of different frequencies are fed simultaneously across spatial channels.

The review then considers developments in waveform diversity. Early work in the co-design of waveforms and antennas together is recognized, as well as recent work in the simultaneous transmission of different signals from different spatial channels. Key among this work is the design of multiple input – multiple output (MIMO) systems. It is shown that the purposes and implementations of MIMO systems are different from the frequency diverse array. While MIMO aims to provide widely separated signals across multiple independent paths to reduce the effects of fading, the frequency diverse array transmits highly overlapping signals closely spaced in frequency to provide new modes for radar and communication.

2.1.1. Array Antennas

A phased array is an antenna composed of individual antennas, or radiating/receiving elements. The elements are arranged and excited in such a way so that the sum of the radiated fields from all elements adds constructively in the direction of interest. The resultant antenna beam can be steered electronically by altering the excitation across the elements, as shown in Fig. 3-3. Unlike conventional mechanically scanned antennas, phased arrays offer the advantages of rapid and flexible scan without moving parts, and the ability to form multiple beams simultaneously.

Phased arrays for radio frequencies have existed for over 100 years. Bondyopadhyay [14] documents that the first application of an array antenna was by Guglielmo Marconi in 1901[1]. Skolnik claims that perhaps the first application of phased array technology to

[1] Sir John Ambrose Fleming, the first Chair of the University College London Department of Electrical Engineering, served as Scientific Advisor to the Marconi Company [15]

radar was the FH MUSA, also called the Mark 8, an azimuth scanning array for naval fire control systems [16]. Skolnik has also reported that phased arrays were widely used by the United States, Great Britain, and Germany during World War II [17]. Besides the Mark 8, the United States employed the AP/APQ-7 navigation and bombing radar. Britain employed phased arrays in height finding radars, while Germany employed a number of phased arrays, including the MAMMUT radar. Australia had an experimental phased array radar for shore defence as early as 1940 [18].

Over time, the enabling technologies of the phased array have improved. Fixed beam implementations have evolved into electronically scanned arrays. Mechanical phase shifters have been replaced by electronic devices, vacuum tubes have given way to solid state transmitters, and radiating elements have migrated to printed circuit board implementations. However, the underlying theory of the phased array has changed little since Marconi's famous transatlantic wireless communications experiment.

The phased array is fundamentally built upon the principle of the interferometer [19], where the interference pattern from two signals is used to derive information about phase, frequency, time delay, and direction of arrival. The interferometer represents the first attempt to exploit spatial diversity for the forming and analysis of signals. Interferometry was being used for optics applications long before phased arrays were applied to radar. Pauls [20] recalls the early work of Fizeau (1867) and Michelson (1890) in optical interferometry for the measurement of astronomical objects. In that work, the diameter of natural satellites was able to be measured by examining the interference patterns caused by light sources observed through two small apertures. In the early 1940s, the principle of the optical interferometer was extended to radio interferometry by British and Australian researchers [21]-[22]. Interferometry for radar has more commonly been applied to synthetic aperture radar. Graham [23] was the first to suggest synthetic interferometry for topographic mapping. This first interferometric SAR was an analogue system that produced topographic images by projecting interference patterns directly on film from cathode ray tube devices [23, 24]. Rodriguez

and Martin [25] wrote a seminal paper describing the theory and design of interferometric synthetic aperture radars in 1992. For earth observation applications, Rosen [26] reports that repeat-pass interferometric synthetic aperture radar (InSAR) has been used to obtain sub-wavelength resolution imaging beginning with SeaSAT (launched in 1978), and continuing through ERS-1, ERS-2, JERS-I, RadarSAT-1, and ENVISAT. The migration of interferometric SAR techniques from space-based platforms to higher resolution aircraft created additional difficulties, primarily due to variations of the platform flight path from straight and level flight. Two-pass techniques presented further challenges due to the likelihood that the two flight paths would not be identical. Griffiths et al. examined a two-aperture interferometric approach to mitigate the difficulties of two-pass airborne interferometric SAR [27].

Antonik et al. [28] found novel uses for the interferometer in radar applications for embedded communications as well as the denial of bistatic hosting. The unique contribution of this work was that the interferometer and a main array were designed jointly with the applied signals to achieve a new capability. Griffiths et al. [29], [30] extended that work, including a Butler matrix implementation.

Beam steering in a phased array is typically achieved by applying a linear phase shift across the face of the aperture [31]. As the frequency of the radiated signal varies, the electrical spacing between elements also varies, causing the phase progression across the aperture to change. This causes the antenna beam to scan as frequency varies, which limits the effective bandwidth of the array [32]. The aperture scanning effect can be mitigated through the use of true time delay [32]-[35]. In true time delay, the time of propagation for the paths of all radiating elements is made to be equal, causing all signals to add in phase for every frequency component in the waveform. However, this is costly to implement at the element level, so that true time delay is usually implemented on a subarray basis [32], [34], [36]. However, more recent advances in direct digital synthesis of the local oscillator at each element make true time delay at the element level more practical. In addition, direct digital synthesis at the element level

enables the concept of the frequency diverse array. This may allow the compensation of frequency scan by the deliberate and progressive change in frequency between elements.

2.1.2. Frequency Scanned Arrays

In some cases, designers purposely exploit the change in phase progression as frequency varies. This is the basis of the frequency scanned array [37]. Skolnik claims that frequency scanning was the first form of electronic steering to be employed in operational radars [17], and that frequency scanning has "probably seen more application than any other electronic scanning method" [16]. Early radars in the United States, including the AN/SPS-39, -48, and -52 were all frequency scanned in elevation, with mechanical rotation providing scan in azimuth. The AN/SPS-39 was a parabolic reflector fed by a linear array, the elements of which were fed in series from a folded delay line, known as a serpentine feed. A change in frequency resulted in different electrical lengths to each element, changing the phasing to each radiator.

Stevenson [38] described the theory of a slotted waveguide in 1948, and Spradley [39] built a two-dimensional scanning array using slotted waveguides in 1958. The array provided independent phase control at every element to allow electronic phase scanning in the H-plane. The array was also fed by a frequency-sensitive serpentine feed to permit frequency scanning in the E-plane. Spradley's experiments motivated Ishimaru and Tuan [40] to develop a general theory of frequency scanned arrays. The first operational planar phased arrays were the AN/SPS-32 and AN/SPS-33 [17]. Development on these systems began in 1956 and 1958, respectively.

Milne [41] discussed and implemented a combination of pulse compression with frequency scanning for three-dimensional radars. In typical serpentine-fed frequency scanned arrays, the signal pulse length should be much greater than the feed delay in order to prevent a smeared beam and a consequent loss of gain. This limits the use of

very wideband signals in frequency scanned arrays. Milne devised an approach to transmit a wideband frequency modulated signal through a floodlight illuminator. Wideband pulse compression was then applied, with the antenna sidelobes serving as a weighting filter for range sidelobe suppression. This work demonstrates the importance of designing the antenna and waveform jointly.

A key feature of frequency scanned arrays is that frequency is varied as a function of time to achieve beam steering. By contrast, the frequency diverse array developed in this thesis applies different frequency components simultaneously, with the different constituent frequencies applied to different spatial channels of the array.

2.1.3. Waveform Diversity

For many years, conventional radars transmitted and received the same waveform, and processed that waveform identically on every pulse or burst within a coherent processing interval. Constant false alarm rate processing [42] was introduced in the late 1950s [43], and adaptive arrays appeared in the 1960s and 1970s [44], [45]. For the first time, the processing of received signals changed depending on the environment. However, even these early realizations of adaptivity were in reality implementations of deterministic algorithms.

More recently, knowledge-based radar signal and data processing has been developed. Knowledge-based processing takes advantage of known information about the target scene and interference environment, and alters algorithms, data, and parameters based on this information. For example, space-time adaptive processing requires the selection and use of secondary data to form an estimate of the interference in the cell being examined. Typically, these secondary cells are selected symmetrically from ranges about the cell under test. This assumes, however, that the neighbouring range cells are statistically similar to the cell of interest. Specifically, the secondary cells are usually assumed to be independent and identically distributed. If the neighbouring cells do not

resemble the cell under test for the null hypothesis, adaptive processing performance will suffer. Using multi-scan radar measurements, map data, known radar location, antenna pointing direction, and other sources of information, a knowledge-based system can recognize cells that are more likely to be representative, and use those cells in adaptive processing to improve performance [46], [47]. In addition to filtering (space-time adaptive processing or STAP), knowledge-based processing has also been shown to improve the detection and tracking stages of a radar processor [48] - [50].

STAP and knowledge-based processing provided adaptivity on the receive portion of the radar system. Recent work has extended adaptivity to the transmitted waveform as well. With waveform diversity, the transmitted signal changes to better match the target and interference environment.

Prior to the 1990s, waveform diversity did not exist as a separate research area, but instead activities occurred as a part of a variety of other efforts. Interest in high power microwave effects accelerated interest in waveform manipulation during the 1950s.

In 1953, Dicke [51] became the first to suggest the use of linear frequency modulation (LFM) to achieve pulse compression. In LFM, the carrier frequency of a pulse is changed linearly with time over the duration of the pulse. A matched filter on receive results in an effective pulse length less than the transmitted pulse, thereby achieving improved range resolution while radiating energy corresponding to the longer transmitted pulse. The 1960s then saw an explosion of interest in waveform design for clutter rejection, electromagnetic compatibility, and spread spectrum techniques for communication and radar. A number of people began to investigate optimum transmit waveforms in the presence of clutter [52]-[60].

Ultra-wideband (UWB) techniques and impulse radar were also pursued, due to the high range resolution they offered. Fig. 2-1 shows the impulse response of a B-57 aircraft, measured on August 17, 1970 [61]. This was an early example of matching the

transmitted radar waveform to the intended target. Other early work in this area is described in [62]-[64].

Figure removed from online version

Fig. 2-1: Impulse response of a B-57 aircraft (August 17, 1970)

Also during this period, temporal-spatial compression [65] was demonstrated using various antenna designs. This technique took advantage of the dispersion in an antenna system, using it as a pulse compression network to maximize signal parameters. Fig. 2-2 shows the transmitting transfer function achieved with a 100 picosecond pulse excitation, demonstrating temporal-spatial compression using a log-periodic antenna. Temporal-spatial compression was also demonstrated using a pair of co-planar log-periodic antennas, as well as 20 foot TEM horns. The major breakthrough of this work, just being fully realized now, is that the antenna system and transmitted and received waveforms should be designed jointly for maximum effect. Recall that Milne [41] utilized an antenna pattern to suppress the range sidelobes of a compressed pulse, suggesting a similar conclusion.

Figure removed from online version

Fig. 2-2: Temporal-spatial compression with a log periodic antenna, Model APN-502A

The use of diversity expanded further with the exploitation of polarisation modulation. Van Etten [66] extended the linear frequency modulation concept by simultaneously transmitting orthogonal polarisations, with the frequency difference between channels varying over time, as illustrated in Fig. 2-3. This technique induced a polarization rotation over the duration of the transmitted pulse. The same effect can be accomplished on a pulse-to-pulse basis in order to increase signal-to-noise ratio.

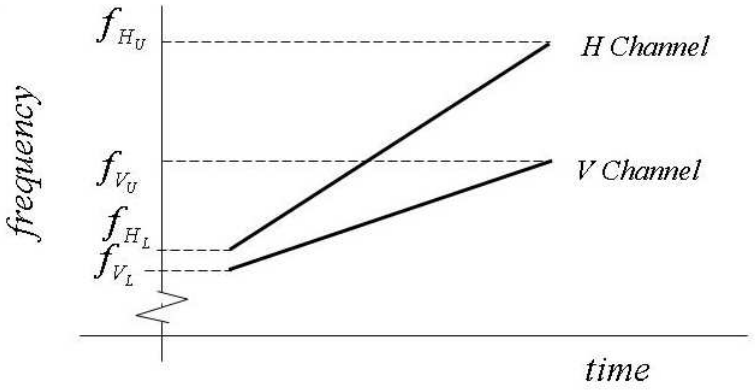

Fig. 2-3: Polarisation rotation. In the quasi-stationary condition, a polarisation rotation is induced over the duration of the transmitted pulse.

Interest in UWB applications also continued, along with polarization diversity, leading Wicks to develop an orthogonally polarized quadraphase electromagnetic radiator [67] for wideband applications. This design presented a nearly dispersionless, dual orthogonally-polarized antenna with 100:1 bandwidth. At about the same time, “clutter shredding” was demonstrated to suppress interference and resolve closely spaced targets. Clutter shredding resolves individual scatterers on a distributed object, providing noise-limited regions suitable for detection processing of objects of interest. Fig. 2-4 shows improved measured resolution with bandwidth utilizing widely spaced aperture elements in a sparse array. The detected objects in this result were 8 foot long, half-inch copper water pipes, separated by a distance of 2 inches in range and 12 inches in cross-range at a range of 2 miles. Just as previous works showed the importance of

joint design of signals and antennas, the clutter shredding work combined ultra-wideband waveforms with sparse aperture techniques, but also introduced the importance of joint signal processing design.

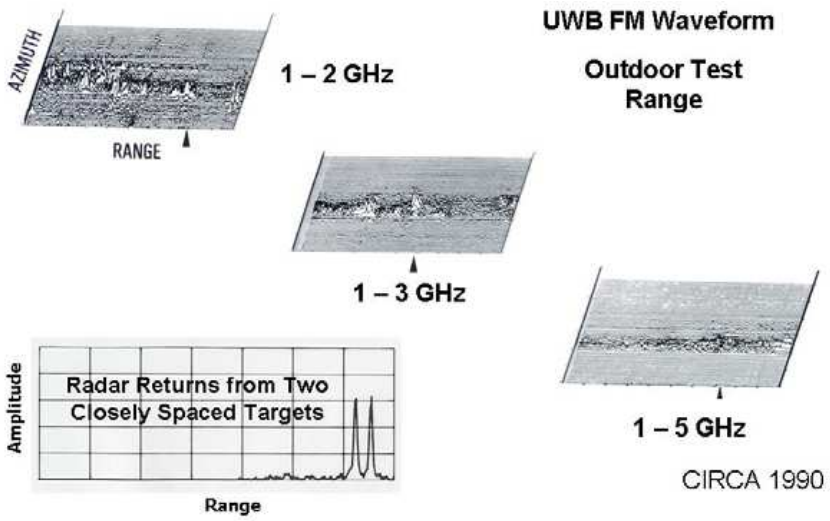

Fig. 2-4: Clutter shredding for suppression of interference and resolution of closely spaced targets.

Interest in wireless communications increased rapidly in the 1990s, and waveform diversity began to emerge as a distinct technology. Waveform diversity techniques were exploited to provide multiple independent channels for message signals in order to increase redundancy and reduce bit error rates. Wireless systems utilized diversity in time, space, frequency, and polarization. Besides communications, renewed interest was shown in optimal waveforms for radar applications. Guerci and others [68]-[71] investigated the joint design of transmit and receive reference waveforms in the presence of targets and interference. Building on previous waveform design and knowledge-based activities, a fully adaptive radar is now possible, where the radiated waveforms and the processing of those waveforms vary, and are mathematically optimized, dynamically in response to the environment.

Returning to the concept of joint design of antenna and waveform systems, distributed apertures began to be considered as a generalization of classically designed multi-static radar system concepts. Distributed apertures are currently being investigated for their fine angular resolution, with orthogonal waveforms and frequency diversity applied for the suppression of grating lobes [72], [73]. Such systems are being proposed for precision engagement, as well as for ground moving target indication applications. Distributed apertures combined with waveform diversity can produce fine angular resolution while suppressing grating lobes. At the same time, others are extending traditional multiple-input multiple-output techniques with frequency diversity for radar applications [74], [75]. Also, by exploiting spatial diversity in lieu of bandwidth, radio frequency tomography is demonstrating improved resolution with spatially distributed sensors and ultra-narrow band emissions [76].

An approach to achieve simultaneous radar and embedded communications was developed in the 1990s by Wicks, as reported in [28]. And in 2000, the U.S. Air Force, Army, and Navy organized a Tri Service Waveform Diversity Working Group to address single-aperture sensors performing other functions, including navigation and communications. This Working Group led to the establishment of an annual international conference on waveform diversity and design. A variety of other efforts were also launched, including a U.S. Air Force Office of Scientific Research Multi-disciplinary University Research Initiative, and demonstrations at the U.S.A.F. Research Laboratory Rome Research Site and the Naval Research Laboratory. In fact, due to the new interest in and evolving nature of adaptive transmit technology, the IEEE has recently adopted a new standard definition of the term *waveform diversity* [77]: "Adaptivity of the radar waveform to dynamically optimize the radar performance for the particular scenario and tasks. May also exploit adaptivity in other domains, including the antenna radiation pattern (both on transmit and receive), time domain, frequency domain, coding domain and polarization domain". Notice that the IEEE definition of waveform diversity explicitly encompasses multiple dimensions, including

the spatial (antenna) domain. This new definition specifically recognizes the importance of the joint design of signals and antennas.

It should be noted that many of today's waveform and spatially diverse capabilities are made possible due to the advent of lightweight digital electronics. Since Gordon E. Moore published his famous monograph in 1965 [78], the number of components per device, and hence processing power, has doubled roughly every two years. This review of prior work has revealed a number of important contributions to waveform diversity, but the early pioneers were limited by vacuum tube semiconductors, mechanical switches, hardware signal processors (e.g., surface acoustic wave pulse compression devices), and slide rule computers. The state of technology limited engineers from realizing the kernels of waveform diversity imagined at that time. By contrast, today's technology offers programmable waveform generators, which allow a different waveform to be applied to each spatial channel. Moreover, the individual oscillators can be tied together to achieve coherency. Today it is possible to generate more complex waveforms than can currently be analysed.

While the future validity of Moore's Law has been hotly debated for over a decade [79], [80], the near term suggests that further reductions in size and power will be achieved through three-dimensional integration of integrated circuits [81]. These reductions in size, weight, and power will further enable waveform diversity on a single aperture or platform. In addition, the development of distributed positioning, navigation, and timing systems [82], [83] will make waveform diversity possible for distributed multi-channel systems with waveform diversity technology.

2.1.4. Multiple Input – Multiple Output Systems

Kaye and George were the first to devise a multiple input – multiple output scheme for communications applications [1]. This 1970 work derived the general form of an optimum receiver for multiple channels combined with multiplex transmission of pulse amplitude modulated (PAM) signals, utilizing the minimum mean square error criterion. In general, the multiple channels were allowed to be randomly time variant. The goal of this work was to reduce the effect of signal fading by the introduction of multiple, independent paths from the transmitter to the receiver. The mitigation of fading resulted in increased channel capacity and improved bit error rates. Van Etten [2] extended this work in 1975 for the zero-forcing and minimum error probability criteria. Nearly a decade later, Winters [3] - [6] performed a series of investigations to explore optimum signal combining for spatial diversity, in order to mitigate both Rayleigh fading and co-channel interference.

A series of papers in the 1990s addressed the channel capacity improvements of MIMO communication systems. Foschini introduced the Bell-laboratories Layered Space-Time (BLAST) architecture [7], a MIMO structure which transmitted parallel data streams simultaneously on the same frequency for multipath mitigation. Foschini and Gans [8] computed the channel capacity of the BLAST architecture in white noise, and Telatar [9] also computed channel capacity limits of multi-antenna architectures. All of the above work was performed to investigate or evaluate the transmission of a signal from one point to another in the presence of fading or co-channel interference.

Fishler et al. [10] and Robey et al. [11] were the first to suggest MIMO technology for radar applications. Similar to reducing the effects of fading on a communications channel, *statistical MIMO* was proposed to reduce the effects of target scintillation due to radar cross section (RCS) fluctuations of a target. Fig. 2-5 shows the measured RCS of an aircraft target as a function of angle. It can be clearly seen that small changes in angle can result in large changes in the RCS. Swerling [84] created four classes of

fluctuating targets in order to study the probability of detection of complex targets. The first two cases assume a Rayleigh probability density function, implying that the target is composed of many independent scatterers of roughly equal size. The first case assumes scan-to-scan fluctuation while the second case assumes a more rapid pulse-to-pulse fluctuation. The other two cases assume one dominant scatterer and several smaller scatterers, representing scan-to-scan and pulse-to-pulse fluctuations, respectively.

Figure removed from online version

Fig. 2-5: Radar cross section of a B-26 aircraft as a function of angle [85].

Interest in MIMO radar has exploded since its initial introduction, and several conference sessions and at least one book [86] have been devoted to the topic. Besides improved detection performance against fluctuating targets and multipath, MIMO radar is said to enable adaptive array techniques for improved resolution and interference rejection, and more flexible beam pattern design [12]. More recent work is investigating the use of the MIMO construct for bistatic and distributed sensor applications [74], [13]. However, MIMO radar is not without its skeptics. Daum and Huang recently presented a lively debate over MIMO radar in [87], challenging among other things a loss in signal-to-noise ratio and system cost.

The original *statistical MIMO* concepts were developed to provide multiple independent signal paths for the reduction of fading. These approaches utilized widely spaced elements, including bistatic and netted sensor configurations, and used large frequency separations between spatial channels. More recent *coherent MIMO* approaches are being considered for more closely spaced elements, but these approaches still tend to use relatively large frequency separations between spatial channels, so that there is no significant overlap of the spectra of signals between spatial channels. On the other hand, the frequency diverse array utilizes very small changes in frequencies between channels, exploiting the principle of stationary phase. The frequency diverse array also provides very different beam properties than MIMO in range, as well as in angle and time. These new beam properties enable new capabilities, such as range-dependent beamforming and auto-scanning in angle without the need for phase shifters or mechanical beam steering.

2.1.5. Frequency Diverse Arrays

The initial publication of the frequency diverse array concept by Antonik et al. [88], [89] and the filing of patents under this work by Wicks and Antonik [90], [91], [92] generated significant interest in the frequency diverse array. Secmen et al. [93] published a paper describing the time and angle periodicity of the array pattern, and also presented a clever graphical representation of this radiated field, which was a polar version of the representation shown by Antonik et al in [89]. Sammartino et al [74] examined the performance of a frequency diversity configuration as part of an analysis of various algorithms and implementations for multiple input – multiple output and netted radar systems. However, this analysis specifically considered the case of transmitted signals separated widely in frequency, such that the spectra were neither overlapping nor contiguous. Huang et al [94] performed a detailed electromagnetic simulation of the frequency diverse array including realistic antenna structures. More recently, Sammartino and Baker [75] have designed a frequency diverse system for

bistatic radar applications, utilizing widely separated spatial channels and non-linear spacing between elements. Also, Higgins and Blunt [95] have further explored range and angle coupled beamforming using frequency diverse chirp signals. This work analyzed and computed the ambiguity diagrams for waveforms similar to those suggested in [89] and [92].

This thesis describes the original frequency diverse array configuration with closely spaced elements radiating waveforms of different frequencies, with significant spectral overlap between spatial channels. The thesis describes the theory of the frequency diverse array, makes predictions via simulation, and validates the predictions through full experimentation of radiated waveforms.

2.2 Summary of Prior Work

A review of the relevant literature shows that the frequency diverse array is a novel contribution, separate and distinct from previously published works. The frequency diverse array provides new degrees of freedom in range, angle, and time for the design and control of antenna radiation patterns. The described research provides antenna patterns that vary in direction as a function of range, that are periodic in time, and that scan in angle without the need for phase shifters or mechanical steering. In addition, extended versions of the frequency diverse array concept may allow for new radar modes, such as the operation of moving target indication and synthetic aperture radar at the same time.

Chapter 3

Antenna Array Theory

In this chapter, the basic theory underpinning beam formation in array antennas is introduced. This provides a platform from which the novel frequency diversity concepts are developed in Chapter 4.

3.1. Phased Array

To find the electric field of a radiating element, it is first convenient to find the magnetic vector potential from the impressed current density. In the manner of Lo [96], the magnetic vector potential due to a single element in the far field is:

$$\overline{A}(\bar{r}) = \frac{\mu}{\pi}\frac{e^{-jkr}}{r}\int_V \overline{J}(r_i')e^{j\,k\,r_i'\cos\xi}dV', \tag{3-1}$$

where:

$\overline{J}(r_i')$	=	Electric current distribution in the element
$\bar{r}$	=	Position vector of the observation point
$\bar{r}_i'$	=	Position vector of the source
V	=	Volume of the source element
dV'	=	Differential volume element of the source

$\cos\xi$ = $\hat{r}\cdot\hat{r}_i'$

k = Free space wave number, $\frac{2\pi}{\lambda}$

The electric field in the far-field region ($r > \frac{2D^2}{\lambda}$, where D is the largest dimension of the antenna) is then:

$$\bar{E}(r) = -j\omega\bar{A} + \frac{1}{j\omega\varepsilon}\nabla\nabla\cdot A \quad . \tag{3-2}$$

For an array of elements this becomes

$$\bar{E}(r) \approx \frac{-j\omega\mu\, e^{-jkr}}{4\pi r}\,\bar{f}(\theta,\phi) \quad , \tag{3-3}$$

where: $$\bar{f}(\theta,\phi) = \sum_{i=1}^{N}\bar{f}_i(\theta,\phi) \tag{3-4}$$

and $\bar{f}_i(\theta,\phi)$ are the element patterns of the individual elements.

Note that $\bar{f}(\theta,\phi)$ is related to the integration of current density over volume in (3-1) for all elements.

Assuming that all elements in the array are identical, and neglecting mutual coupling,

$$\bar{f}_i(\theta,\phi) = I_i\ \bar{f}_0(\theta,\phi) \quad , \tag{3-5}$$

where I_i is the current excitation of the i^{th} element, and $\bar{f}_0(\theta,\phi)$ is the element pattern of a single element.

Then,

$$\bar{E}(r) \approx \frac{-j\omega\mu e^{-jkr}}{4\pi r} \bar{f}_0(\theta,\phi) F(\theta,\phi) \quad , \tag{3-6}$$

where

$$F(\theta,\phi) = \sum_i I_i e^{jk\hat{r}\cdot r_i} \quad . \tag{3-7}$$

$F(\theta,\phi)$ is known as the array factor, which represents the antenna pattern for an array of identical isotropic elements. The array factor describes the variation of the electric field with angle.

Consider a single point source located in space in a rectangular coordinate system with an arbitrary reference, as shown in Fig. 3-1.

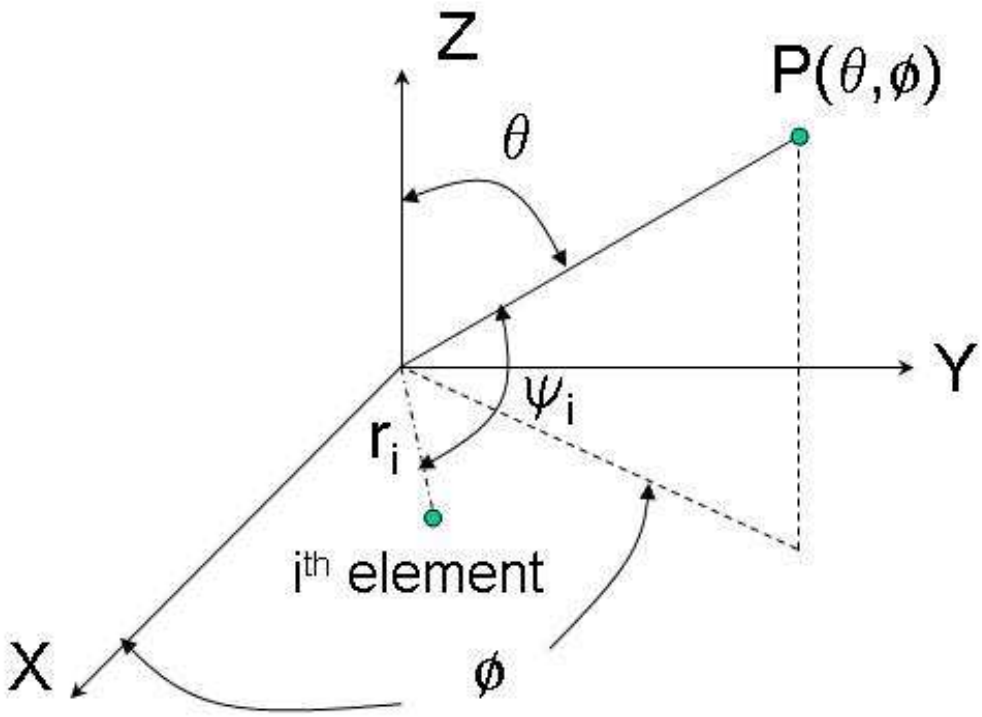

Fig. 3-1: Geometry for the calculation of the electric field of a single isotropic radiator

The array factor for the single element in Fig. 3-1 can be written as:

$$F_i(\theta,\phi) \quad = \quad I_i\, e^{j[\frac{2\pi}{\lambda} r_i \cos\psi_i + \alpha_i]} \tag{3-8}$$

where:

I_i = magnitude of the current distribution,

r_i = the distance of the element from an arbitrary reference,

ψ_i = angle between the distance vector and the pointing vector, or the direction cosine,

α_i = initial phase applied to the element, and

λ = wavelength of the radiated signal.

Now consider a linear array of an odd number of elements, N, placed along the *x*-axis as shown in Fig. 3-2. The array factor for the linear array is simply the sum of the contributions from each of the individual elements:

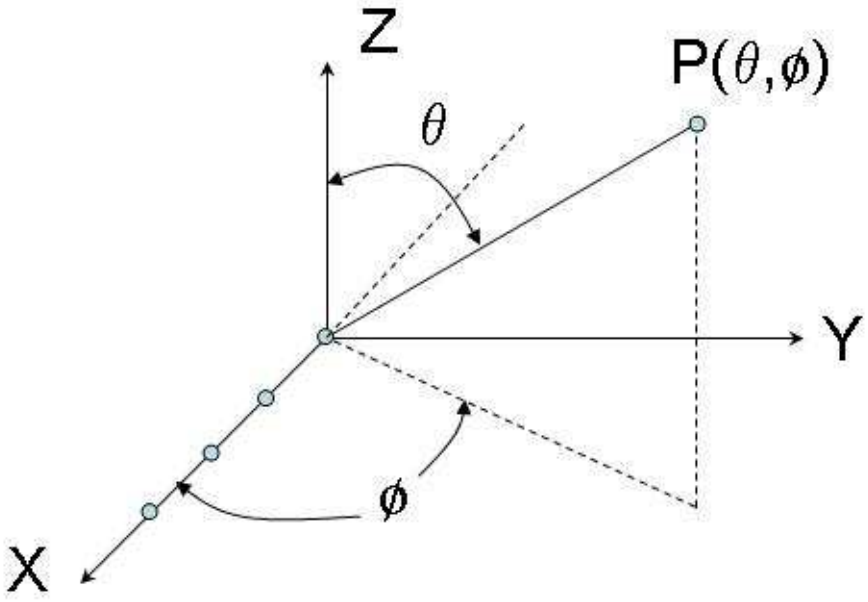

Fig. 3-2: A linear array of isotropic radiators

$$F(\theta,\phi) = \sum_i I_i e^{j\left[\frac{2\pi}{\lambda} r_i \cos\psi_i + \alpha_i\right]} \tag{3-9}$$

$$= \sum_i I_i e^{j\alpha_i} e^{j\left[\frac{2\pi}{\lambda} r_i \cos\psi_i\right]}. \tag{3-10}$$

Let

$$W_i = I_i e^{j\alpha_i}, \tag{3-11}$$

where W_i represents the complex weighting of the aperture current distribution for the ith element. For simplicity, let the magnitude of the current distribution of each element be unity, and also let the initial phase of each element be zero. Then W_i = 1 for all *i*.

Also let the elements be placed along the *x*-axis with spacing *d*, such that:

$$r_i = x_i = id, \qquad 0 < i < N-1, \tag{3-12}$$

where *N* is the number of elements.

Next consider only field points in the *x*-*z* plane, such that $\cos\psi_i = \sin\theta$. Equation 3-3 then becomes:

$$F(\theta) = \sum_{i=0}^{N-1} e^{j\left[\frac{2\pi}{\lambda} id \sin\theta\right]} . \tag{3-13}$$

This is essentially the expression given by in [31], except that the result given there is normalized by $\frac{1}{\sqrt{N}}$ to show that each element receives $\frac{1}{N}$ of the total input power.

The arrangement of elements in the *x*-*z* plane is illustrated in Fig. 3-3. Notice that the path length from each element to the planar wave front in direction θ varies linearly across the array. This change in path length causes a phase shift, which affects the contribution of each element to the total radiated field.

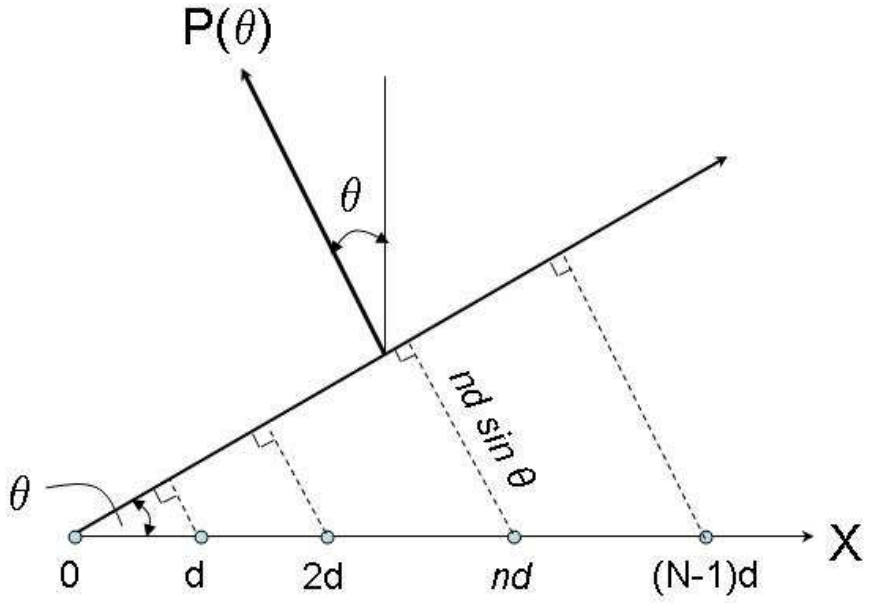

Fig. 3-3: Path lengths of elements across an array increase linearly in direction off broadside.

To simplify equation (3-13), first place the array reference at the array centre as shown in Fig. 3-4.

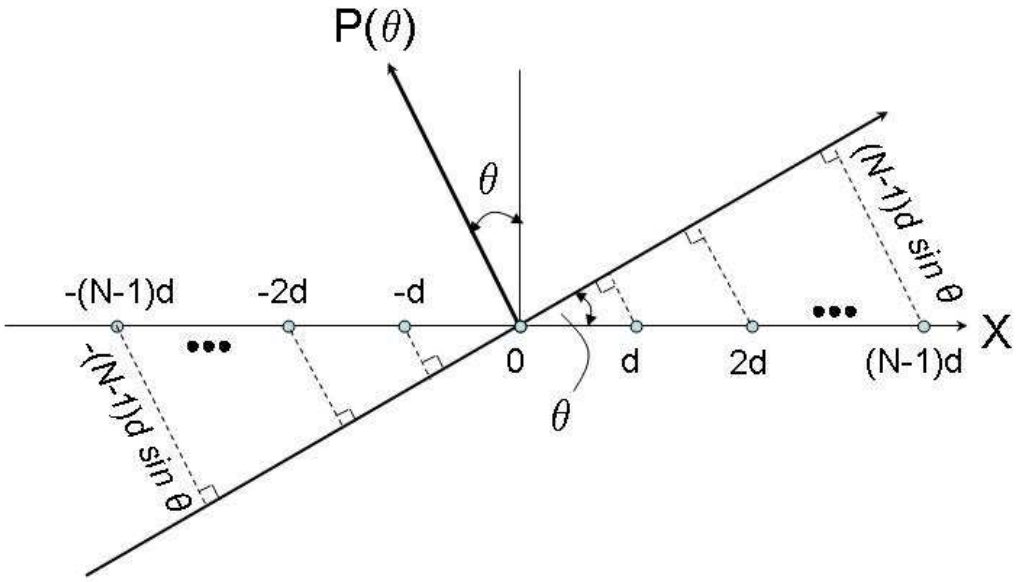

Fig.3-4: Array reference taken at centre

Equation (3-13) then becomes:

$$F(\theta) = \sum_{i=-\frac{(N-1)}{2}}^{\frac{N-1}{2}} e^{j\left[\frac{2\pi}{\lambda} id \sin\theta\right]} \quad . \tag{3-14}$$

Introducing the change of variable $n = i + \frac{(N-1)}{2}$, and normalizing so that $F(\theta)$ is unity at $\theta = 0$,

$$F(\theta) = \frac{1}{N} \sum_{n=0}^{N-1} e^{j\left[\frac{2\pi}{\lambda} nd \sin\theta\right]} e^{-j\left[\frac{2\pi}{\lambda}\left(\frac{N-1}{2}\right) d \sin\theta\right]} \tag{3-15}$$

$$= \frac{1}{N} e^{-j\left[\frac{(N-1)\pi}{\lambda} d \sin\theta\right]} \sum_{n=0}^{N-1} e^{j\left[\frac{2\pi}{\lambda} nd \sin\theta\right]} \quad . \tag{3-16}$$

$$= \frac{1}{N} e^{-j\left[\frac{(N-1)\pi}{\lambda} d \sin\theta\right]} \times \left[1 + e^{j\frac{2\pi}{\lambda} d \sin\theta} + e^{j\frac{2\pi}{\lambda} 2d \sin\theta} + \cdots e^{j\frac{2\pi}{\lambda}(N-1) d \sin\theta}\right] . \tag{3-17}$$

But

$$1 + x + x^2 + \cdots + x^{N-1} = \frac{x^N - 1}{x - 1} \quad . \tag{3-18}$$

Substituting

$$x = e^{j\frac{2\pi}{\lambda} d \sin\theta} \quad , \tag{3-19}$$

$$
\begin{aligned}
F(\theta) &= \frac{1}{N}\left[\frac{e^{j\frac{2\pi}{\lambda}Nd\sin\theta}-1}{e^{j\frac{2\pi}{\lambda}d\sin\theta}-1}\right]e^{-j\frac{\pi}{\lambda}(N-1)d\sin\theta} \\
&= \frac{1}{N}\left[\frac{e^{j\frac{2\pi}{\lambda}Nd\sin\theta}-1}{e^{j\frac{2\pi}{\lambda}d\sin\theta}-1}\right]e^{-j\frac{\pi}{\lambda}N\,d\sin\theta+j\frac{\pi}{\lambda}d\sin\theta} \\
&= \frac{1}{N}\left[\frac{\left(\frac{e^{j\frac{\pi}{\lambda}Nd\sin\theta}}{e^{-j\frac{\pi}{\lambda}Nd\sin\theta}}-1\right)\left(e^{-j\frac{\pi}{\lambda}Nd\sin\theta}\right)}{\left(\frac{e^{j\frac{\pi}{\lambda}d\sin\theta}}{e^{-j\frac{\pi}{\lambda}d\sin\theta}}-1\right)\left(e^{-j\frac{\pi}{\lambda}d\sin\theta}\right)}\right] \\
&= \frac{1}{N}\left(\frac{e^{j\frac{\pi}{\lambda}Nd\sin\theta}-e^{-j\frac{\pi}{\lambda}Nd\sin\theta}}{2j}\right)\left(\frac{2j}{e^{j\frac{\pi}{\lambda}d\sin\theta}-e^{-j\frac{\pi}{\lambda}d\sin\theta}}\right), \qquad (3\text{-}20)
\end{aligned}
$$

and

$$
F(\theta) = \frac{\sin\left(\frac{\pi}{\lambda}N\,d\sin\theta\right)}{N\sin\left(\frac{\pi}{\lambda}d\sin\theta\right)}\ . \qquad (3\text{-}21)
$$

The array of (3-21) is shown in Fig. 3-5 for a 10-element linear array with $d=\frac{\lambda}{2}$.

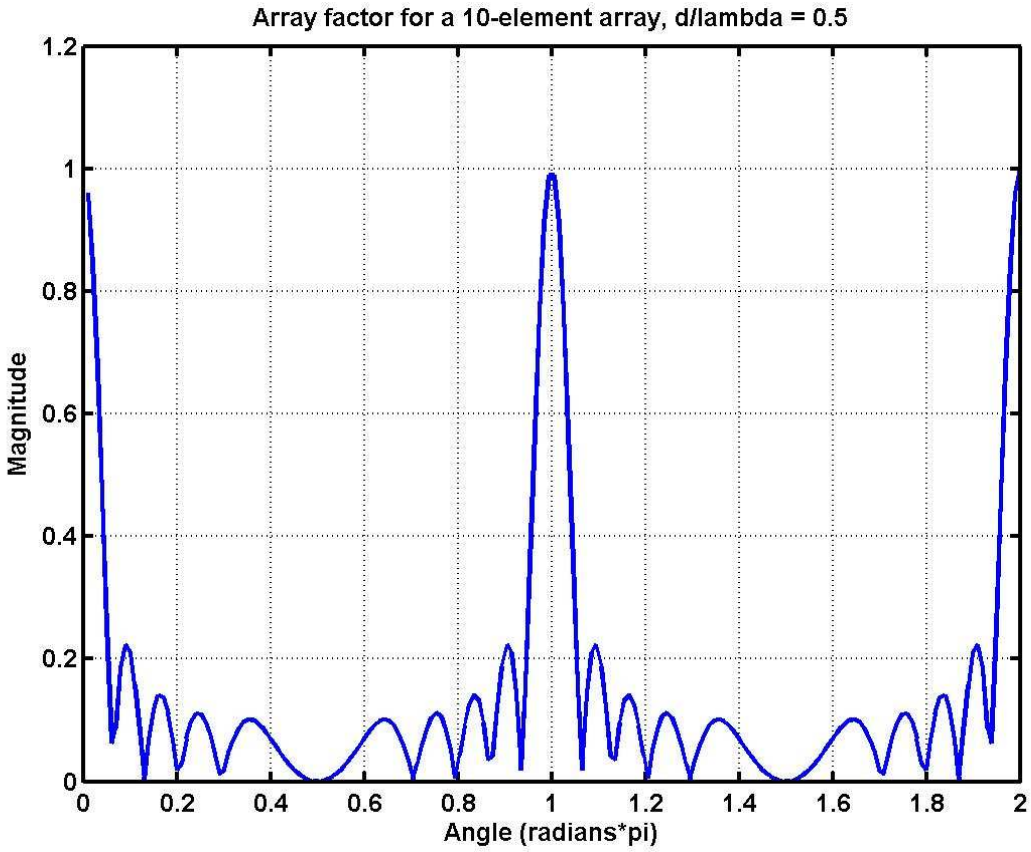

Fig. 3-5: Array factor for a 10-element array with half-wavelength spacing

Returning to equation (3-10), and substituting the expression for the complex weight in (3-11), the array factor can be expressed as:

$$F_i(\theta,\phi) \quad = \quad \sum_{i=-N}^{N} W_i \, e^{j[\frac{2\pi}{\lambda} r_i \cos\psi_i]} \qquad . \tag{3-22}$$

Again make the substitution of (3-12) and let

$$k \quad = \quad \frac{2Nd\cos\psi_i}{\lambda} \; . \tag{3-23}$$

Then let $N' = 2N$ and count from the end of the array:

$$F_i(k) \quad = \quad \sum_{i=0}^{N'} W_i \, e^{j[\frac{2\pi}{N'}]ik} \qquad . \tag{3-24}$$

Equation (3-24) is in the form of a discrete Fourier transform. Therefore, the array factor and the aperture illumination function are related through the Fourier transform in *k*-space. Variants of the *k* domain are sometimes known as spatial frequency, direction cosine space, *T*-space, sine space, or *u*-*v* space.

T-space represents the projection of points in space on a unit hemisphere to the *x*-*y* plane. Figure 3-6 illustrates T-space coordinates, where P is a point on the unit hemisphere, Z is the antenna boresight direction, and the spherical coordinates θ and ϕ are defined in the usual way. Using simple coordinate transformations, the *T*-space coordinates in the *x* and *y* directions become:

$$T_x \quad = \quad \sin\theta \cos\phi \quad , \tag{3-25-a}$$

$$T_y \quad = \quad \sin\theta \sin\phi \quad . \tag{3-25-b}$$

Letting $\phi = 0^\circ$, notice that $T_x = \sin\theta$. Likewise, letting $\phi = 90^\circ$ yields $T_y = \sin\theta$. This explains why T-space is sometimes called sine space.

"Real space" is defined as those points in space for which

$$\sqrt{T_x^{\,2} + T_y^{\,2}} < 1 \quad . \tag{3-26}$$

Physically, real space represents points in space for angles from antenna boresight to the horizon. The condition in Equation (3-26) also ensures that $\sin\theta \leq 1$.

A uniformly weighted aperture can be represented in Woodward's notation [97] as a *rect* function. Therefore, the array factor of a uniformly weighted array, computed by the Fourier transform, is a *sinc* function. This *sinc* function has nulls spaced at the reciprocal of the aperture length in wavelengths, and first sidelobes of approximately -13 dB with respect to the peak. The array factor of Figure 3-5 has been recomputed in Figure 3-7, showing the result as a function of sin θ instead of θ.

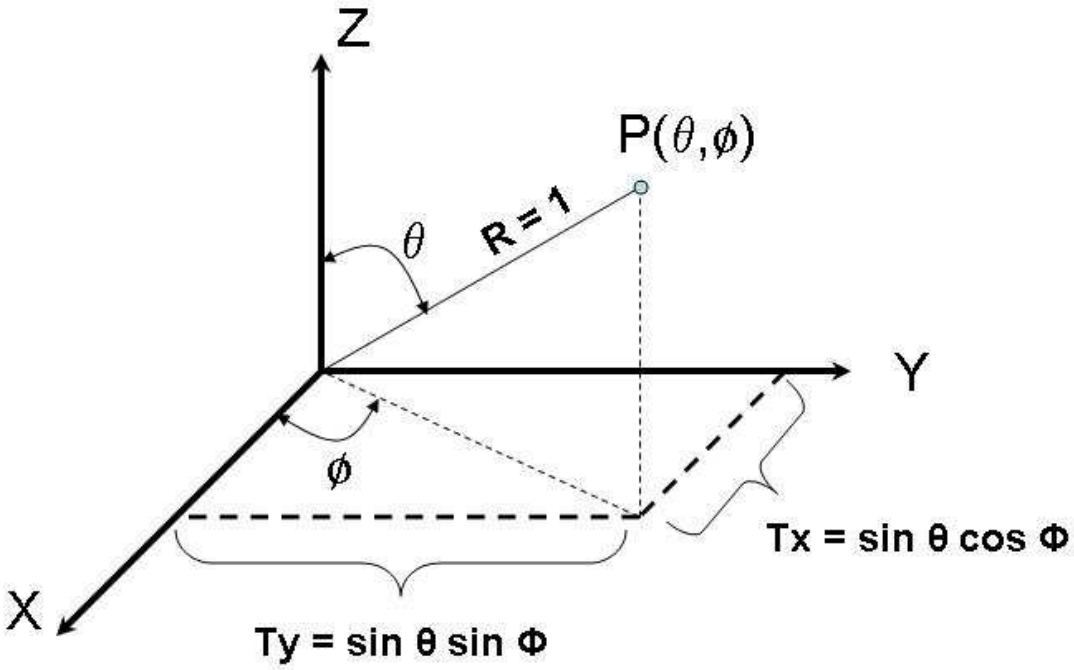

Fig. 3-6: T-space coordinates

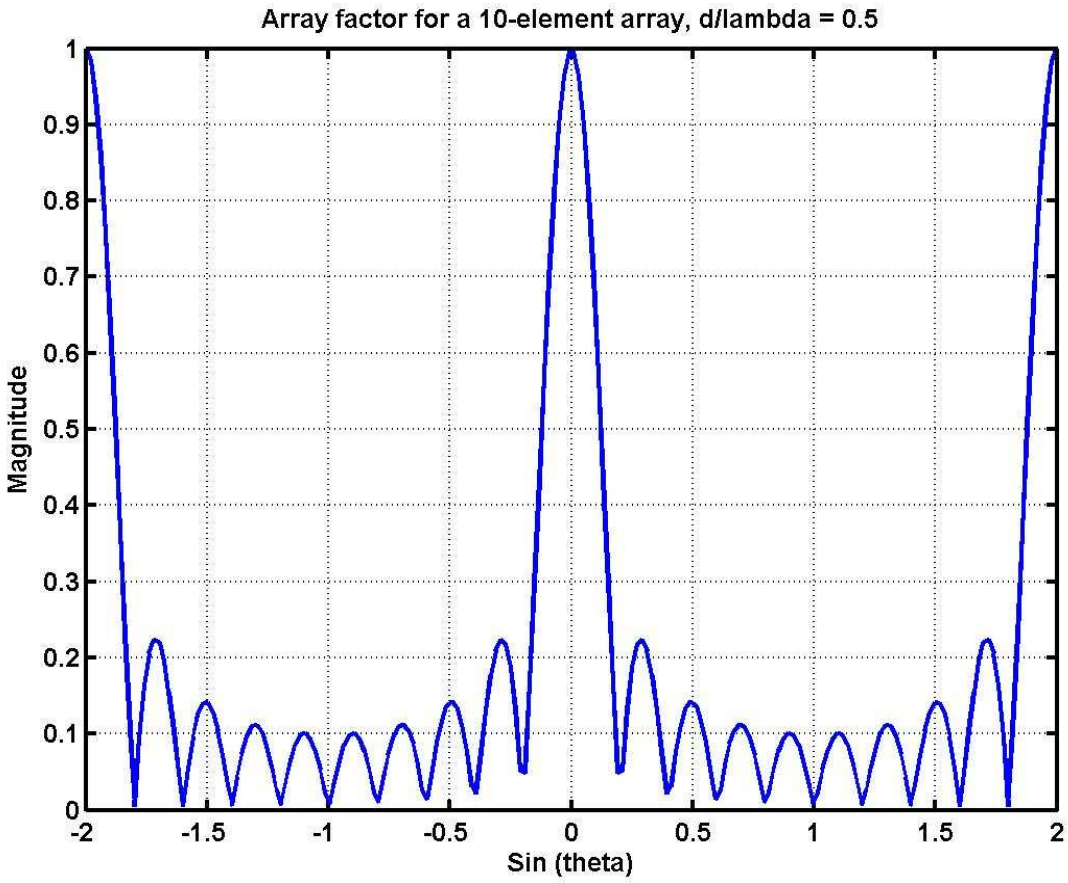

Fig. 3-7: Array factor of a 10-element array as a function of sin (θ). Pattern follows a *sinc* function in accordance with the Fourier transform.

The Fourier transform also explains the ambiguity of the pattern in angle, by analogy with time and frequency domain signals. If a time waveform is sampled at multiples of period *T*, the frequency spectrum of the signal becomes periodic (ambiguous) at the frequency sampling rate, $f_s = \frac{1}{T}$. In a similar manner, an aperture illumination function which is sampled at multiples of the element spacing in wavelengths (the locations of the array elements) becomes ambiguous at spatial frequencies of the reciprocal of this separation, or $\frac{\lambda}{d}$. In antenna theory, these ambiguities are known as grating lobes [31].

Notice in Figure 3-7 that an element spacing of λ/2 was used, and grating lobes appear at $\sin(\theta) = \pm 2$, even though $|\sin\theta| < 1$ for all θ. This indicates that the grating lobes fall outside of real space, and therefore consume no power in the sense that power cannot be radiated into imaginary space.

3.2. Beam Steering

In a dish or wire antenna system, steering of the main beam is accomplished by mechanically pointing the boresight of the antenna to the desired look direction. Electronically scanned antennas utilize two primary techniques to achieve beam steering: phase scanning or frequency scanning.

3.2.1. Phase Scanned Antennas

Equation (3-13) and Fig. 3-3 illustrated that the pattern in a given direction θ depends upon the path length distance from each element to the phase front. At a constant angle, the phase was shown to progress linearly across the elements. This same principle can be used to intentionally induce the beam to focus in a particular direction. By applying a linear phase shift across elements, the phase front adds constructively in the desired direction. In order to steer a planar wave front to angle θ_0, the phase of each successive element across the face of the array must be advanced by a phase of:

$$\psi_i = \frac{2\pi}{\lambda} i\, d \sin\theta_0 \ . \qquad (3\text{-}27)$$

In other words, the path length for the i^{th} element increases by $(id) \sin \theta_0$ so that the contribution from each element adds constructively in direction θ_0.

When this additional phase term is included in (3-13), Equation (3-21) becomes:

$$E(\theta) \;=\; \frac{\sin\left(\frac{\pi}{\lambda} N\, d\,(\sin\theta - \sin\theta_0)\right)}{N \sin\left(\frac{\pi}{\lambda} d\,(\sin\theta - \sin\theta_0)\right)} \quad . \tag{3-28}$$

This result is plotted in Fig. 3-8 for the case of Fig. 3-5, with $\theta_0 = \pi/6$. Notice that the beam shape is invariant with scan angle in sin θ space.

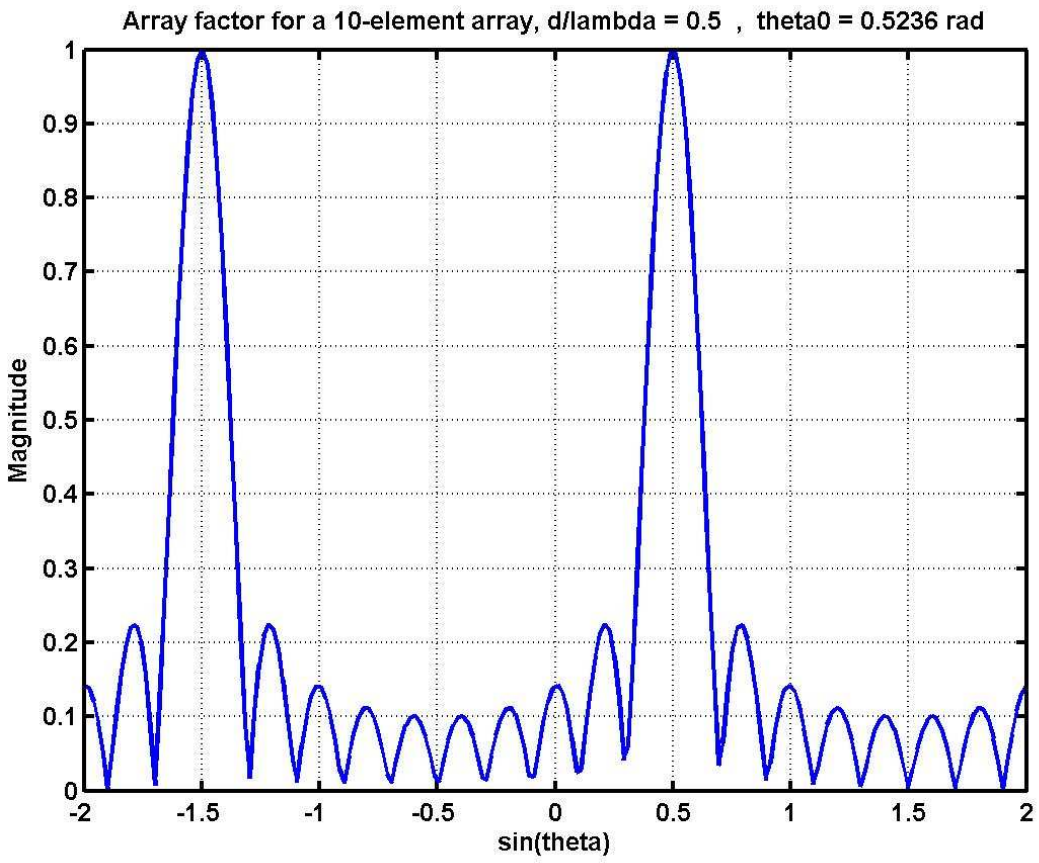

Fig. 3-8: Array factor for an electronically scanned 10-element array, $\theta_0 = \pi/6$.

The beam scanning properties of phased arrays can also be observed through the Fourier transform relationship between the aperture illumination function and the array factor. If the aperture illumination function is denoted as $f(x)$, and the array factor is denoted as $F(k)$, then:

$$f(x) \quad \Leftrightarrow \quad F(k). \tag{3-29}$$

But from the shifting theorem of Fourier transforms,

$$f(x)e^{j\omega x} \quad \Leftrightarrow \quad F(k-\omega). \tag{3-30}$$

In other words, applying a linear phase shift across the aperture results in a translation in spatial frequency space. Figure 3-7 illustrates that an array with element spacing of $\lambda/2$ can be electronically scanned a full $\pi/2$ radians before a grating lobe begins to appear in real space.

In phase steering an electrically scanned antenna, the length of the feed line to each element is generally equal. This is usually accomplished by a corporate feed network, as illustrated in Fig. 3-9. This feed structure attains its name since it resembles an inverted organizational chart for a corporation. Other types of feed structures are also possible, including Rotman lens [98] and Butler matrix [99] configurations.

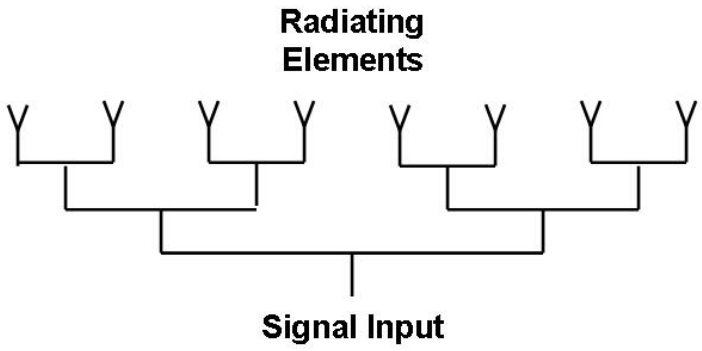

Fig. 3-9: Corporate feed structure for phase steering. All feed lines are equal length

3.2.2. Frequency Scanned Antennas

An alternative method to electronically steer an array of antennas is by frequency scanning [39], [40], [100]. Frequency scanning was the first form of electronic steering to be employed in operational radars [17], and, at least at one time, was the most widely used technique due to its simplicity, reliability, and relatively low cost [16].

Recall that phase is given by:

$$\psi = \frac{2\pi}{\lambda} l \quad , \tag{3-31}$$

where l is the path length, suggesting that a change of frequency can also induce a linear phase shift across an array to produce beam steering.

Consider a linear array of elements as in Fig. 3-3. The phase difference between successive elements to a planar wave front in direction θ is:

$$\psi = \frac{2\pi d}{\lambda} \sin\theta \quad . \tag{3-32}$$

In a manner similar to Hammer [37] or Ajioka [101], let successive elements be fed in series by a transmission line of length *S*, as shown in Fig. 3-10.

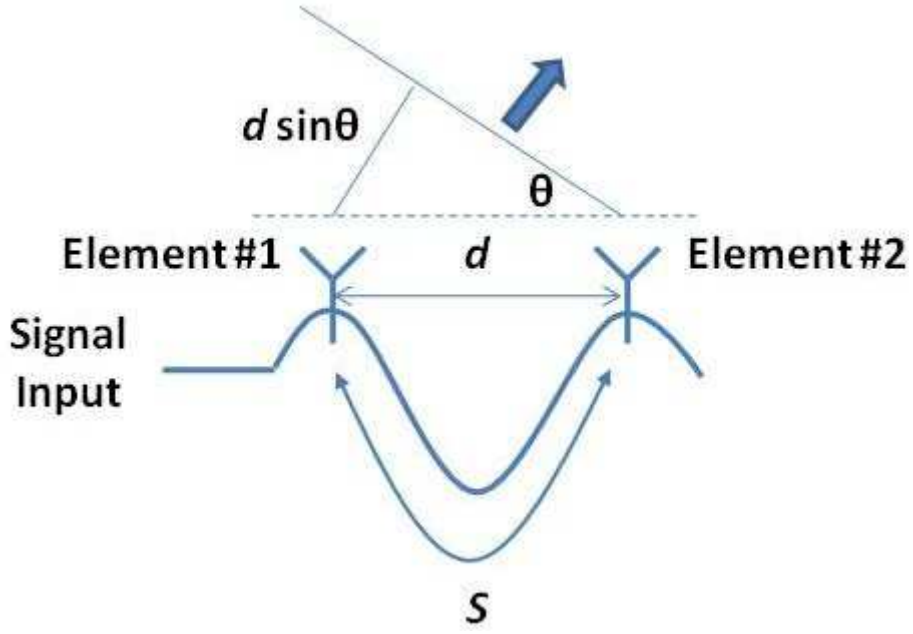

Fig. 3-10: Frequency scan array fed by serpentine feed

Signals from the two successive elements will be in phase in direction θ when:

$$\frac{2\pi}{\lambda} d \sin\theta = \frac{2\pi}{\lambda_g} S - 2\pi n \ , \qquad (3\text{-}33)$$

where: λ is the wavelength in free space,
d is the distance between radiating elements,
λ_g is the wavelength in the waveguide feed line,
S is the length of feed line between elements, and
n is any integer.

Solving for sin θ,

$$\sin\theta = \frac{S\lambda}{d}\left(\frac{1}{\lambda_g} - \frac{n}{S}\right). \tag{3-34}$$

Ajioka [101] then lets λ_{gm} be the feed line wavelength at the frequency for which *s* is *m* guide wavelengths long. That is,

$$\lambda_{gn} = \frac{S}{n}. \tag{3-35}$$

Substituting into (3-32) obtains

$$\sin\theta = \frac{s\lambda}{d}\left(\frac{1}{\lambda_g} - \frac{1}{\lambda_{gn}}\right), \tag{3-36}$$

which is called the frequency scan equation.

Differentiating, Drabowitch et al [102] derived an approximate expression for the change in angle with respect to a change in frequency for small angles. Specifically,

$$d(\sin\theta) = \frac{s}{d}\frac{\lambda_g}{\lambda}\frac{df}{f} \quad . \tag{3-37}$$

Examination of (3-34) through (3-37) shows that the scan angle of the antenna changes more rapidly with frequency when the delay in the feed is large compared to the spacing of the elements along the array, and that steering angle is proportional to the relative length of the waveguide, the ratio of the waveguide and free space wavelengths, and to the relative change in frequency.

In frequency scanned arrays the path lengths of feed lines to the radiators are not equal. The increasing line lengths along the array introduce a linearly progressive phase shift, and the frequency-sensitive properties of the transmission line result in a scan with frequency. Two common feed systems are used for frequency scanned arrays. Fig. 3-11 shows a series feed, where a folded transmission line is tapped at regular intervals to supply power to the radiating elements. The series feed is relatively simple to implement, and is therefore widely used in practice. Fig. 3-12 shows a parallel feed system. The parallel feed is similar to the corporate structure of Fig. 3-9, except that the delay lines are not equal length, and instead become progressively longer across the array.

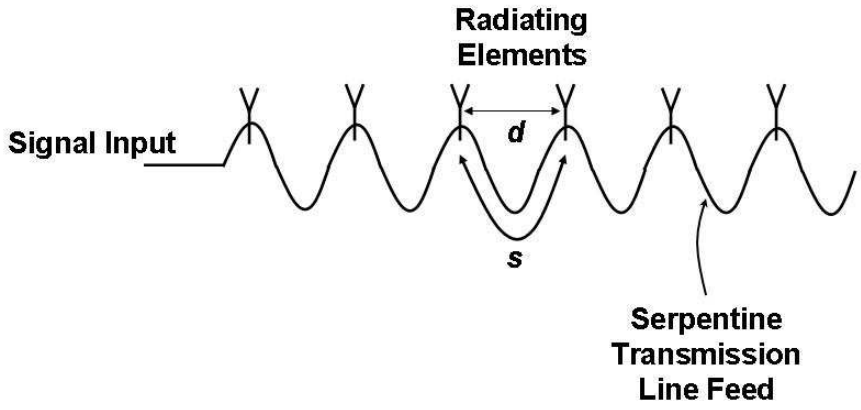

Fig. 3-11: Serpentine transmission line feed system for a frequency scanned array.

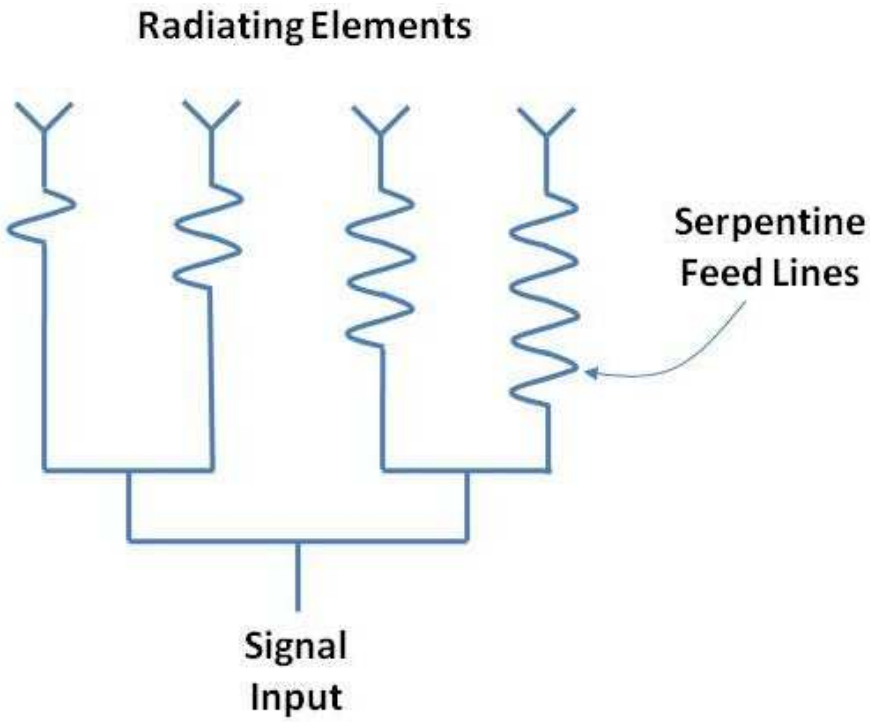

Fig. 3-12: Parallel feed system for frequency scan array

This chapter discussed conventional array theory, including beam steering and frequency scanned arrays. A key characteristic of the frequency scanned array is that the same signal is applied to all radiating elements, and frequency is varied over time to effect beam steering. The next chapter will discuss the new development of a frequency diverse array. The frequency diverse array is fundamentally different than the frequency scanned array in that it applies different signals of various frequencies simultaneously to each spatial channel. It will be shown that this provides additional degrees of freedom for the control of antenna patterns.

Chapter 4

Frequency Diverse Arrays

4.1. Concept

This chapter describes the new concept of a frequency diverse array. The frequency diverse array provides additional degrees of freedom for the design of array antennas, providing novel beam formation and control. The baseline configuration of a frequency diverse array is that a continuous wave signal is radiated from each spatial channel. A small frequency shift, on the order of a few Hertz, is applied between channels. This small frequency shift results in a beam pattern for which the beam focus direction changes as a function of range, angle, and time. This is significantly different than the conventional phased array, where the beam pointing direction is independent of range and time in the far-field.

In previous sections it was assumed that the signal input to each radiator in an array was identical, except for possibly an amplitude weighting for sidelobe control and a phase

shift for beam steering. This section examines array performance when all signals are not identical.

Consider a conventional phased array composed of ideal isotropic radiators, as shown in Fig. 4-1. As was seen in Chapter 3, if all of the waveforms emitted from the radiating elements are identical with identical phase, the antenna beam will point at broadside, or orthogonal to the face of the aperture. Now consider a far field target T at an angle θ with respect to the broadside direction. If all of the waveforms are identical continuous wave (CW) signals, then the only difference between the returns from adjacent radiating elements 1 and 2 is due to path length difference:

$$R_1 - R_2 \quad = \quad d \sin\theta \ , \tag{4-1}$$

where d is the spacing between elements.

The path length difference results in a phase shift from element 1 to element 2:

$$\psi \quad = \quad \frac{2\pi d}{\lambda} \sin\theta \ . \tag{4-2}$$

An incremental phase shift ψ from element-to-element (linear phase progression across the aperture) will steer the antenna mainbeam to angle θ, as was seen in Section 3.2.

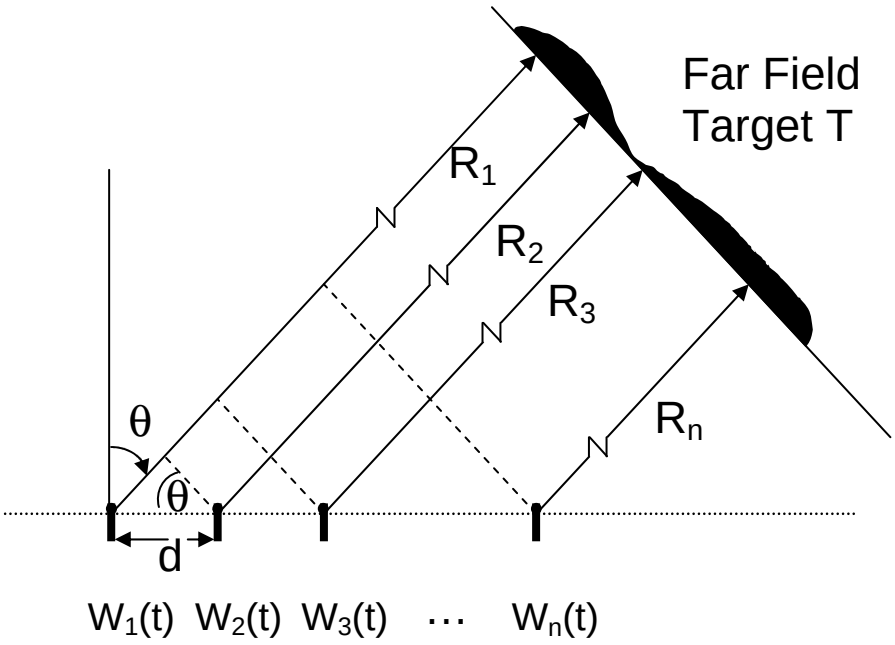

Fig. 4-1: Path length geometry for a target at angle θ in the far field.

Now allow the frequency of the waveform radiated from each element to increase by a small amount from element-to-element. This is illustrated in Fig. 4-2.

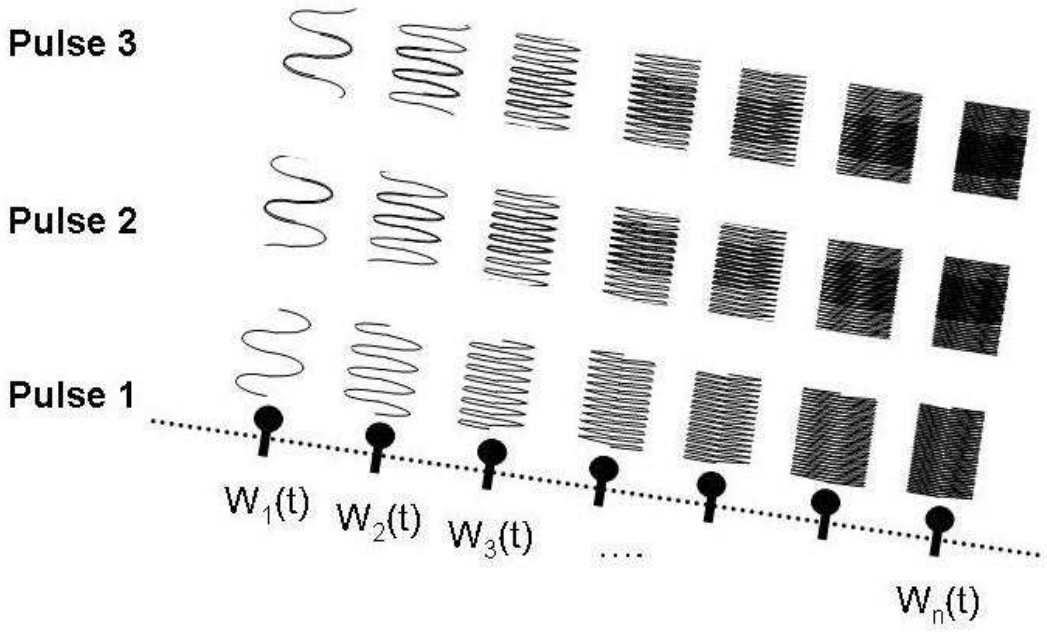

Fig 4-2: Frequency diverse array with frequency increasing linearly across elements.

For element 1, the phase due to one-way path length is:

$$\psi_1 = \frac{2\pi}{\lambda_1} R_1 = \frac{2\pi f_1}{c} R_1 \quad . \tag{4-3}$$

For element 2, the phase becomes:

$$\psi_2 = \frac{2\pi}{\lambda_2} R_2 = \frac{2\pi f_2}{c} R_2 \tag{4-4}$$

$$= \frac{2\pi (f_1 + \Delta f)(R_1 - d\sin\theta)}{c} \tag{4-5}$$

$$= \frac{2\pi f_1}{c} R_1 - \frac{2\pi f_1 d\sin\theta}{c} + \frac{2\pi R_1 \Delta f}{c} - \frac{2\pi \Delta f\, d\sin\theta}{c} \quad . \tag{4-6}$$

The phase difference between elements 1 and 2, in radians, is then:

$$\Delta\psi = \psi_1 - \psi_2 \tag{4-7}$$

$$= \frac{2\pi f_1 d \sin\theta}{c} - \frac{2\pi R_1 \Delta f}{c} + \frac{2\pi \Delta f\, d \sin\theta}{c} \quad . \tag{4-8}$$

Strictly speaking, this equation violates the monochromatic assumption. However, we invoke the quasi-stationary assumption in that Δf is negligible in computing the path length difference.

The first term in equation (4-8) is just the traditional phase shift required for beam steering, as in (2-17) or (20-20). The new terms in equation (4-8) due to frequency diversity are $-\frac{2\pi R_1 \Delta f}{c}$ and $\frac{2\pi \Delta f\, d \sin\theta}{c}$. The first of these two terms is range and frequency offset dependent, while the second term is dependent on the scan angle and frequency offset. The first new term is important because it shows that for a frequency diverse array the apparent scan angle of the antenna now depends on range.

The frequency diverse array is similar to the concept of frequency scanned antennas, except that the frequency shift is simultaneously applied spatially across elements, rather than solely as a function of time.

The phase shift of (4-8) causes the beam to focus at some apparent angle θ', corresponding in the conventional case to:

$$\Delta\psi = \frac{2\pi d}{\lambda}\sin\theta' = \frac{2\pi f d}{c}\sin\theta' \quad . \tag{4-9}$$

Substituting for $\Delta\psi$ and solving for the apparent angle, θ', yields:

$$\theta' = \arcsin\left[\frac{f_1 \sin\theta}{f} - \frac{R_1 \Delta f}{f\, d} + \frac{\Delta f \sin\theta}{f}\right]. \qquad (4\text{-}10)$$

Equation (4-10) indicates that the apparent beam angle can be controlled by the frequency offset between channels and the element spacing. Let the nominal scan angle (θ) be zero, indicating that the beam is not intentionally scanned by means of a linear phase progression across the array. Also let the element spacing be $\frac{\lambda}{2}$. Then the apparent scan angle can be written as:

$$\theta' = \arcsin\left[-\frac{2R_1 \Delta f}{c}\right]. \qquad (4\text{-}11)$$

As an example, let $\Delta f = 150\,Hz$. Near the face of the antenna $(R_1 = 0)$, $\theta' = 0^\circ$. This indicates that the beam focuses in the broadside direction, as would be expected for the case of no linear phase progression. However, at R_1 = 100 km, θ' = 5.7°.

Note that some combinations of R_1 and Δf in Equation (4-11) can result in $\sin\theta' > 1$. In other words, the apparent beam steer angle is outside of real space. It will be shown later that the frequency diverse array pattern is in fact periodic in angle.

To look at the rate of change of θ' with respect to range, first note that:

$$\frac{d\left[\sin^{-1}(x)\right]}{dx} = \frac{1}{\sqrt{1-x^2}}. \qquad (4\text{-}12)$$

Then

$$\frac{d\theta'}{dR_1} = \frac{1}{\sqrt{1-\left(\frac{-2R_1\Delta f}{c}\right)^2}} \cdot \left(\frac{-2\Delta f}{c}\right) \quad . \tag{4-13}$$

Notice that the rate of change becomes infinite when

$$1 = \left(\frac{2R_1\Delta f}{c}\right)^2 \quad , \tag{4-14}$$

or

$$R_1 = \frac{c}{2\Delta f} \quad . \tag{4-15}$$

$\frac{d\theta'}{dR_1}$ is plotted in Fig. 4-3 for various values of Δf .

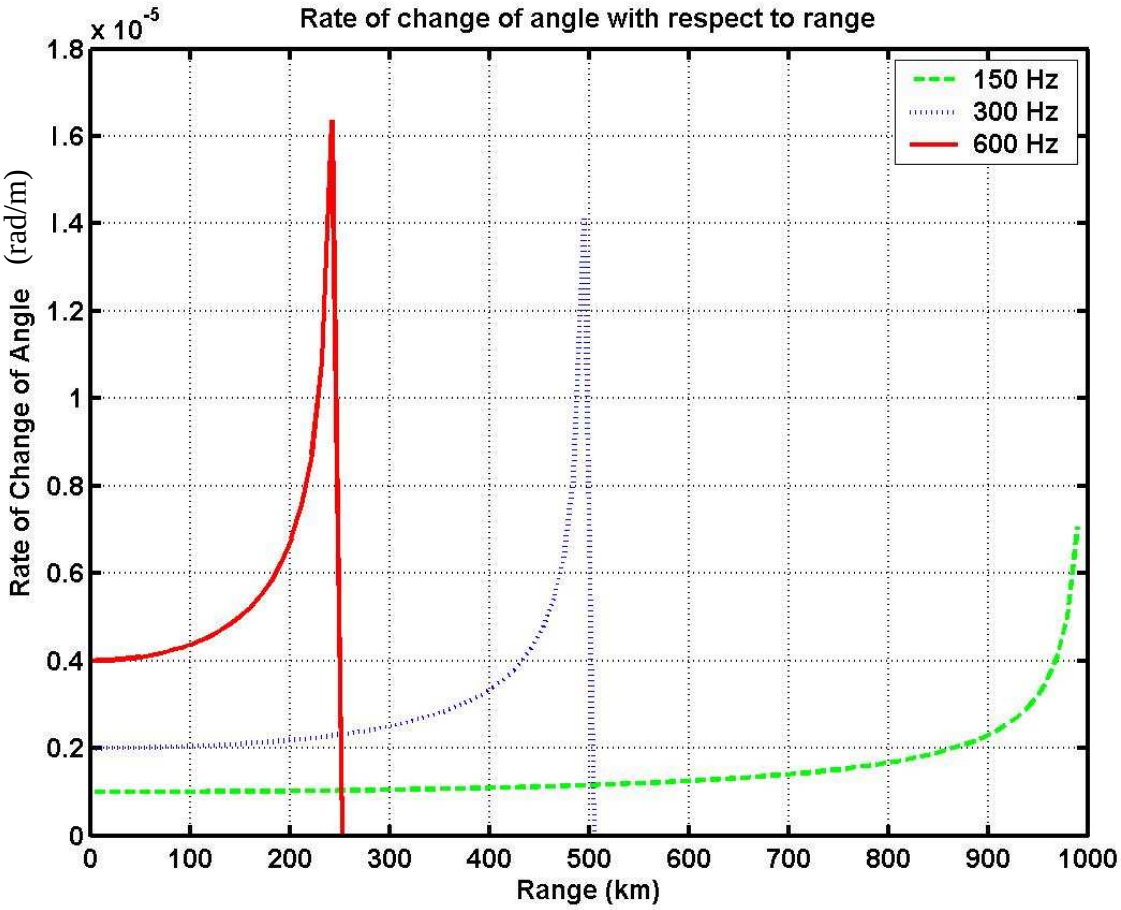

Fig. 4-3: Rate of change in apparent angle as a function of range for a frequency diverse array.

4.2. Time Variation of the Frequency Diverse Array Signal

The time signal of a frequency diverse array at boresight can be found directly using Woodward's notation [97]. Let the signal radiated by the i^{th} spatial channel be a cosine:

$$x_i(t) \;=\; \cos(2\pi\, f_i\, t). \tag{4-16}$$

The spectrum of the i[th] signal is then a pair of delta functions at $\pm f_i$:

$$X_i(f) = \frac{1}{2}\{\delta(f + f_i) + \delta(f - f_i)\}. \quad (4\text{-}17)$$

The Fourier transform pair for the cosine waveform is illustrated in Fig. 4-4.

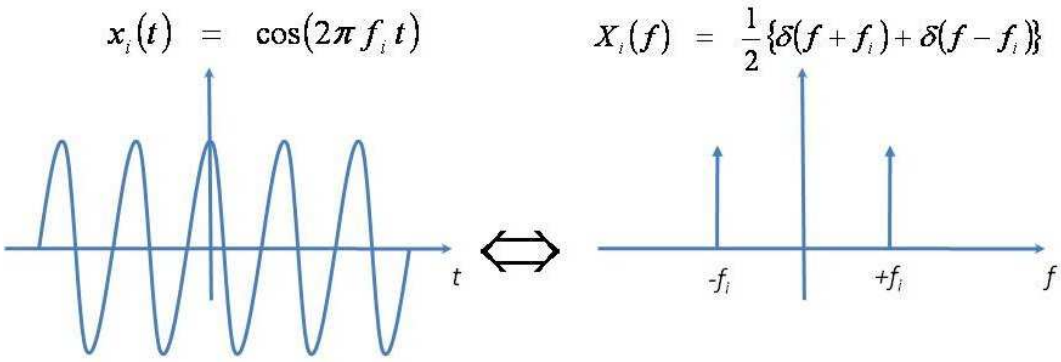

Fig. 4-4: Fourier transform pair for the cosine waveform

The total output time waveform of the frequency diverse array from N channels is the sum of the contributions from each element.

$$x_i(t) = \sum_{i=1}^{N} \cos(2\pi f_i t) \ . \quad (4\text{-}18)$$

The linearity property of Fourier transforms states:

$$a\, x_1(t) + b\, x_2(t) \ \Leftrightarrow \ a\, X_1(f) + b\, X_2(f) \quad , \quad (4\text{-}19)$$

so each frequency component f_i of the frequency diverse array signal adds a pair of delta functions to the output spectrum at $\pm f_i$. The spectrum of the frequency diverse array signal is shown in Fig. 4-5.

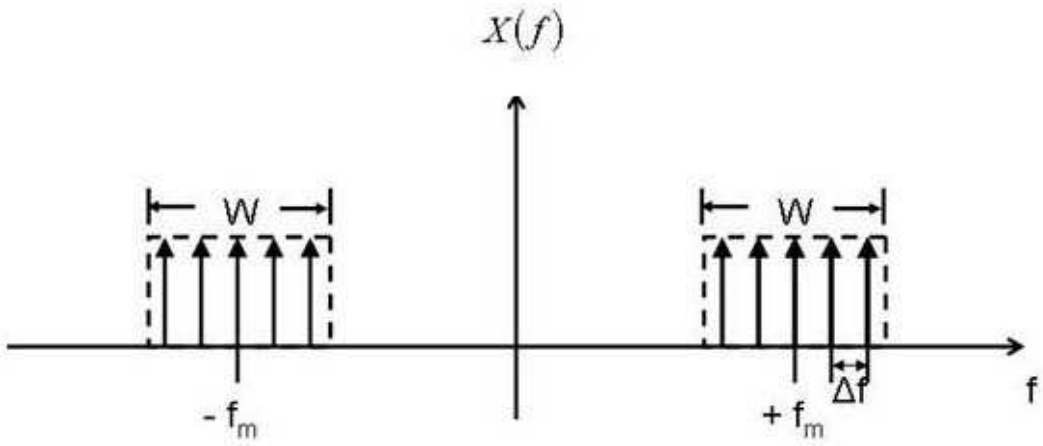

Fig. 4-5: Spectrum of the frequency diverse array waveform.

The spectrum can be thought of as a series of impulses sampling a pair of rectangular functions located at $\pm f_m$. The rectangular function is given by:

$$rect(f) = \begin{cases} 1 , & |f| < \frac{1}{2} \\ 0 , & elsewhere \end{cases} . \tag{4-20}$$

The rectangular functions of Fig. 4-5 are two shifted and scaled *rect* functions:

$$rect\left(\frac{f - f_m}{W}\right) \text{ and } rect\left(\frac{f - f_m}{W}\right) ,$$

where: f_m is the middle frequency component and
$W = N\Delta f$.

These *rect* functions are sampled (multiplied) by a train of impulses spaced at Δf, $rep_{\Delta f}\{\delta(f)\}$:

$$rep_{\Delta f}\{\delta(f)\} = \sum_{n=-\infty}^{\infty} \delta(f - n\Delta f) . \tag{4-21}$$

The spectrum of the frequency diverse array signal can then be written as:

$$X(f) = \left\{ rect\left(\frac{f - f_m}{W} \right) + rect\left(\frac{f + f_m}{W} \right) \right\} \times rep_{\Delta f} \{ \delta(f) \} . \quad (4\text{-}22)$$

To compute the resultant time waveform, recall also that the *rect* function and the *sinc* function form a Fourier transform pair:

$$sinc(t) \Leftrightarrow rect(f) , \quad (4\text{-}23)$$

where

$$sinc(t) = \frac{\sin(\pi t)}{\pi t} . \quad (4\text{-}24)$$

Recall also the shifting and scaling properties of the Fourier transform, respectively:

$$x(t) e^{j 2\pi f_m t} \Leftrightarrow X(f - f_m), \quad (4\text{-}25)$$

$$x(at) \Leftrightarrow \frac{1}{|a|} X\left(\frac{f}{a} \right) . \quad (4\text{-}26)$$

Making use of (4-23), (4-25) and (4-26),

$$rect\left(\frac{f \pm f_m}{W} \right) \Leftrightarrow |W| \text{sinc}(Wt) e^{\mp j 2\pi f_m t} . \quad (4\text{-}27)$$

A train of impulses spaced at Δf in frequency transforms into a train of pulses spaced at $1/\Delta f$ in the time domain as:

$$rep_{\frac{1}{\Delta f}} \{ \delta(t) \} \Leftrightarrow |\Delta f| \cdot rep_{\Delta f} \{ \delta(f) \} . \quad (4\text{-}28)$$

In (4-22) the *rep* function of (4-21) is multiplied by the *rect* functions of (4-27). The transform of (4-22) can then be found readily with the use of the convolution property of Fourier transforms:

$$f_1(t) \otimes f_2(t) \quad \Leftrightarrow \quad F_1(f) \times F_2(f) \ . \tag{4-29}$$

The time waveform of the frequency diverse array can finally be written as:

$$x(t) = \left[|W| \text{sinc}(Wt) e^{j2\pi f_m t} + |W| \text{sinc}(Wt) e^{-j2\pi f_m t} \right] \otimes \left| \frac{1}{\Delta f} \right| rep_{\frac{1}{\Delta f}} \{\delta(t)\} \tag{4-30}$$

$$= |W| \text{sinc}(Wt) \left[e^{j2\pi f_m t} + e^{-j2\pi f_m t} \right] \otimes \left| \frac{1}{\Delta f} \right| rep_{\frac{1}{\Delta f}} \{\delta(t)\} \tag{4-31}$$

$$= 2 \left| \frac{W}{\Delta f} \right| (\text{sinc}(Wt) \cos(2\pi f_m t)) \otimes rep_{\frac{1}{\Delta f}} \{\delta(t)\} \tag{4-32}$$

$$= 2N \, rep_{\frac{1}{\Delta f}} \{\text{sinc}(N\Delta f t) \cos(2\pi f_m t)\}. \tag{4-33}$$

The frequency diverse array signal is sketched in Fig. 4-6. Notice that the waveform is periodic with period $\frac{1}{\Delta f}$, and consists of a *sinc* function modulated by a cosine at frequency f_m, where f_m corresponds to the middle frequency of the N components.

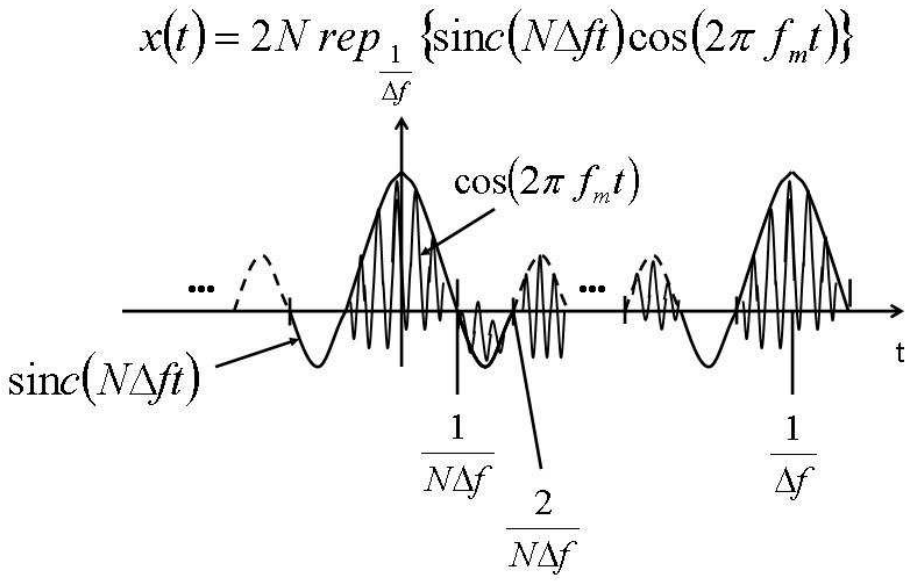

Fig. 4-6: Frequency diverse array time waveform

The magnitude of the frequency diverse array time waveform is illustrated for N=5 in Fig. 4-7.

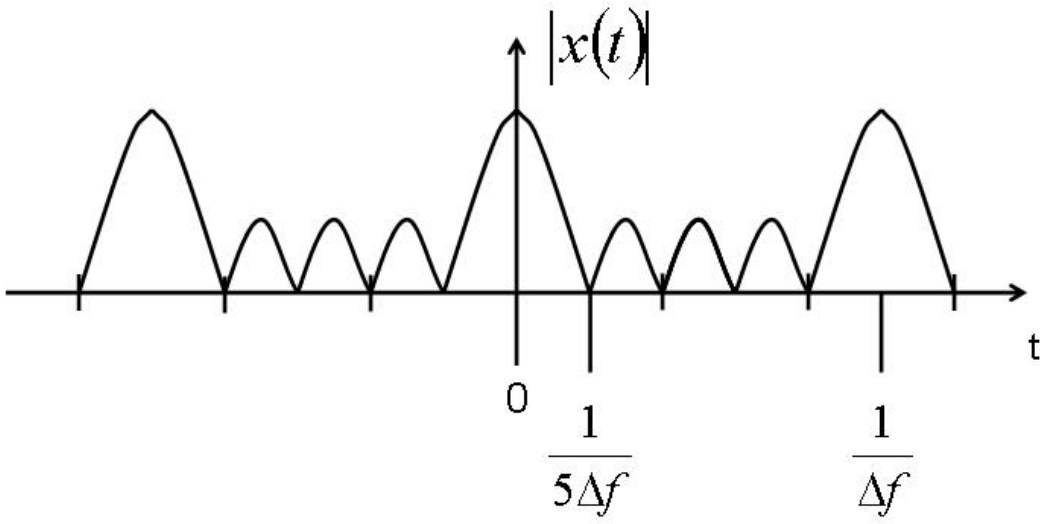

Fig. 4-7: Magnitude of the frequency diverse array time waveform for *N*=5.

4.3. Propagation of the Pattern

The spatial pattern of Section 4.1 and the time waveform in Section 4.2 do not take into account the propagating nature of a transverse electromagnetic wave. Electromagnetic waves must satisfy Maxwell's equations [103], namely (for free space):

$$\overline{\nabla} \times \overline{E} = -\mu \frac{\partial \overline{H}}{\partial t} \tag{4-34}$$

and

$$\overline{\nabla} \times \overline{H} = \varepsilon \frac{\partial \overline{E}}{\partial t} + \sigma \overline{E}\,. \tag{4-35}$$

Let $\overline{E}$ and $\overline{H}$ be sinusoids of the form of Equation (4-16). These sinusoids are the real part of a complex exponential, so the electric and magnetic fields can be written in phasor form as:

$$\overline{E} = E_x e^{j\omega t}\hat{a}_x \ , \tag{4-36}$$

$$\overline{H} = E_y e^{j\omega t}\hat{a}_y \ , \tag{4-37}$$

The electric and magnetic fields are orthogonal and oriented along the x and y axes respectively. Note that

$$\overline{\nabla}\times\overline{E} = \begin{vmatrix} \hat{a}_x & \hat{a}_y & \hat{a}_z \\ \dfrac{\partial}{\partial x} & \dfrac{\partial}{\partial y} & \dfrac{\partial}{\partial z} \\ E_x e^{j\omega t} & 0 & 0 \end{vmatrix} = \left(\frac{\partial\left(E_x e^{j\omega t}\right)}{\partial z}\right)\hat{a}_y - \left(\frac{\partial\left(E_x e^{j\omega t}\right)}{\partial y}\right)\hat{a}_z . \tag{4-38}$$

Assuming that there is no component of the electric field in the z direction,

$$\frac{\partial\left(E_x e^{j\omega t}\right)}{\partial z} = -\mu\frac{\partial\overline{H}}{\partial t} = -j\omega\mu H_y e^{j\omega t}, \tag{4-39}$$

and

$$\frac{\partial E_x}{\partial z} = -j\omega\mu H_y . \tag{4-40}$$

Similarly,

$$\frac{\partial H_y}{\partial z} = -\left(j\omega\varepsilon+\sigma\right)E_x . \tag{4-41}$$

Then

$$\frac{\partial\overline{E}}{\partial z} = -j\omega\mu\overline{H} \tag{4-42}$$

$$\frac{\partial\overline{H}}{\partial z} = -\left(j\omega\varepsilon+\sigma\right)\overline{E} \ . \tag{4-43}$$

Differentiating,

$$\frac{\partial^2\overline{E}}{\partial z^2} = -\omega^2\mu\varepsilon\overline{E} + j\omega\mu\sigma\overline{E} \tag{4-44}$$

$$\frac{\partial^2\overline{H}}{\partial z^2} = -\omega^2\mu\varepsilon\overline{H} + j\omega\mu\sigma\overline{H} . \tag{4-45}$$

One solution to the above equations is:

$$\overline{E} = E_0 e^{j\omega t} e^{-\gamma z} \hat{a}_x \tag{4-46}$$

$$\overline{H} = H_0 e^{j\omega t} e^{-\gamma z} \hat{a}_y \ , \tag{4-47}$$

where

$$\gamma^2 = -\omega^2 \mu\varepsilon + j\omega\mu\sigma \, . \tag{4-48}$$

γ is called the propagation constant and is usually written as:

$$\gamma = \alpha + j\beta \, , \tag{4-49}$$

where α and β are known as the attenuation and phase constants respectively. In free space over short distances, $\alpha \approx 0$, and the electric field can be written as:

$$\overline{E} = E_0 e^{j(\omega t - \beta z)} \hat{a}_x \, . \tag{4-50}$$

Therefore, the electric field is a sinusoid travelling in the positive z direction. The wave travels a distance z in time t, providing a phase velocity of:

$$v_p = \frac{\omega}{\beta} = \frac{1}{\sqrt{\mu_0 \varepsilon}} = c \, . \tag{4-51}$$

Notice that

$$\beta = \frac{\omega}{c} = \frac{2\pi f}{c} = \frac{2\pi}{\lambda} \ , \tag{4-52}$$

which is the wave number of (3-1). Comparing (4-49) to (3-6), the contribution to the electric field from the n^{th} element can be written as:

$$E_n = \frac{a_n}{R_n} f(\theta, \phi) e^{j(\omega_n t - k_n R_n)} \, . \tag{4-53}$$

Strictly speaking, the element pattern $f(\theta, \phi)$ is a function of frequency. But a fundamental constraint of the frequency diverse array is that $\Delta\omega << \omega_0$. Also assume that the elements are isotropic radiators with identical element patterns. The total electric field can then be written as the sum of *N* terms (4-52) similar to Secman [93]:

$$E = \sum_{n=0}^{N-1} \frac{a_n}{R_n} e^{j(\omega_n t - k_n R_n)} \quad , \tag{4-54}$$

where from (4-5):

$$\begin{aligned} \omega_n &= \omega_0 + n\Delta\omega \\ k_n &= k_0 + n\Delta k \\ \Delta k &= \frac{2\pi}{\Delta\lambda} \\ R_n &= R_0 - nd\sin\theta \quad . \end{aligned} \tag{4-55}$$

Then,

$$E = \sum_{n=0}^{N-1} \frac{a_n}{R_n} e^{j[(\omega_0 + n\Delta\omega)t - (k_0 + n\Delta k)R_n]}. \tag{4-56}$$

In general, the coefficients a_n incorporate the frequency dependence, ω_n. Also, $\omega_n \approx \omega_{n+1}$. For uniform aperture weighting, all a_n are identical, $a_n = a_0$, and can be brought in front of the summation. a_0 can also be normalized to unity without loss of generality. The $1/R_n$ term controls the fall off in electric field with range from (4-6). R_0 and R_N vary by $(N-1)d\sin\theta$, so in terms of amplitude, $R_n \approx R_0$ for all n. However, this assumption can not be made in terms of phase, since even small changes in R can cause large changes in phase. Under these assumptions,

$$
\begin{aligned}
E &= \frac{1}{R_o}\sum_{n=0}^{N-1} e^{j[(\omega_0 + n\Delta\omega)t - (k_0 + n\Delta k)(R_0 - nd\sin\theta)]} \\
&= \frac{1}{R_o}\sum_{n=0}^{N-1} e^{j\left[\omega_0 t + n\Delta\omega t - k_0 R_0 + k_0 nd\sin\theta - n\Delta k R_0 + n^2\Delta kd\sin\theta\right]} \\
&= \frac{1}{R_o}\sum_{n=0}^{N-1} e^{j[(\omega_0 t - k_0 R_0) + n(\Delta\omega t + k_0 d\sin\theta - \Delta k R_0 + n\Delta kd\sin\theta)]} \qquad (4\text{-}57) \\
&= \frac{1}{R_o} e^{j[(\omega_0 t - k_0 R_0)]} \sum_{n=0}^{N-1} e^{j[\, n(\Delta\omega t + k_0 d\sin\theta - \Delta k R_0 + n\Delta kd\sin\theta)]}.
\end{aligned}
$$

Let

$$\psi = \Delta\omega t + k_0 d\sin\theta - \Delta k R_0 + n\Delta kd\sin\theta. \qquad (4\text{-}58)$$

The last term in (4-57) is much less than the other terms, provided that:

$$(1)\quad \Delta\omega t >> n\Delta kd\sin\theta \qquad (4\text{-}59)$$

$$\text{or}\quad t >> \frac{nd\sin\theta}{c}. \qquad (4\text{-}60)$$

This condition is true for times greater than the delay across the aperture.

$$(2)\quad k_0 d\sin\theta >> n\Delta kd\sin\theta \qquad (4\text{-}61)$$

$$\text{or}\quad f_0 >> n\Delta f. \qquad (4\text{-}62)$$

This is a fundamental condition of the frequency diverse array.

(3) $R_0 >> nd\sin\theta.$ (4-63)

This condition requires that the nominal target range be much greater than the projected aperture length. Conditions (1) and (3) are independent of Δω. Condition (2) is the standard assumption for far field in array theory.

When the above conditions are satisfied, we can neglect the last term in (4-58):

$$\psi = \Delta\omega t + k_0 d\sin\theta - \Delta k R_0. \quad (4\text{-}64)$$

Then

$$E = \frac{1}{R_o} e^{j[(\omega_0 t - k_0 R_0)]} \sum_{n=0}^{N-1} e^{jn\psi}. \quad (4\text{-}65)$$

But

$$\sum_{n=0}^{N-1} X^n = \frac{X^N - 1}{X - 1}. \quad (4\text{-}66)$$

Letting $X = e^{j\psi}$,

$$E = \frac{1}{R_o} e^{j[(\omega_0 t - k_0 R_0)]} \cdot \frac{e^{j\psi N} - 1}{e^{j\psi} - 1}. \quad (4\text{-}67)$$

Following the method of (3-18) to (3-21), the magnitude of the electric field of the frequency diverse array can be expressed as:

$$|E| = \frac{1}{R_0} \left| \frac{\sin\left(\frac{N\psi}{2}\right)}{\sin\left(\frac{\psi}{2}\right)} \right|. \quad (4\text{-}68)$$

Consider the periodicity of the electric field. The field will be a maximum when:

$$\psi \;=\; \Delta\omega t + k_0 d \sin\theta - \Delta k R_0 \;=\; 2\pi m \quad , \tag{4-69}$$

where m is an integer.

Solving for t, the field will be maximum when:

$$t \;=\; \left(\frac{1}{\Delta f}\right) m + \frac{R_0}{c} - \frac{(d/\lambda_0)\sin\theta}{\Delta f} \quad , \tag{4-70}$$

and the field is periodic in time with period $\left(\frac{1}{\Delta f}\right)$. This is consistent with the results of Section 4-2.

Solving for range, the field will be maximum when:

$$R_0 \;=\; \left(\frac{-c}{\Delta f}\right) m + ct + \frac{(d/\lambda_0) c \sin\theta}{\Delta f} \quad , \tag{4-71}$$

Which is periodic at $\left(\frac{c}{\Delta f}\right)$, the range equivalent of $\left(\frac{1}{\Delta f}\right)$.

In angle:

$$\sin\theta \;=\; \left(\frac{\lambda}{d}\right) m + \frac{\Delta f}{f_0 d}(R_0 - ct) \quad . \tag{4-72}$$

This is periodic at the reciprocal of the element spacing in wavelengths, which corresponds to the spatial locations of conventional grating lobes.

The relationship between time and angle for a frequency diverse array is illustrated in Fig. 4-8. At $t = 0$ at some point in the far field, the signals from all spatial channels are in phase, despite being at different frequencies. The wave front is parallel to the face of the antenna, and the wave focuses in the direction of the antenna boresight. At a later time t_1, the stationary phase point is delayed progressively across spatial channels, causing a rotation of the wave front. The degree of rotation increases with time. This causes the beam to scan in angle, as illustrated in Fig. 4-9.

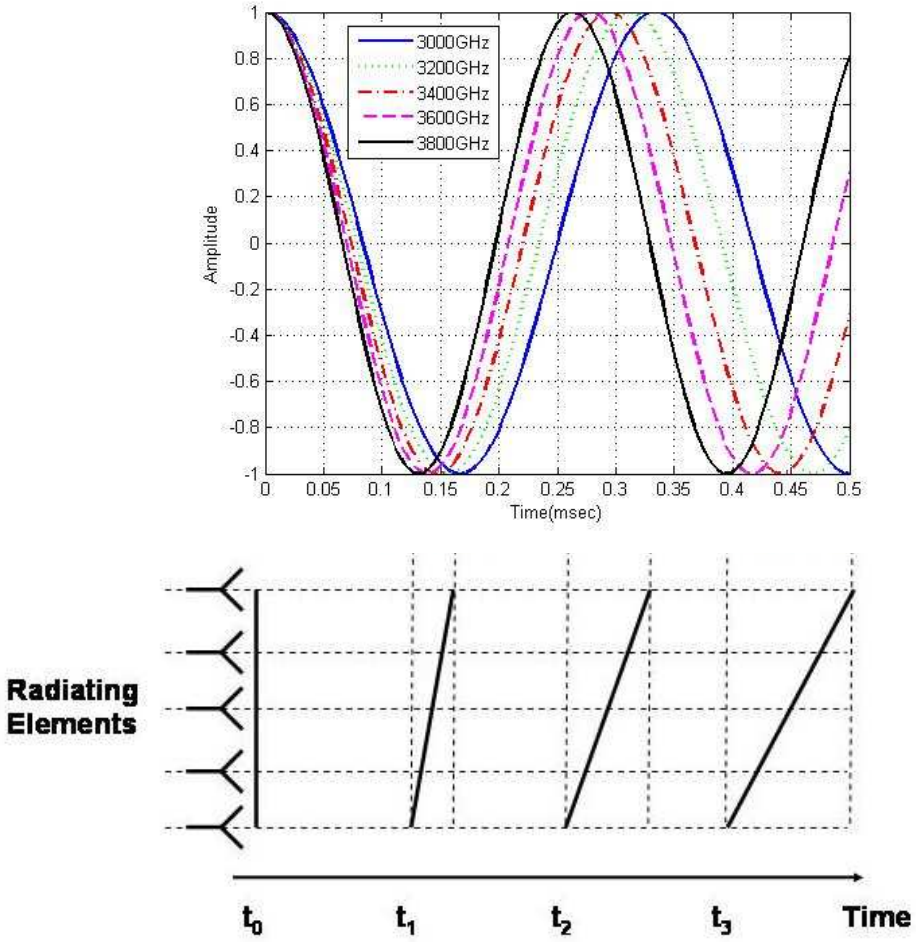

Fig. 4-8: Rotation of the wave front with time

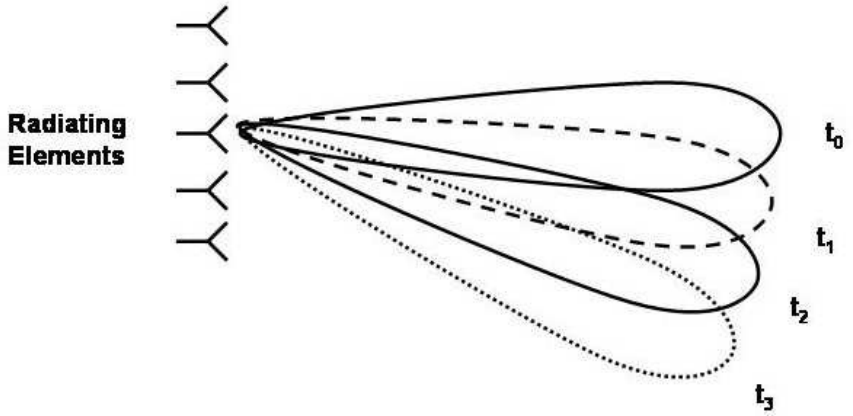

Fig. 4-9: Rotation of the wave front causes the beam to scan with time.

Recall from (4-49) that the radiated field is a transverse electromagnetic wave travelling in the +Z direction. Taking the real part of (4-49), the electric field due to the i^{th} element can be written as a sinusoid of the form:

$$E_i \quad = \quad \cos\left(\omega_i\, t - \beta_i\, Z\right) \ . \tag{4-73}$$

This function is sinusoidal in both time and distance, and helps to explain the complicated relationship between phase, time, and distance in a frequency diverse array. Fig. 4-10 plots the constituent signals of a 5-channel frequency diverse array as a function of distance in a waterfall fashion for several instants of time.

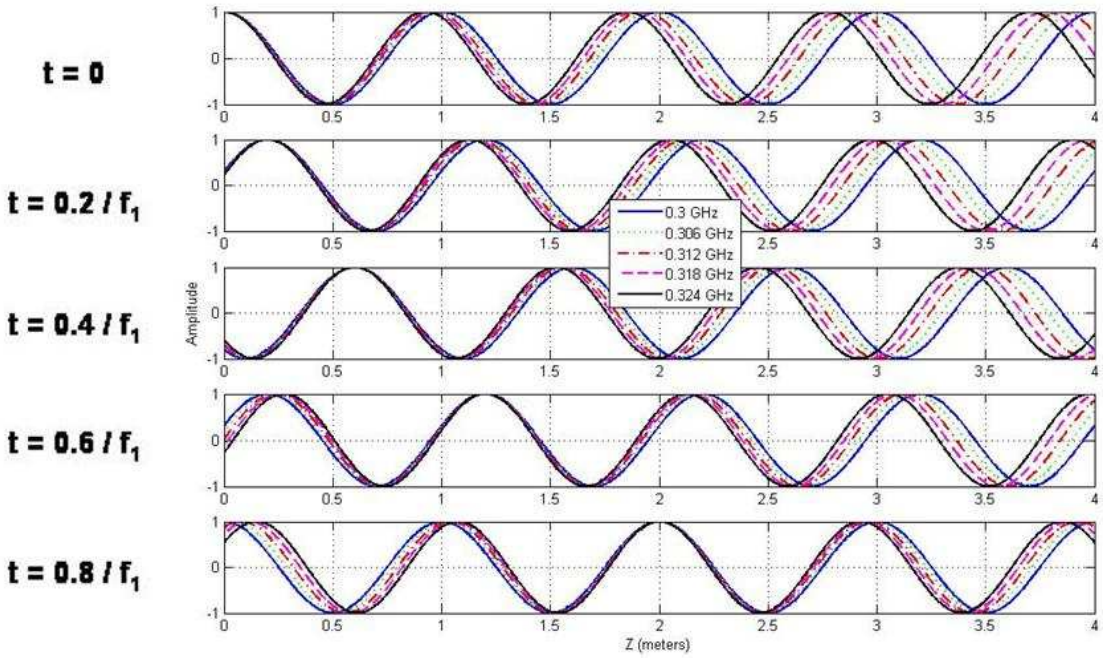

Fig. 4-10: Waterfall chart displaying the constituent signals as a function of distance for several instants of time.

4.4. Time Rate of Change of Angle

In the last section it was shown that the direction of the wave front changes over time. It is useful to look at the rate of this change in angle. Again consider the phase of the electric field from (4-64), expressing angle as a function of time:

$$\psi \;=\; \Delta\omega t + k_0 d \sin\theta(t) - \Delta k R_0 \;=\; 2\pi n \quad . \tag{4-74}$$

Differentiating with respect to time as in [93] yields:

$$\Delta\omega + k_0 d \cos\theta \frac{d\theta}{dt} \;=\; 0 \quad . \tag{4-75}$$

Then

$$\frac{d\theta}{dt} \;=\; \frac{-\Delta\omega}{k_0\, d \cos\theta} \quad . \tag{4-76}$$

Using $\Delta\omega \;=\; 2\pi f$ and $k_0 \;=\; \frac{2\pi}{\lambda_0}$,

$$\frac{d\theta}{dt} \;=\; \frac{-\Delta f}{(d/\lambda_0)\cos\theta} \quad . \tag{4-77}$$

Equation (4-75) shows that the rate of scan is not constant, but varies sinusoidally over angle. The time rate of change of angle is plotted in Figures 4-11 and 4-12 for Δf = 100 Hz and Δf = 200 Hz when d/λ = 0.45.

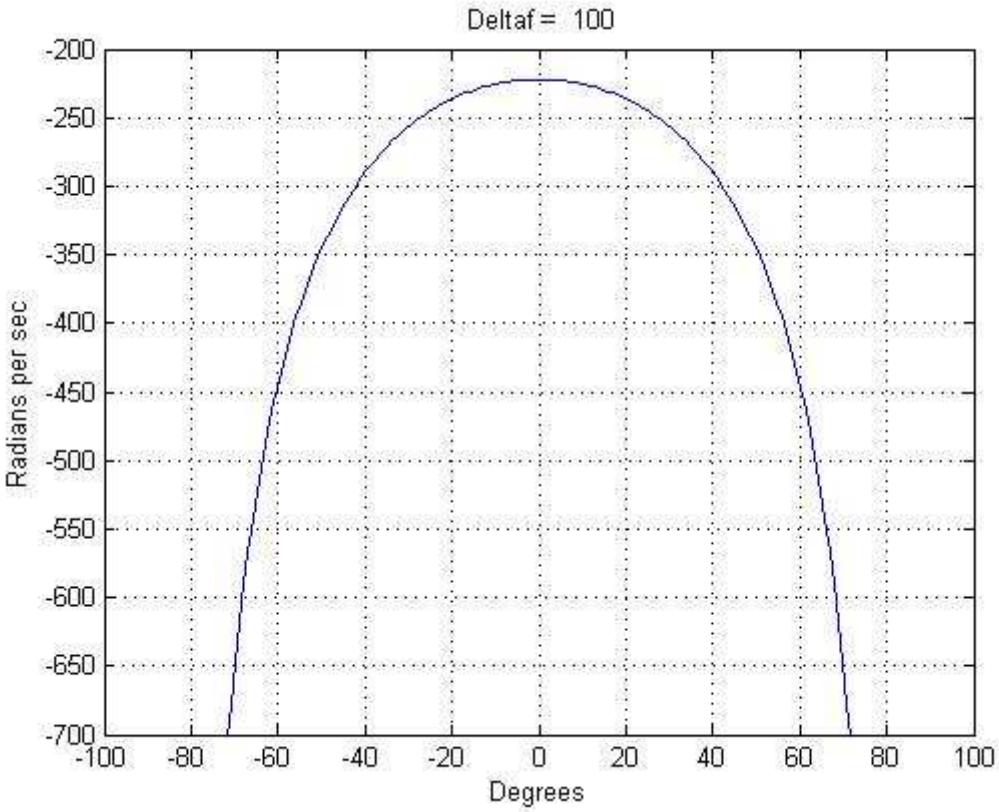

Fig. 4-11: Rate of change of angle for Δf = 100 Hz and d/λ = 0.45.

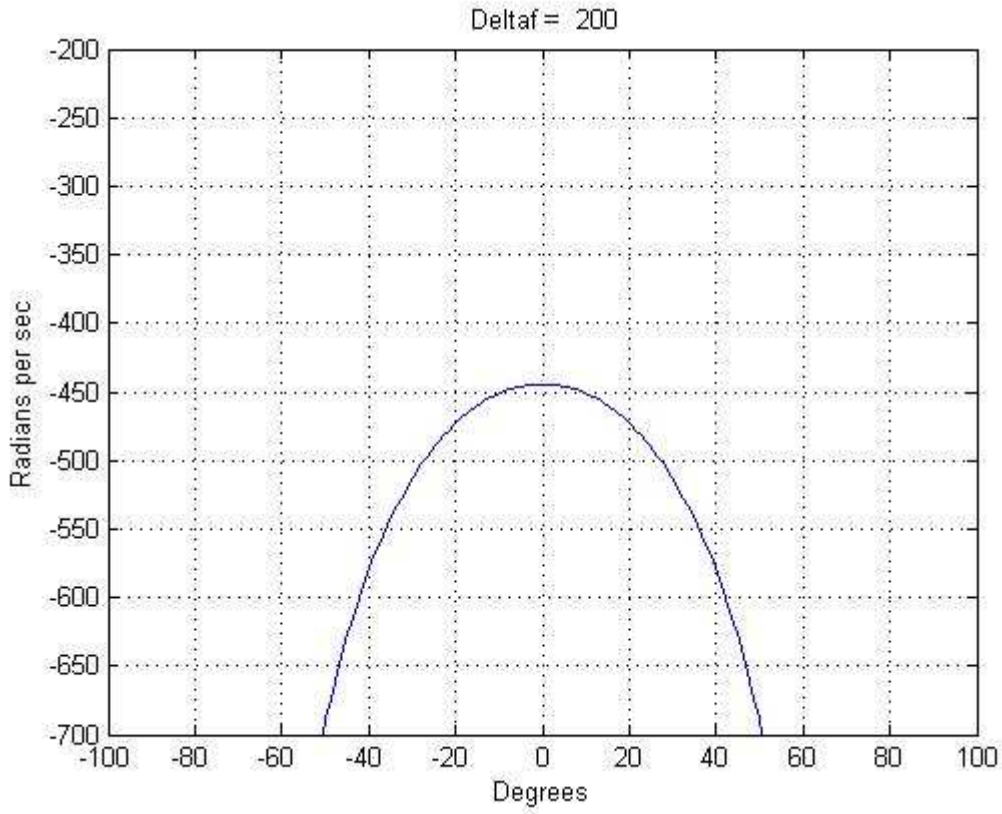

Fig. 4-12: Rate of change of angle for Δf = 200 Hz and d/λ = 0.45.

From (4-75) the differential time *dt* to scan a differential angle is

$$dt = \frac{-(d/\lambda_0)\cos\theta}{\Delta f} d\theta \quad . \tag{4-78}$$

The total time required to scan through some angle can be found by integration:

$$
\begin{aligned}
t &= \int_{\theta_1}^{\theta_2} \frac{-(d/\lambda_0)\cos\theta}{\Delta f}\, d\theta \\
&= \frac{-(d/\lambda_0)}{\Delta f} \int_{\theta_2}^{\theta_2} \cos\theta\, d\theta \\
&= \frac{-(d/\lambda_0)}{\Delta f} \left[\sin\theta\right]_{\theta_1}^{\theta_2}
\end{aligned}
\tag{4-79}
$$

Equation (4-79) is actually a re-statement of (4-10) when the initial scan angle is zero and $t = \frac{R}{c}$. The time to scan through real space ($-90^\circ \le \theta \le +90^\circ$) as a function of Δf is plotted in Figures 4-13 and 4-14 for d/λ of 0.45 and 0.90.

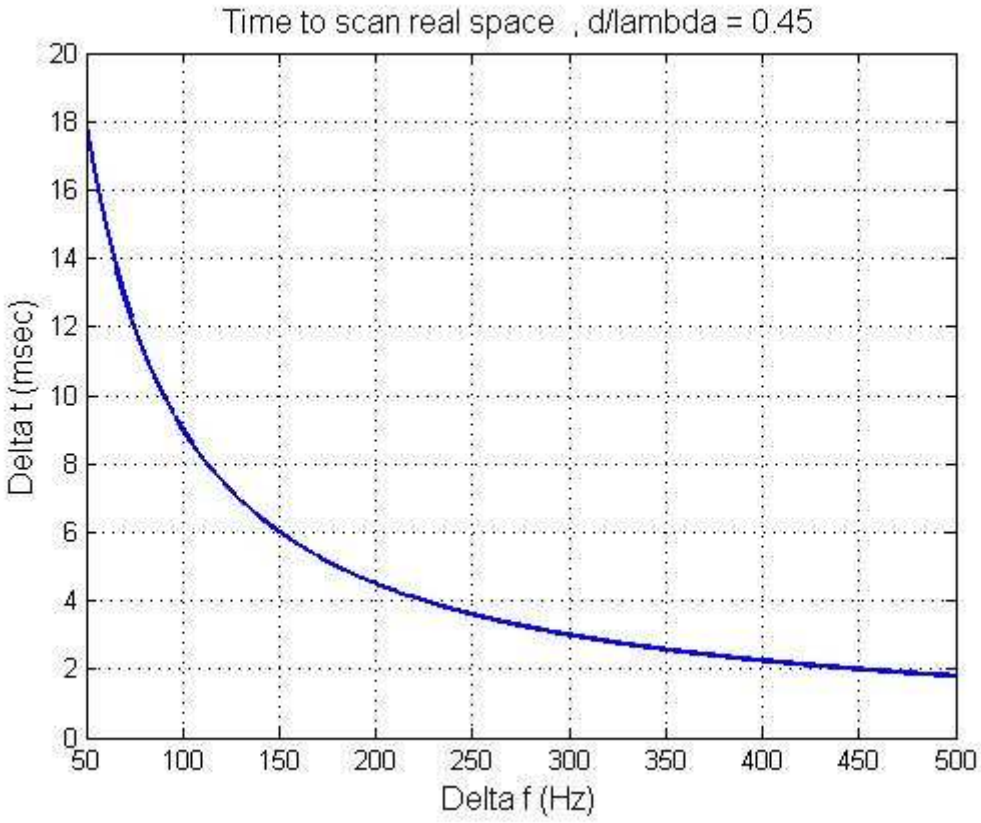

Fig. 4-13: Time to scan real space for $d/\lambda = 0.45$

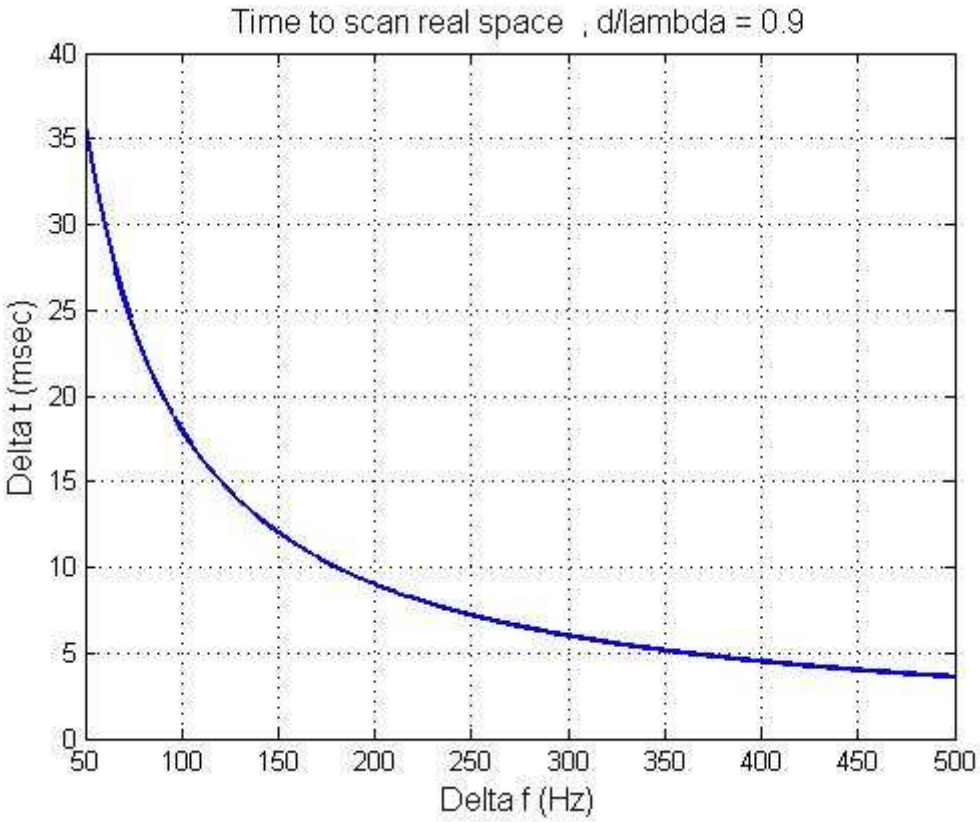

Fig. 4-14: Time to scan real space for $d/\lambda = 0.90$

This section has derived the range, time, and angle characteristics of the frequency diverse array. In the following sections, these concepts will be explored further in simulation and experiments.

Chapter 5

Range-Angle Patterns for the Frequency Diverse Array

5.1 Simulation Results

The previous chapter derived the key characteristics of a frequency diverse array. The frequency diverse array was shown to possess periodicities in time, range, and angle. These properties provide additional degrees of freedom for the design of antenna beams for novel applications. This chapter explores the characteristics of the frequency diverse array over a wide range of design variables.

Equation (4-10) showed the dependence of the frequency diverse array beam steer angle on range. In particular, it was shown that:

$$\theta' = \arcsin\left[\frac{f_1 \sin\theta_0}{f} - \frac{R_1 \Delta f}{c\left(d/\lambda\right)} + \frac{\Delta f \sin\theta_0}{f}\right] \quad . \tag{5-1}$$

The last term is negligible since $\Delta f << f$, a fundamental condition of the frequency diverse array. By a similar reasoning, the ratio (f_1/f) in the first term is approximately equal to unity. Therefore,

$$\sin\theta' \approx \left[\sin\theta_0 - \frac{R_1 \Delta f}{c\left(d/\lambda\right)} \right] . \qquad (5\text{-}2)$$

Equation (5-2) shows that the angle dependence on range can be controlled by appropriate selection of the frequency shift between spatial channels, Δf, the spacing between channels in wavelengths, d/λ, and a nominal steer angle θ_0.

Scan angle is plotted in Fig. 5-1 for the case of zero nominal scan and $d/\lambda = 0.45$. This data is shown parametrically on Δf for frequency offsets of 0 Hz, 100 Hz, and 200 Hz. Notice that the rate of change of angle with range increases for larger values of Δf.

Scan angle as a function of range is re-plotted in Fig. 5-2 when a 30° initial beam steer is included. The beam steers to 90° at a range of about 338 km as predicted by Equation (5-2).

Figures 5-1 and 5-2 show one period of angle vs. range. Clearly the pattern is repetitive in angle at the antenna grating lobes. As discussed in Section 4.3 the frequency diverse array signal is time periodic at $\frac{1}{\Delta f}$, corresponding to periodicity in range at $\frac{c}{\Delta f}$, and periodic in angle at $\frac{\lambda}{d}$, which denotes antenna grating lobes.

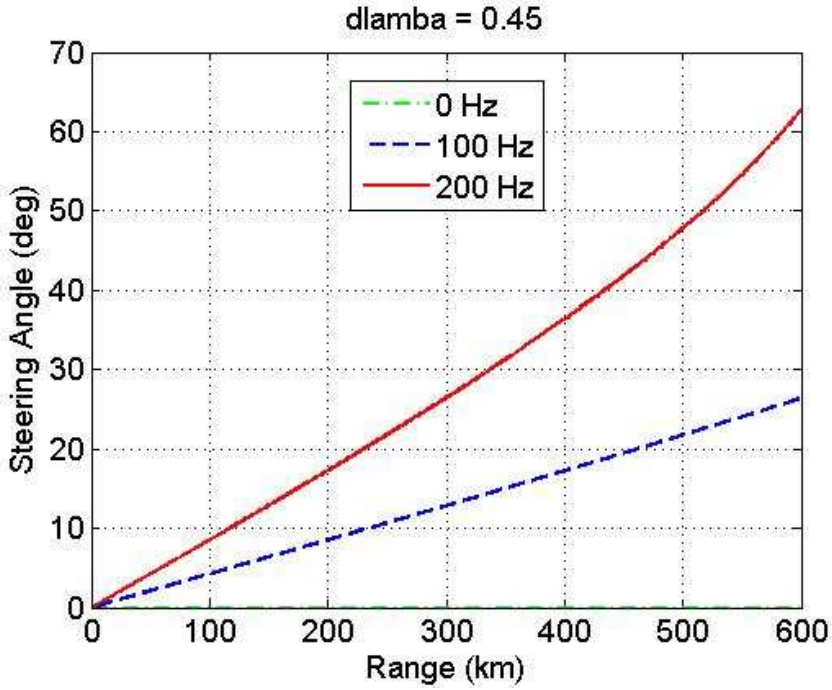

Fig. 5-1: Scan as a function of range for various frequency offsets, $d/\lambda = 0.45$.

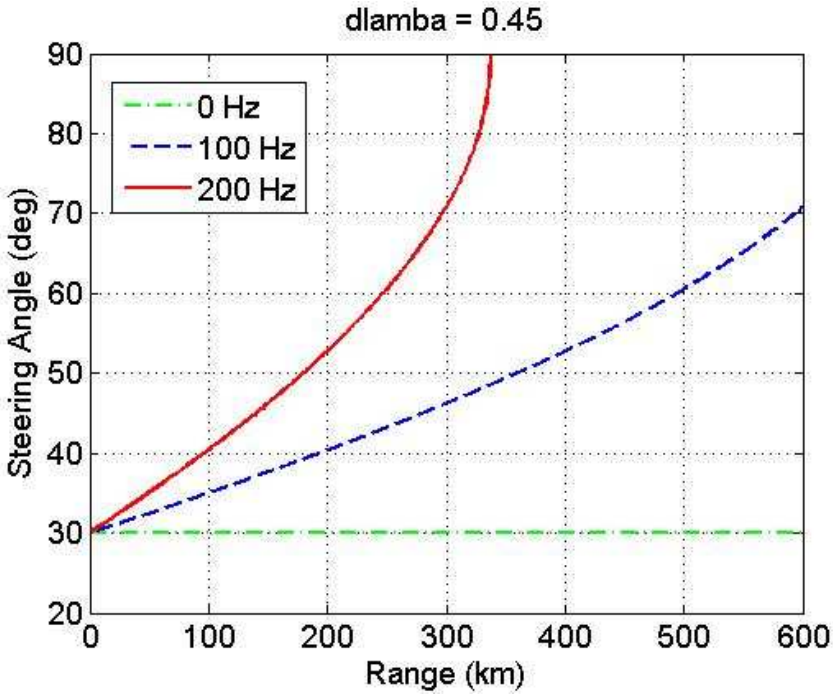

Fig. 5-2: Scan as a function of range for various frequency offsets, $d/\lambda = 0.45$, nominal scan angle $\theta_0 = 30°$.

Equation (5-2) or (4-79) shows that the beam scan angle is a linear function of range (or equivalently time) in *sin θ* space. Letting $t = \frac{1}{\Delta f}$ in (4-79) produces:

$$\frac{1}{\Delta f} = \frac{-(d/\lambda)}{\Delta f}\left[\sin\theta_2 - \sin\theta_1\right] \text{ , and} \tag{5-3}$$

$$\sin\theta_2 - \sin\theta_1 = -\frac{\lambda}{d} \text{ .} \tag{5-4}$$

In other words, $t = \frac{1}{\Delta f}$ corresponds to the time required to scan to the next grating lobe in *sin θ* space. A sketch of the frequency diverse array beam pattern peaks in range-angle space is shown in Fig. 5-3. This structure of the frequency diverse array pattern was first shown by Antonik et al in [89]. As indicated in (5-4), a scan time of $\frac{1}{\Delta f}$, or a range difference of $\frac{c}{\Delta f}$, displaces the pattern by one grating lobe so that the beam pattern repeats.

It was shown in the previous section that beam formation and control primarily depended upon the frequency offset, Δf , and the element spacing in wavelengths, d/λ. The following sections will begin to explore those design parameters.

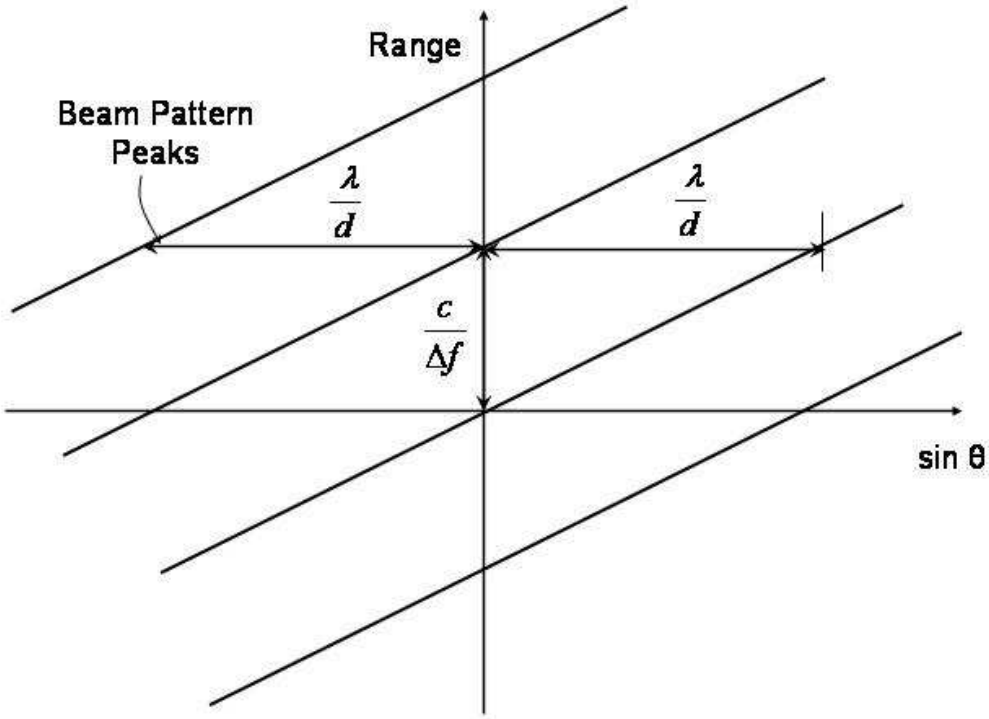

Fig. 5-3: Notional frequency diverse array beam locations in range-angle space.

5.1.1 Nominal Beam Pattern

As a baseline, first consider the case where $\Delta f = 0$. This corresponds to the conventional phased array. From (4-70) and (4-71), the pattern is periodic in time and range at infinity; that is, the pattern is not periodic at all in these domains.

Fig. 5-4 shows the beam pattern for the baseline case for a uniformly illuminated 5-element 3.2 GHz array with $\Delta f = 0$. Element spacing is 0.45 wavelengths. As expected, the beam pattern appears as a *sinc* function which does not change with range. Grating lobes are located at $\lambda/d = 2.22$, and so therefore fall well outside of real space.

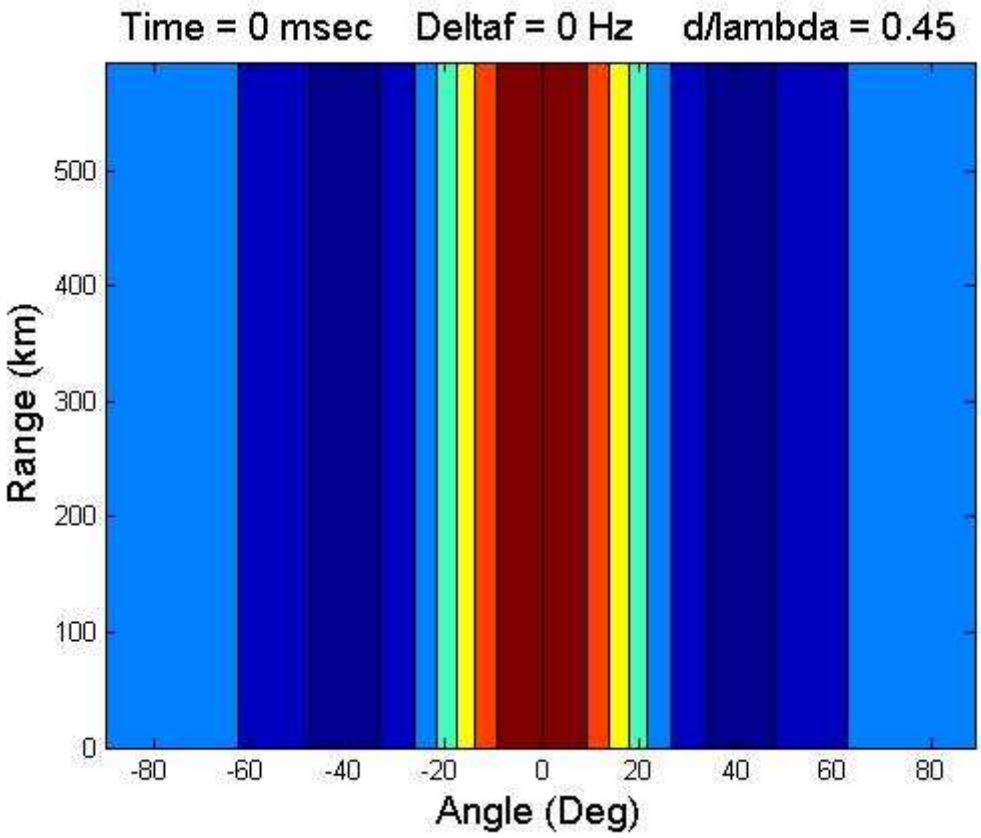

Fig. 5-4: Range-angle pattern for a frequency diverse array with $\Delta f = 0$, $d/\lambda = 0.45$, $f_0 = 3.2$ GHz, $N = 5$.

5.1.2 Variation with Element Spacing, $\Delta f = 0$

When element spacing is increased grating lobes appear closer to, or within, real space. As in the traditional phased array case, grating lobes appear at:

$$\theta_{gl} = \arcsin\left(\frac{\lambda}{d}\right) \quad . \tag{5-5}$$

The grating lobes predicted by (5-5) are shown in Table 5-1 for four values of element spacing.

Table 5-1: Locations of grating lobes for 4 element spacings

d/λ	$T = \lambda/d$	$\theta_{gl} = \arcsin(T)$
0.45	2.22	not in real space
0.90	1.11	not in real space
1.35	0.74	47.7°
1.80	0.56	34.1°

To extend the baseline case of Section 5.1.1, range-angle patterns were computed for $\Delta f = 0$ and the four element spacings of Table 5-1: 0.45, 0.90, 1.35, and 1.80 wavelengths. The case of $d/\lambda = 0.45$ is the baseline case presented in Fig. 5-4. The results of the other cases are provided in Figures 5-5 through 5-7. The performance is as predicted in Table 5-1. When $d/\lambda = 0.90$, the peak of the grating lobes falls just outside of real space, but significant contributions fall into the visible space. Grating lobes for $d/\lambda = 1.35$ and 1.80 fall well within real space in accordance with Table 5-1.

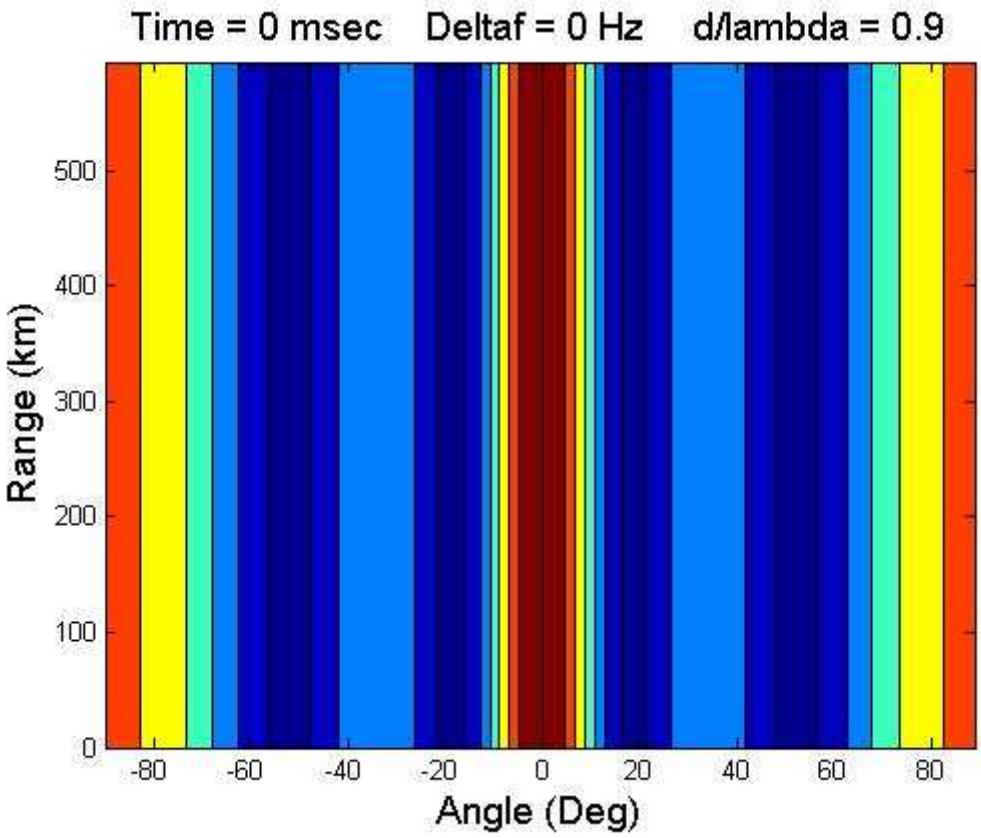

Fig. 5-5: Range-angle pattern for a frequency diverse array with $\Delta f = 0$, $d/\lambda = 0.90$.

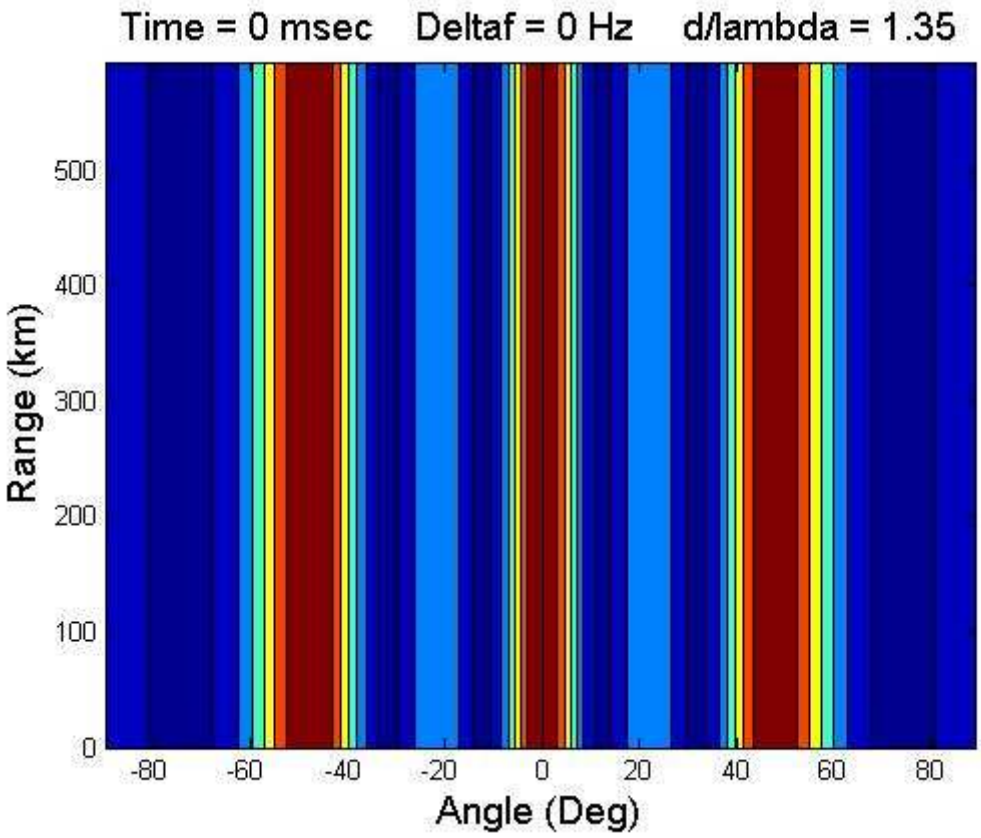

Fig. 5-6: Range-angle pattern for a frequency diverse array with $\Delta f = 0$, $d/\lambda = 1.35$.

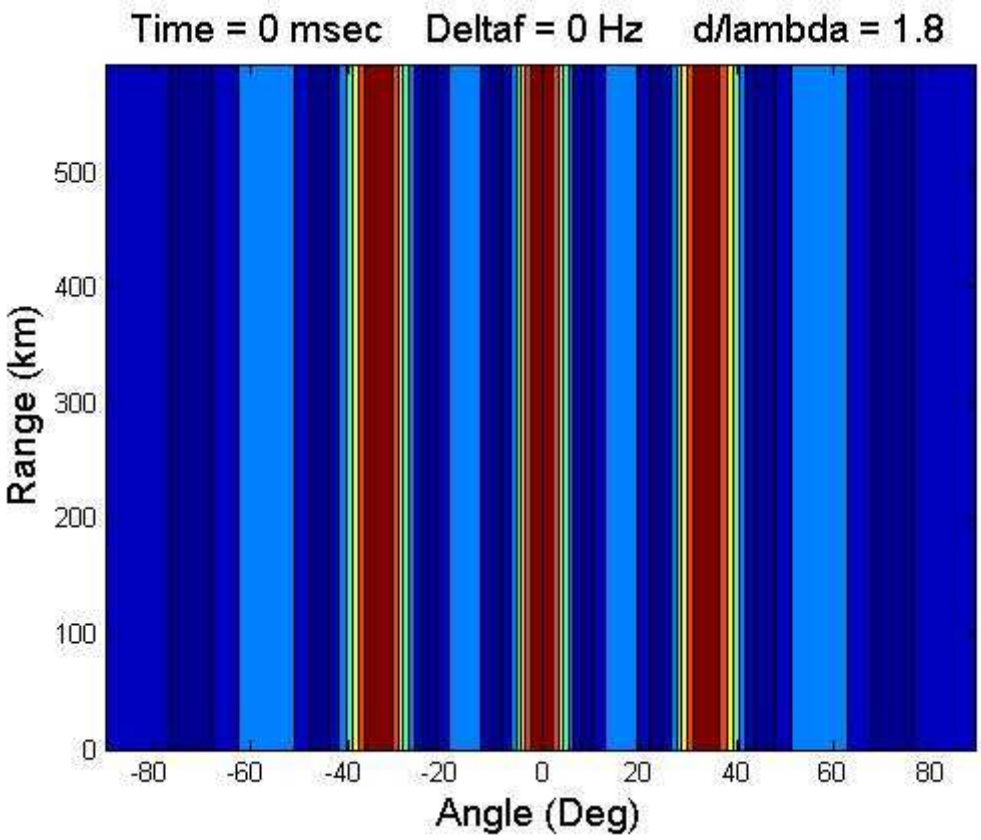

Fig. 5-7: Range-angle pattern for a frequency diverse array with $\Delta f = 0$, $d/\lambda = 1.80$.

5.1.3 Variation with Frequency Offset, d/λ = 0.45.

When frequency offset is non-zero, the beam pattern is no longer constant in range, and the range-dependent nature of the frequency diverse array becomes evident. Recall from (5-2) that when no initial beam scan is applied:

$$\sin\theta' = \left[-\frac{R\,\Delta f}{c\,(d/\lambda)}\right] . \tag{5-6}$$

To explore the variation of the frequency diverse array pattern with channel-to-channel frequency offset included, the element spacing is first held fixed at $d/\lambda = 0.45$. The range-angle patterns for this case are shown in Figures 5-8 through 5-13 for frequency offsets of 100, 200, 300, 500, 1000, and 2000 Hz respectively. When $\Delta f = 100$ Hz, the beam steer angle is 26.4° at a range of 600 km as predicted by (5-6). By (4-71) the signal repeats in range at 3000 km.

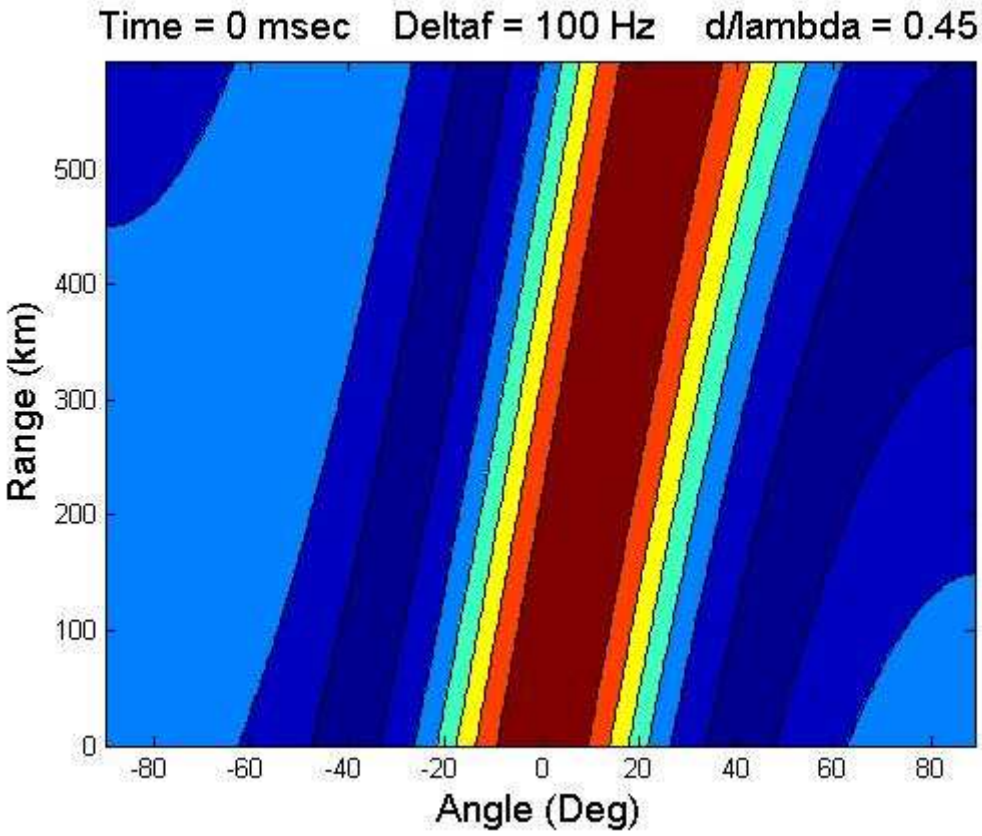

Fig. 5-8: Range-angle pattern for a frequency diverse array with $\Delta f = 100$ Hz and $d/\lambda = 0.45$.

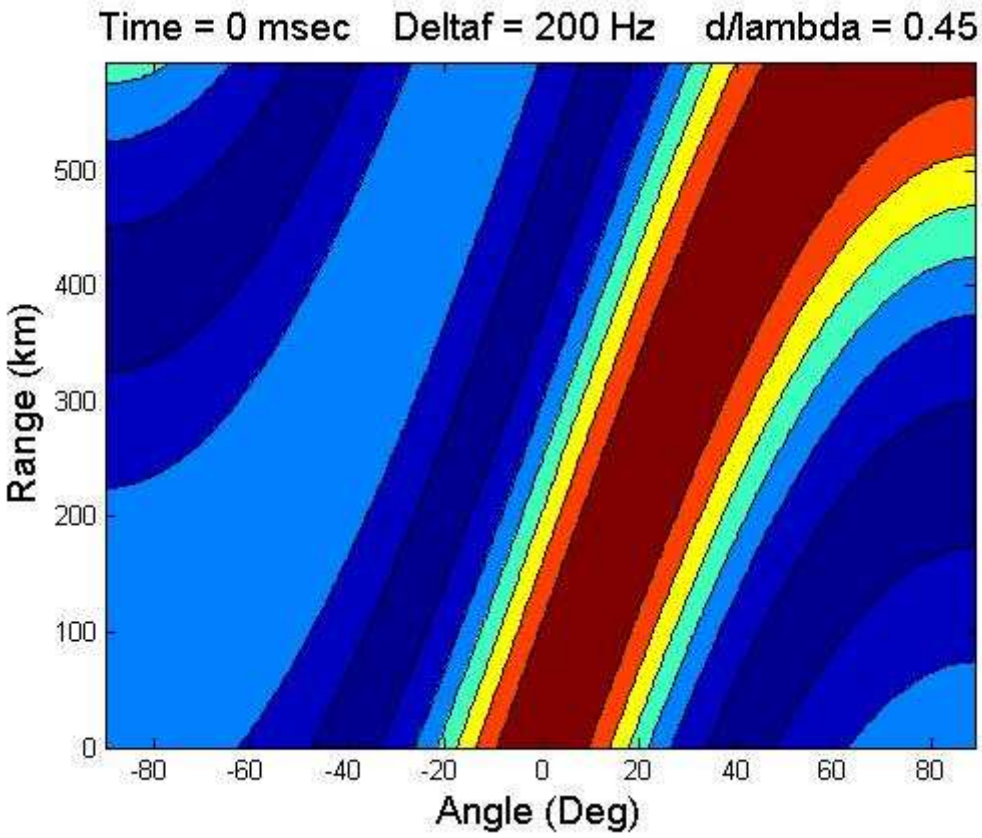

Fig. 5-9: Range-angle pattern for a frequency diverse array with Δf = 200 Hz and d/λ = 0.45.

When Δf = 200 Hz (Fig. 5-9) the beam scan increases to 62.7° at 600 km. At Δf = 300 Hz the beam scans to 90° at a range of 450 km, as shown in Fig. 5-10. Fig. 5-11 shows that at Δf = 500 Hz the beam scans to 90° at 270 km, while the pattern repeats in range at 600 km as predicted by (4-71).

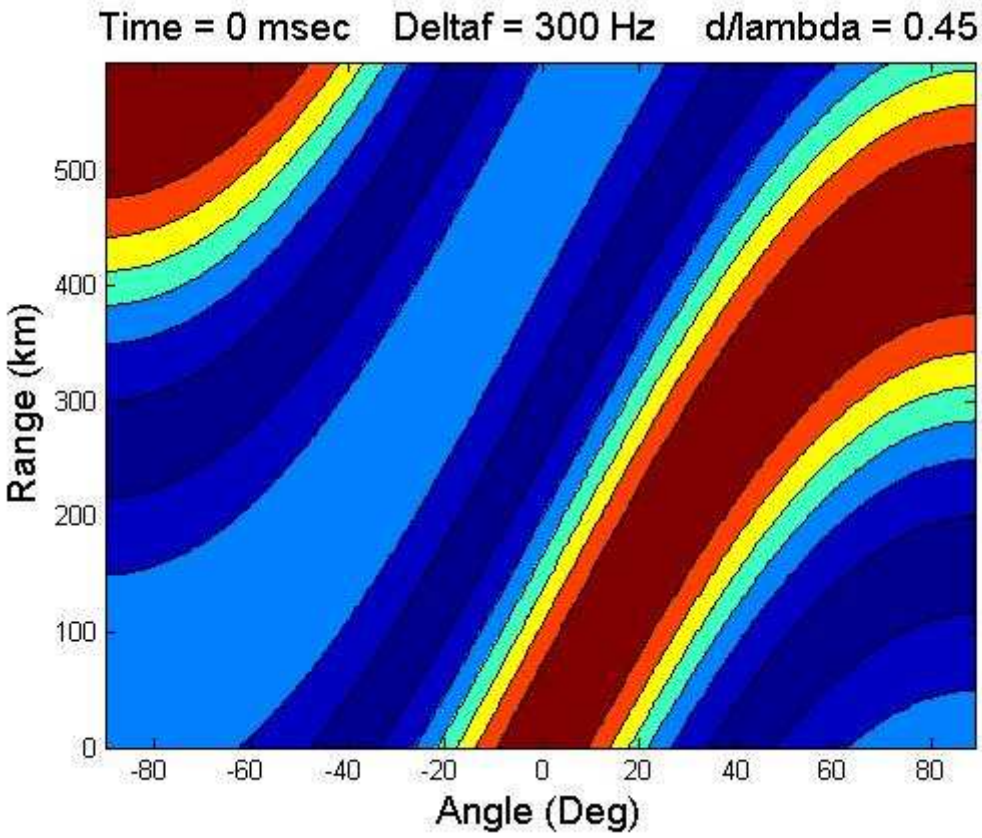

Fig. 5-10: Range-angle pattern for a frequency diverse array with Δf = 300 Hz and d/λ = 0.45.

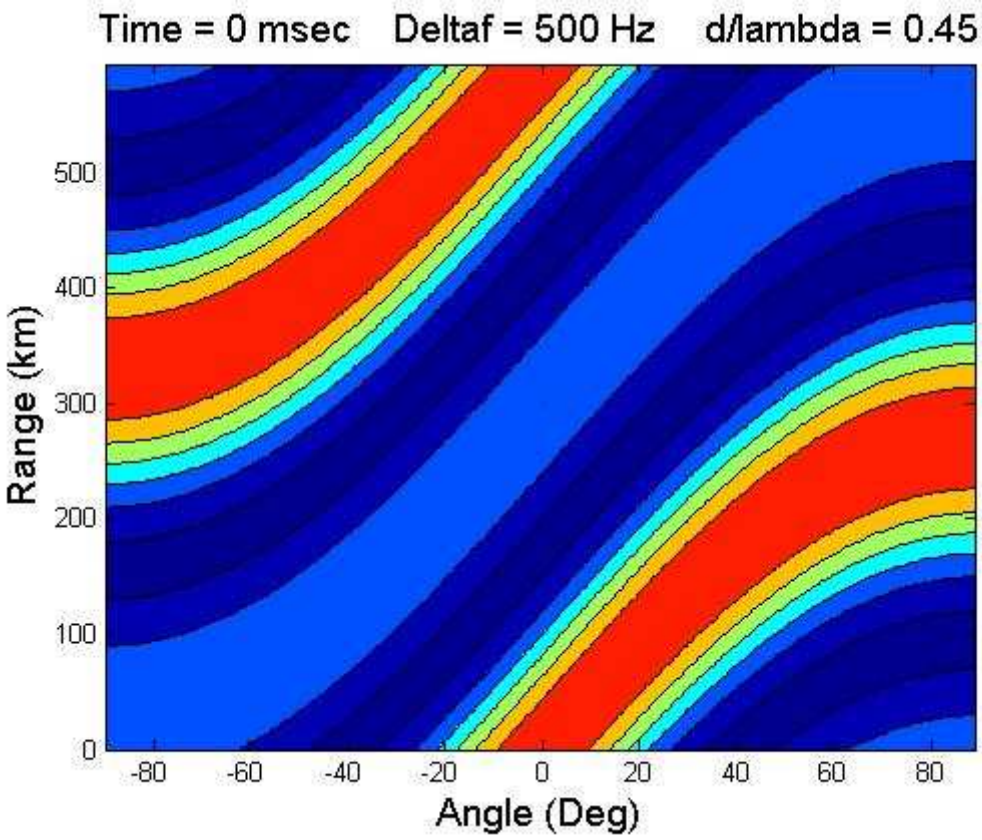

Fig. 5-11: Range-angle pattern for a frequency diverse array with Δf = 500 Hz and d/λ = 0.45.

As the frequency offset is increased, the range at which the beam scans to the edge of real space and the range of ambiguities decreases. Fig. 5-12 shows that the beam scans to 90° at 135 km when Δf = 1000 Hz, and the pattern becomes range-ambiguous at 300 km. When Δf = 2000 Hz as in Fig. 5-13, the beam scans to the edge of real space at 67.5 km and the first range ambiguity is at 150 km.

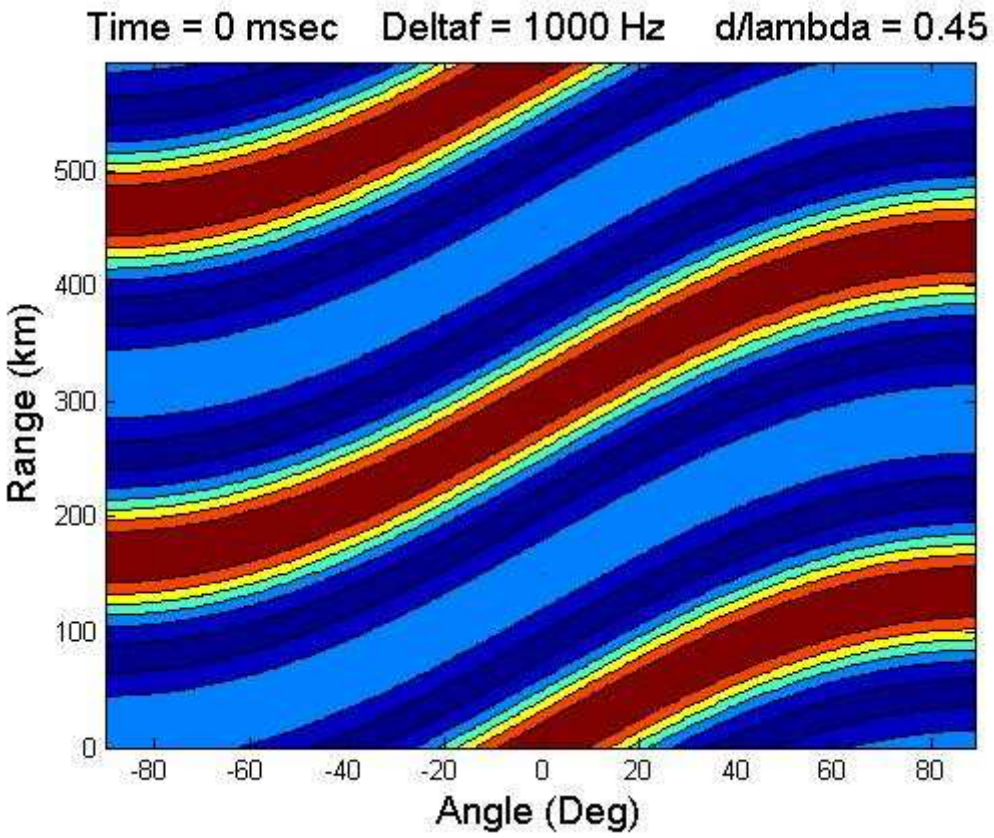

Fig. 5-12: Range-angle pattern for a frequency diverse array with Δf = 1000 Hz and d/λ = 0.45.

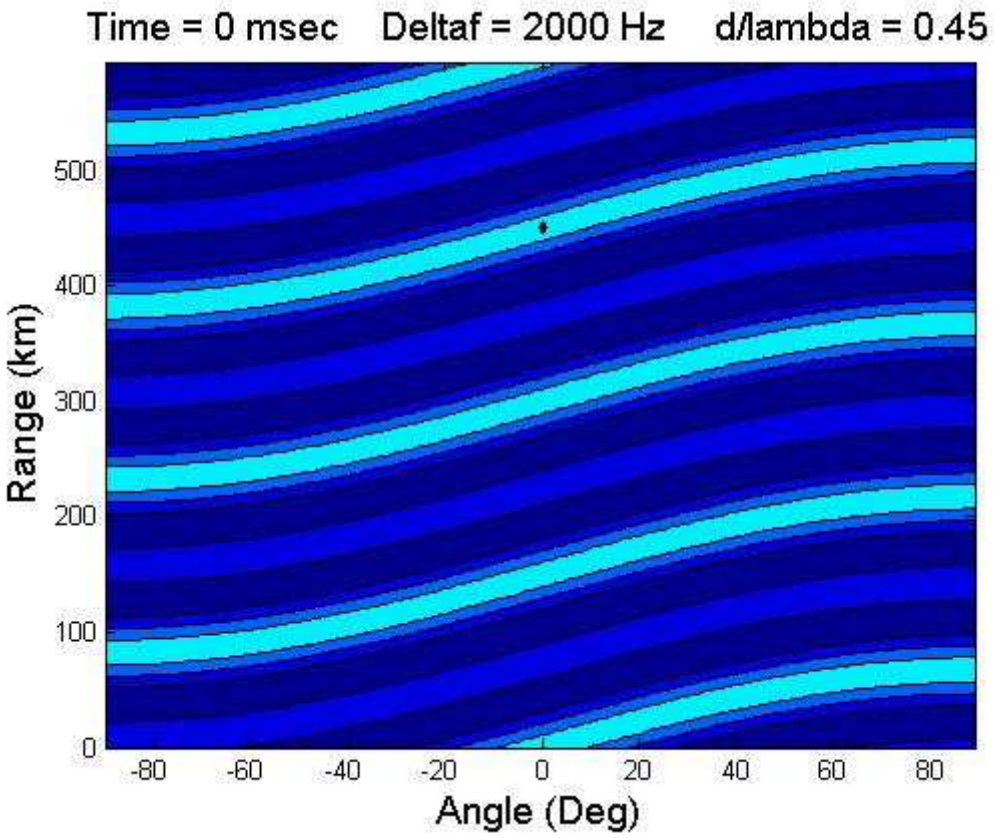

Fig. 5-13: Range-angle pattern for a frequency diverse array with Δf = 2000 Hz and d/λ = 0.45.

5.1.4 Variation with Frequency Offset, d/λ = 1.80.

The cases of Section 5.1.3 are repeated here for an element spacing of 1.80 wavelengths in order to explore the impact of frequency offset on an additional spatial arrangement of elements. As before, range-angle patterns are computed for frequency offsets of 100, 200, 300, 500, 1000, and 2000 Hz. The results are provided in Figures 5-14 through 5-19.

Observe from (5-6) that increasing the element spacing reduces the effect of induced beam steer. As an example, recall that a frequency offset of 100 Hz induced a 26.4°

beam steer at 600 km when $d/\lambda = 0.45$. That same 100 Hz frequency offset induces only a 6.4° beam steer at the same range when $d/\lambda = 1.80$. As element spacing is increased, grating lobes become apparent in angle. However, the distance to the first range ambiguity is a function of frequency offset only, so the range periodicities in this section are the same as those of the previous section for identical values of Δf.

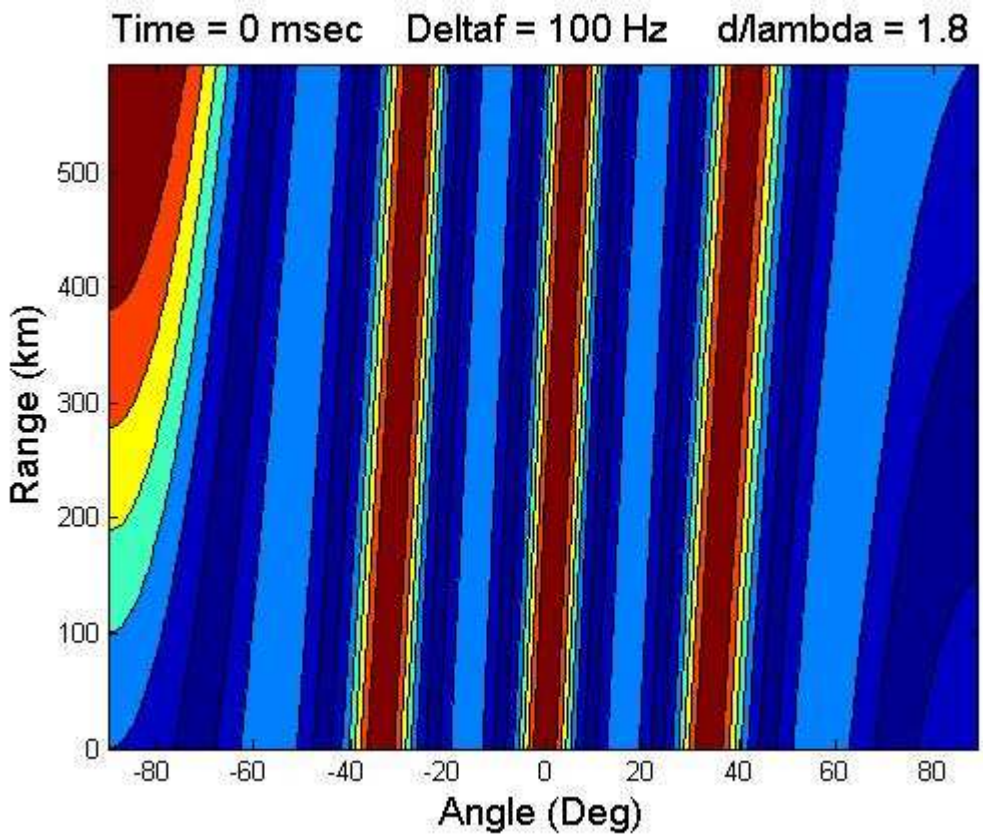

Fig. 5-14: Range-angle pattern for a frequency diverse array with $\Delta f = 100$ Hz and $d/\lambda = 1.80$.

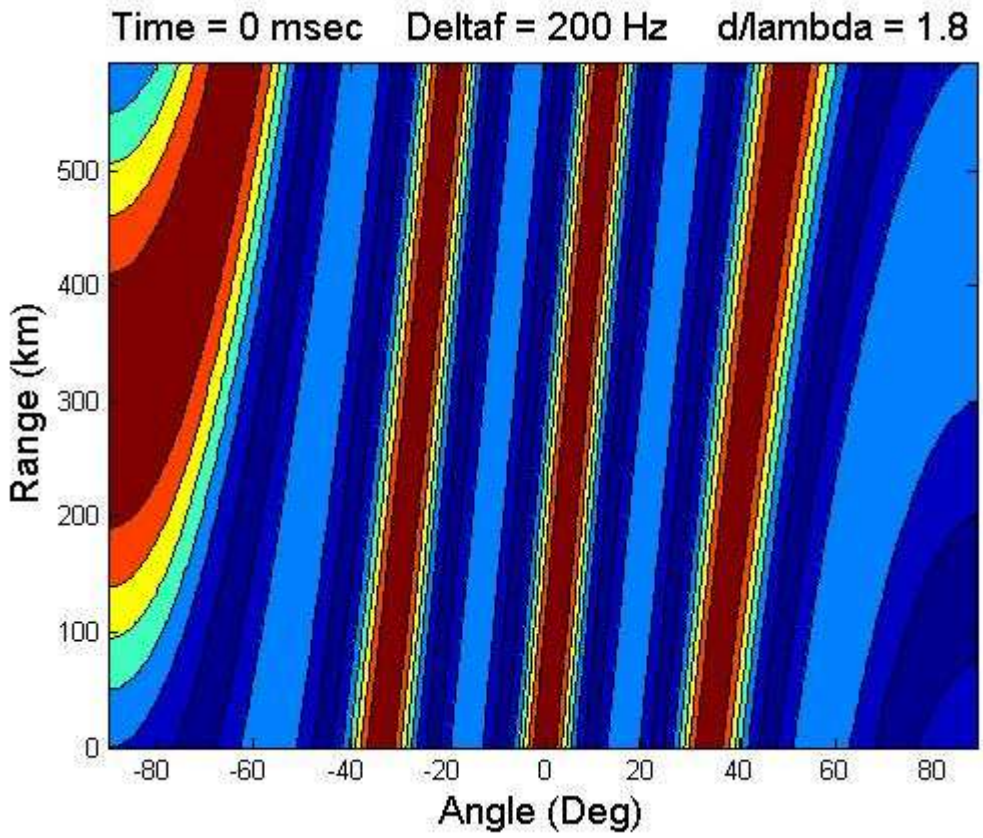

Fig. 5-15: Range-angle pattern for a frequency diverse array with Δf = 200 Hz and d/λ = 1.80.

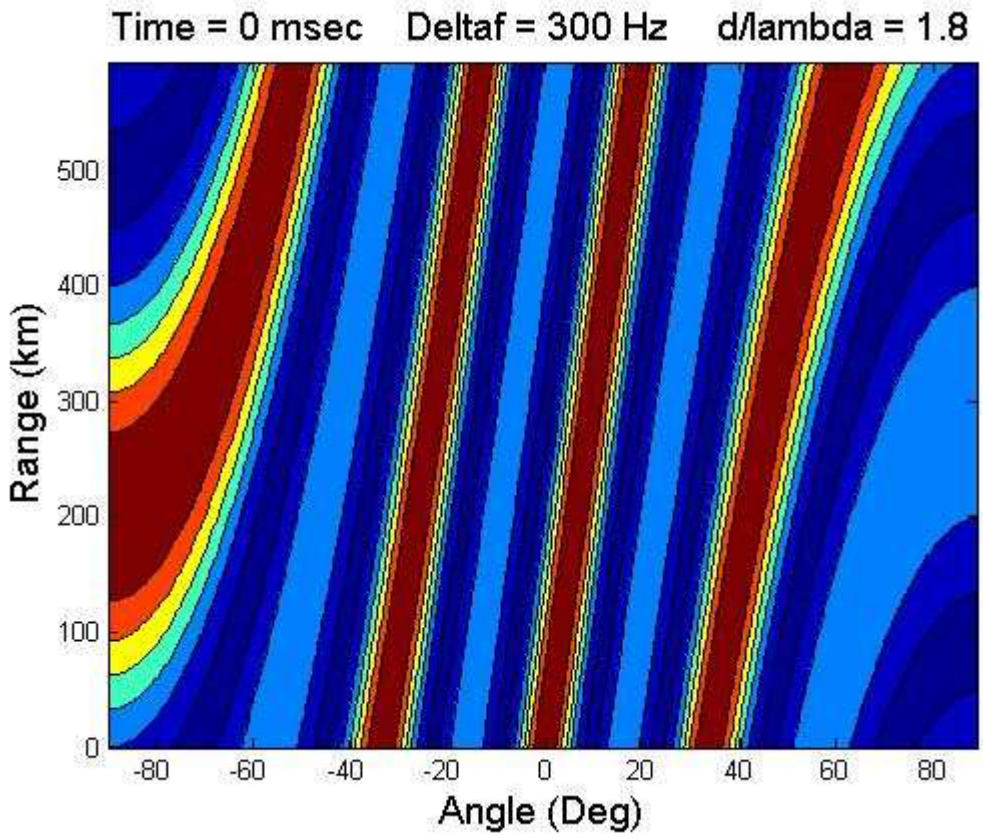

Fig. 5-16: Range-angle pattern for a frequency diverse array with Δf = 300 Hz and d/λ = 1.80.

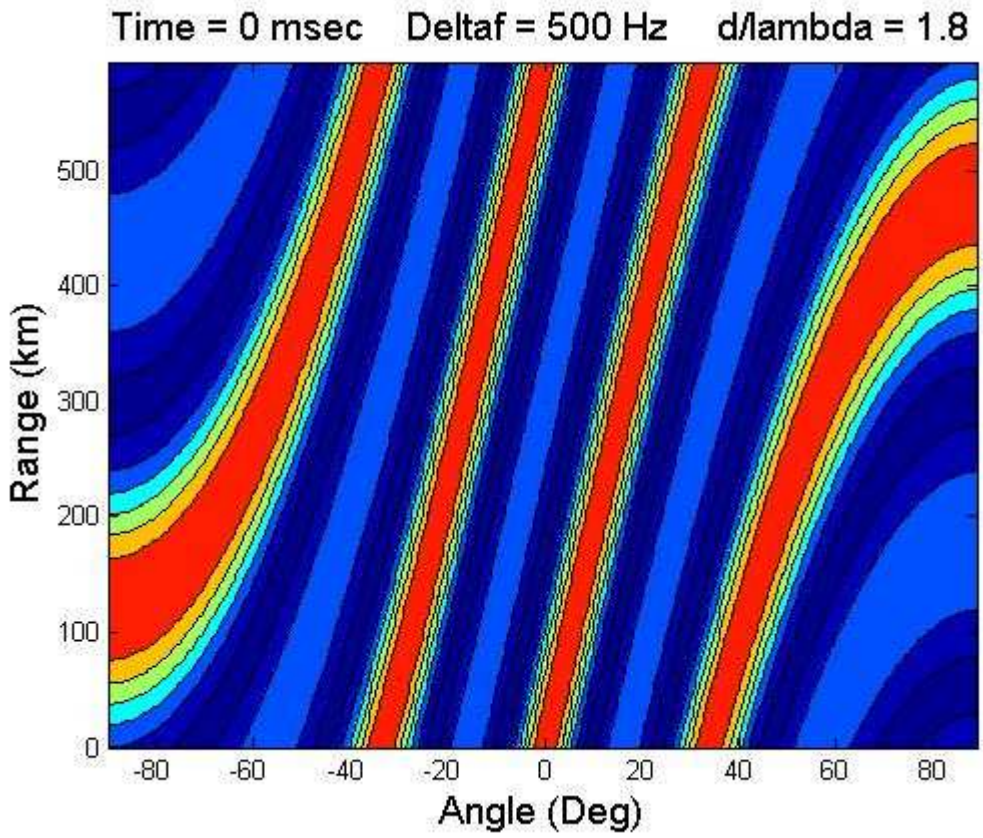

Fig. 5-17: Range-angle pattern for a frequency diverse array with Δf = 500 Hz and d/λ = 1.80.

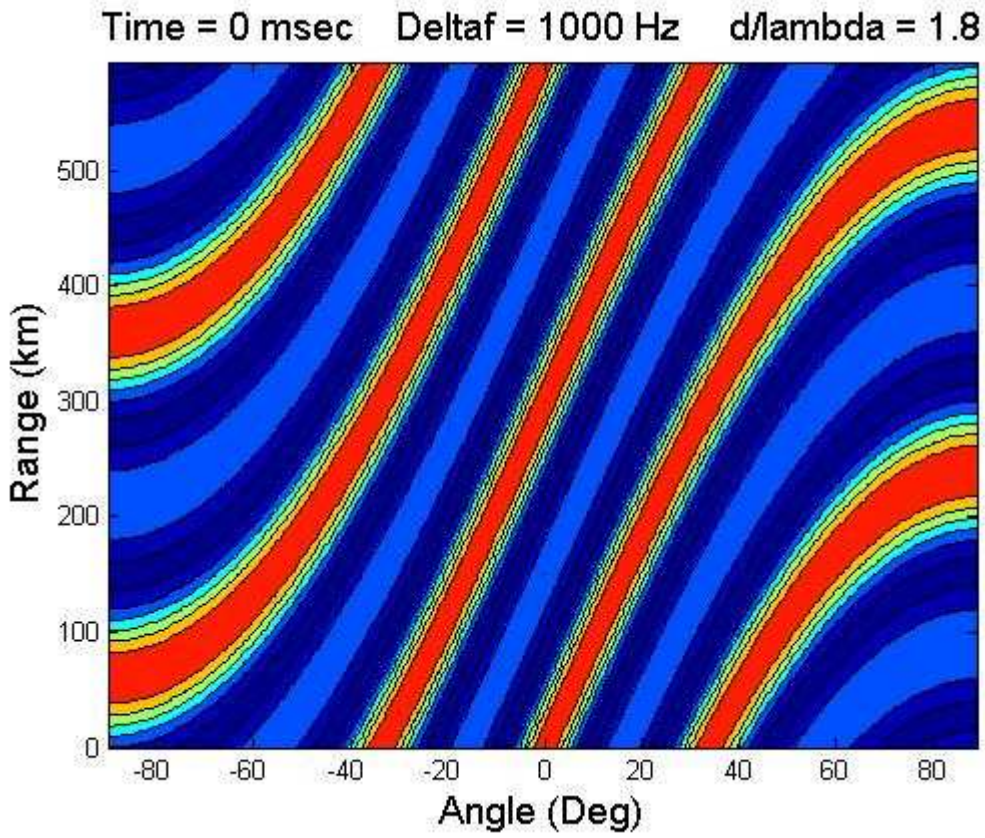

Fig. 5-18: Range-angle pattern for a frequency diverse array with Δf = 1000 Hz and d/λ = 1.80.

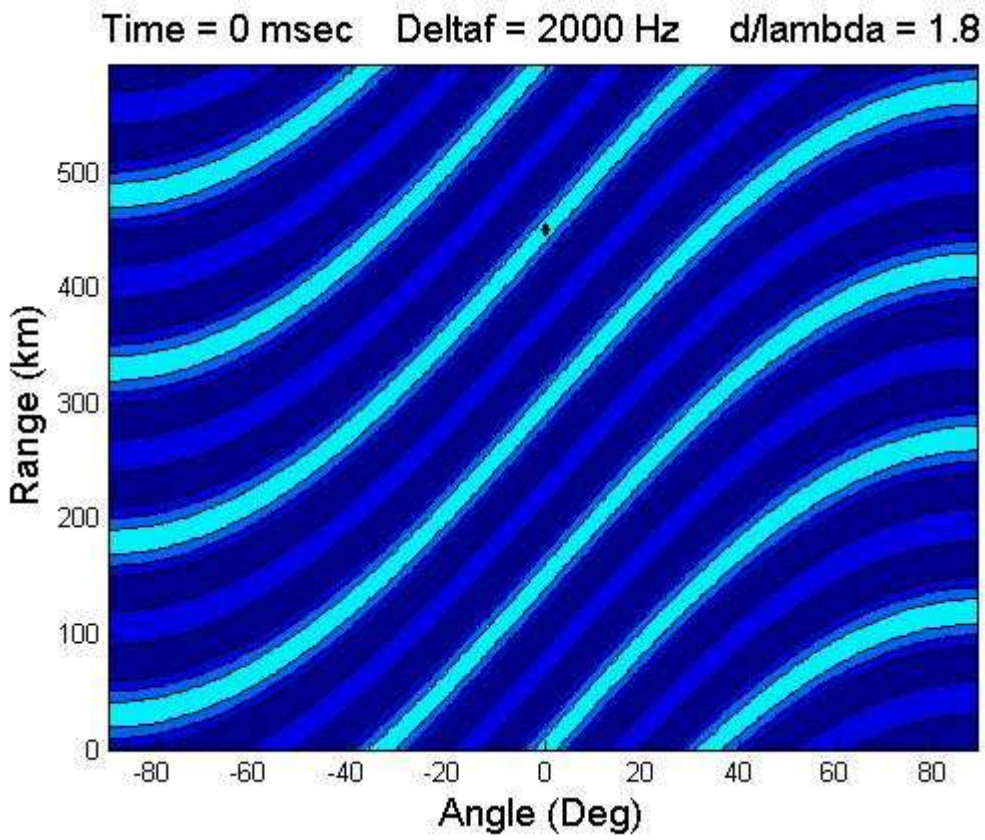

Fig. 5-19: Range-angle pattern for a frequency diverse array with Δf = 2000 Hz and d/λ = 1.80.

5.1.5 Variation with Element Spacing

The previous section looked at the range-angle pattern parametrically on the frequency offset, Δf. In this section, Δf is held fixed as the element spacing is varied. Two frequency offsets are examined: Δf = 300 Hz and 1000 Hz. The results for Δf = 300 Hz are provided in Figures 5-20 through 5-23, and the cases of Δf = 1000 Hz are presented in Figures 5-24 through 5-27.

From (4-70) and (4-71), time and range periodicities depend only on Δf and are therefore identical to the periodicities of the previous section for the same frequency

offsets. The grating lobes also remain as in Table 5-1 for the respective element spacings.

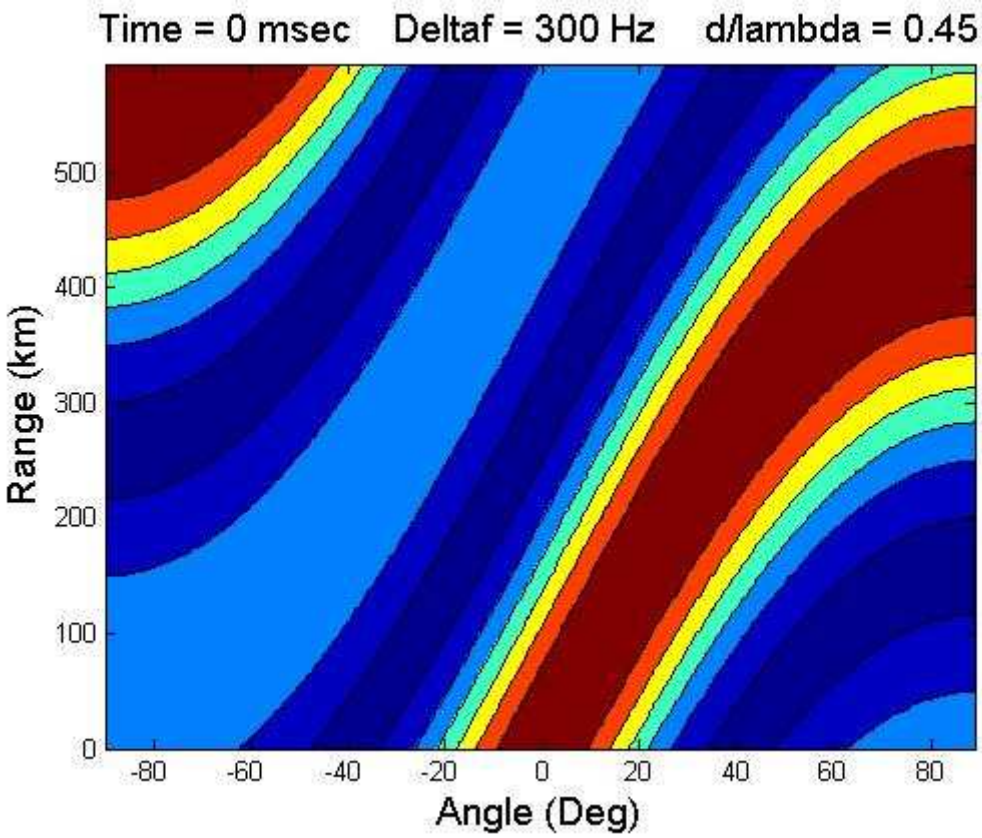

Fig. 5-20: Range-angle pattern for a frequency diverse array with Δf = 300 Hz and d/λ = 0.45.

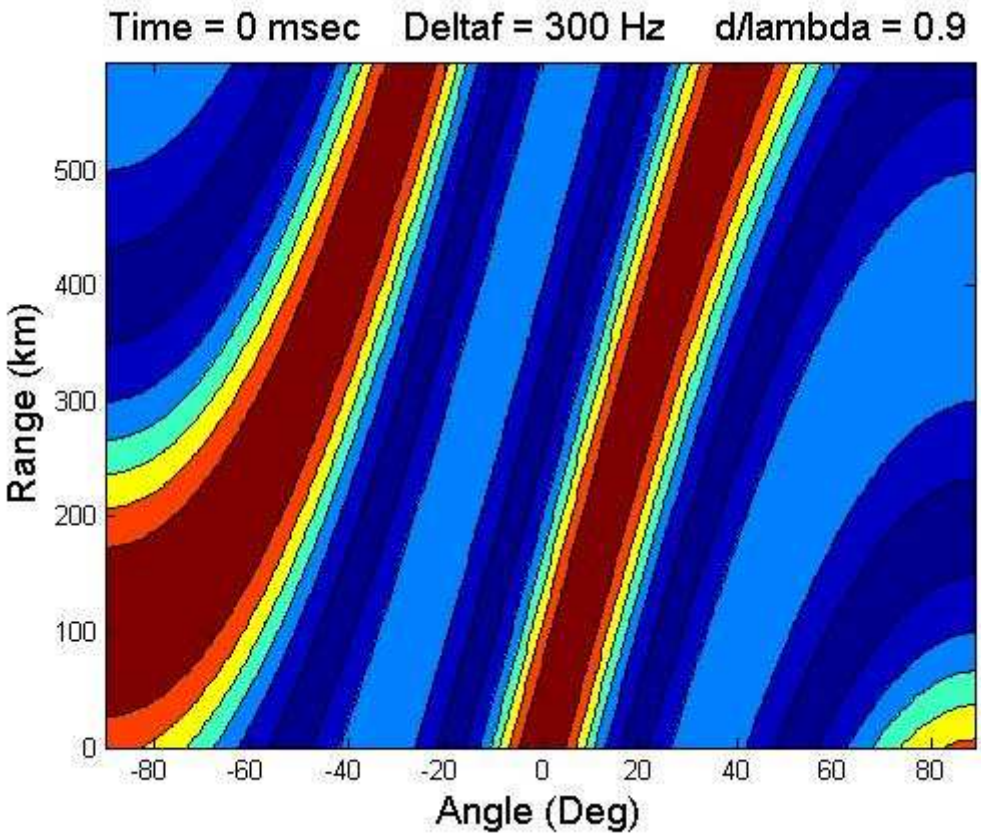

Fig. 5-21: Range-angle pattern for a frequency diverse array with Δf = 300 Hz and d/λ = 0.90.

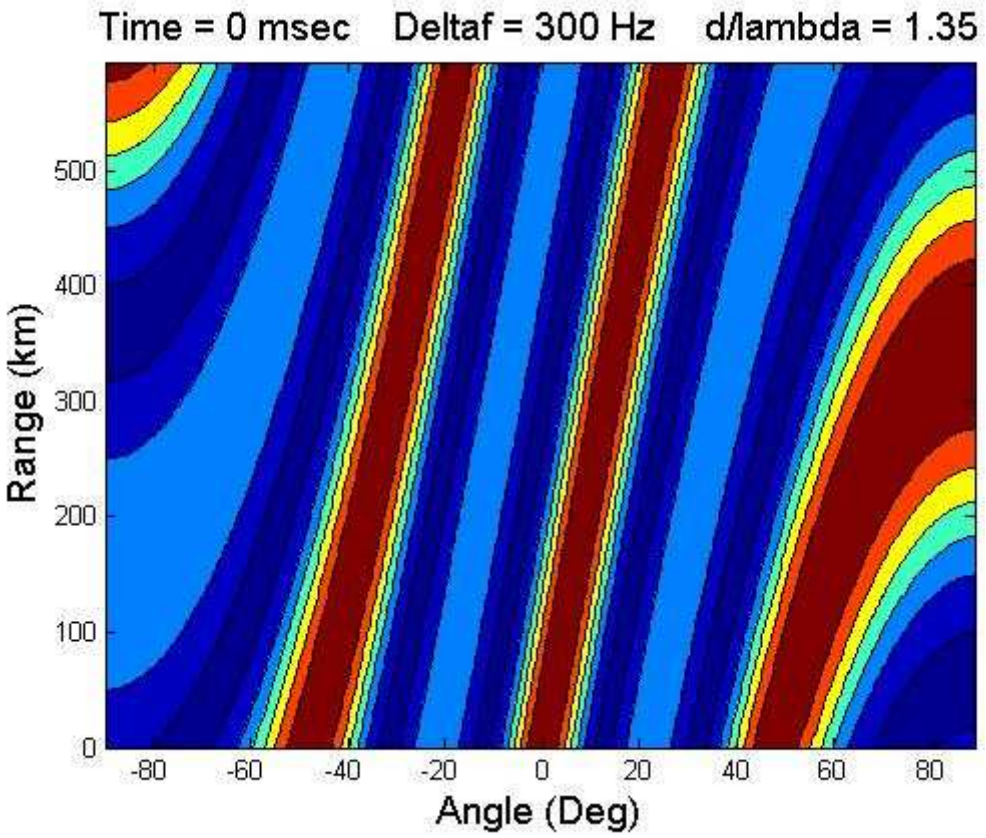

Fig. 5-22: Range-angle pattern for a frequency diverse array with Δf = 300 Hz and d/λ = 1.35.

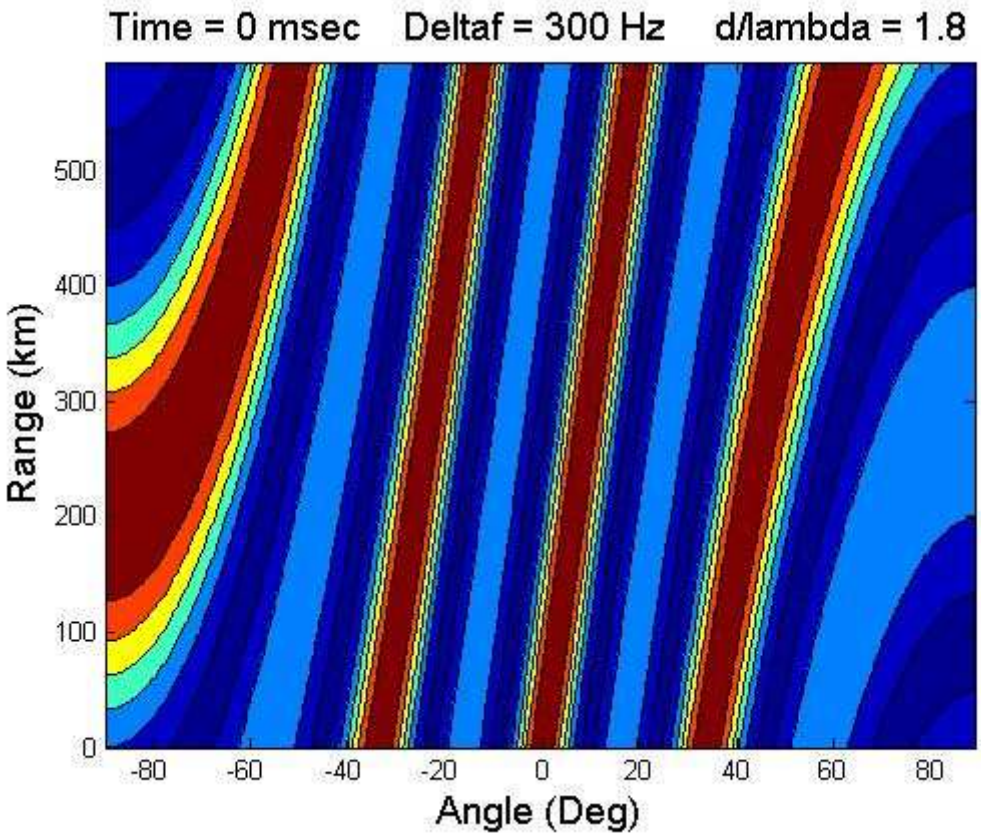

Fig. 5-23: Range-angle pattern for a frequency diverse array with Δf = 300 Hz and d/λ = 1.80.

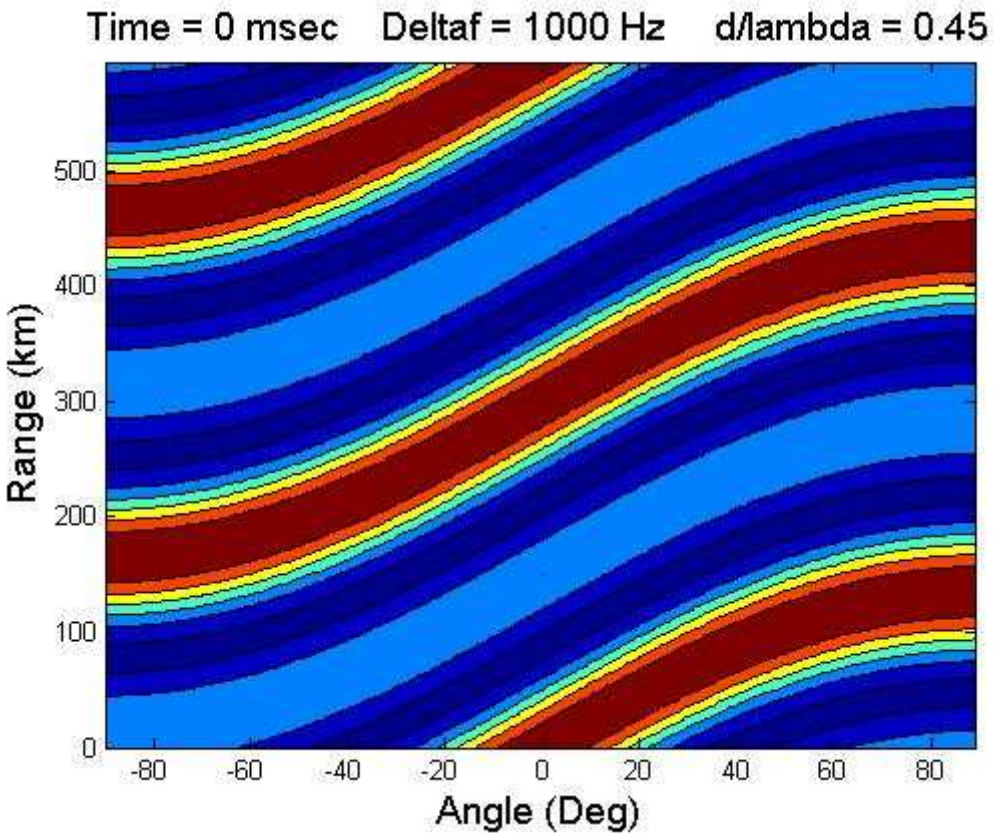

Fig. 5-24: Range-angle pattern for a frequency diverse array with Δf = 1000 Hz and d/λ = 0.45.

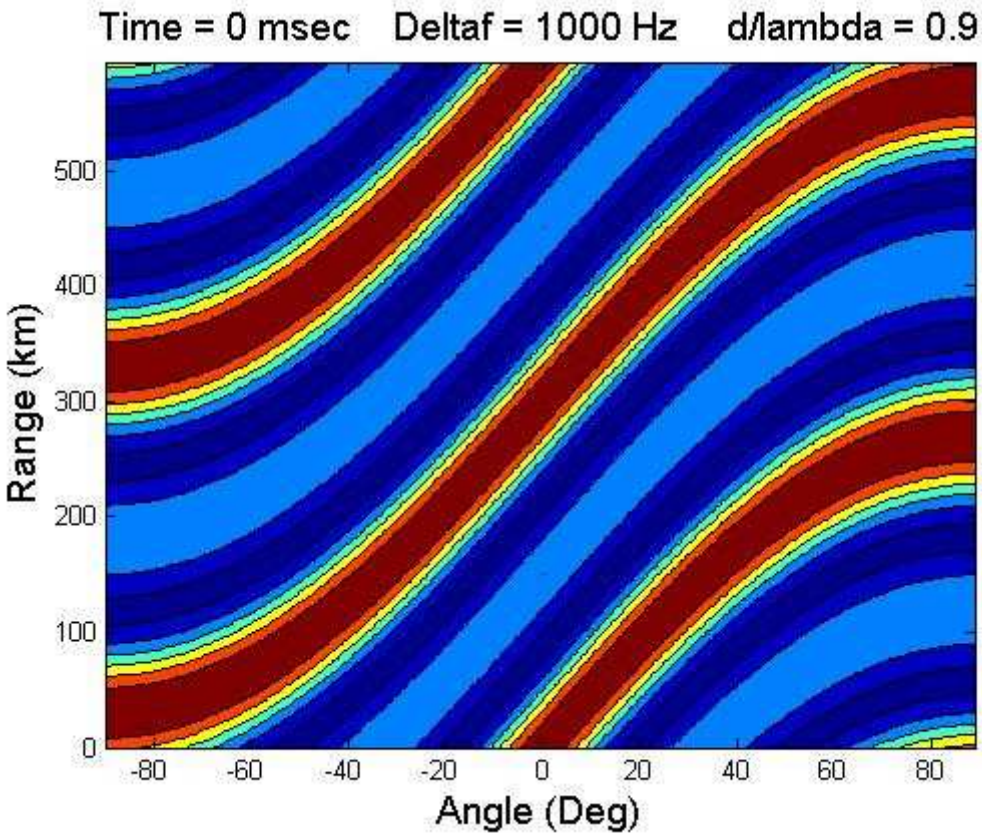

Fig. 5-25: Range-angle pattern for a frequency diverse array with Δf = 1000 Hz and d/λ = 0.90.

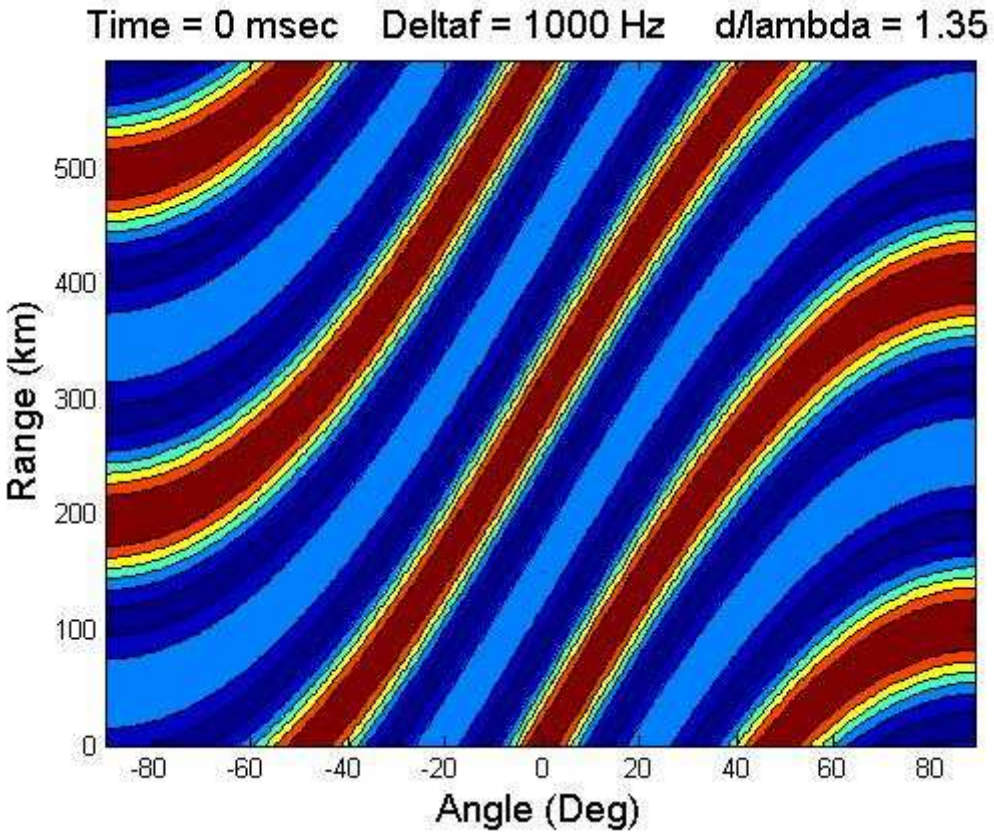

Fig. 5-26: Range-angle pattern for a frequency diverse array with Δf = 1000 Hz and d/λ = 1.35.

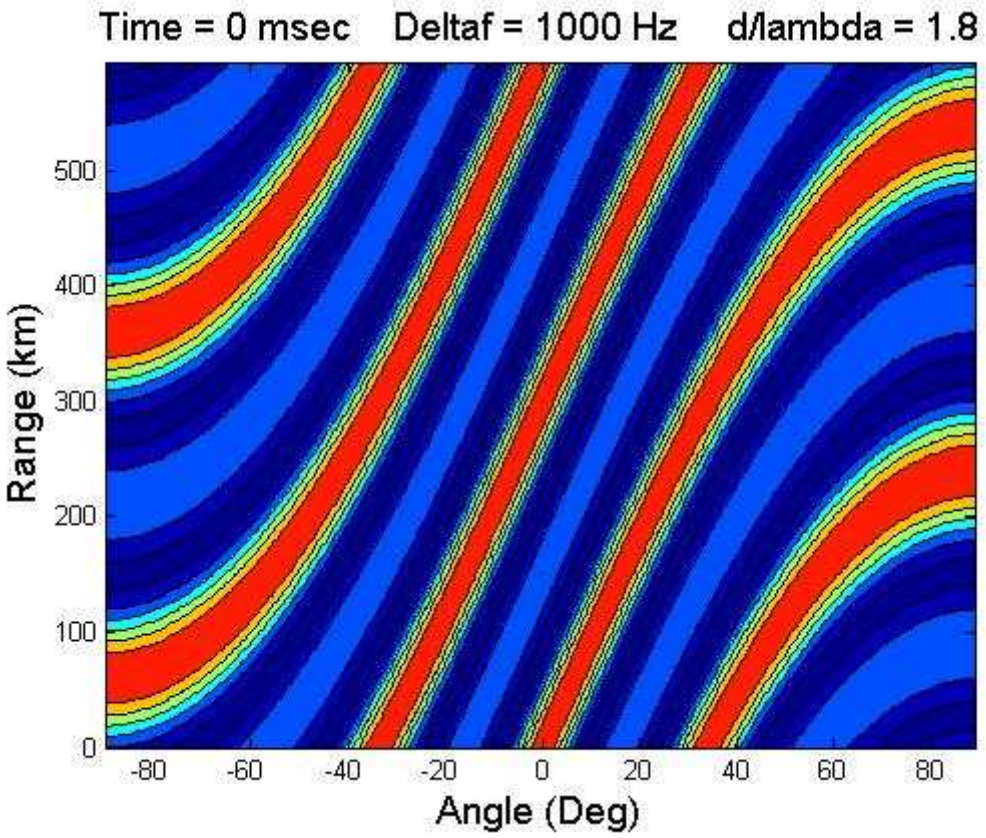

Fig. 5-27: Range-angle pattern for a frequency diverse array with Δf = 1000 Hz and d/λ = 1.80.

Note that the rate of change of apparent beam steering direction increases for larger frequency offsets and nominal steering directions. This raises a system design issue for the selection of waveform and array parameters. Examination of Equation (4-11) reveals that apparent scan direction can change rapidly for some combinations of frequency offset, range, element spacing, and centre frequency.

5.1.6 Propagation of the Pattern

As noted in Section 4.3, the frequency diverse array pattern propagates in time as a transverse electromagnetic wave. Section 5.1 illustrated that the beam pattern repeats after time $\frac{1}{\Delta f}$. This is demonstrated in Figures 5-28 through 5-33, which show the electric field for several instants of time for the case of Δf = 100 Hz and d/λ = 0.45. The beam patterns at t = 0 and t = 10 msec are identical.

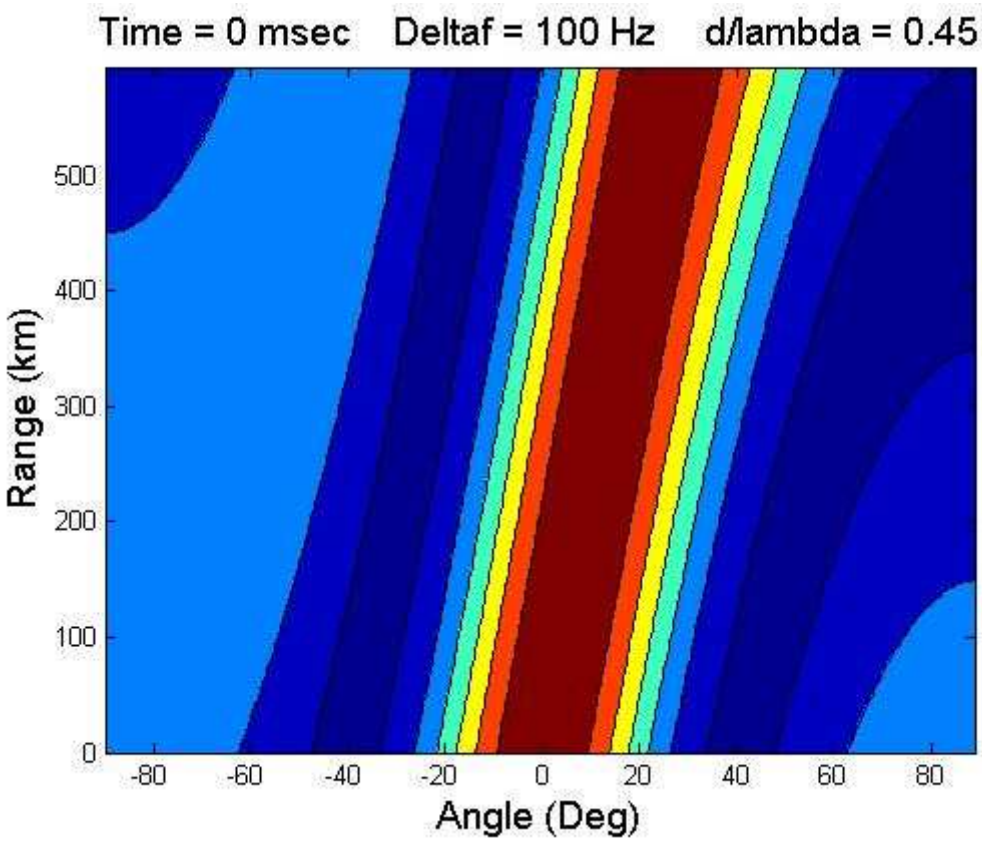

Fig. 5-28: Electric field at time instant of t = 0 msec.

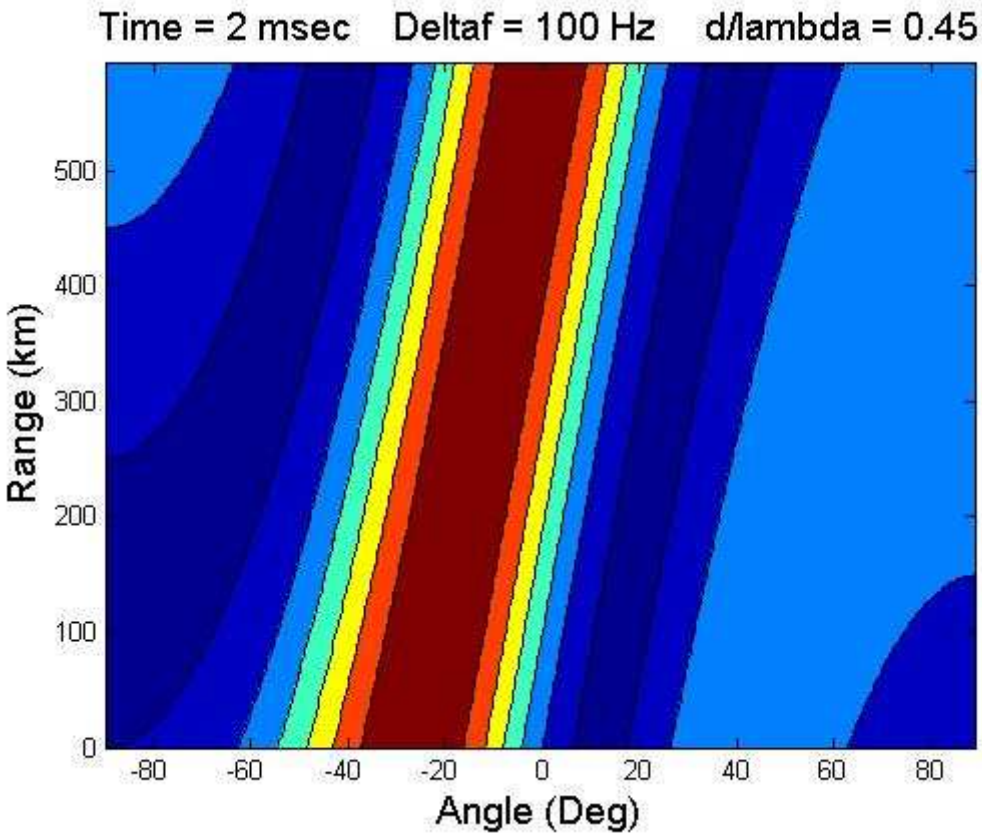

Fig. 5-29: Electric field at time instant of t = 2 msec.

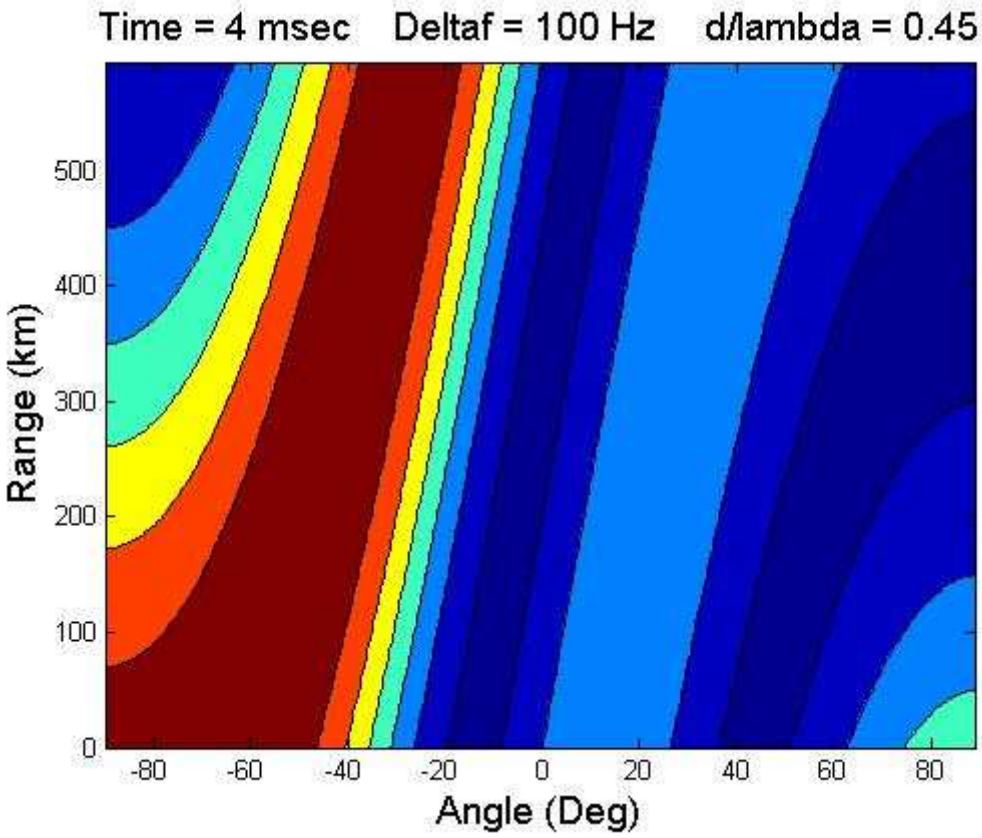

Fig. 5-30: Electric field at time instant of t = 4 msec.

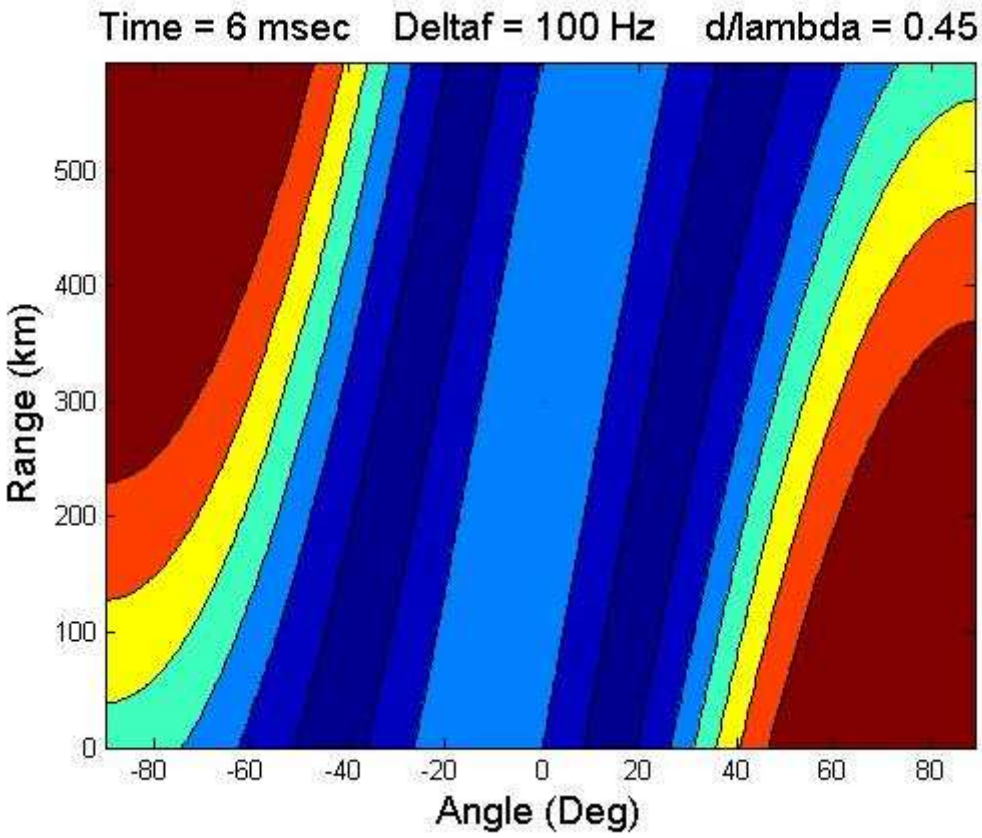

Fig. 5-31: Electric field at time instant of t = 6 msec.

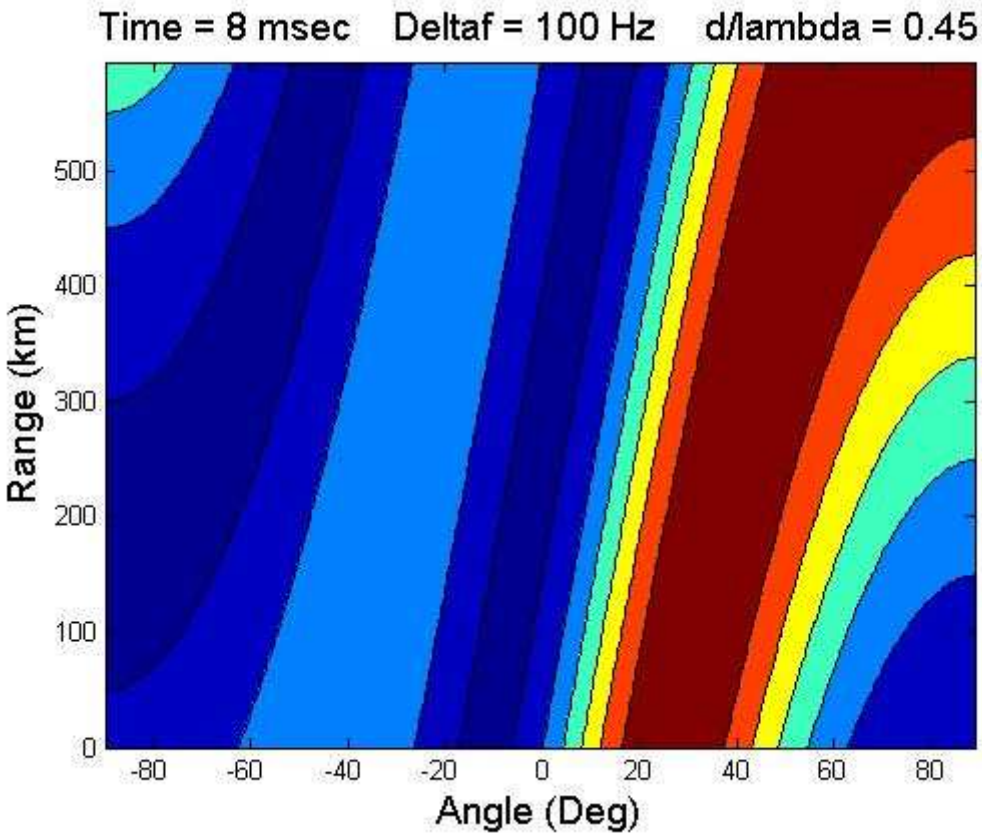

Fig. 5-32: Electric field at time instant of t = 8 msec.

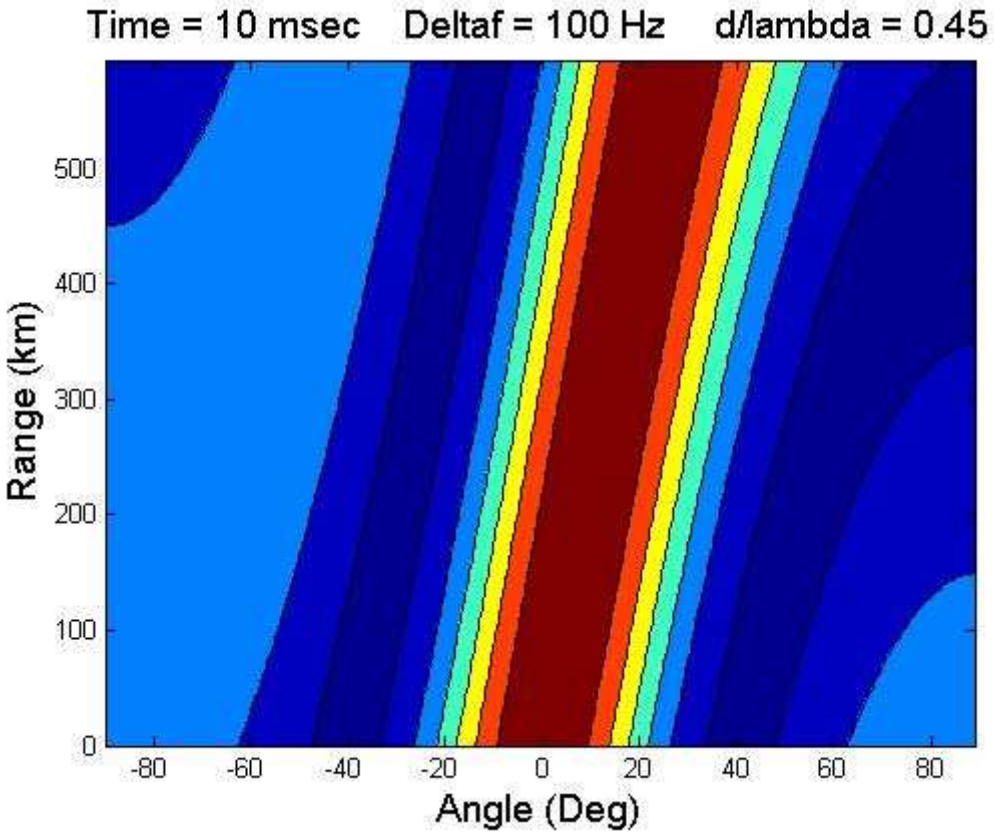

Fig. 5-33: Electric field at time instant of t = 10 msec.

5.2 Summary of Predicted Performance

This chapter explored through simulation beam formation and control of the frequency diverse array. Frequency offset and element spacing were varied to affect time periodicity, range periodicity, angle periodicity, and scan rate. The simulations confirmed the theory of Chapter 4. In particular, range periodicity was shown to behave as predicted in (4-71), and be equal to $\frac{c}{\Delta f}$. Angle periodicity was shown to vary in accordance with (4-72), and be equal to $\frac{\lambda}{d}$. When both frequency offset and element spacing varied, the beam steer angle at any range was shown to be:

$$\sin\theta' = \left[\sin\theta_0 - \frac{R_1 \Delta f}{c\left(d/\lambda\right)} \right] , \tag{5-5}$$

while the time to scan through an angle $\theta_2 - \theta_1$ is:

$$t = \frac{-\left(d/\lambda_0\right)}{\Delta f} \left[\sin\theta\right]_{\theta_1}^{\theta_2} . \tag{5-6}$$

The next chapter will describe a series of measurements to experimentally verify the above results.

Chapter 6

Experimental Measurements

6.1 Introduction

This chapter describes the design and execution of a measurement programme to experimentally validate the theory and simulation of the frequency diverse array.

Experiments were performed in Rome, N.Y., USA. These experiments included both bench tests and radiated field measurements. The measurement programme required the design, construction, and assembly of transmitting, receiving, and data recording equipment. The measurement system is described in Section 6.2, and the measured results are presented in Section 6.3.

6.2 Measurement System

For the radiated field tests, a frequency diverse array was built and mounted on a 16 metre tower. A two-channel receiver was placed on an adjacent tower, approximately 72 metres from the transmit array. Inputs to the receiver were collected from a fixed antenna located on the receive tower and from an antenna placed at various rooftop locations. This provided measurements from geographically separated receive locations. The two received signals were then input into a single multi-channel digital sampling oscilloscope so that the received signals from two locations could be recorded simultaneously.

6.2.1 Antenna Subsystem

A 3 GHz transmit antenna was constructed of an array of 15 microstrip patch radiators. The elements were mounted to a backplane fabricated of aluminium stock, and arranged in a configuration of 3 rows and 5 columns. The radiators were mounted at a separation of 4.35 cm, providing an element spacing of $d/\lambda = 0.45$ at a frequency of 3.1 GHz. The 3 elements in each column were combined into a single subarray, resulting in 5 spatial channels. The array elements were dual-polarized, although only horizontal polarization was used for experimentation. The full transmit array mounted on the backplane is shown in Fig. 6-1.

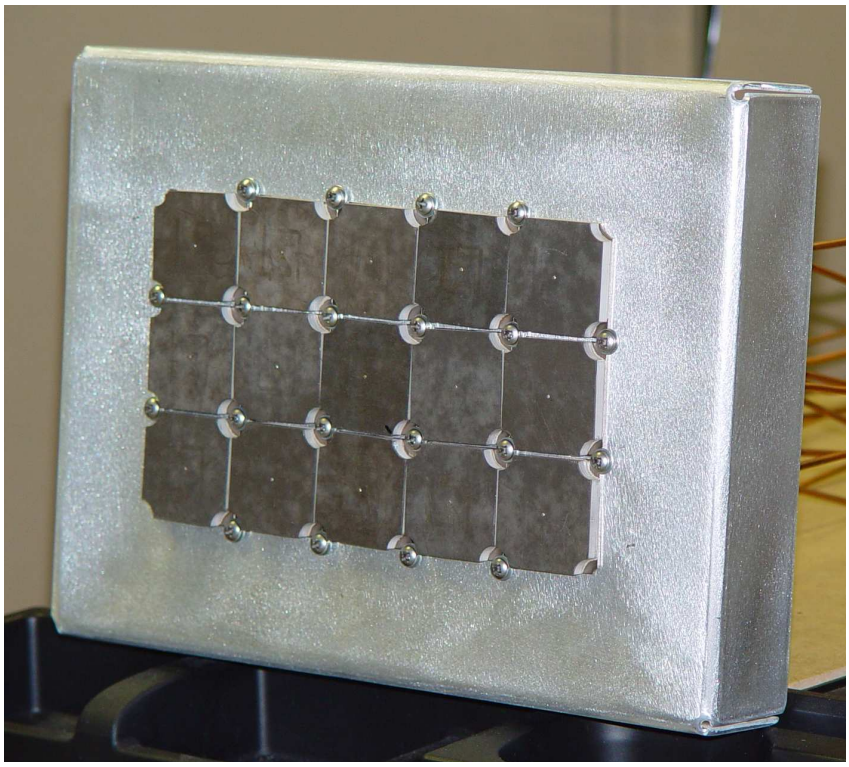

Fig. 6-1: 3 GHz transmit antenna test article

The antenna pattern for the full array was measured in a semi-anechoic chamber, with all radiating elements corporate-fed from a single source. The resulting sum pattern for the uniformly illuminated array is shown in Fig. 6-2. This pattern shows a predicted *sinc* response, with first sidelobes approximately 13 dB down from the peak, first null at 23º azimuth, and good symmetry. Backlobe responses appear at the noise level of the chamber.

The element pattern for the centre element as mounted in the array was also measured, as shown in Fig. 6-3. Pattern measurements were taken clockwise over a 120º interval from 247° to 67°. A straight line connects data points over the region where no data was collected. Also, the output level for the single element was significantly lower than for the full array, resulting in a lower measurement signal-to-noise ratio. However, the element pattern does show the broad angular response of the microstrip patch radiator.

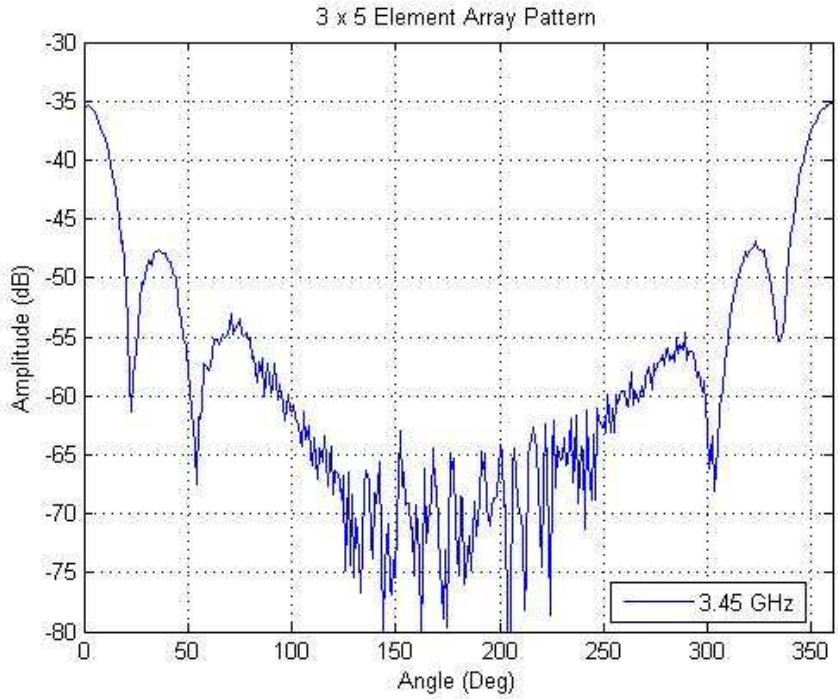

Fig. 6-2: Measured antenna pattern of 3 x 5 element array test article

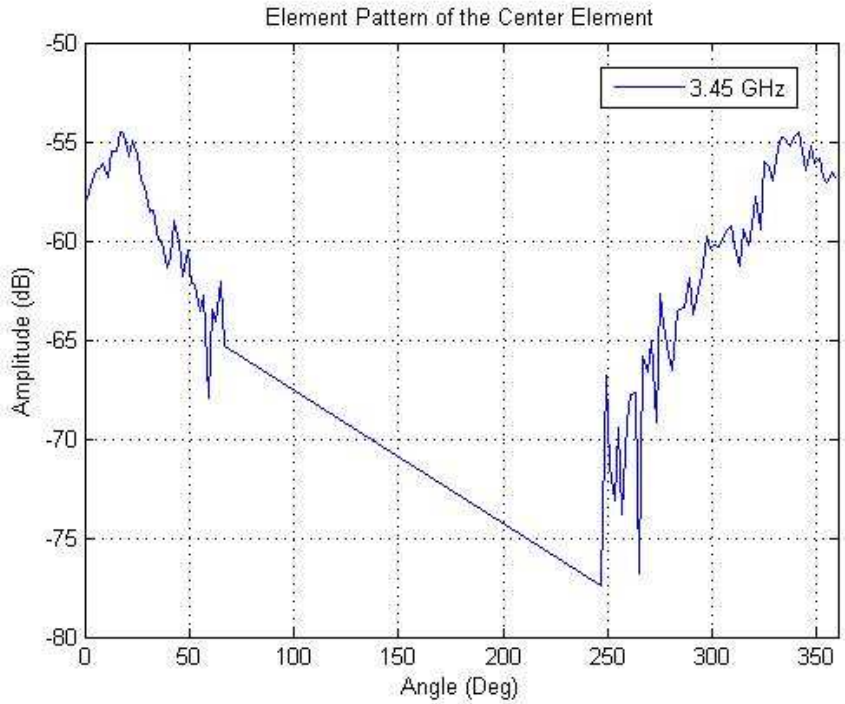

Fig. 6-3: Element pattern of the centre array element. Data was taken clockwise over a 120º interval from 247° to 67°

6.2.2 Transmitter Subsystem

Each 3-element column subarray of the constructed frequency diverse array was driven by a separate signal generator. A CW tone was radiated from each column, with the frequency of each tone increased by Δf from channel-to-channel. All signal generators were triggered by a common clock. The signal in each channel was amplified and phase corrected, and then split using a 1:4 divider. The unused power divider output was either terminated or padded for use as a signal monitoring test point. A block diagram of a transmitter channel is shown in Fig. 6-4. All 5 channels of the transmitter subsystem are shown mounted in position in Fig. 6-5.

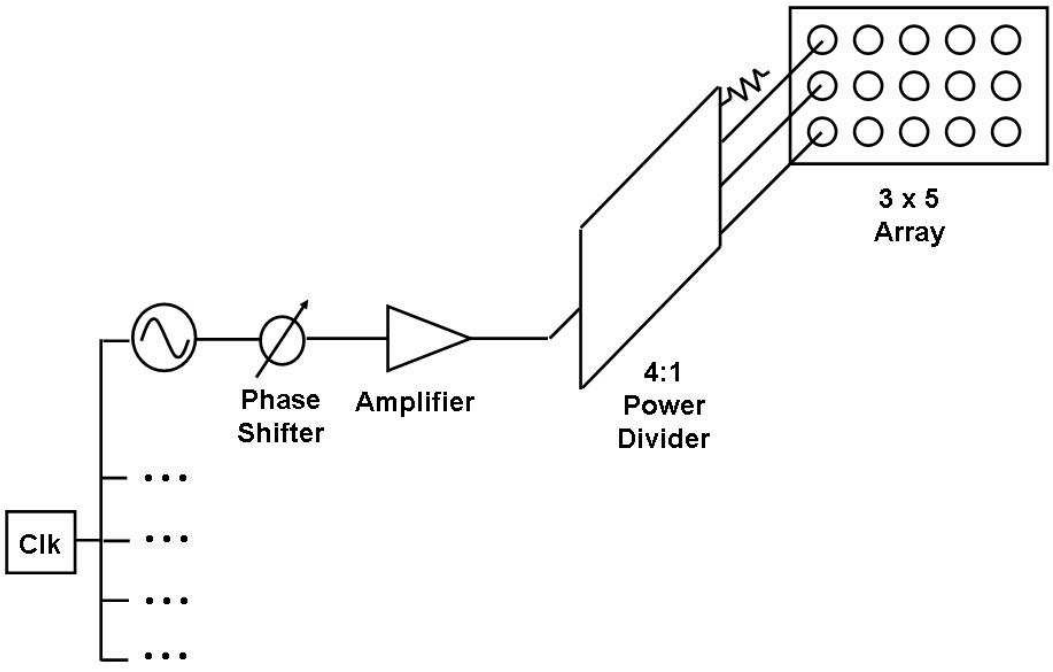

Fig. 6-4: Block diagram of a transmitter channel

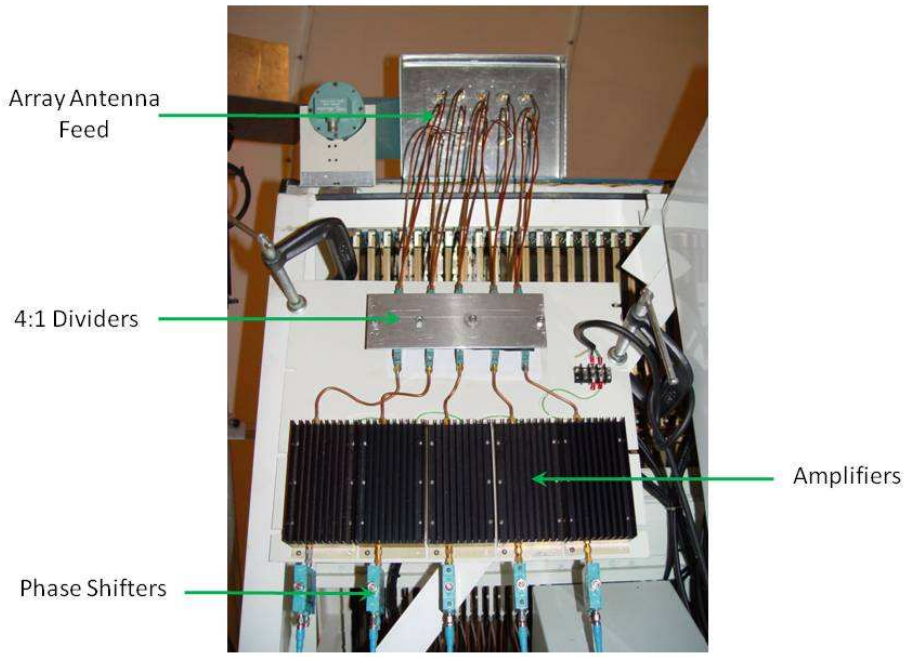

Fig. 6-5: Assembled transmitter channels mounted in place.

6.2.3 Receiver Subsystem

Two receive channels were developed and installed in a shelter located on a tower approximately 72 metres from the transmit array. For each channel, the transmitted signal was captured by a standard gain EMCO horn antenna, amplified in a low noise amplifier, and band-pass filtered for 3.1 GHz. The signal was then mixed down to an intermediate frequency of 10 MHz, low-pass filtered, and amplified. A block diagram of a receiver channel is given in Fig. 6-6, with a fully constructed channel shown in Fig. 6-7.

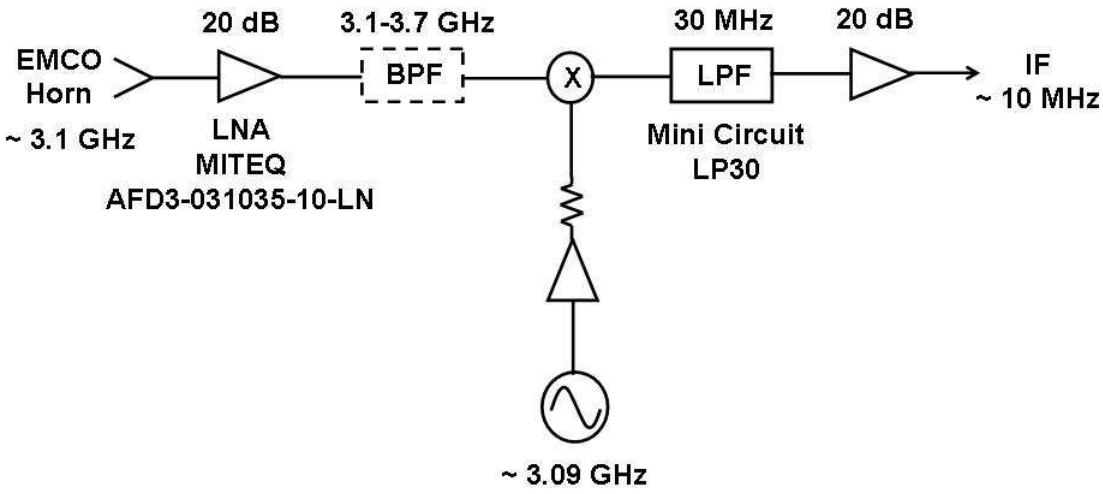

Fig. 6-6: Block diagram of a receiver channel

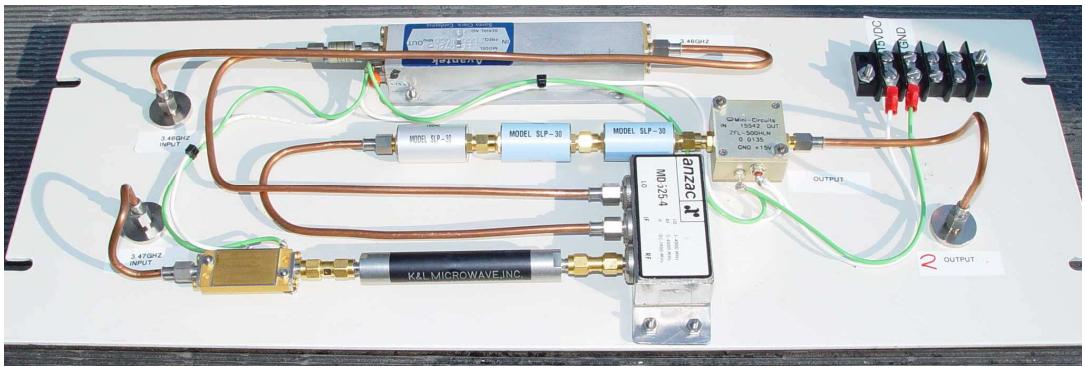

Fig. 6-7: Fabricated receiver channel

6.2.4 Recording Subsystem

The IF signal output from each receiver channel was recorded on a Lecroy digital oscilloscope. The Lecroy has a built-in 8-bit analogue-to-digital converter, which was sampled at a rate of at least 50 MS/sec. This sampling rate provides significant margin against aliasing of the 10 MHz IF signal. The Lecroy has a storage capacity of about 4 million samples, which provides a limited continuous recording time.

When configured for frequency diverse array experiments, the LeCroy recording system was set to continuous record mode. In this case, the LeCroy continuously records samples at the sampling rate until the memory is filled, as illustrated in Fig. 6-8.

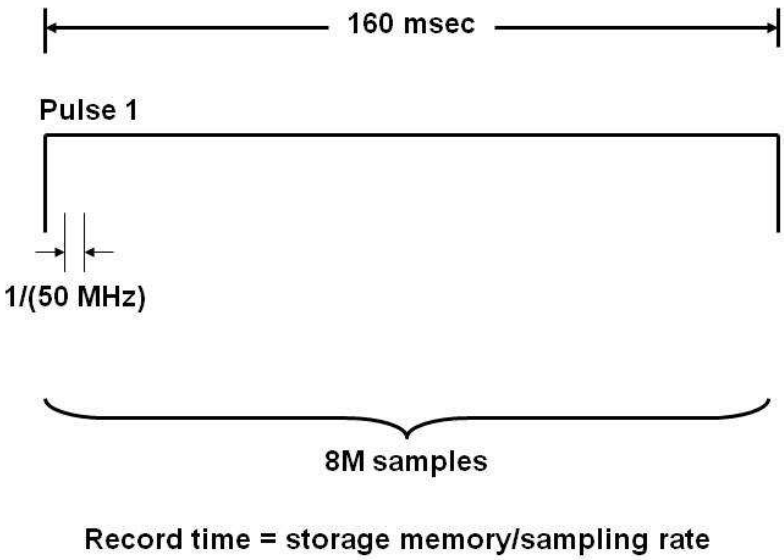

Fig. 6-8: Lecroy recording timeline for continuous record

6.3 Measurements and Results

The experimental measurements consist of trials to demonstrate the time dependence of the frequency diverse array signals, the auto-scanning property of the frequency diverse array, and the range dependence of the frequency diverse array pattern.

6.3.1 Time Variation of the Pattern

As an initial step, a series of bench tests were performed to investigate the time dependence of the frequency diverse array without the complications of radiated field measurements. Five signal generators were utilised to produce continuous wave signals. A small linear frequency shift, Δf, was applied from channel-to-channel across the signal generator set. The output of each generator was supplied to an 8:1 combiner, and the resultant summed output was detected and applied to a digital oscilloscope. The combined output represents the time response of a frequency diverse array at a single angle (boresight) in the far-field. Various frequency shifts were applied to demonstrate the effect on the time waveform.

The bench test configuration is illustrated in Fig. 6-9. Measured outputs are shown in Figure 6-10 through 6-12 for frequency shifts of 100 Hz, 1 kHz, and 10 kHz respectively. Examination of the measured data shows excellent agreement with the theory of Section 4.2. The frequency diverse array signal is periodic with period $1/\Delta f$, and the sidelobe structure is well-behaved and in agreement with the results predicted in Figures 4-6 and 4-7.

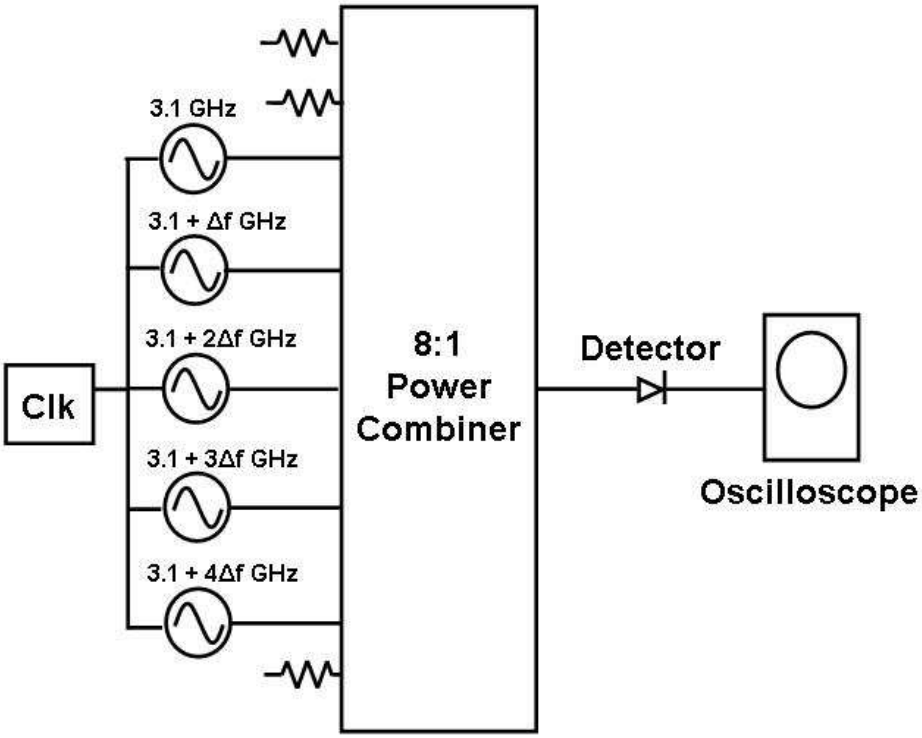

Fig. 6-9: Bench test configuration to demonstrate time dependence of the FDA waveform.

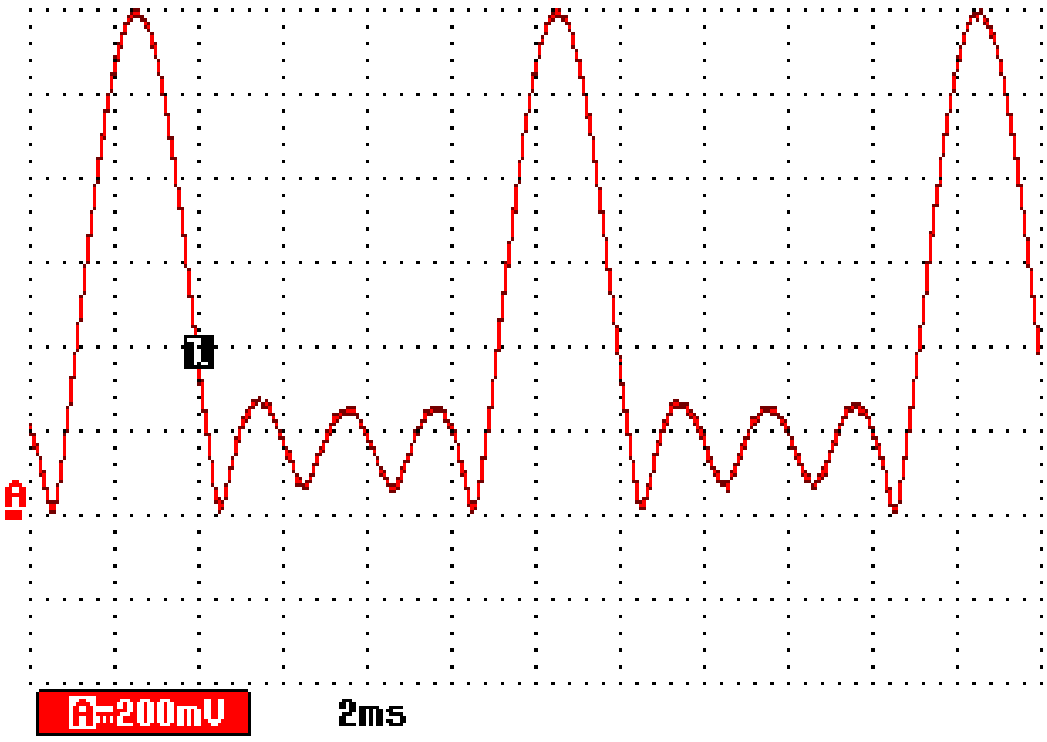

Fig. 6-10: Bench test output for $\Delta f = 100$ Hz. FDA signal is periodic with a period of 10 ms.

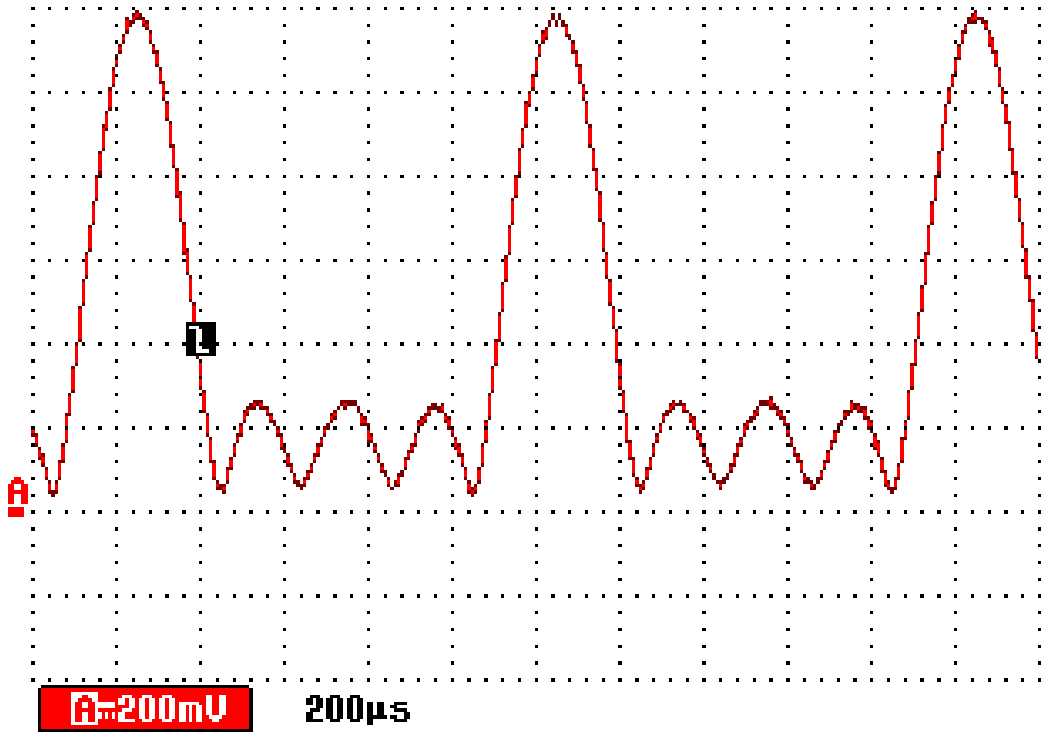

Fig. 6-11: Bench test output for $\Delta f = 1$ kHz. FDA signal is periodic with a period of 1 ms.

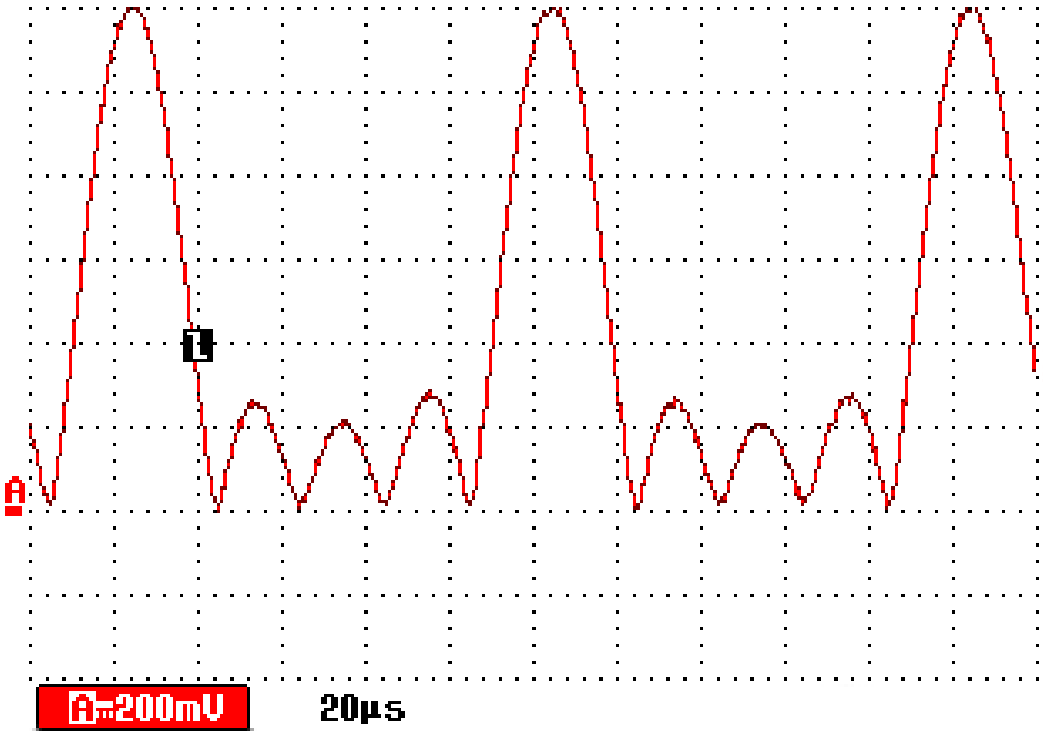

Fig. 6-12: Bench test output for Δf = 10 kHz. FDA signal is periodic with a period of 0.1 ms.

Subsequent to the bench tests, radiated field measurements were taken to further validate the time periodicity of the frequency diverse array signal. The 5-channel array and associated hardware described in Section 6.2 were utilized for data collection. The electric field was first measured close to the transmit array, but in the far zone of the antenna. The far field region begins approximately at:

$$R_{far-field} = \frac{2D^2}{\lambda} \quad , \tag{6-1}$$

where D is the largest aperture dimension. Then,

$$R_{far-field} = \frac{2(N\,d)^2}{\lambda} \quad . \tag{6-2}$$

For N = 5, d = 4.35 cm, and f = 3.1 GHz, the far field begins at about 1 m. A probe was therefore placed approximately 2 m from the transmit array as shown in Fig. 6-13. This signal was detected and recorded by a digital oscilloscope. A close-range probe measurement for a 5-channel system with Δf = 100 Hz is shown in Fig. 6-14. This measurement shows excellent time sidelobe structure and a period of $1/\Delta f$ = 10 ms as expected.

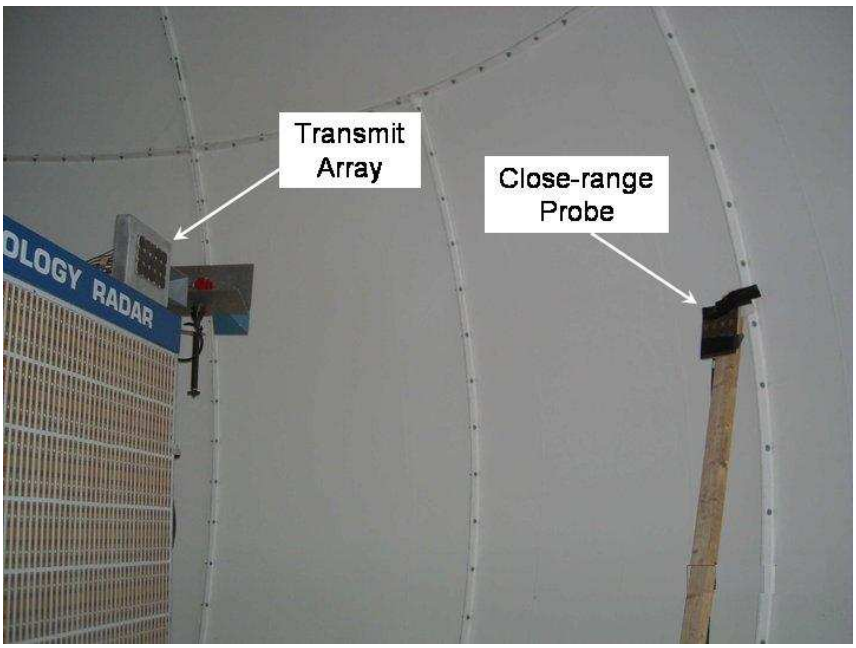

Fig. 6-13: Probe used to measure electric field close to transmit array.

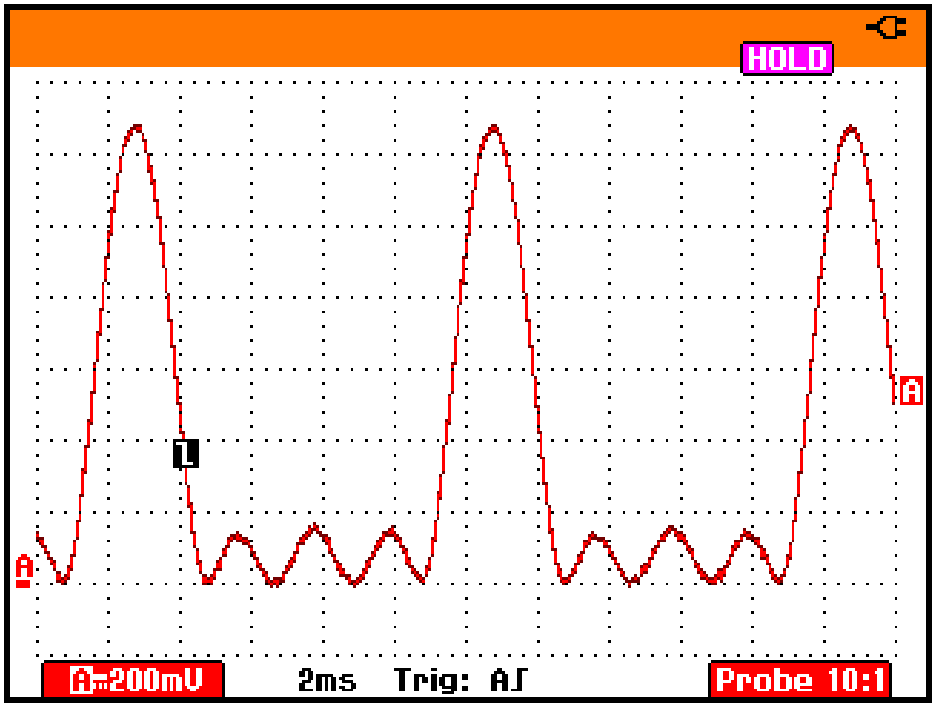

Fig. 6-14: Close range measurement of electric field time waveform for 5-channel frequency diverse array, Δf = 100 Hz.

A spectrum analyzer measurement for a similar signal (N = 5, Δf = 100 Hz) received approximately 2 km from the transmit array is shown in Fig. 6-15. Even for monochromatic signals, the spectrum analyzer display shows significant spectral overlap between channels due to hardware effects and instrument response characteristics. The time waveform for this case is presented in Fig. 6-16 along with a moving average. The signal is shown to be periodic in time at 10 ms as expected, and is also shown to have the correct number of sidelobes. However, there is some asymmetry in the sidelobe structure due to real-world effects such as multipath.

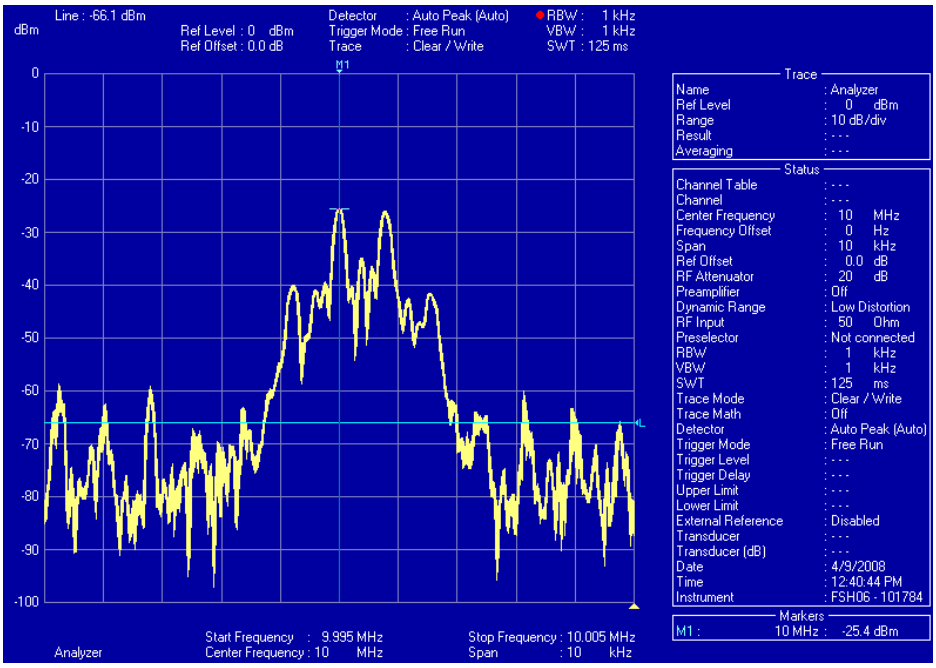

Fig. 6-15: Spectrum analyzer display for signal received at 2 km, $N = 5$, $\Delta f = 100$ Hz

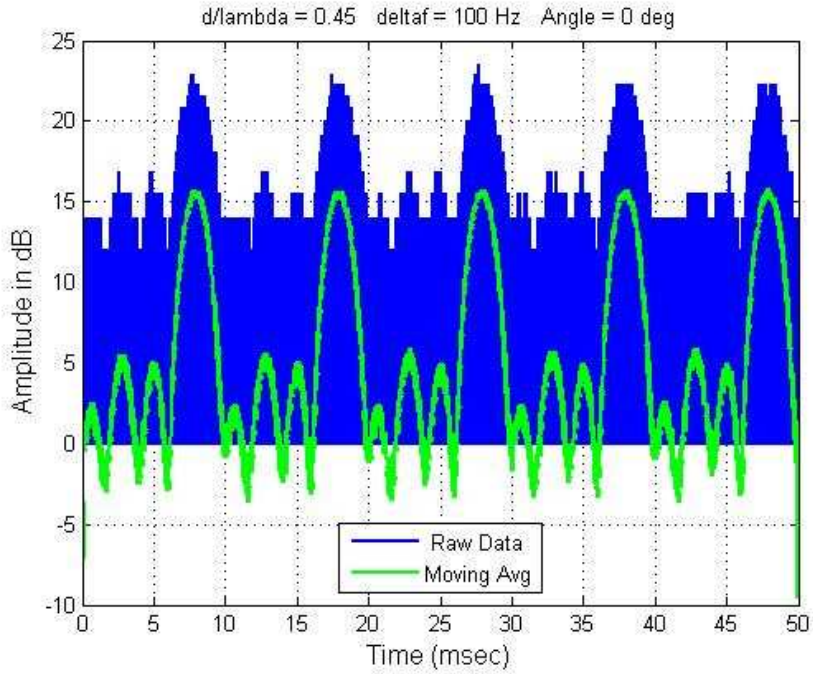

Fig. 6-16: Time waveform of signal received at 2 km, $N = 5$, $\Delta f = 100$ Hz

The close-range probe measurement, spectrum analyzer display, and received signal for two other 5-channel cases are presented in Figures 6-17 and 6-18. Fig. 6-17 shows the recorded data for a signal radiated with Δf = 1 kHz, and Fig. 6-18 displays the measurements for Δf = 10 kHz. Notice that when Δf = 1 kHz the received spectrum appears as a single broad response. As the frequency offset increases to Δf = 10 kHz, the individual components of the frequency diverse array spectrum become evident.

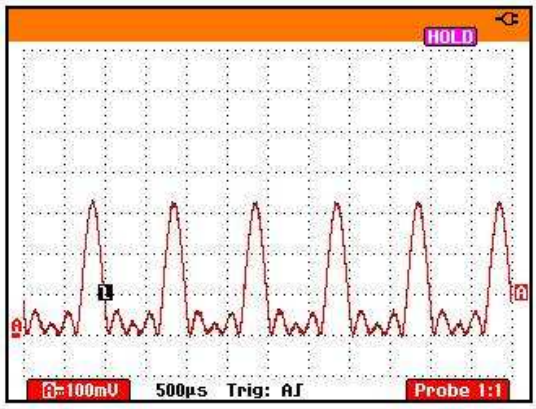

(a) Close-range probe measurement

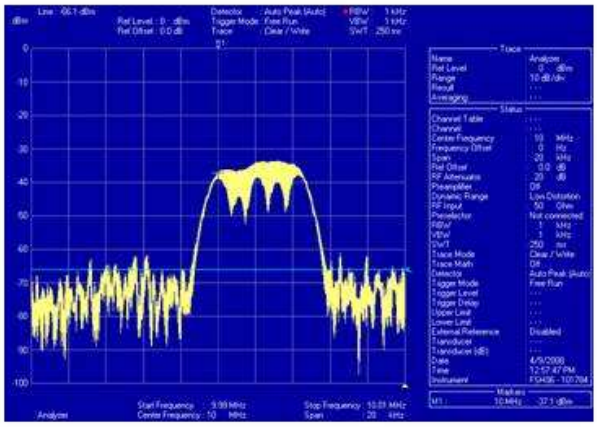

(b) Spectrum of received signal

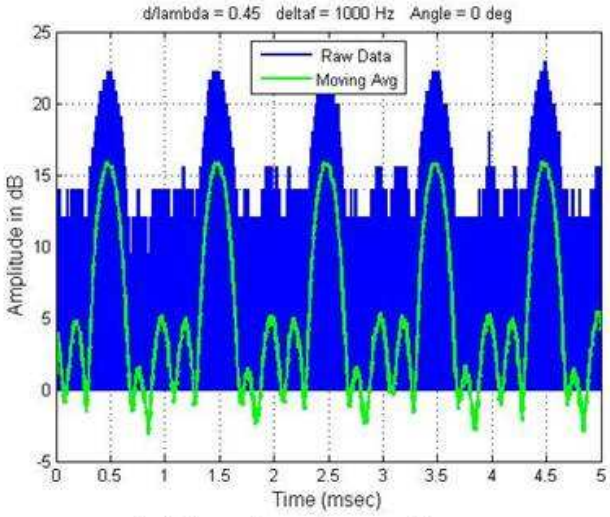

(c) Received waveform

Fig. 6-17: Frequency diverse array signal, $N = 5$ and $\Delta f = 1$ kHz.

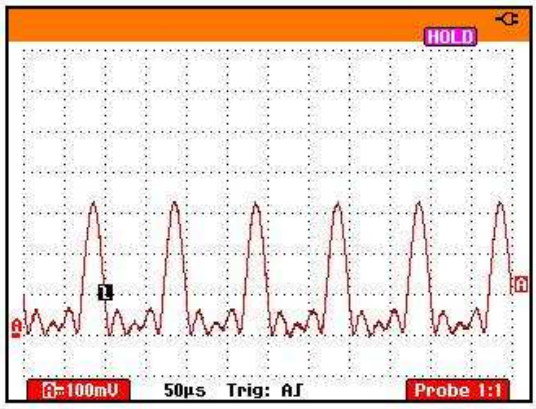

(a) Close-range probe measurement

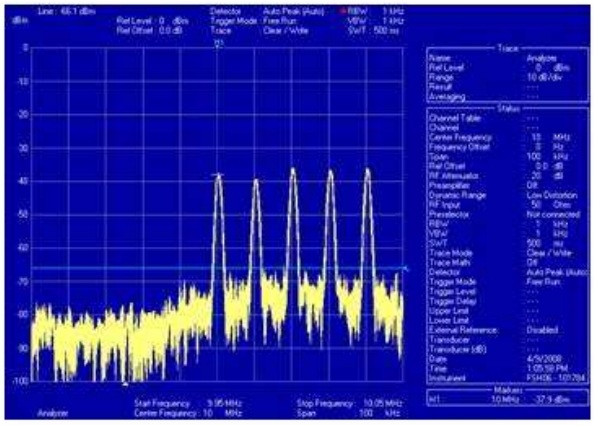

(b) Spectrum of received signal

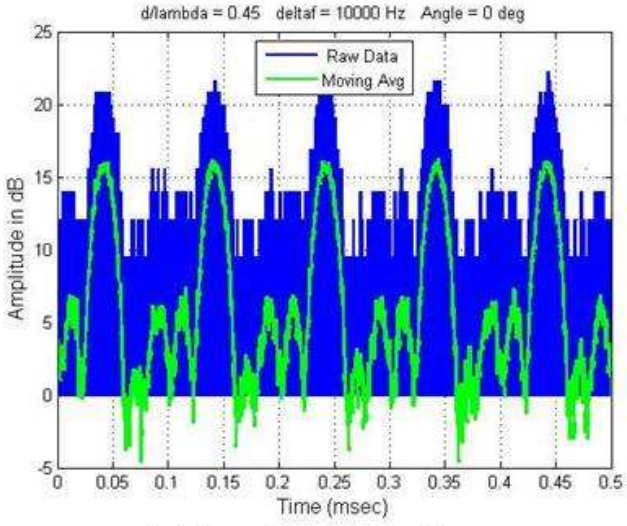

(c) Received waveform

Fig. 6-18: Frequency diverse array signal, N = 5 and Δf = 10 kHz.

6.3.2 Angle Dependence of the Pattern

Experiments were also performed to demonstrate the auto-scanning property of the frequency diverse array. Continuous wave signals of different frequencies, separated by Δf, were radiated by different spatial channels spaced a distance of d/λ. The transmitted signals were recorded simultaneously at two receivers placed at known angular separations. The delays between the simultaneously recorded signals were then measured in relation to the frequency shift, Δf, and compared to the expected time delay given by Equation (4-79) in Section 4.3.

The spatial arrangement of the transmitter and receivers is illustrated in Fig. 6-19, with nominal locations of the tripod-mounted receiver indicated. A view of the test area from the transmitter is provided in Fig. 6-20. The horn antenna for one receive channel was located directly on the receive tower, and the transmit array boresight was aligned in the direction of this antenna. The horn antenna for the second receive channel was mounted on a tripod, and placed at different locations on the roof structure adjacent to the transmit and receive towers so that the electric field could be measured at various geographical points. Cable lengths for the two channels were made to be approximately equal. Receiver placements are shown in Figures 6-21 through 6-23 to depict the environment in the vicinity of the installation, and the rack-mounted receiver equipment is shown in Fig. 6-24.

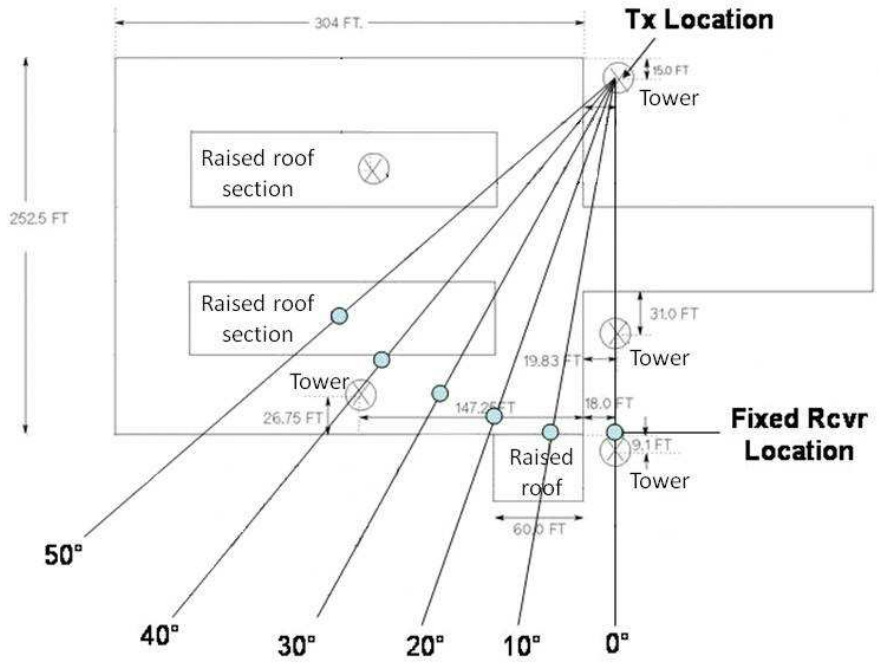

Fig. 6-19: Spatial arrangement of transmitter and receivers

Fig. 6-20: View of test area from transmitter

Fig. 6-21: Fixed receive horn #1 with co-located tripod mounted receive horn

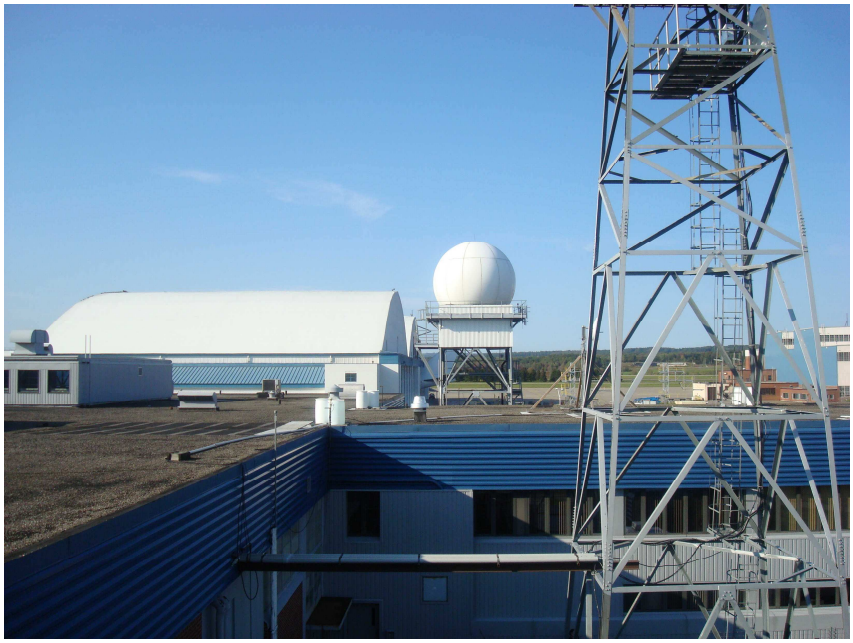

Fig. 6-22: View from fixed receive horn to transmitter

Fig. 6-23: Receive horn #2 on movable tripod

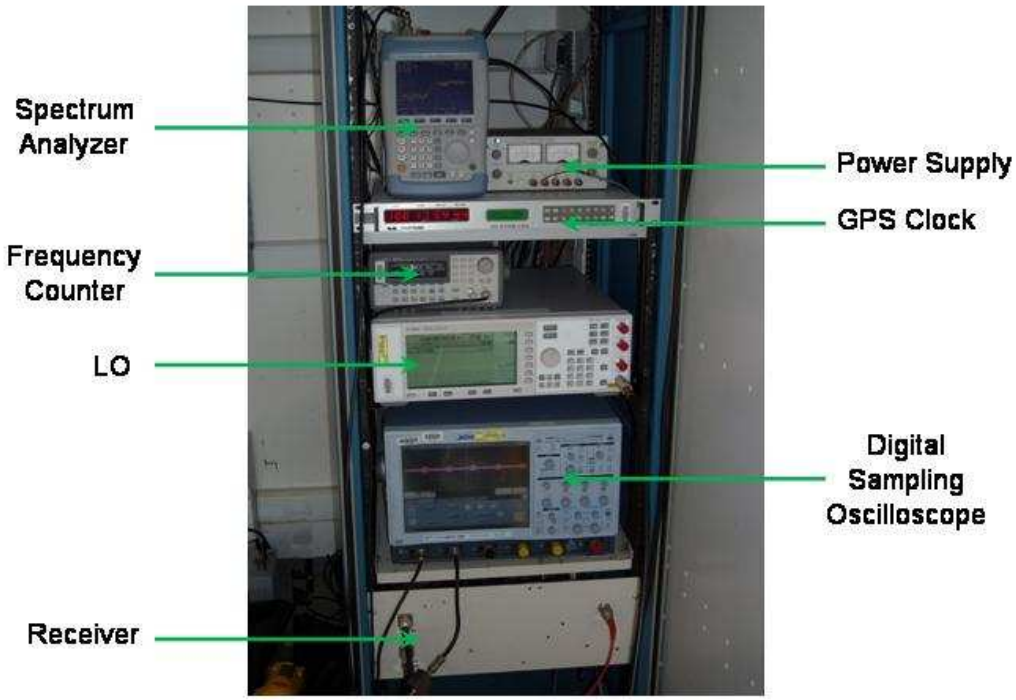

Fig. 6-24: Receiver equipment installed in rack

Delay was measured as a function of angle for Δf = 100 Hz for angles between 0° and 35°. Two spatial channels of the full array were excited so that the behaviour of the frequency diverse array could be investigated for a variety of element spacings. With 5 channels and a nominal element spacing of 0.45λ, this allowed for the study of beam behaviour with d/λ = 0.45, 0.90, 1.35, and 1.80. Once the various combinations of angles and element spacings were investigated for Δf = 100 Hz, the frequency offset was changed to 200 Hz and 300 Hz, and beam behaviour was examined in these cases for large angular separations.

6.3.2.1 Case 1: Δf = 100 Hz, d/λ = 0.45

To explore the scan of the frequency diverse array beam with time, a baseline case was first considered with Δf = 100 Hz and d/λ = 0.45. An element spacing of d/λ = 0.45 represents the nominal design of the array, and is therefore provided by using adjacent channels of the array. Angular separations of 0° to 35° were investigated. At 0° the two receive antennas were essentially co-located on the receive tower, and no delay was expected between the two receive channels. Measurements for the two channels are displayed simultaneously, and a moving average for each channel is also displayed in order to reduce the effect of noisy and high frequency data.

Output data is presented in Figures 6-25 through 6-29 for angular separations of 0°, 10°, 20°, 30°, and 35° respectively. Delay can be observed to increase progressively with angle.

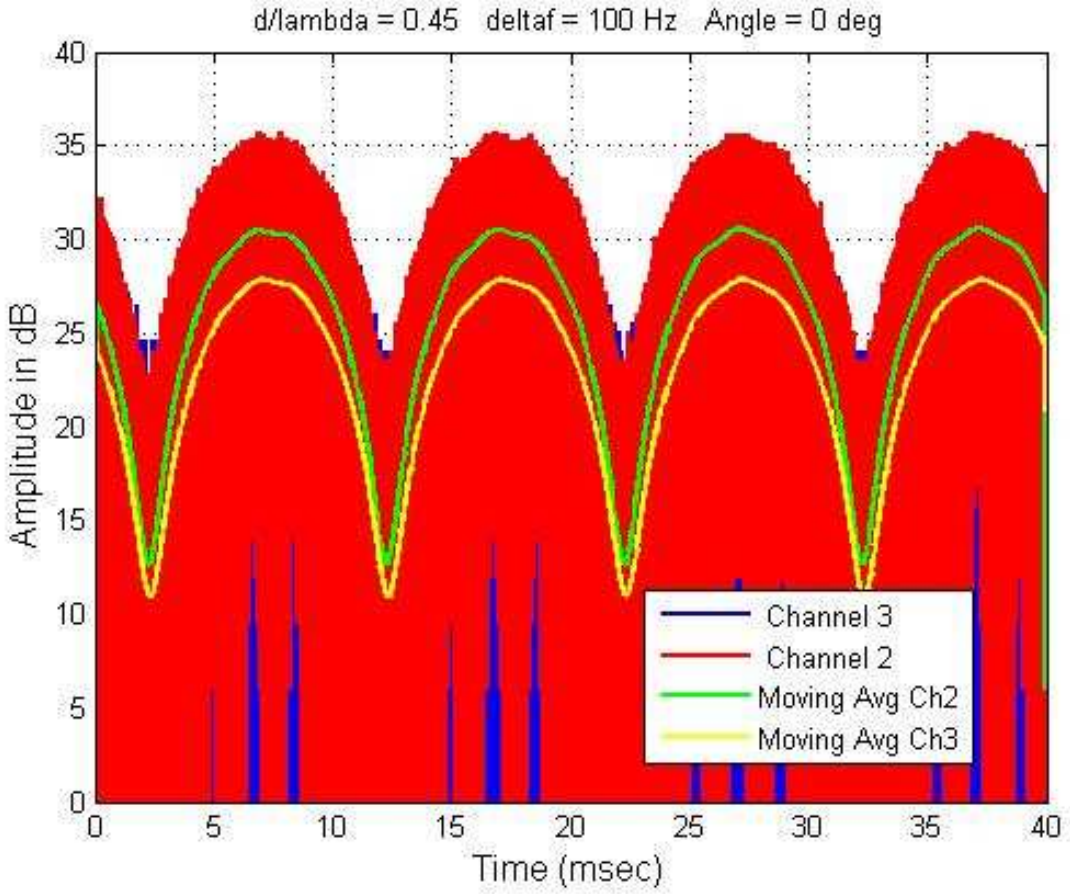

Fig. 6-25: Two-channel measurement for $d/\lambda = 0.45$, $\Delta f = 100$ Hz, $\theta = 0^{o}$. Time delay is -0.1 msec.

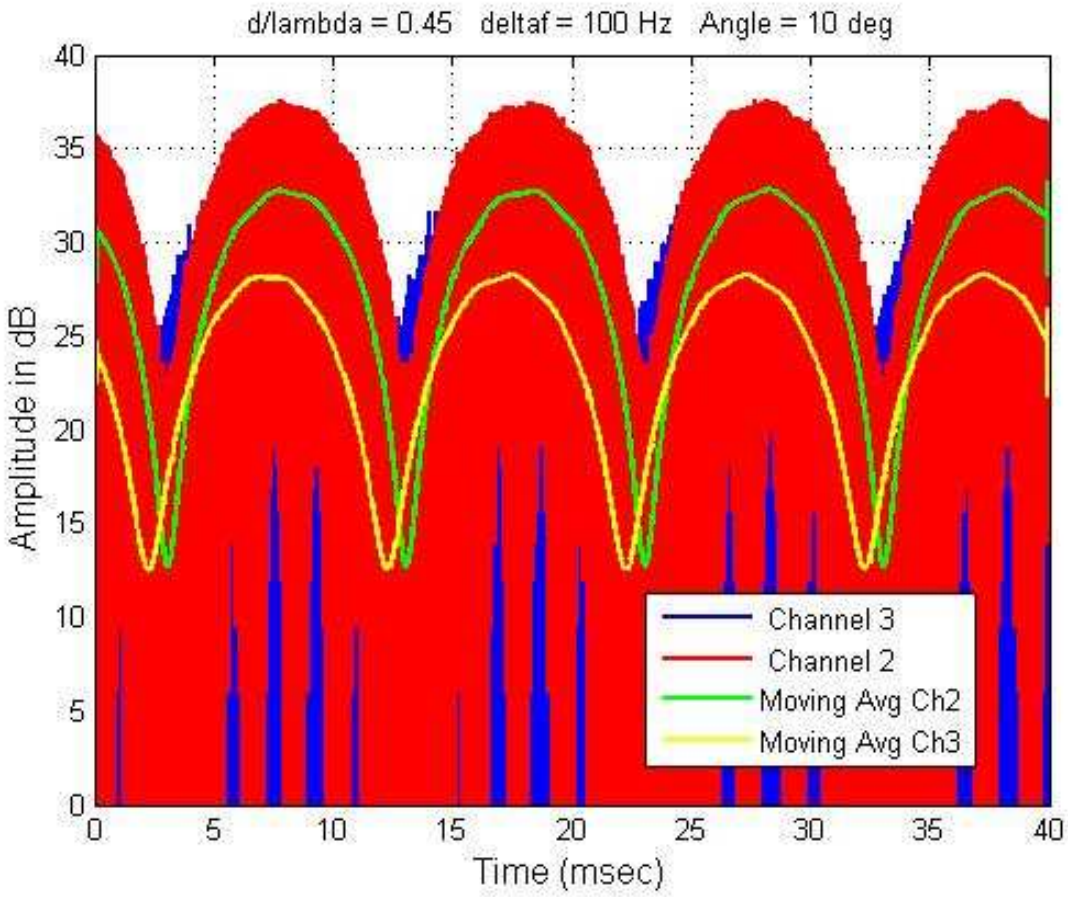

Fig. 6-26: Two-channel measurement for $d/\lambda = 0.45$, $\Delta f = 100$ Hz, $\theta = 10^{o}$. Time delay is 0.8 msec.

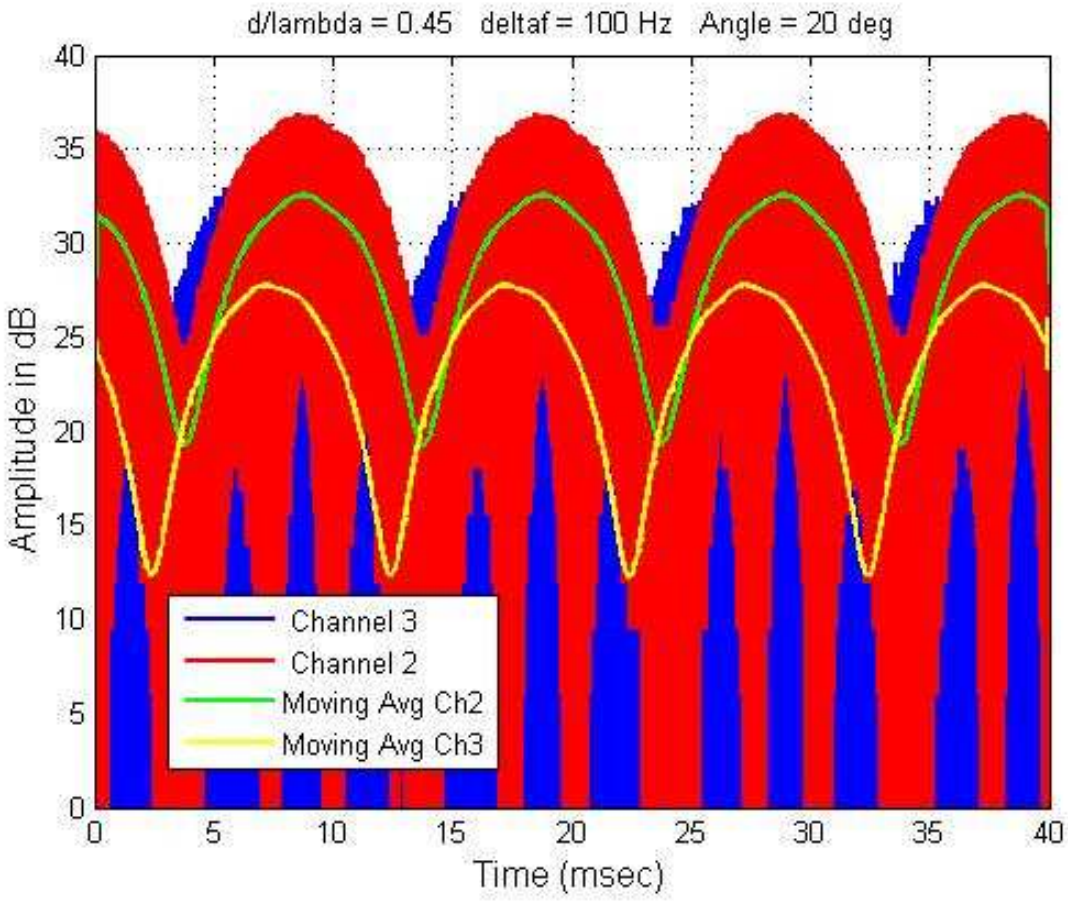

Fig. 6-27: Two-channel measurement for $d/\lambda = 0.45$, $\Delta f = 100$ Hz, $\theta = 20^{o}$. Time delay is 1.4 msec.

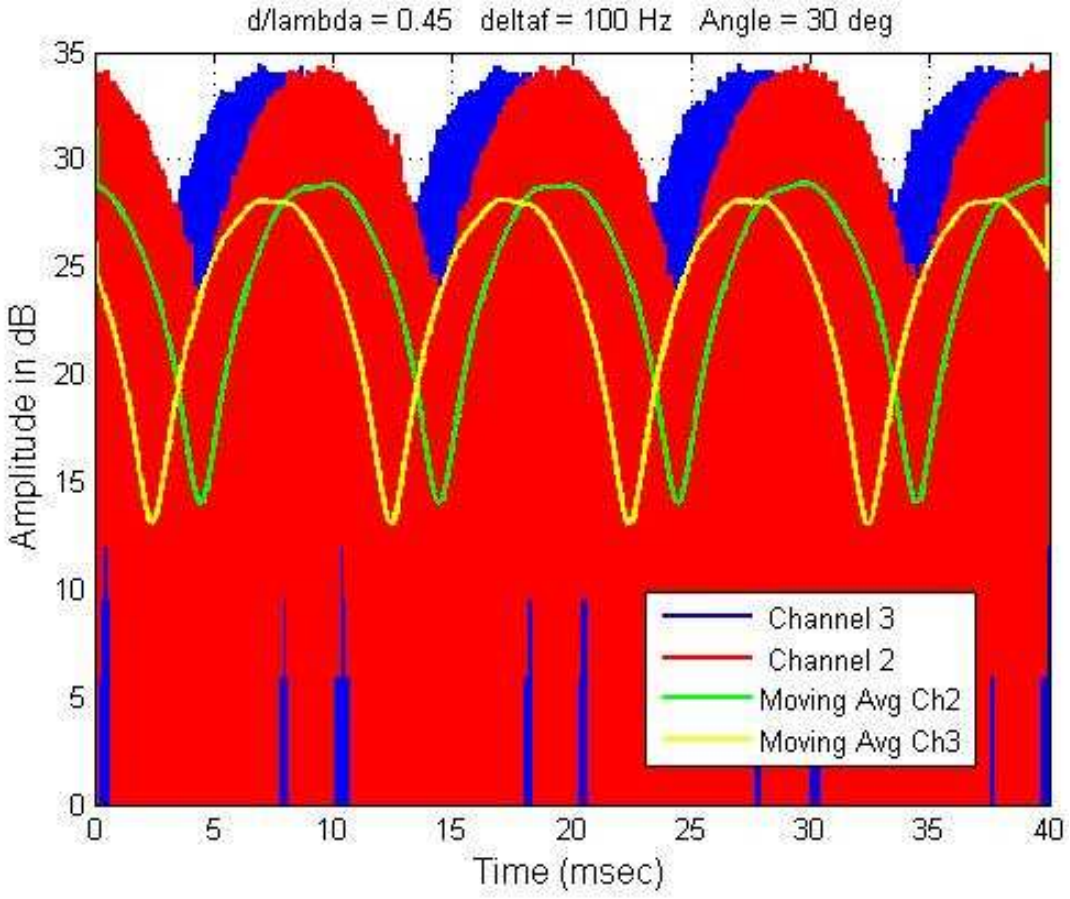

Fig. 6-28: Two-channel measurement for $d/\lambda = 0.45$, $\Delta f = 100$ Hz, $\theta = 30^{o}$. Time delay is 2.0 msec.

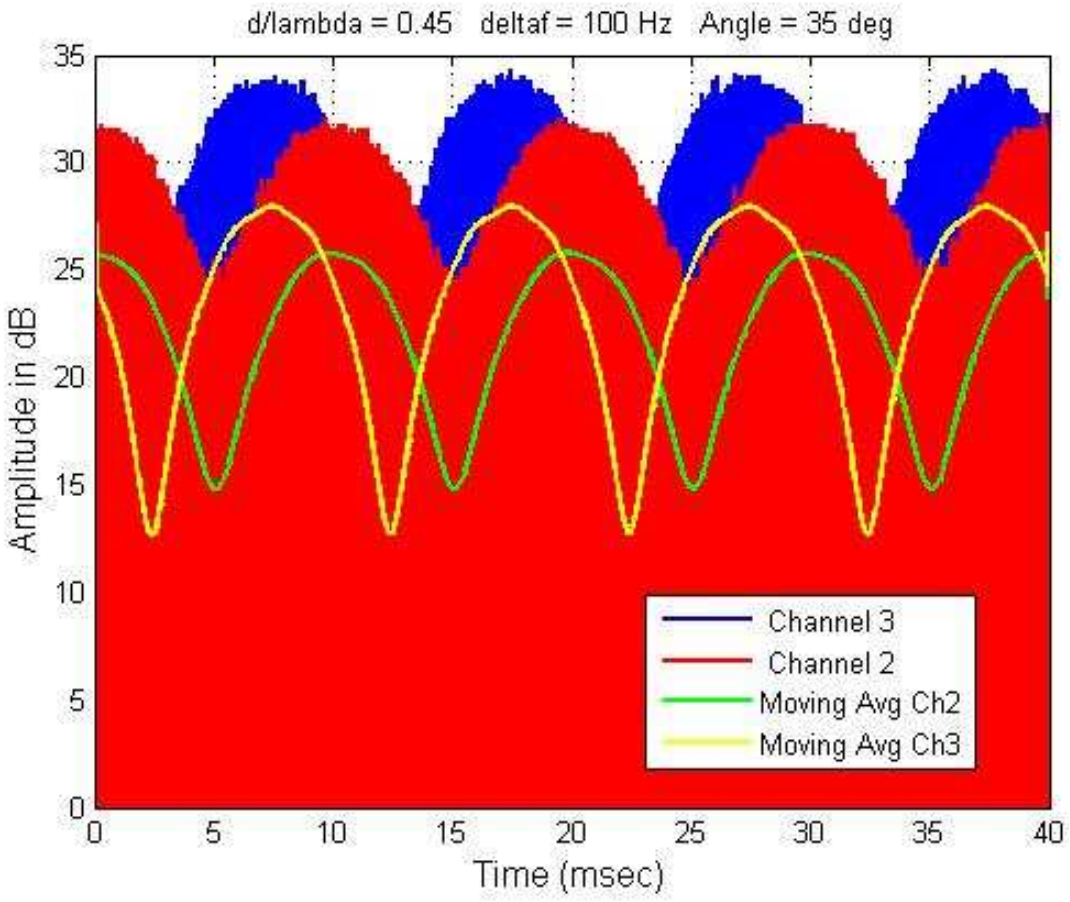

Fig. 6-29: Two-channel measurement for $d/\lambda = 0.45$, $\Delta f = 100$ Hz, $\theta = 35^{o}$. Time delay is 2.7 msec.

A summary of the measurement results of delay as a function of angle for $d/\lambda = 0.45$ and $\Delta f = 100$ Hz is shown in Table 6-1. The agreements between the expected and measured delays are generally quite good. Some variation between the theoretical and measured values is expected, primarily due to variations in equipment between spatial channels on both transmit and receive, placement of antennas, the averaging of noisy data, and the non-ideal multipath environment of the test range configuration.

Table 6-1: Summary of measurements for $d/\lambda = 0.45$, $\Delta f = 100$ Hz

Angle (deg)	**Predicted Delay (msec)**	**Measured Delay (msec)**
0	0.0	-0.1
10	0.8	0.8
20	1.5	1.4
30	2.3	2.0
35	2.6	2.7

6.3.2.2 Case 2: Δf = 100 Hz, d/λ = 0.90

For this case, frequency diverse array spatial channels 1 and 3 were excited to provide an element spacing of $d/\lambda = 0.90$. The received signals and their moving averages are plotted in Figures 6-30 through 6-36 for angular separations ranging from 0° to 58°.

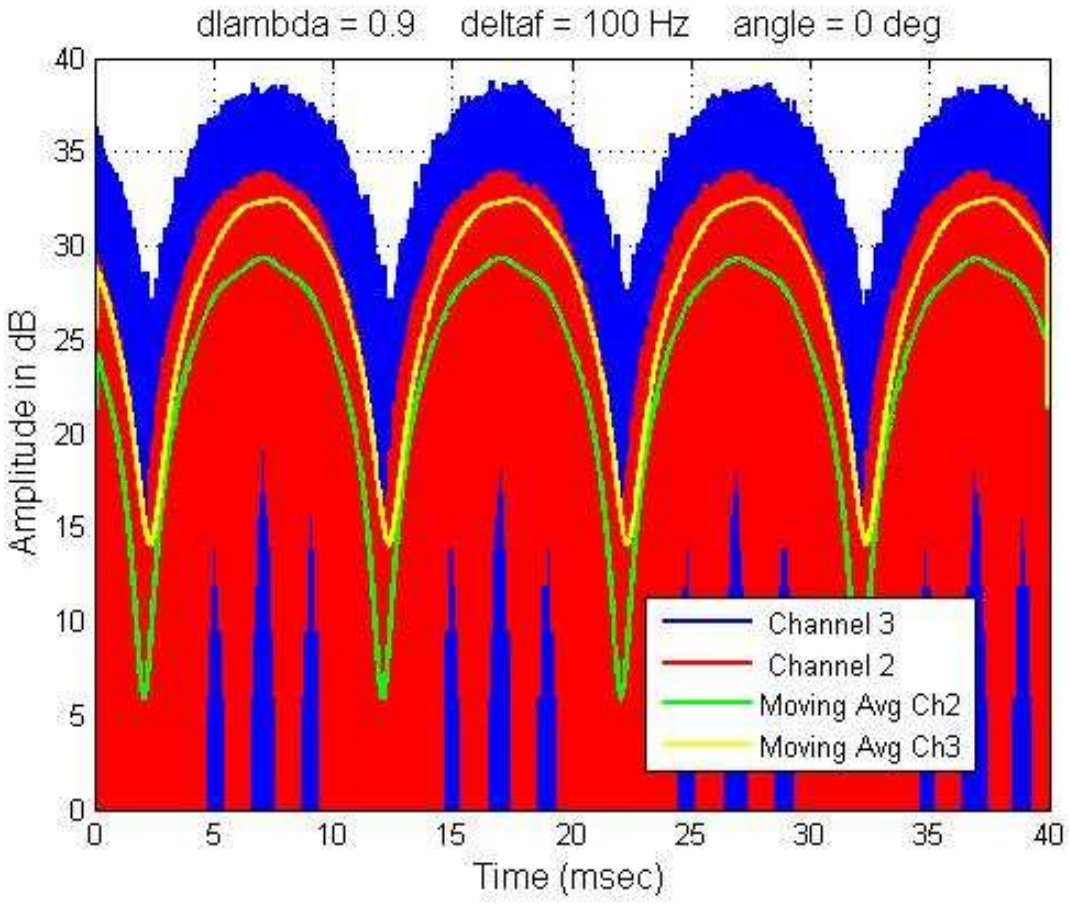

Fig. 6-30: Two-channel measurement for $d/\lambda = 0.90$, $\Delta f = 100$ Hz, $\theta = 0^{o}$. Time delay is 0.3 msec.

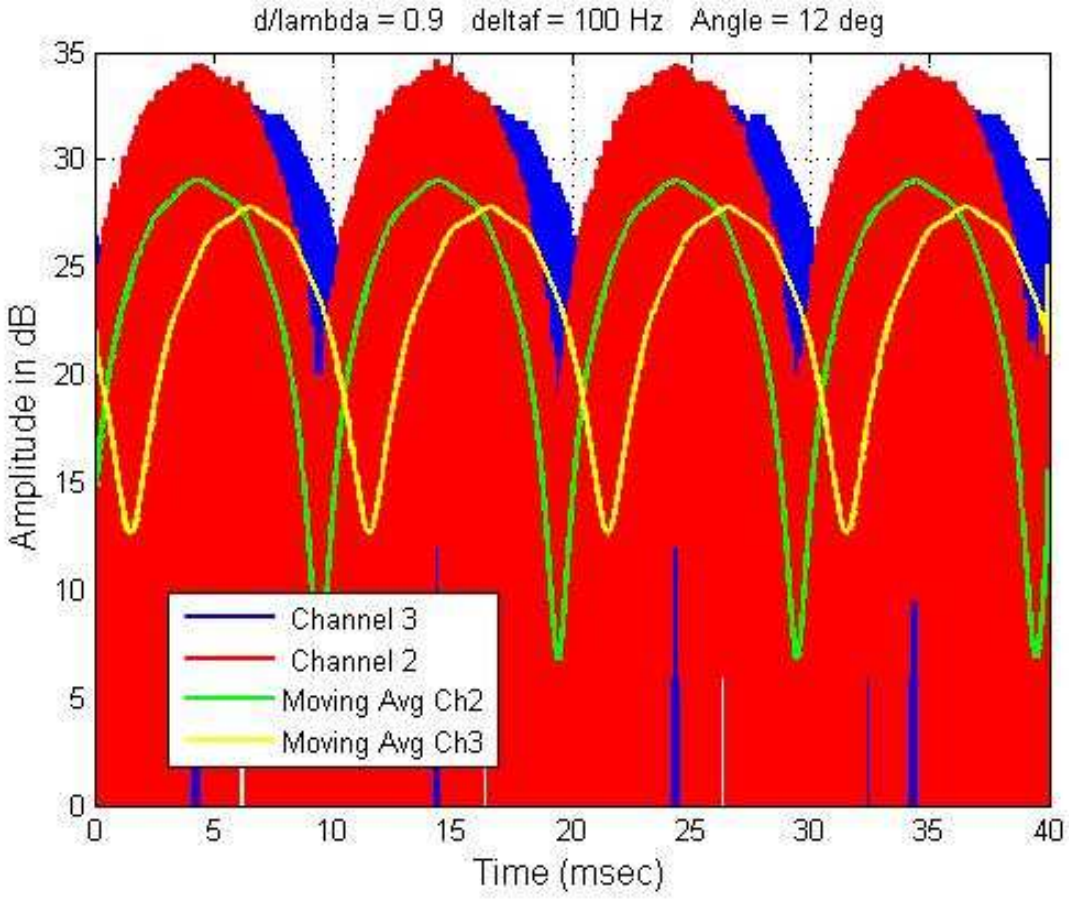

Fig. 6-31: Two-channel measurement for $d/\lambda = 0.90$, $\Delta f = 100$ Hz, $\theta = 12^{o}$. Time delay is 2.1 msec.

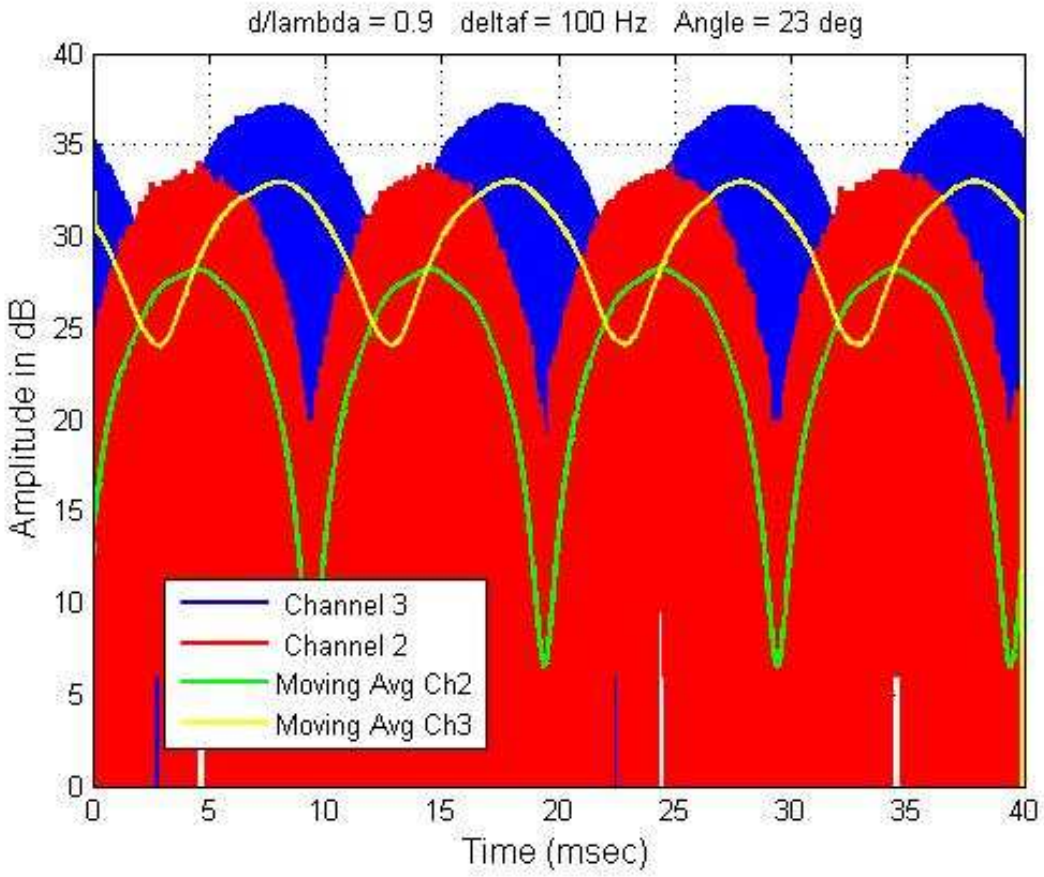

Fig. 6-32: Two-channel measurement for $d/\lambda = 0.90$, $\Delta f = 100$ Hz, $\theta = 23^{\circ}$. Time delay is 3.4 msec.

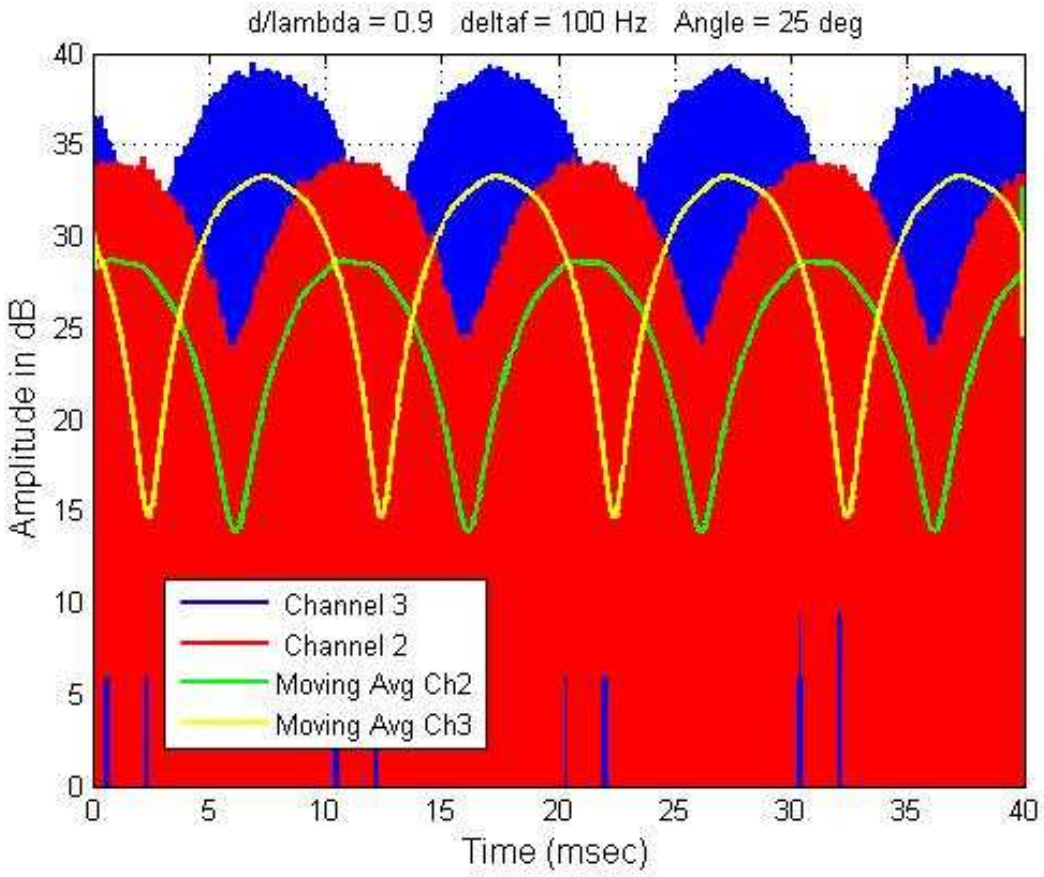

Fig. 6-33: Two-channel measurement for $d/\lambda = 0.90$, $\Delta f = 100$ Hz, $\theta = 25^{\circ}$. Time delay is 3.7 msec.

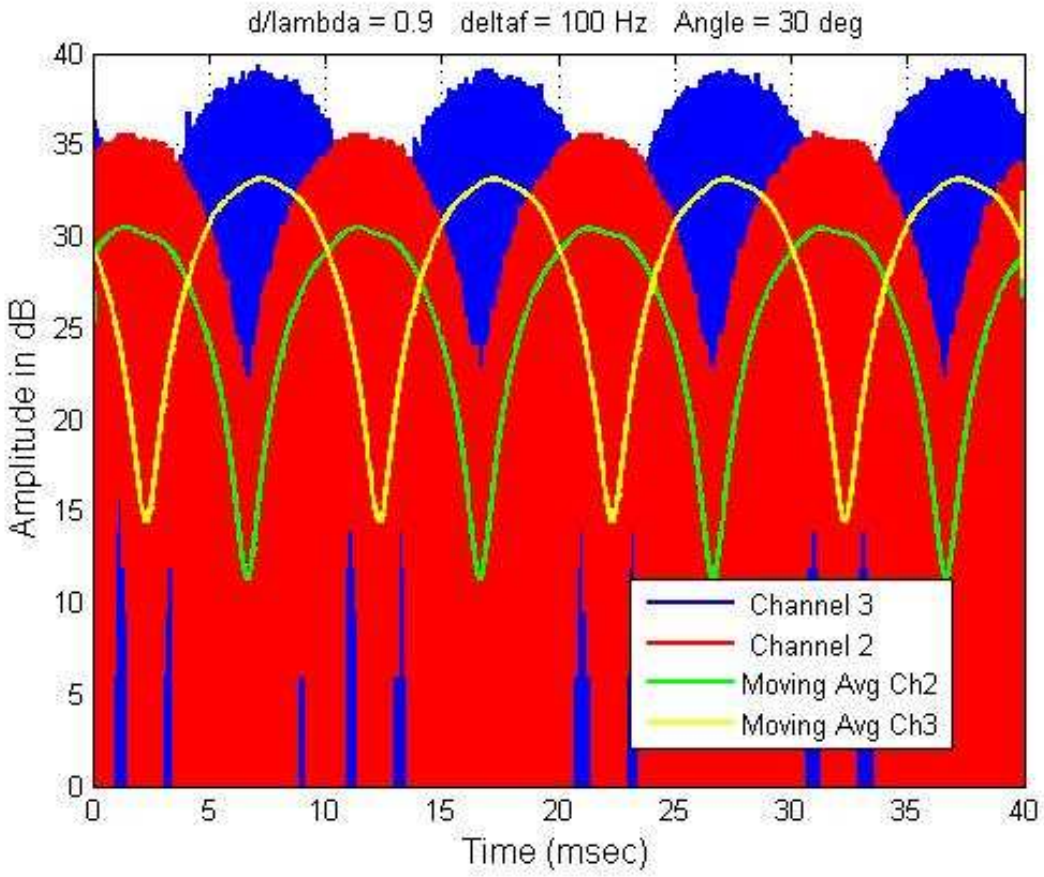

Fig. 6-34: Two-channel measurement for $d/\lambda = 0.90$, $\Delta f = 100$ Hz, $\theta = 30^{\circ}$. Time delay is 4.4 msec.

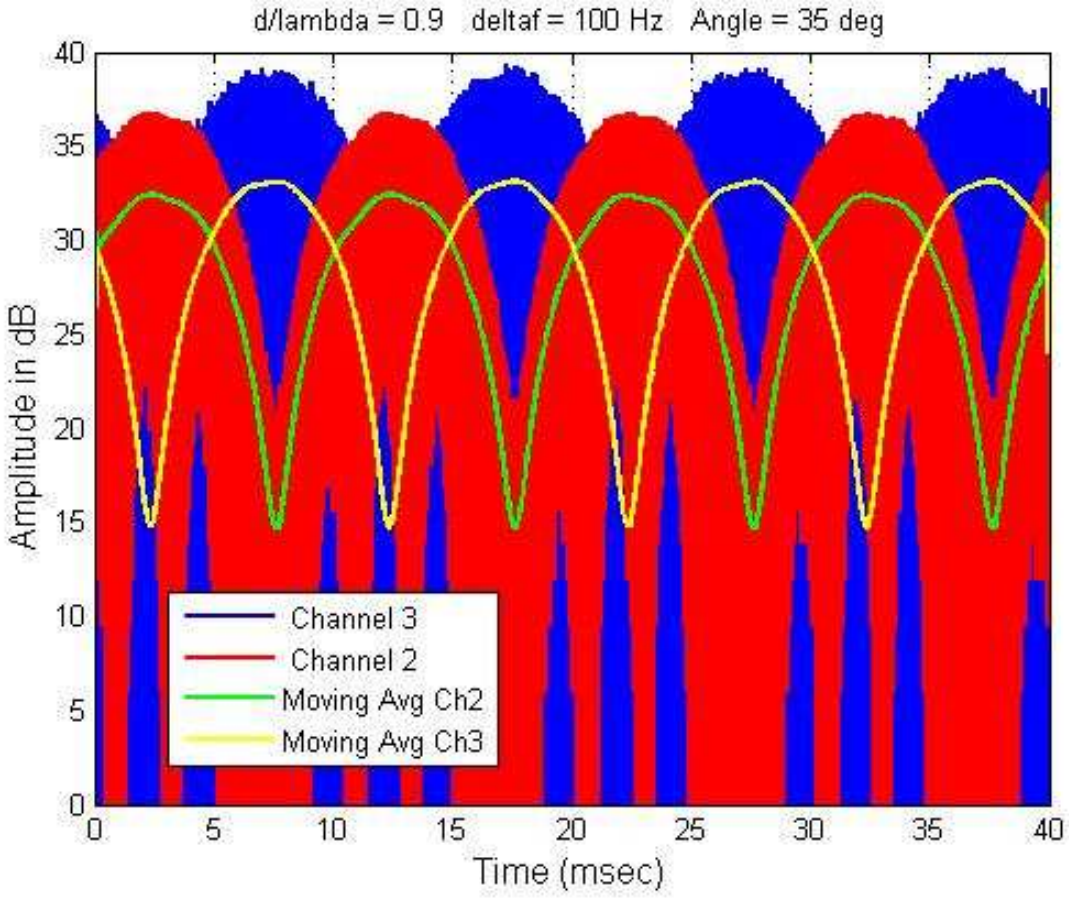

Fig. 6-35: Two-channel measurement for $d/\lambda = 0.45$, $\Delta f = 100$ Hz, $\theta = 35^{o}$. Time delay is 5.3 msec.

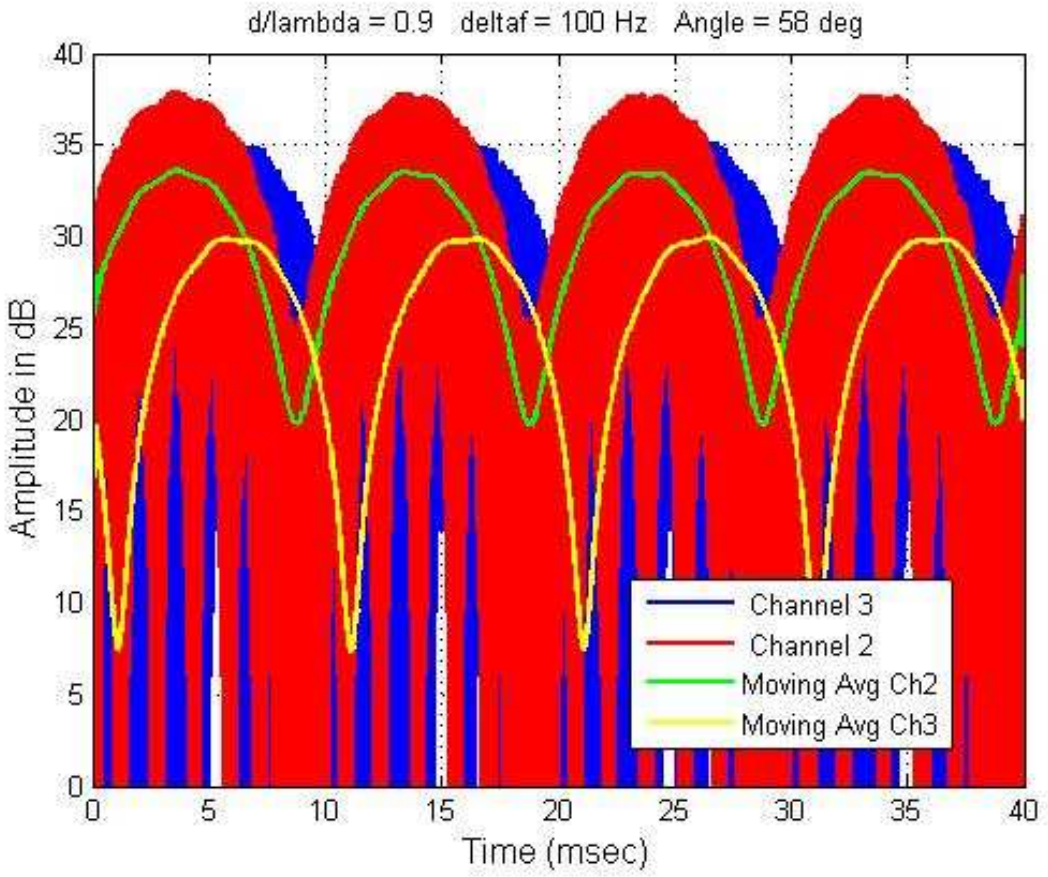

Fig. 6-36: Two-channel measurement for $d/\lambda = 0.90$, $\Delta f = 100$ Hz, $\theta = 58^{o}$. Time delay is 7.7 msec.

A summary of the measurement results of delay as a function of angle for $d/\lambda = 0.90$ and $\Delta f = 100$ Hz is shown in Table 6-2. The results show a good agreement between the predicted and measured delays.

Table 6-2: Summary of measurements for $d/\lambda = 0.90$, $\Delta f = 100$ Hz

Angle (deg)	**Predicted Delay (msec)**	**Measured Delay (msec)**
0	0.0	0.3
12	1.9	2.1
23	3.5	3.4
25	3.8	3.7
30	4.5	4.3
35	5.2	5.3
58	7.6	7.7

6.3.2.3 Case 3: Δf = 100 Hz, d/λ = 1.35

Spatial channels 1 and 4 of the frequency diverse array were excited to provide an element spacing of d/λ = 1.35. The received signals and their moving averages are plotted in Figures 6-37 through 6-41 for angular separations ranging from 0° to 58°.

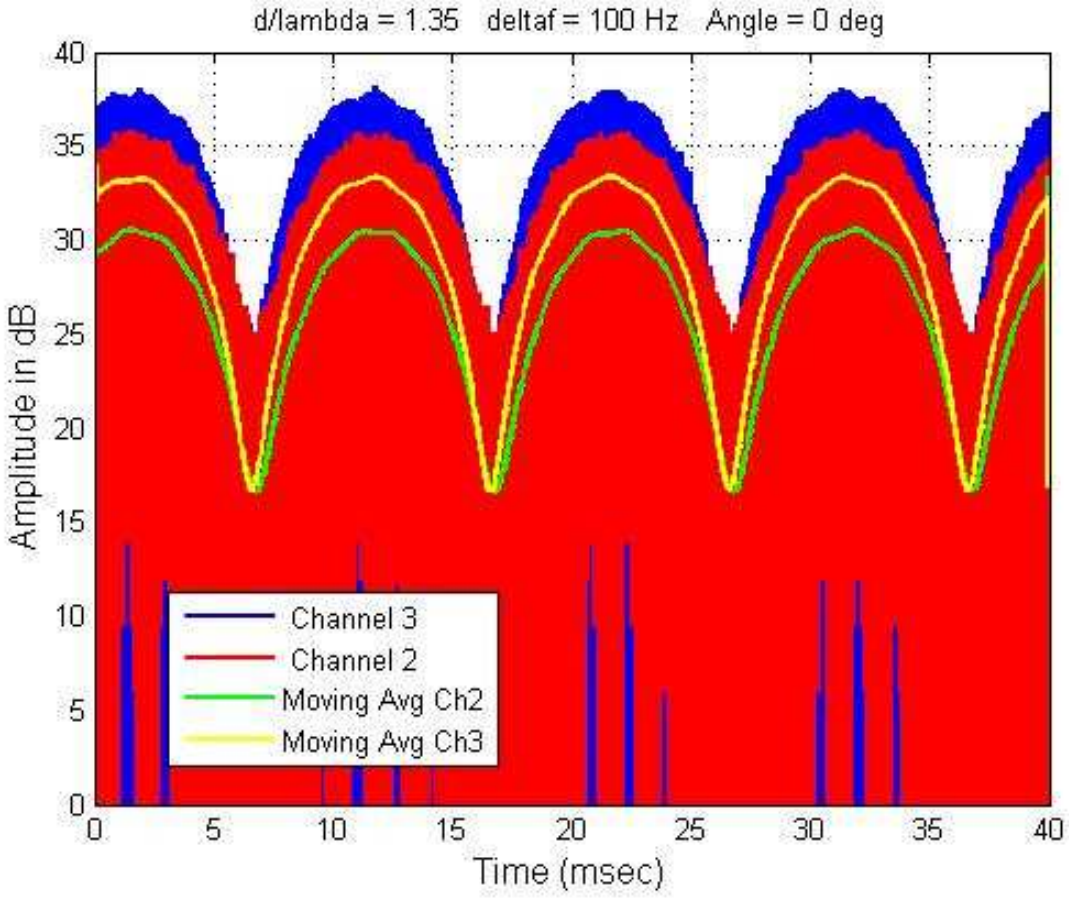

Fig. 6-37: Two-channel measurement for d/λ = 1.35, Δf = 100 Hz, θ = 0º. Time delay is -0.2 msec.

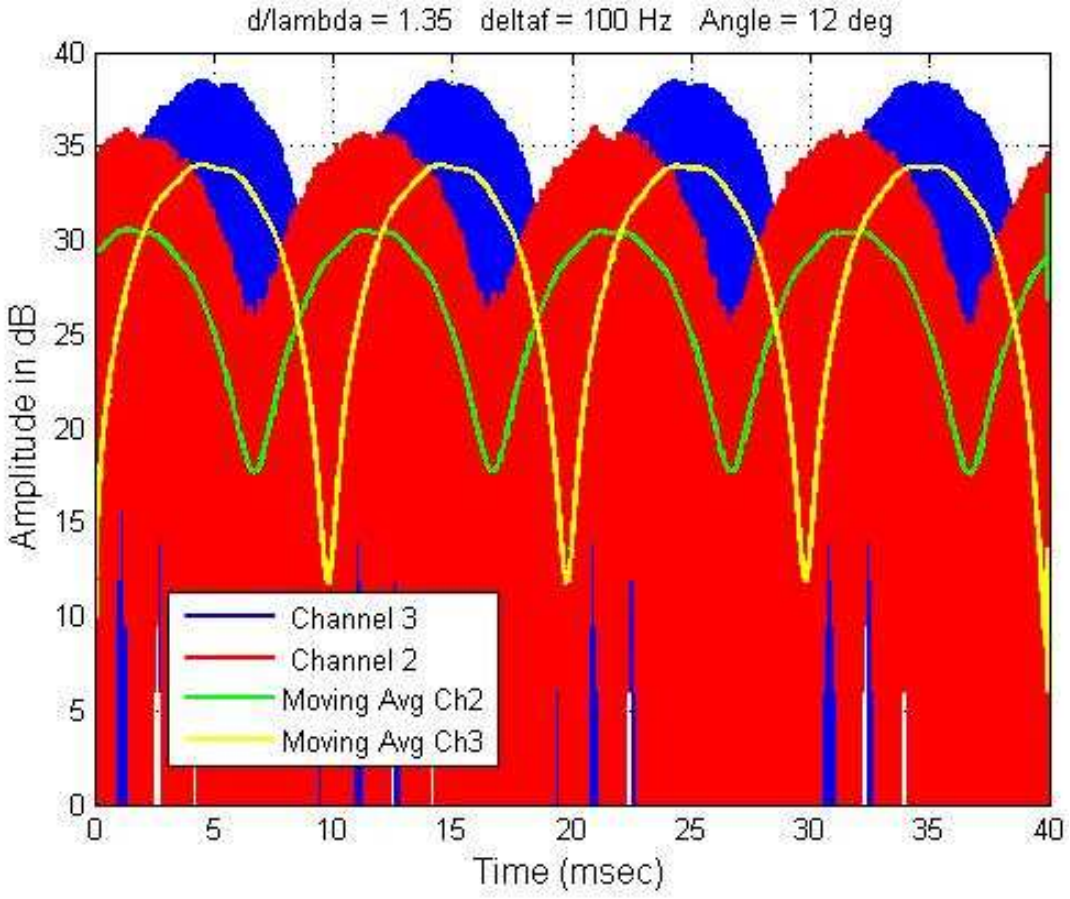

Fig. 6-38: Two-channel measurement for $d/\lambda = 1.35$, $\Delta f = 100$ Hz, $\theta = 12^{o}$. Time delay is 3.1 msec.

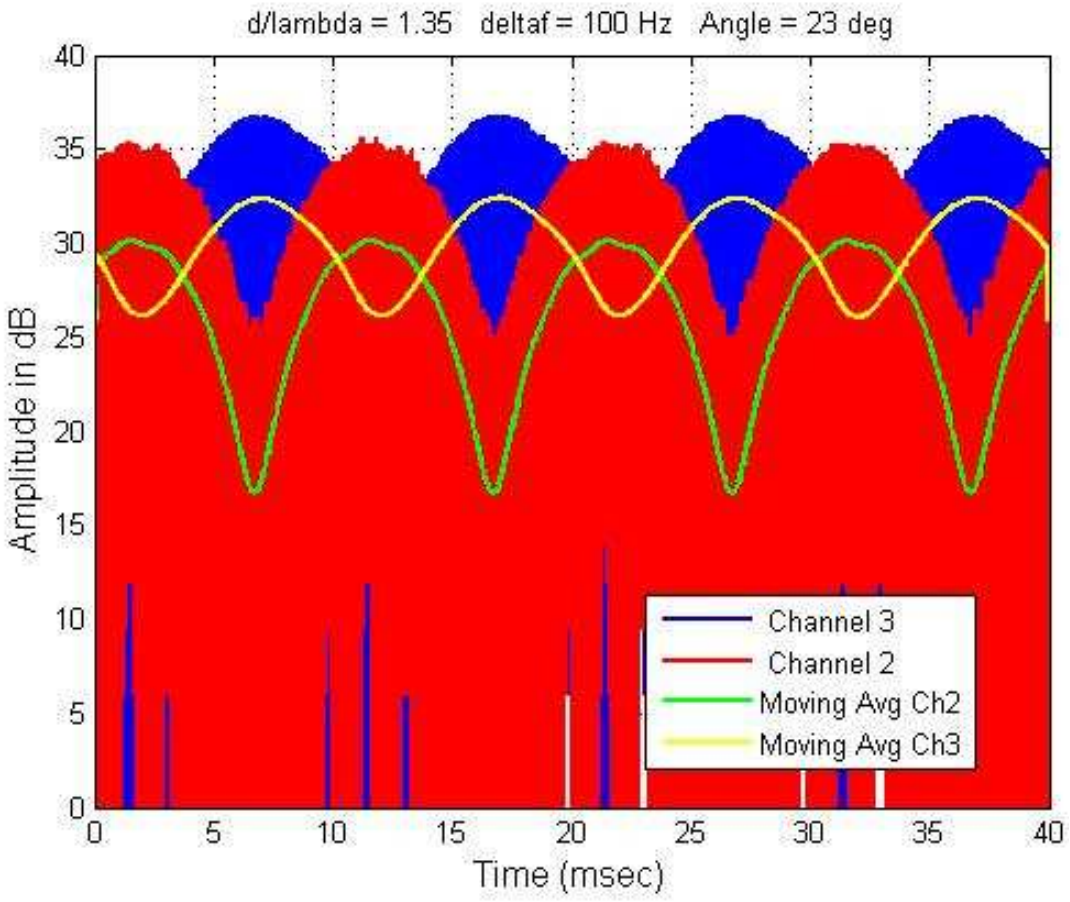

Fig. 6-39: Two-channel measurement for $d/\lambda = 1.35$, $\Delta f = 100$ Hz, $\theta = 23^{\circ}$. Time delay is 5.3 msec.

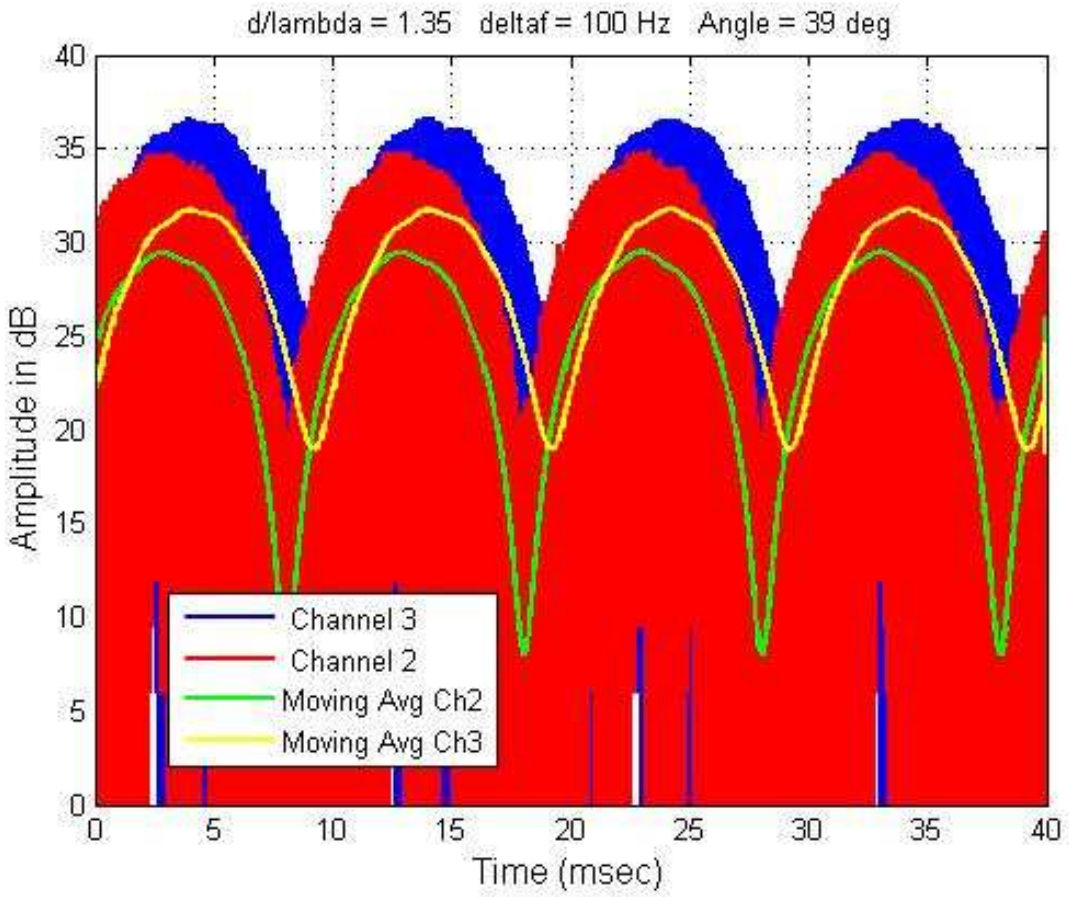

Fig. 6-40: Two-channel measurement for $d/\lambda = 1.35$, $\Delta f = 100$ Hz, $\theta = 39^{\circ}$. Time delay is 8.8 msec.

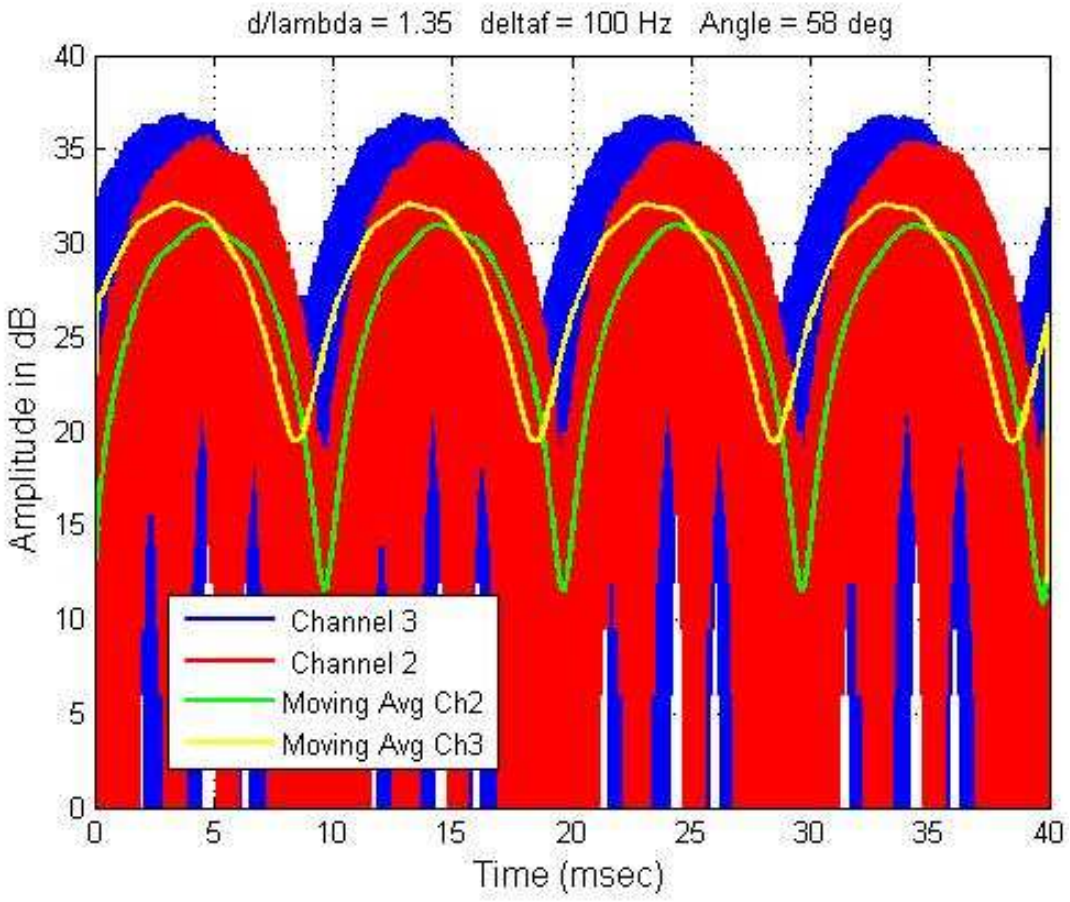

Fig. 6-41: Two-channel measurement for $d/\lambda = 1.35$, $\Delta f = 100$ Hz, $\theta = 58^{\circ}$. Time delay is 11.2 msec.

A summary of the measurement results of delay as a function of angle for $d/\lambda = 1.35$ and $\Delta f = 100$ Hz is shown in Table 6-3. Once again the agreements between the expected and measured delays are generally quite good.

Table 6-3: Summary of measurements for $d/\lambda = 1.35$, $\Delta f = 100$ Hz

Angle (deg)	Predicted Delay (msec)	Measured Delay (msec)
0	0.0	-0.2
12	2.8	3.1
23	5.3	5.3
39	8.5	8.8
58	11.4	11.2

6.3.2.4 Case 4: $\Delta f = 200$ Hz, $d/\lambda = 0.45$

The previous three sections examined scanning of the frequency diverse array with time for different element spacings and $\Delta f = 100$ Hz. This section and the next return to the nominal element spacing of $d/\lambda = 0.45$ and explore the effect of different frequency offsets on beam scan.

From Equation (4-79), the time to scan through real space is inversely proportional to the frequency offset. In this section, frequency offset is increased to $\Delta f = 200$ Hz, double the offset of the previous cases. Therefore, the time to scan through a given angle will be half that for the case of $\Delta f = 100$ Hz. Large angular separations between receive antennas are therefore considered in order to emphasize the delay between receive channels. The case of 39° angular separation is presented in Fig. 6-42, and the case of 58° separation is considered in Fig. 6-43.

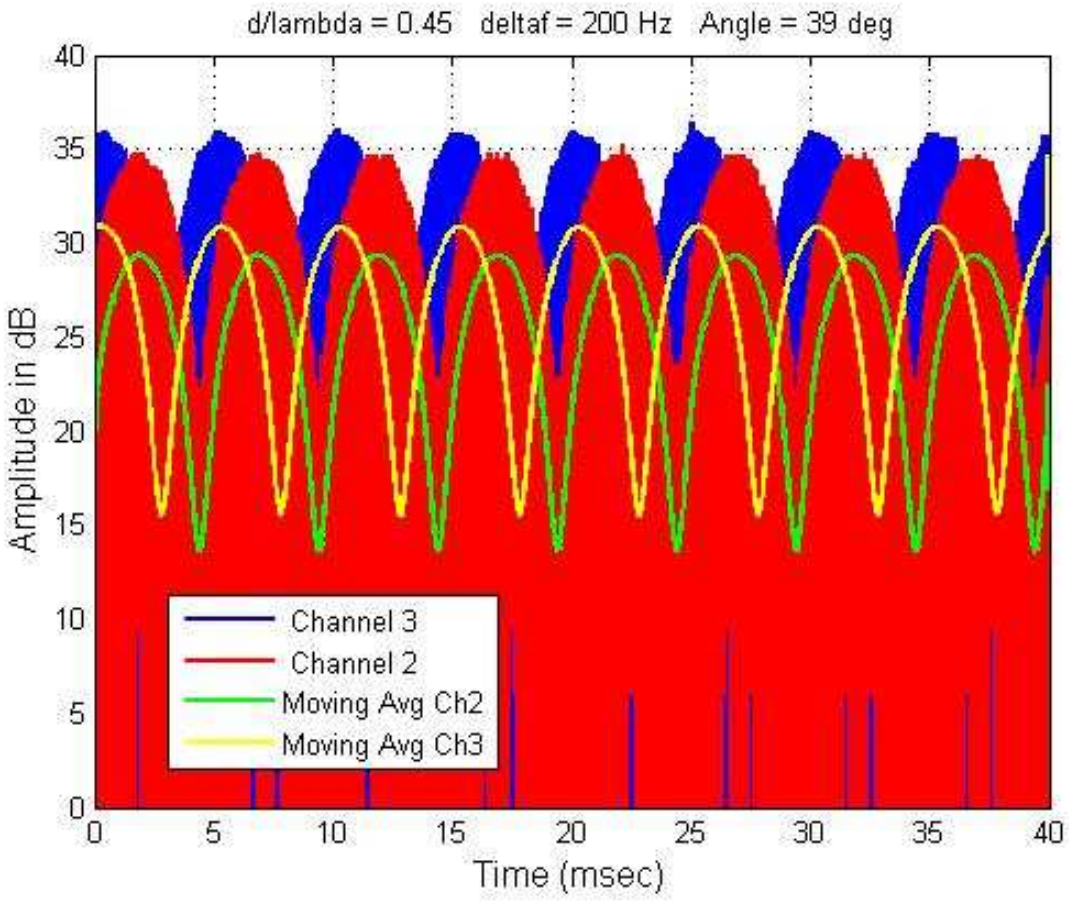

Fig. 6-42: Two-channel measurement for $d/\lambda = 0.45$, $\Delta f = 200$ Hz, $\theta = 39^{\circ}$. Time delay is 1.6 msec.

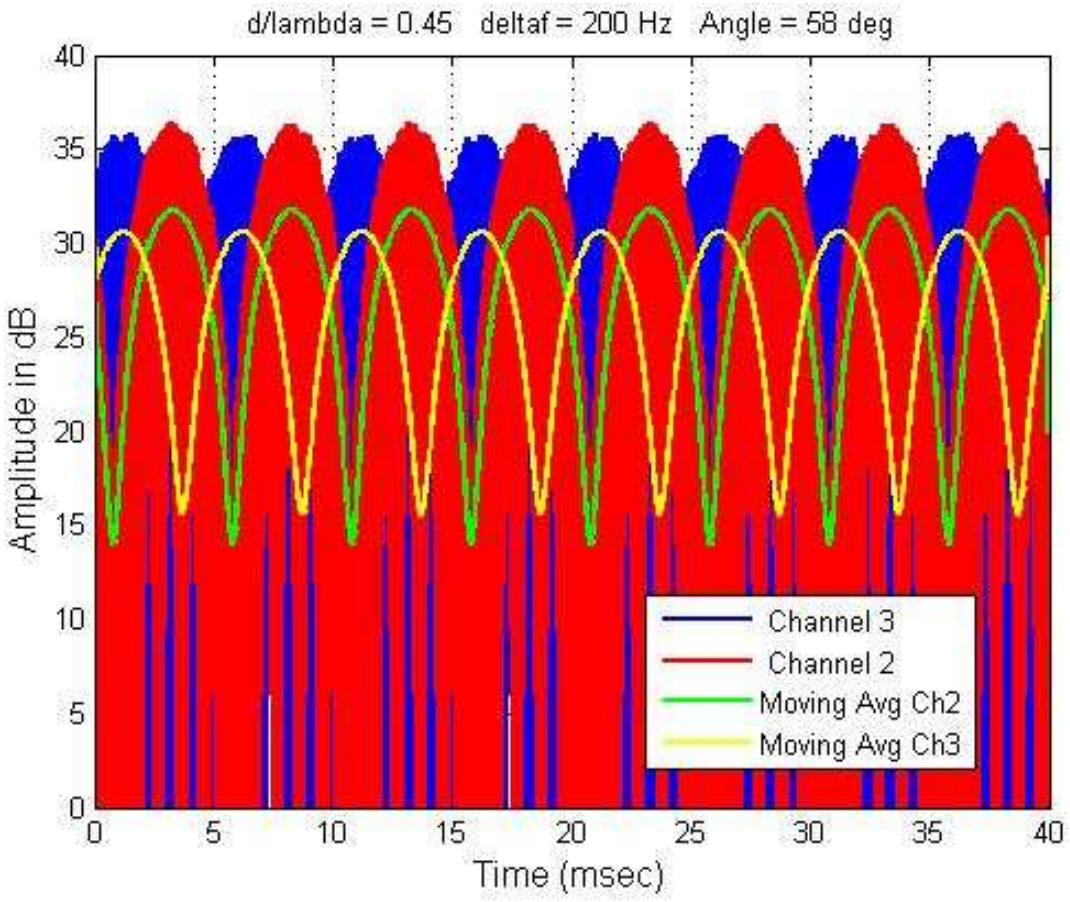

Fig. 6-43 : Two-channel measurement for $d/\lambda = 0.45$, $\Delta f = 200$ Hz, $\theta = 58^{o}$. Time delay is 2.1 msec.

A summary of the measurements for $d/\lambda = 0.45$ and $\Delta f = 200$ Hz is provided in Table 6-4. The agreement between the measured and predicted results is quite good.

Table 6-4: Summary of measurements for $d/\lambda = 0.45$, $\Delta f = 200$ Hz

Angle (deg)	**Predicted Delay (msec)**	**Measured Delay (msec)**
39	1.4	1.6
58	1.9	2.1

6.3.2.5 Case 5: Δf = 300 Hz, d/λ = 0.45

In this case, frequency offset is further increased to Δf = 300 Hz, so that the time to scan through a given angle will be one-third that for the case of Δf = 100 Hz. As in the previous section, large angular separations are utilised between receive antennas in order to emphasize the delay between receive channels. The same angular separations as in the previous section are considered, θ = 39º and θ = 58º, with the results presented in Figures 6-44 and 6-45 respectively.

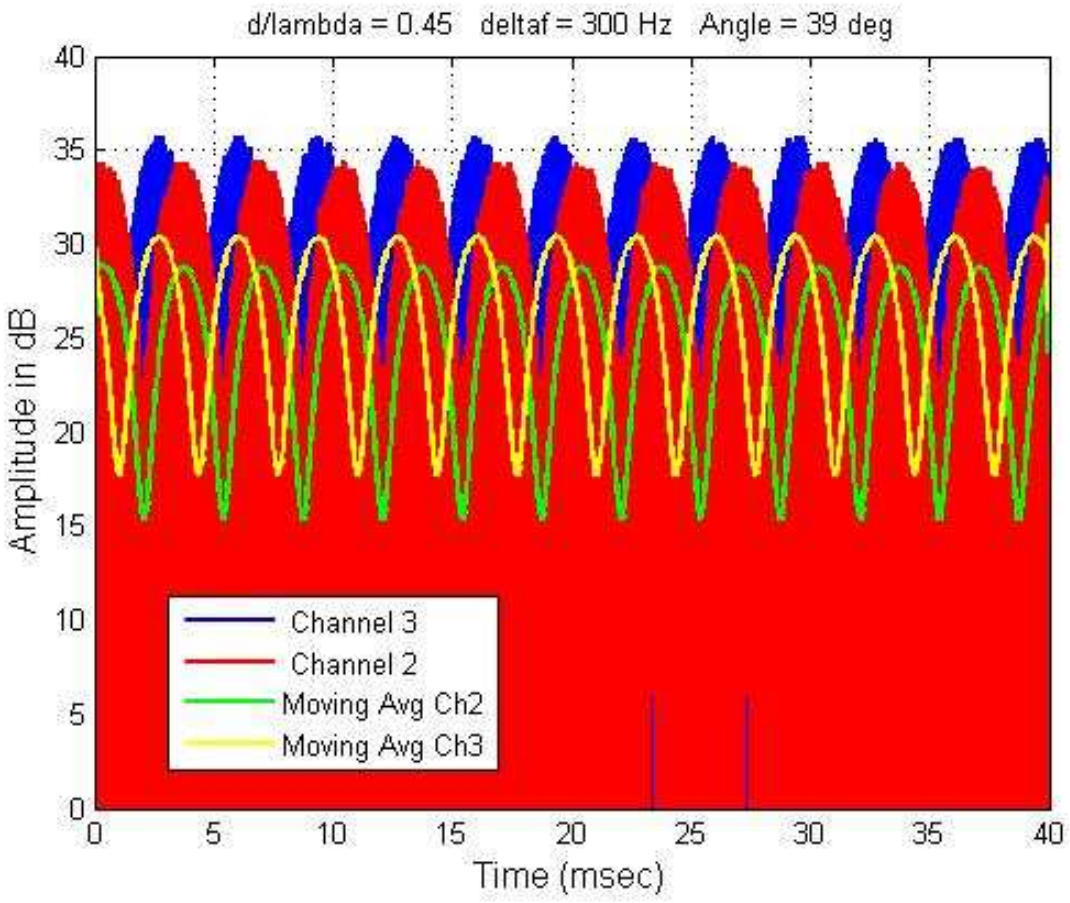

Fig. 6-44: Two-channel measurement for d/λ = 0.45, Δf = 300 Hz, θ = 39º. Time delay is 1.0 msec.

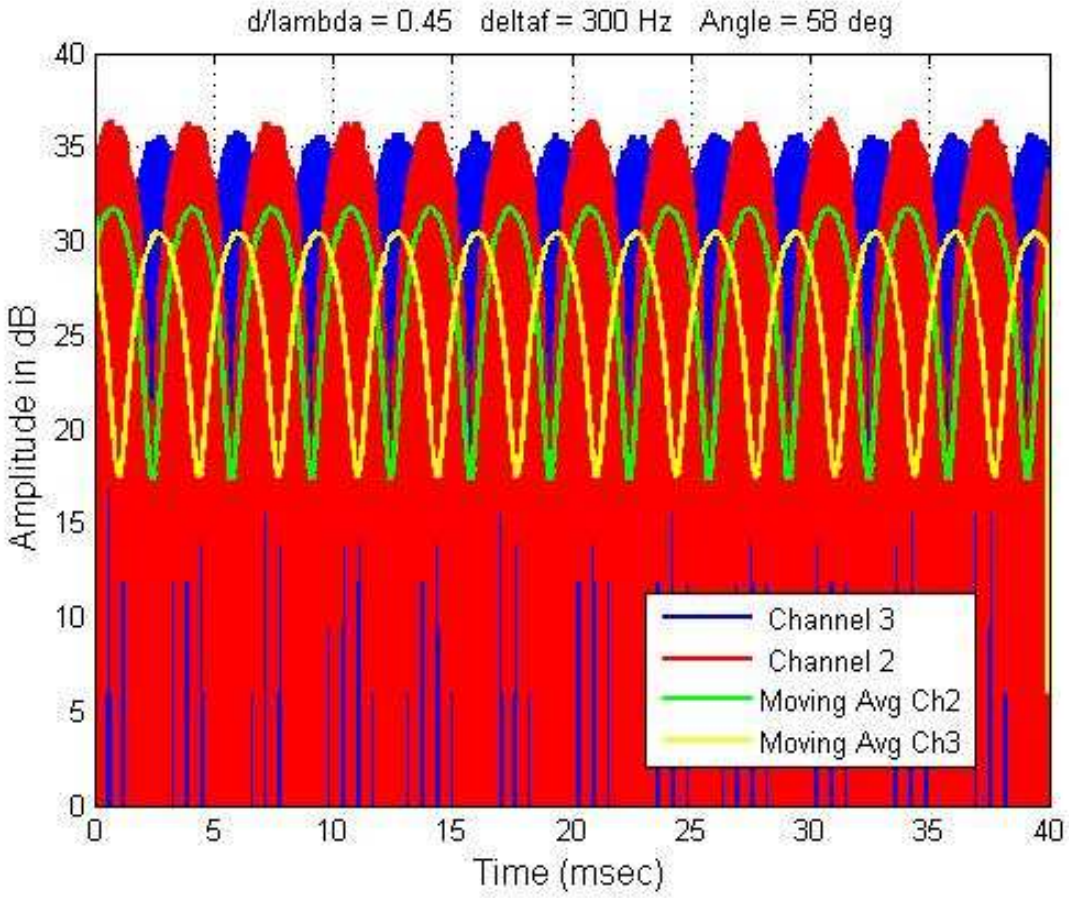

Fig. 6-45: Two-channel measurement for $d/\lambda = 0.45$, $\Delta f = 300$ Hz, $\theta = 58^{o}$. Time delay is 1.4 msec.

The results for this case are summarized in Table 6-5. Again, there is good agreement between the measured and predicted results.

Table 6-5: Summary of measurements for $d/\lambda = 0.45$, $\Delta f = 300$ Hz

Angle (deg)	**Predicted Delay (msec)**	**Measured Delay (msec)**
39	0.9	1.0
58	1.3	1.4

6.3.3 Range Variation of the Pattern

To measure the variation of the frequency diverse array beam with range, the receivers needed to be separated by a larger distance than allowed by the rooftop tests. Therefore, two receivers were placed at a location approximately 2 km from, and within line-of-sight of, the transmit array. The test configuration to measure range variation of the pattern is illustrated in Fig. 6-46. The receivers were separated by distances of 0, 30, 49, and 60 m, and two transmit channels were utilised with a frequency offset between channels of 2.5 MHz. This value of frequency offset ensured that one receiver could be located within a null of the pattern when the other receiver was located in a peak at a separation of 60 m.

Fig. 6-46: Site configuration to measure variation of pattern with range.

A close-range probe measurement of the transmitted signal is shown in Fig. 6-47. High frequency effects limit the output level to the display, but the frequency diverse array signal can clearly be seen to have a period of 400 ns as expected, corresponding to $1/\Delta f$.

The spectrum of the received signal is shown in Fig. 6-48, showing two tones separated in frequency by 2.5 MHz.

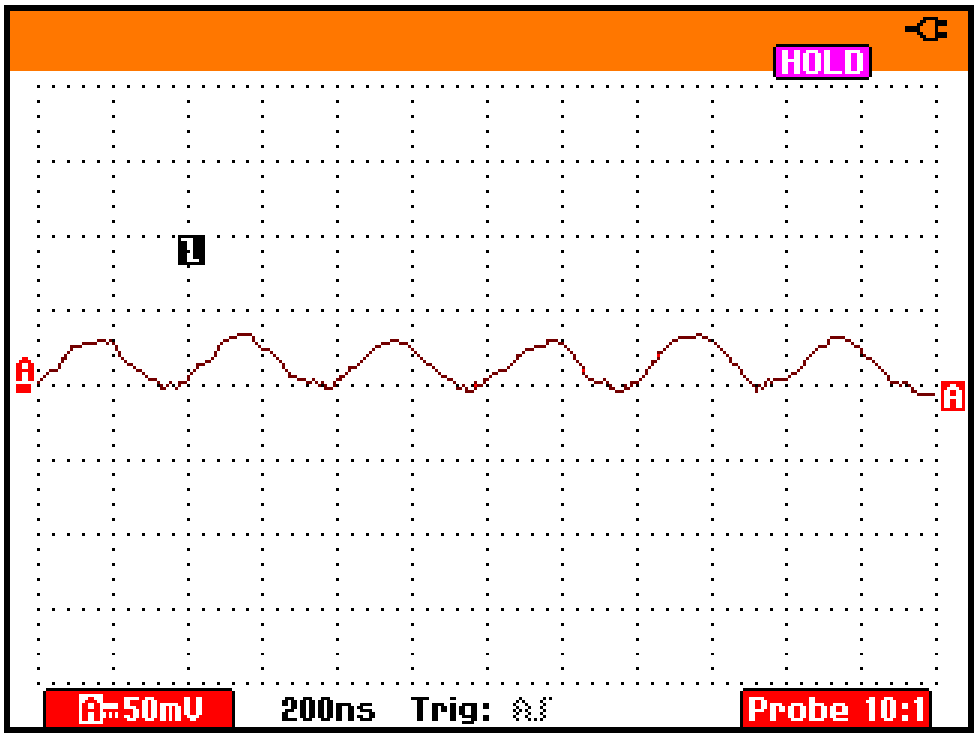

Fig. 6-47: Close-range measurement of FDA signal, Δf = 2.5 MHz.

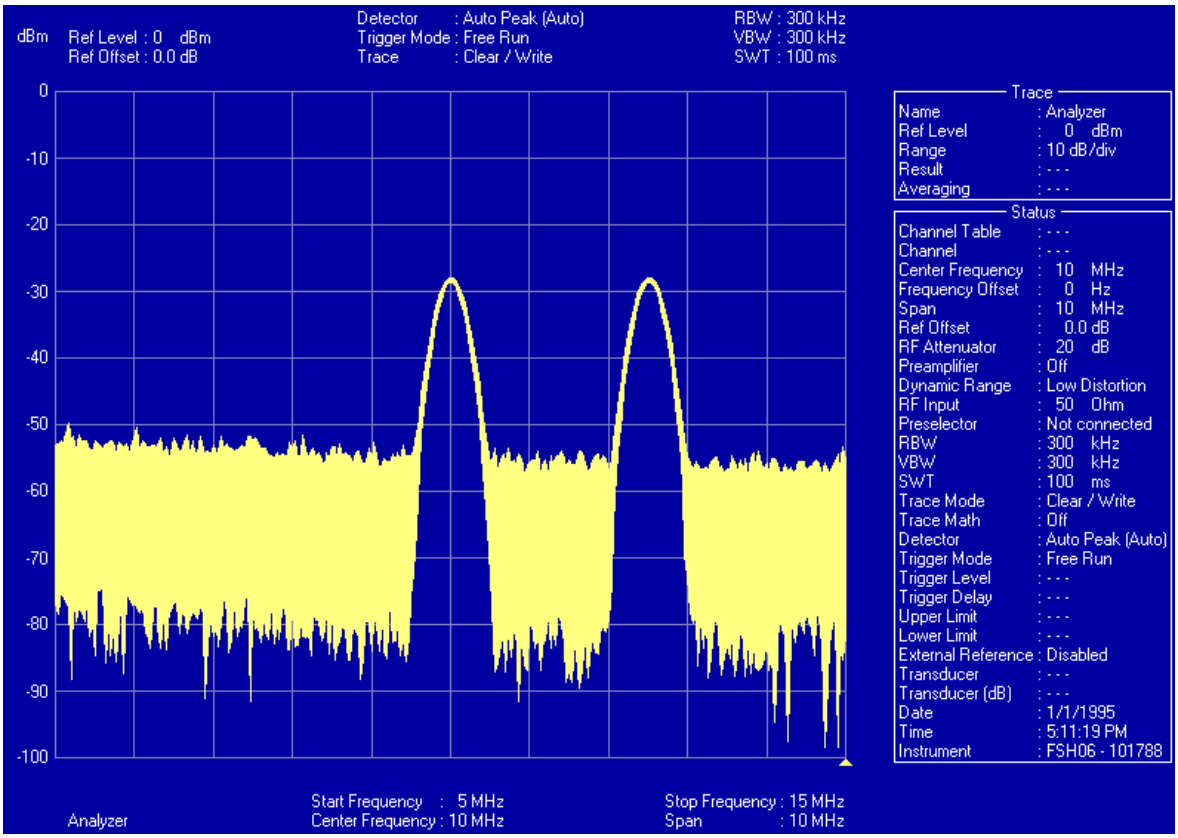

Fig. 6-48: Spectrum of received FDA signal, Δf = 2.5 MHz.

When the two receive antennas are co-located, no delay is expected between the received signals. The measured data supports this as shown in Fig. 6-49. As the separation between receive antennas increases, the delay also increases. Fig. 6-50 shows the two-channel measurement for a range separation of about 31 m. This range separation corresponds to a quarter of a period of the time waveform. When the receive antennas are separated by 59 m, the delay becomes approximately one-half of the frequency diverse array signal period, as shown in Fig. 6-51. Notice that at this range separation at a given instant of time, one receive antenna is located at a peak of the frequency diverse array beam, while the other antenna is located in a null of the beam. As the beam propagates forward in range at the speed of light, the first antenna moves into a null of the beam as the second antenna moves into the beam peak.

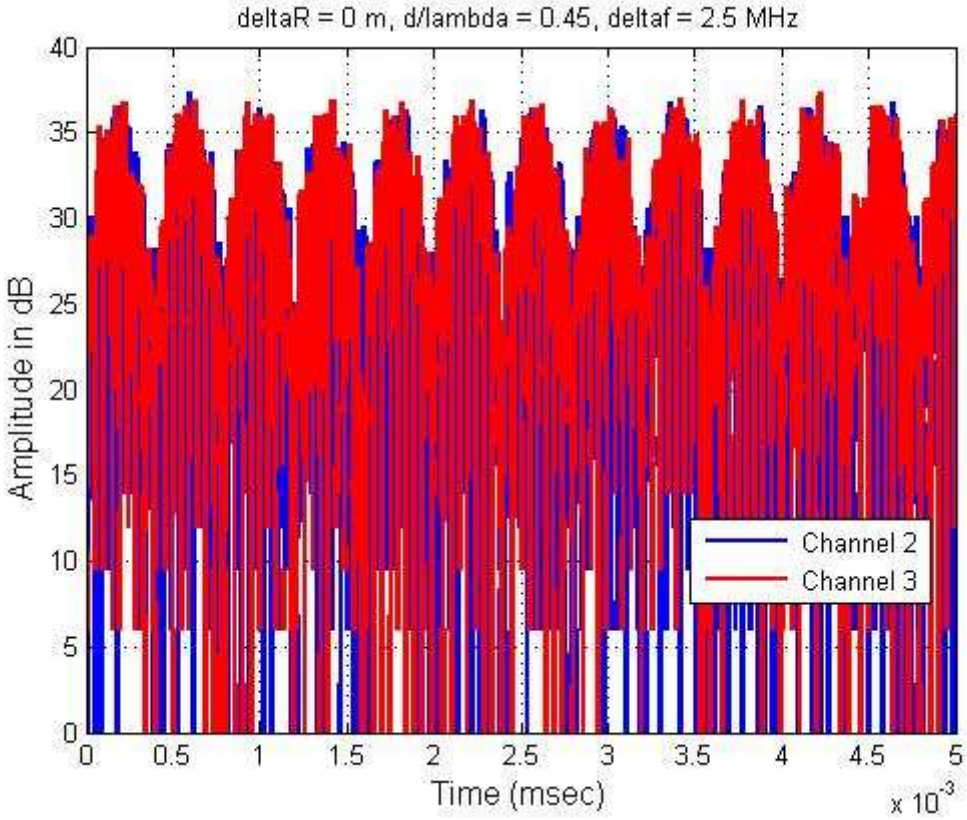

Fig. 6-49: Two-channel measurement, antennas co-located.

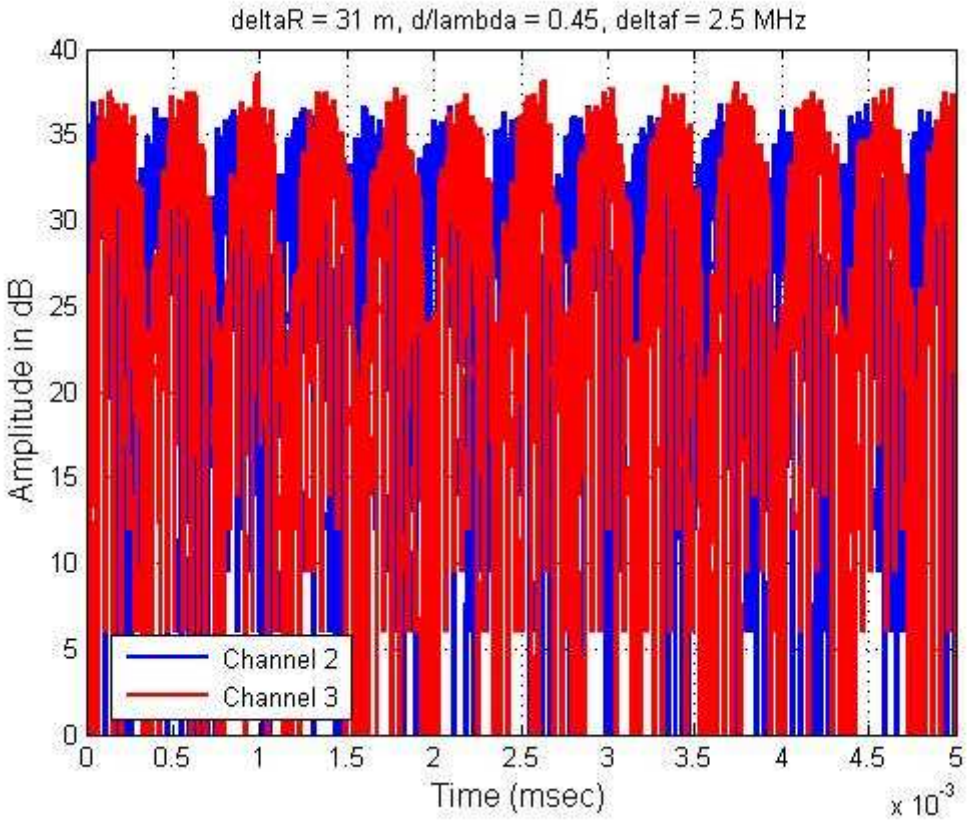

Fig. 6-50: Two-channel measurement, antennas separated by 31 m.

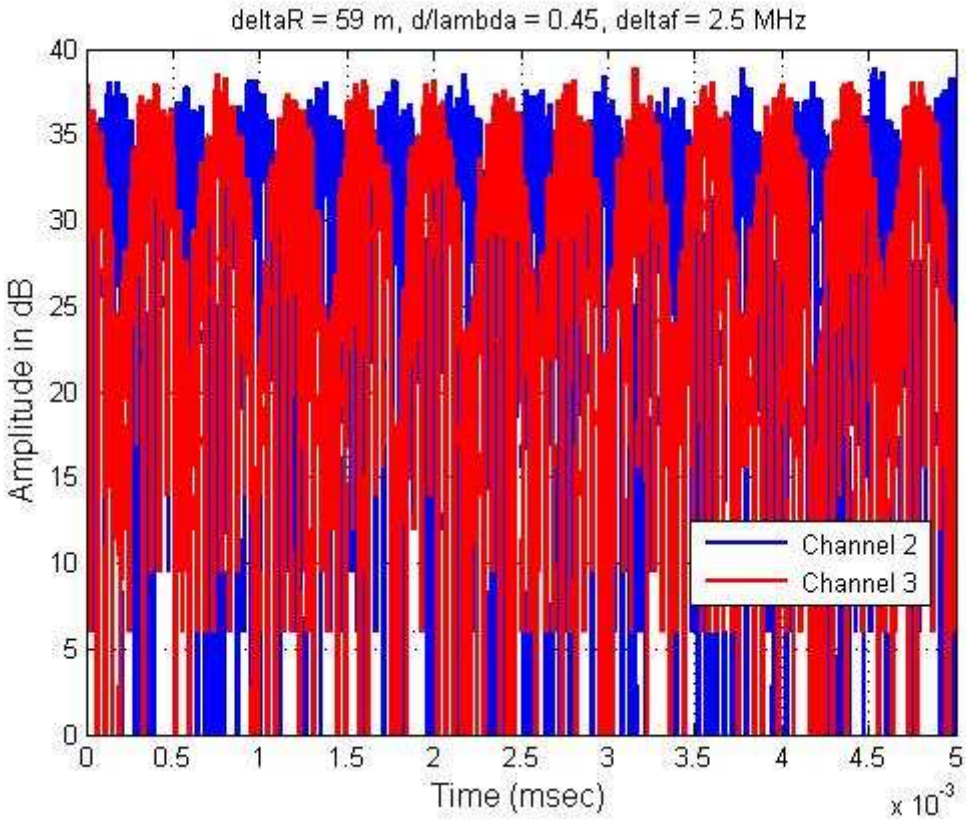

Fig. 6-51: Two-channel measurement, antennas separated by 59 m

6.4 Data Summary

This chapter has presented a large volume of data taken to confirm the theory and simulation presented earlier. Tables 6-1 through 6-5 and Figures 6-49 through 6-51 show that there is good agreement between the measured and predicted results over a wide range of variables. This data will be analyzed in more detail in the next chapter.

Chapter 7

Analysis of Results

This chapter discusses the experimental validation of the theory and simulation of the frequency diverse array. The frequency diverse array is shown to be periodic in time, corresponding to a periodicity in range, and also periodic in angle.

7.1 Variation with Time

Section 4.2 predicted that the frequency diverse array would be periodic in time with period $1/\Delta f$. Specifically, the time waveform of the frequency diverse array was derived to be:

$$x(t) = \quad 2N \; rep_{\frac{1}{\Delta f}} \left\{ \text{sinc}(N\Delta f t) \cos(2\pi \; f_m t) \right\} \quad , \tag{7-1}$$

which was further confirmed in (4-70). The frequency diverse array time waveform is illustrated in Fig. 7-1. These results were verified exceptionally well experimentally

through both bench tests and radiated field measurements. In Section 6.3.1, laboratory measurements were made of the sum of 5 signals separated by Δf from channel-to-channel of 100 Hz, 1 kHz, and 10 kHz. These results are summarized in Table 7-1.

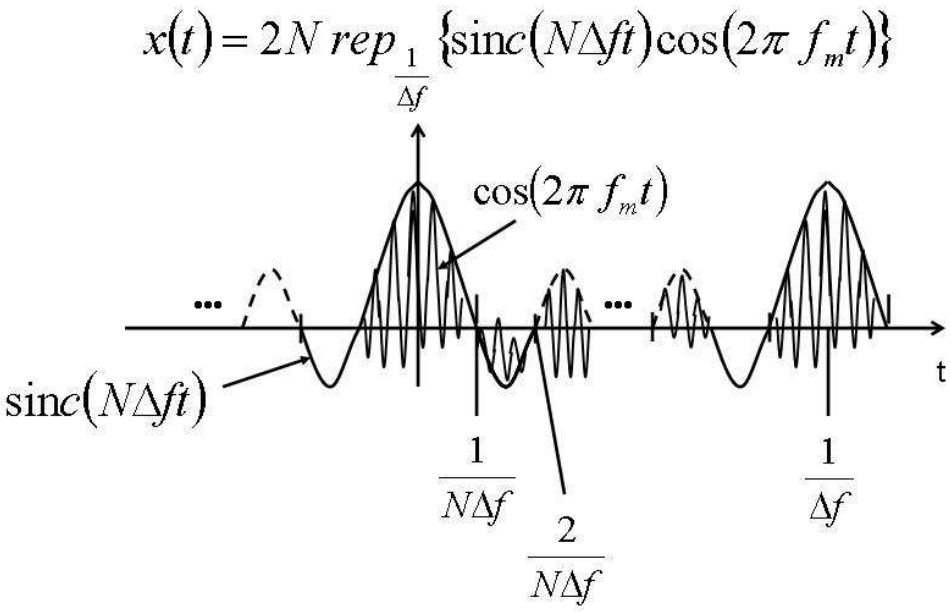

Fig. 7-1: Frequency diverse array time waveform

Table 7-1: Summary of bench test results for time variation of waveform

Δf (Hz)	Predicted Period, $(1/\Delta f)$, (ms)	Measured Period (ms)	Reference
100	10	10	Fig. 6-10
1000	1	1	Fig. 6-11
10000	0.1	0.1	Fig. 6-12

In addition, a number of radiated field measurements were made at a variety of frequency offsets. Again, measured results agreed exceptionally well with theoretical predictions. Results are summarized in Table 7-2 for both 2 and 5 channel arrays for a variety of element spacings.

Table 7-2: Summary of radiated field measurements of time periodicity of waveform

N	d/λ	Angle (deg)	Δ*f* (Hz)	Predicted Period (ms)	Measured Period (ms)	Reference
5	0.45	0	100	10	10	Fig. 6-20 & 6-21
2	0.45	0	100	10	10	Fig. 6-23
2	0.45	10	100	10	10	Fig. 6-24
2	0.45	20	100	10	10	Fig. 6-25
2	0.45	30	100	10	10	Fig. 6-26
2	0.45	35	100	10	10	Fig. 6-27
2	0.90	0	100	10	10	Fig. 6-28
2	0.90	12	100	10	10	Fig. 6-29
2	0.90	23	100	10	10	Fig. 6-30
2	0.90	25	100	10	10	Fig. 6-31
2	0.90	30	100	10	10	Fig. 6-32
2	0.90	35	100	10	10	Fig. 6-33
2	0.90	58	100	10	10	Fig. 6-34
2	1.35	0	100	10	10	Fig. 6-35
2	1.35	12	100	10	10	Fig. 6-36
2	1.35	23	100	10	10	Fig. 6-37
2	1.35	39	100	10	10	Fig. 6-38
2	1.35	58	100	10	10	Fig. 6-39
2	0.45	39	200	5	5	Fig. 6-40
2	0.45	58	200	5	5	Fig. 6-41
2	0.45	39	300	3.3	3.3	Fig. 6-42
2	0.45	58	300	3.3	3.3	Fig. 6-43

Every measurement showed excellent agreement with the theoretical result.

7.2 Beam Scan with Time

The frequency diverse array was shown to be periodic in angle at λ/d in accordance with (4-72). This simply corresponds to the location of grating lobes as in the case of the conventional phased array. More interesting is that at any given range the frequency diverse array scans in angle with time without mechanical rotation or electronic phase shifters. The time to scan through some angle was given in (4-79) or (5-2) as:

$$\Delta t = \frac{-(d/\lambda_0)}{\Delta f}\left[\sin\theta_2 - \sin\theta_1\right]. \tag{7-2}$$

The time to scan through an angle is then directly proportional to the element spacing in wavelengths and inversely proportional to the frequency offset between channels.

Section 5.1.6 discussed the propagation of the frequency diverse array beam pattern over time. The beam was simulated for $d/\lambda = 0.45$ and $\Delta f = 100$ Hz out to a distance of 600 km in order to emphasize the variation of the pattern over range. For small frequency offset over a much shorter distance, the variation in range is less obvious, but the scan of the beam over time is still evident. Figures 7-2 through 7-11 illustrate this for a two-channel system for the case of $d/\lambda = 0.45$ and $\Delta f = 100$ Hz out to a range of 100 m.

Fig. 7-2 shows the range-angle diagram for the above case at $t = 0$. A cut through the diagram at constant range is given in Fig. 7-3. Both plots show that the frequency diverse array beam points normal to the array face at $t = 0$.

At t = 0.8 msec, the beam scans to −10° as shown in Figures 7-4 and 7-5. This agrees with Equation (7-2). It is also apparent that the beamshape begins to skew as the broad beam scans towards the edge of real space. The peak of the beam scans to −20° at t = 1.5 msec as presented in Figures 7-6 and 7-7. At a constant range, the beam continues to scan with time, to −30° at 2.3 msec and to −35° at 2.6 msec. These results are shown in Figures 7-8 through 7-11.

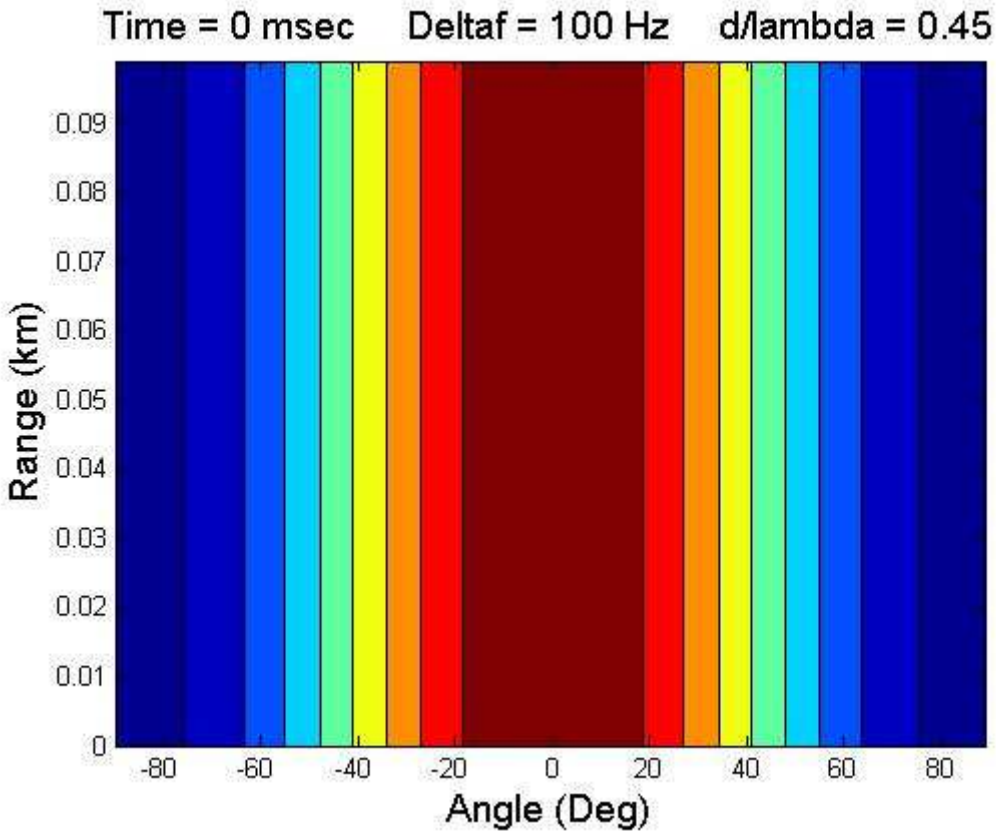

Fig 7-2: Range-angle diagram of FDA beam, d/λ = 0.45, Δf = 100 Hz, t = 0 msec.

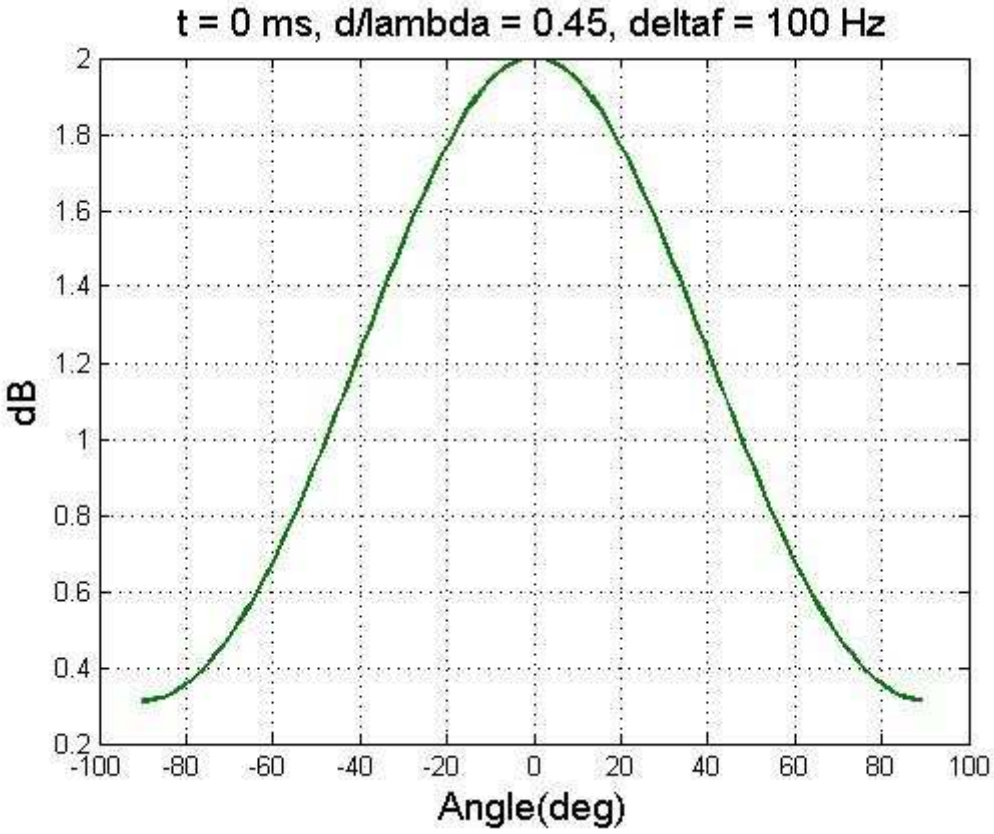

Fig. 7-3: Range cut, $d/\lambda = 0.45$, $\Delta f = 100$ Hz, $t = 0$ msec

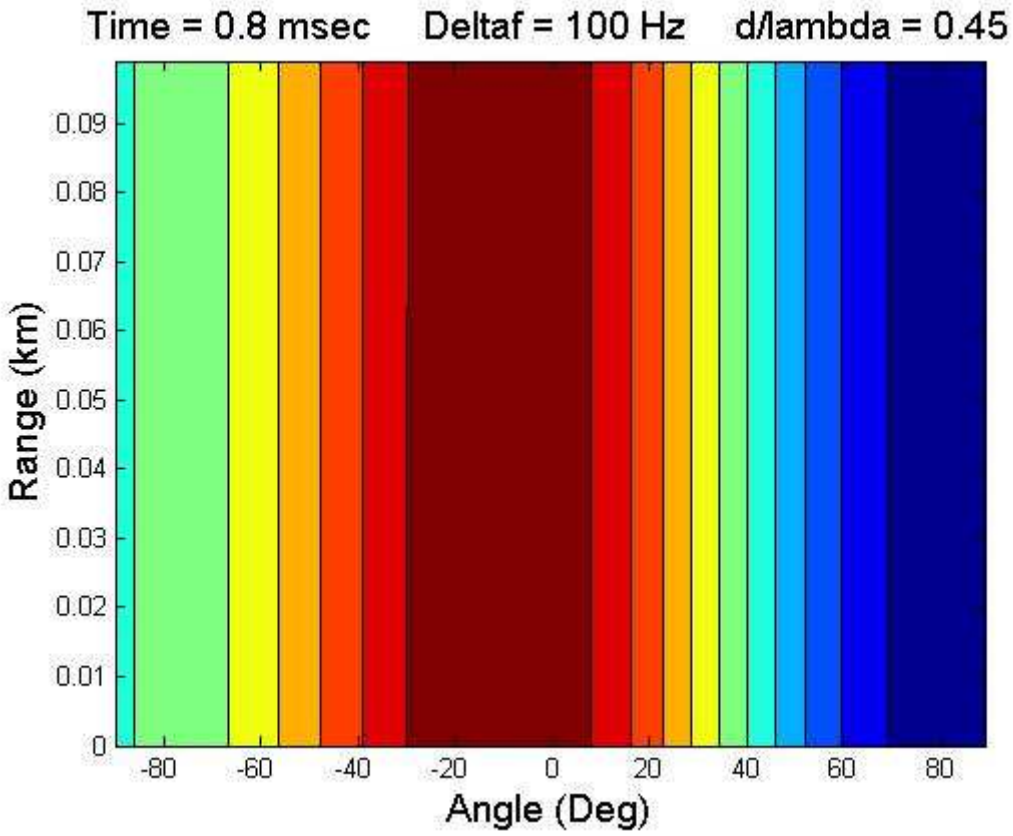

Fig 7-4: Scan with FDA beam over time, $d/\lambda = 0.45$, $\Delta f = 100$ Hz $t = 0.8$ msec.

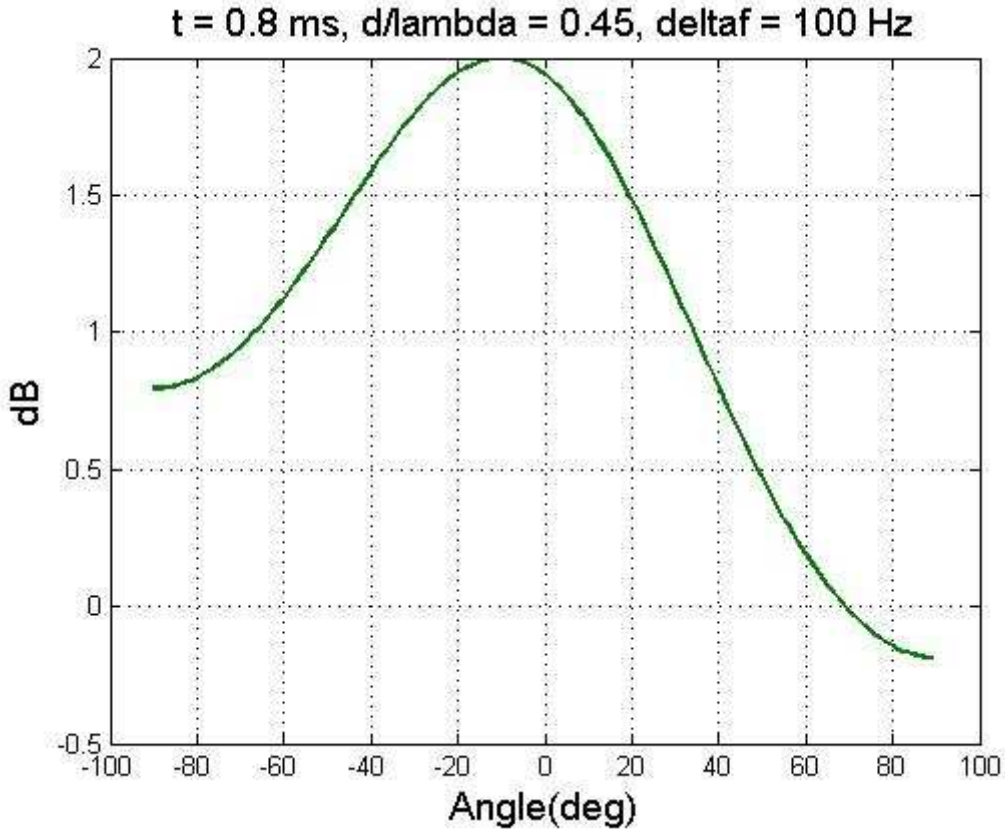

Fig. 7-5: Range cut, $d/\lambda = 0.45$, $\Delta f = 100$ Hz, $t = 0.8$ msec

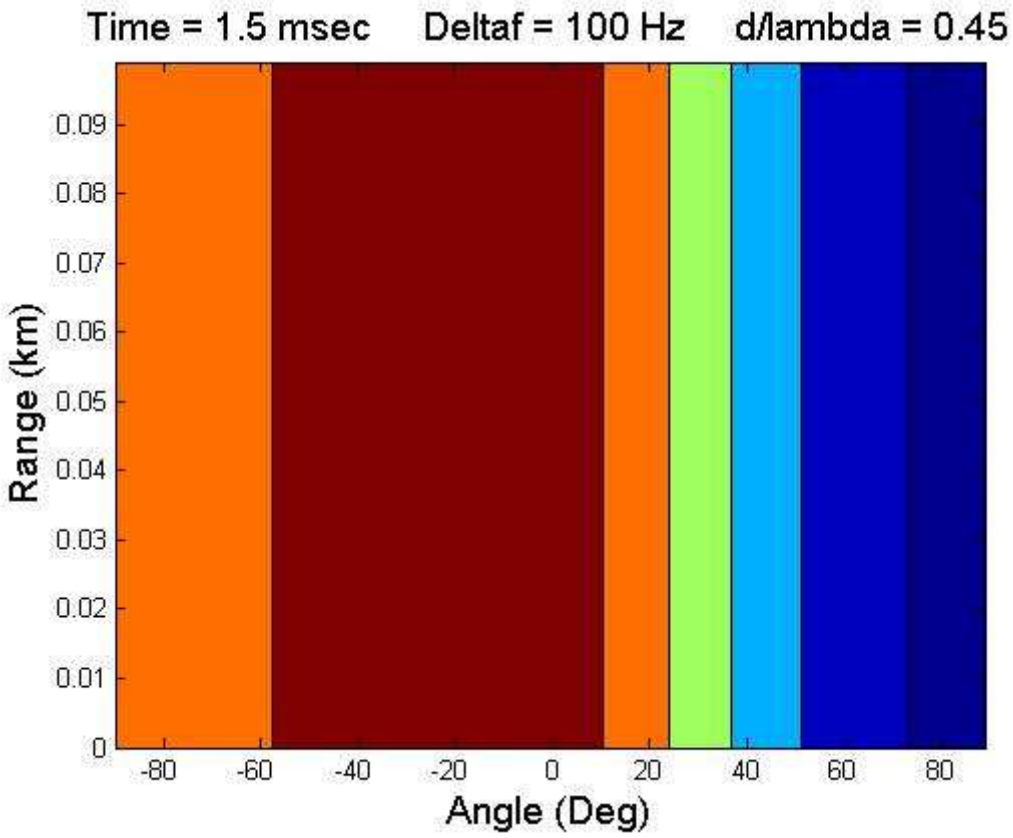

Fig 7-6: Scan with FDA beam over time, $d/\lambda = 0.45$, $\Delta f = 100$ Hz, $t = 1.5$ msec.

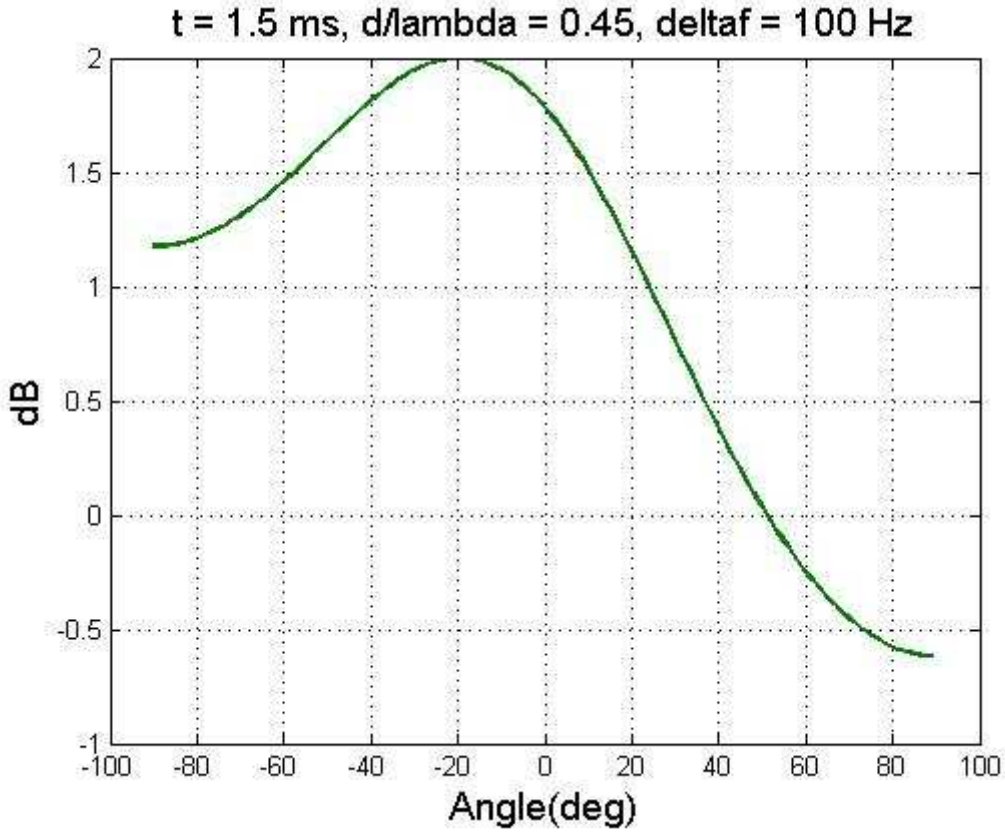

Fig. 7-7: Range cut, $d/\lambda = 0.45$, $\Delta f = 100$ Hz $t = 1.5$ msec

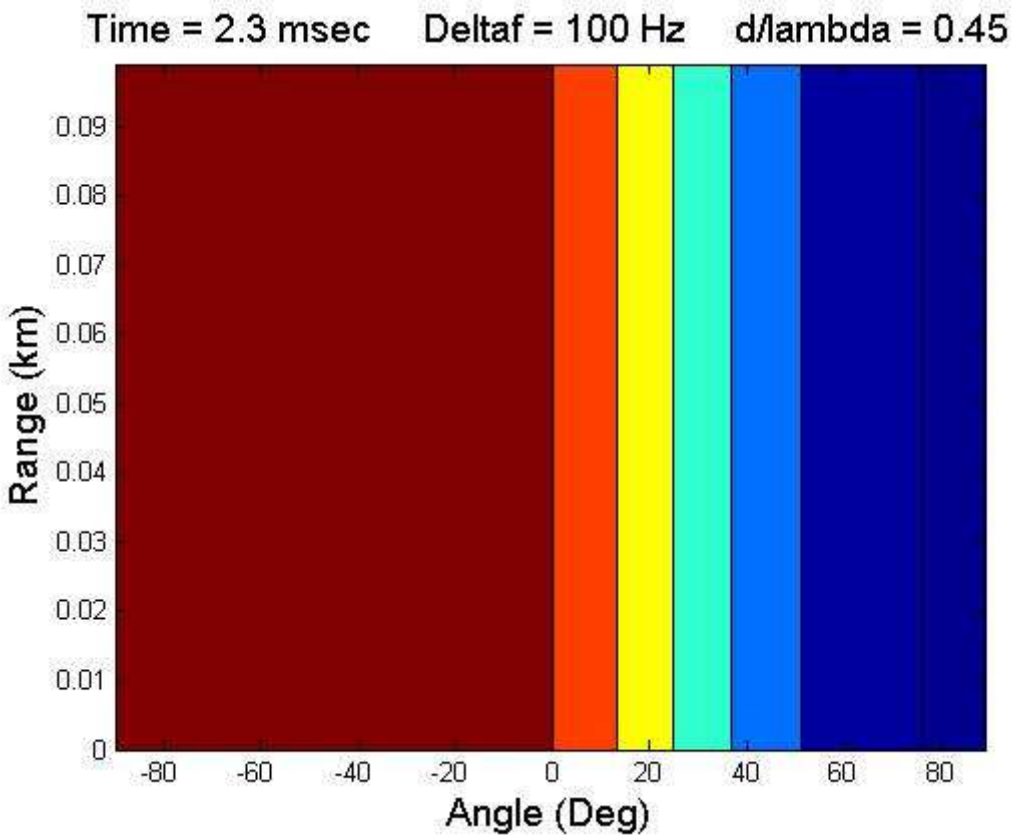

Fig 7-8: Scan with FDA beam over time, $d/\lambda = 0.45$, $\Delta f = 100$ Hz, $t = 2.3$ msec.

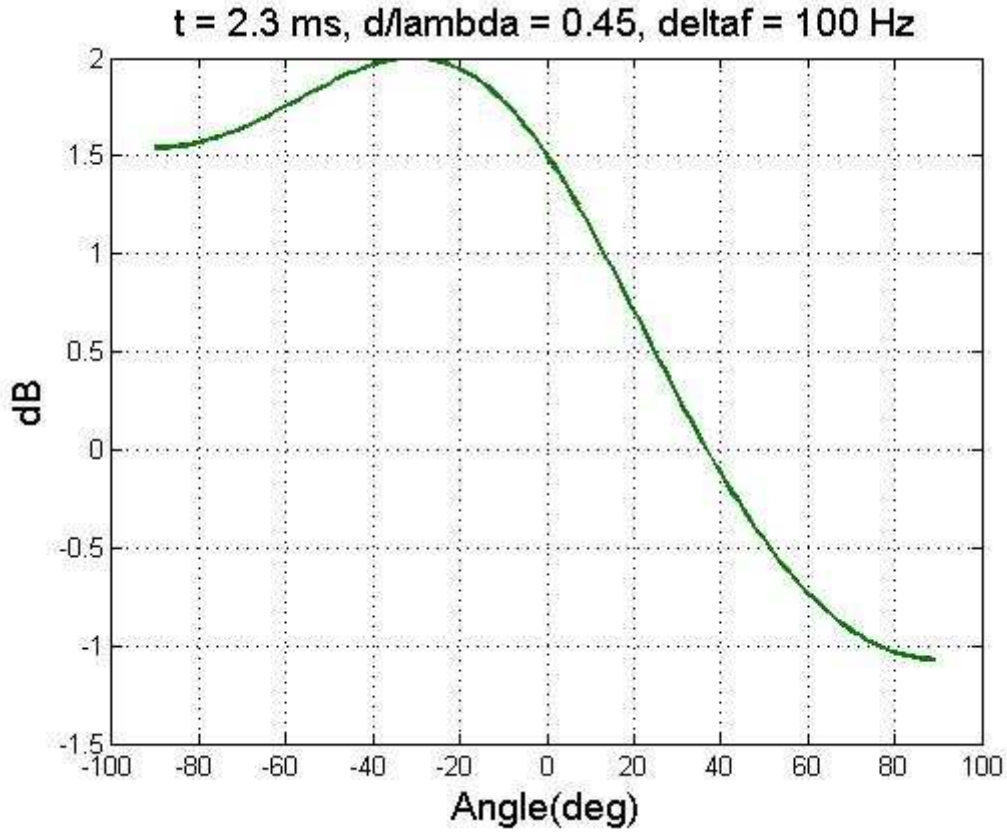

Fig. 7-9: Range cut, $d/\lambda = 0.45$, $\Delta f = 100$ Hz, $t = 2.3$ msec

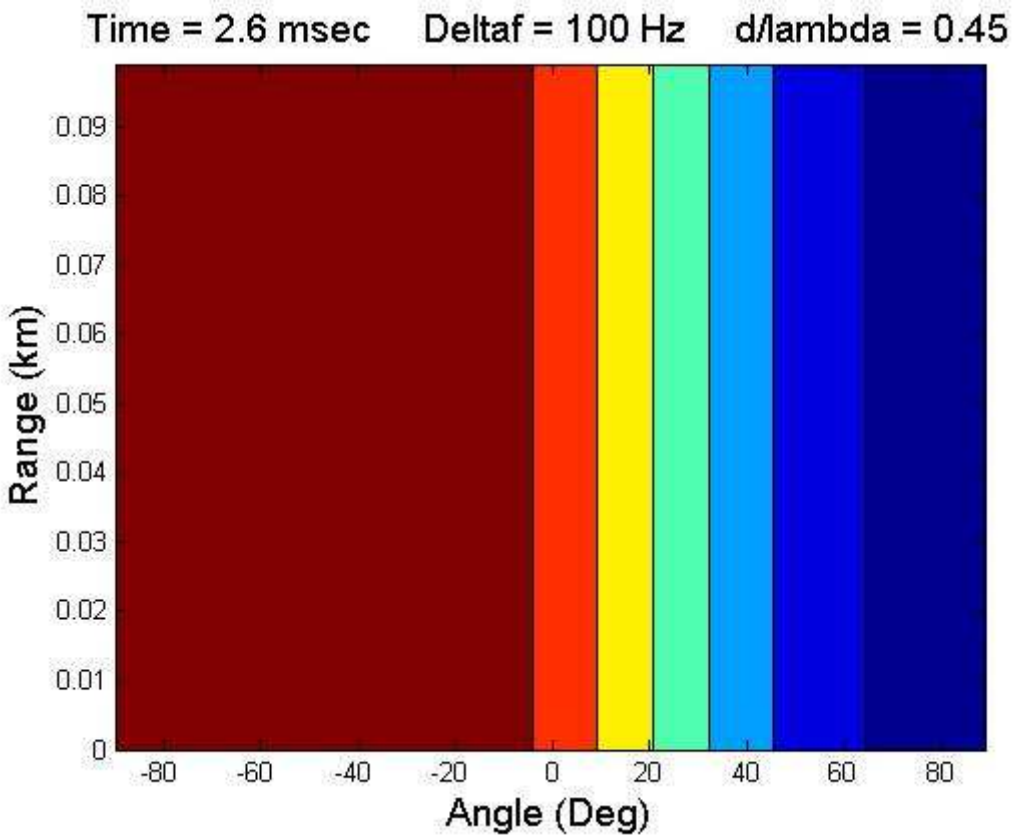

Fig 7-10: Scan with FDA beam over time, $d/\lambda = 0.45$, $\Delta f = 100$ Hz, $t = 2.6$ msec.

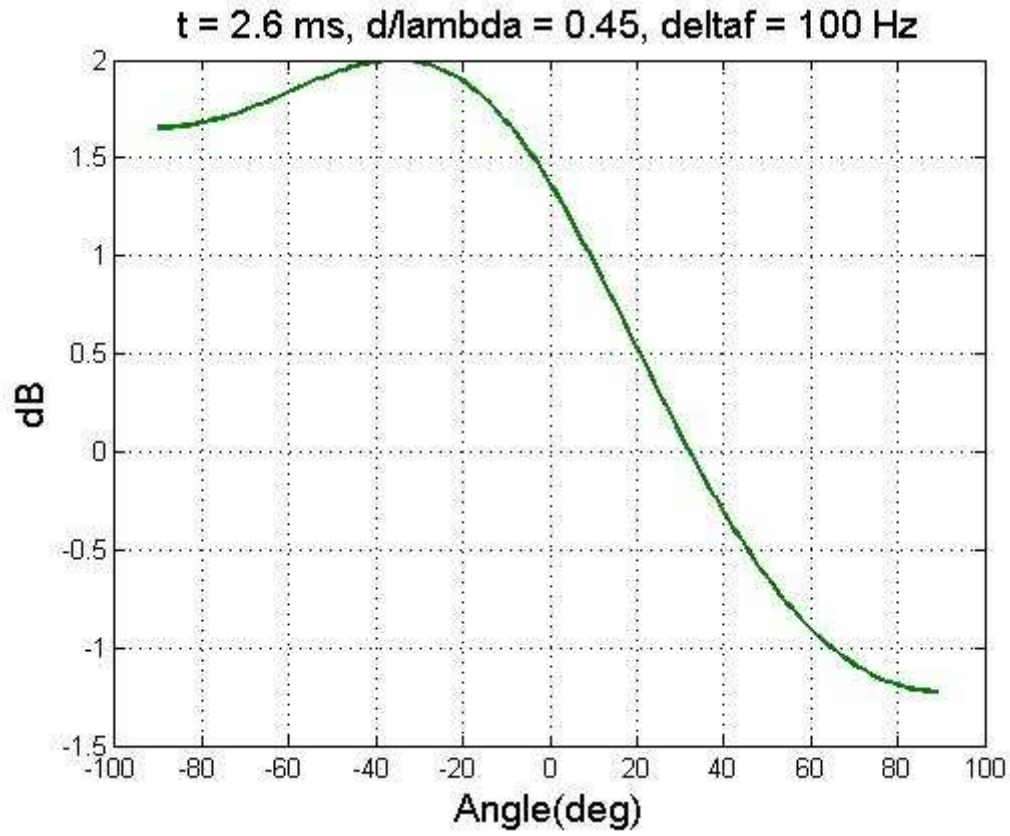

Fig. 7-11: Range cut, $d/\lambda = 0.45$, $\Delta f = 100$ Hz, $t = 2.6$ msec

These results were tested experimentally for a variety of element spacing and frequency shifts. Larger frequency offsets were tested at larger angles to emphasize the expected time delay. Table 7-3 summarizes the results from Section 6.3.2. Note that the sense of the frequency offset was reversed during measurements resulting in a positive rotation in angle.

The measured data validated the theory and simulation remarkably well, within the constraints of real-world effects to be described later.

Table 7-3: Summary of measurements of frequency diverse array scan.

d/λ	Δf	Angle (deg)	Predicted Delay (msec)	Measured Delay (msec)	Reference
0.45	100	0	0.0	-0.1	Fig. 6-23
		10	0.8	0.8	Fig. 6-24
		20	1.5	1.4	Fig. 6-25
		30	2.3	2.0	Fig. 6-26
		35	2.6	2.7	Fig. 6-27
0.90	100	0	0.0	0.3	Fig. 6-28
		12	1.9	2.1	Fig. 6-29
		23	3.5	3.4	Fig. 6-30
		25	3.8	3.7	Fig. 6-31
		30	4.5	4.3	Fig. 6-32
		35	5.2	5.3	Fig. 6-33
		58	7.6	7.7	Fig. 6-34
1.35	100	0	0.0	-0.2	Fig. 6-35
		12	2.8	3.1	Fig. 6-36
		23	5.3	5.3	Fig. 6-37
		39	8.5	8.8	Fig. 6-38
		58	11.4	11.2	Fig. 6-39
0.45	200	39	1.4	1.6	Fig. 6-40
		58	1.9	2.1	Fig. 6-41
0.45	300	39	0.9	1.0	Fig. 6-42
		58	1.3	1.4	Fig. 6-43

7.3 Variation in Range

Fig. 7-1 illustrated the structure of the frequency diverse array waveform. However, recall from Section 4.3 that a transverse electromagnetic wave propagates forward in the positive *Z* direction. Therefore, the waveform of (7-1) propagates forward in time at the speed of light.

This feature of the frequency diverse array was tested experimentally as described in Section 6.3.3. The experiment utilised a two-channel transmit array, with receive antennas placed at various spacings up to 60 m apart in the same line-of-sight of the transmit array. Fig. 7-12 shows a range-angle diagram for the experimental setup, with magnitude of the beam plotted in dB. Fig. 7-13 illustrates the pattern with range for two instants of time. When two targets are separated by 60 m, at some point in time target #1 will be in peak of the beam while target #2 is located in a null. At a time of 200 ns later, target #2 will be in the peak of the beam while target #1 is in the null.

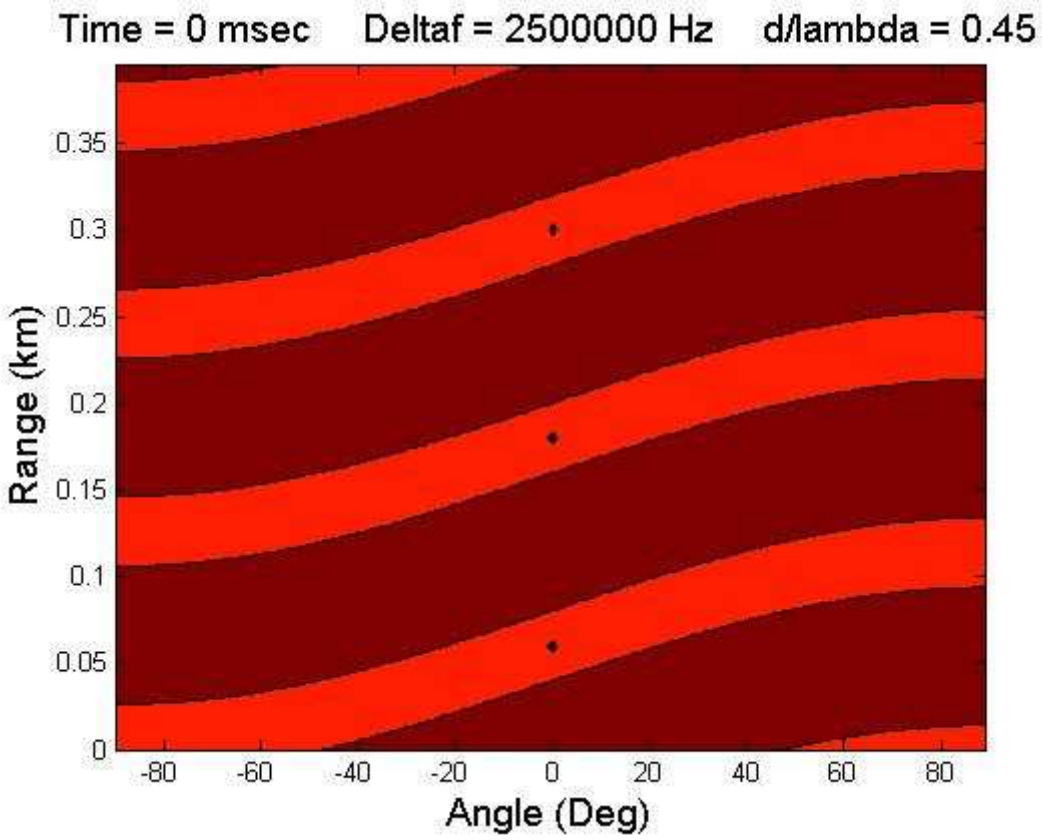

Fig. 7-12: Range-angle diagram, $d/\lambda = 0.45$, $\Delta f = 2.5$ MHz

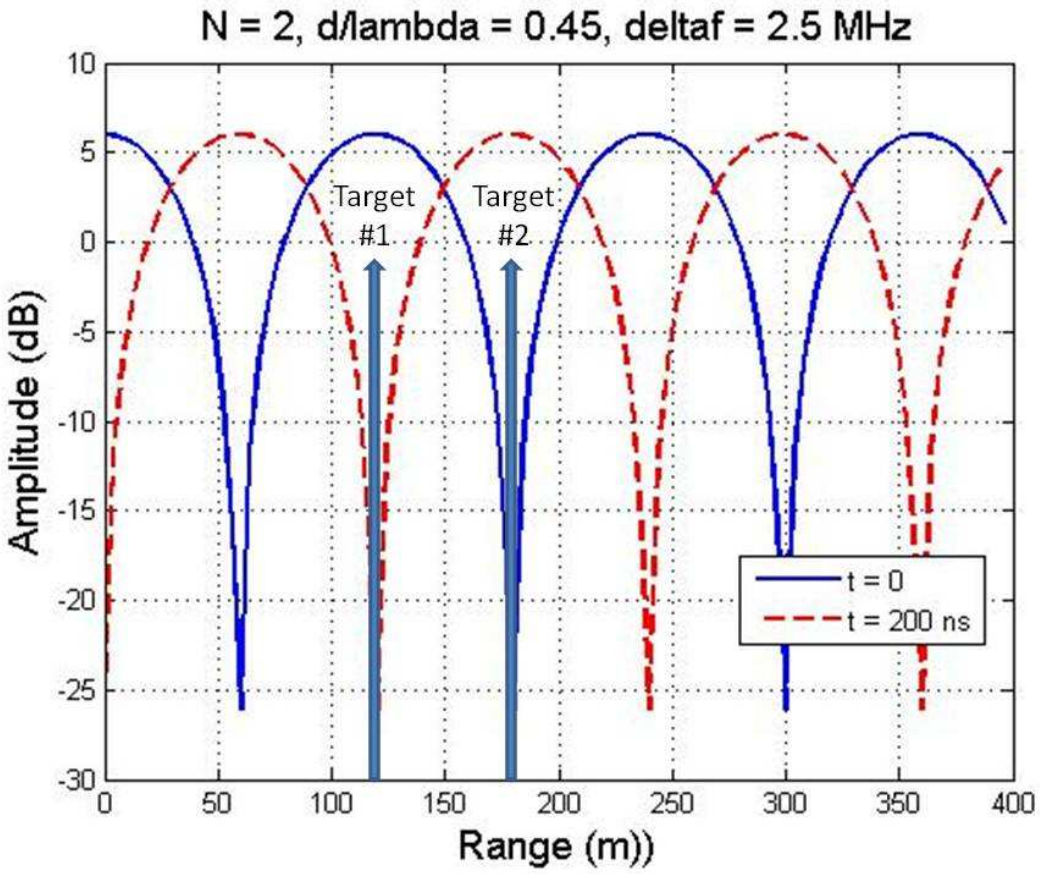

Fig. 7-13: Beam pattern in range for two instants of time

To test this theory and simulation, experiments were performed as described in Section 6.3.3. Two transmit channels were utilised ($d/\lambda = 0.45$), and the frequency offset was set to 2.5 MHz so that the beam peak and null would be separated by 60 m. Receivers were then placed at 0, 31, and 59 m separation, corresponding to zero, one-quarter, and one-half the range periodicity ($c/\Delta f$) respectively. The results shown in Figures 6-47 through 6-49 agree well with the theoretical predictions.

7.4 Beam Formation and Control

The frequency diverse array offers a new dimension of design freedom that results in novel beam formation and control. This section explores how the relationships between range, time, and angle can be exploited to shape the radiation pattern.

Equation (7-1) shows that the frequency diverse array produces a linear relationship between time (and thus range) and angle expressed in sin θ space. Letting $t = 1/\Delta f$ results in:

$$\frac{1}{\Delta f} = \frac{-(d/\lambda_0)}{\Delta f}[\sin\theta_2 - \sin\theta_1] \quad , \tag{7-3}$$

and

$$\sin\theta_2 - \sin\theta_1 = -\frac{\lambda_0}{d} \quad . \tag{7-4}$$

In other words, $t = 1/\Delta f$ corresponds to the time required to scan through one grating lobe.

When the frequency diverse array signal propagates forward in time, corresponding to a range of $R = ct$, the beam at any given range scans with time, as was observed in Section 7.1. When the beam scans far enough, it encounters a grating lobe, or ambiguity in angle. This occurs at $\sin\theta = \lambda/d$ in accordance with (4-72). At range $c/\Delta f$, corresponding to time $1/\Delta f$, the entire pattern repeats.

Like a conventional phased array, the frequency diverse array introduces grating lobes spaced at λ/d in sin θ space. However, the frequency diverse array also introduces a

linear relationship between range and angle in accordance with (7-2). The periodicities in range introduced by the diverse array are manifestations of the grating lobe in real space.

From (7-2), the time to scan from -90° to +90° is given by:

$$\Delta t = \frac{-(d/\lambda_0)}{\Delta f}[1-(-1)] = \frac{-2(d/\lambda_0)}{\Delta f} \quad . \qquad (7\text{-}5)$$

As the element spacing decreases, the time to scan through real space also decreases. The relationships between range, time, and angle can be observed in Figures 7-14 through 7-16, which illustrate range-angle diagrams for 3 element spacings at one instant of time.

In Fig. 7-14, the transmit array element spacing is set to d = 0.25λ. Grating lobes then appear at multiples of sin $\theta = \lambda/d = 4$. The time to scan through real space is then

$$\Delta t = \frac{-2(d/\lambda_0)}{\Delta f} = \frac{1}{2\Delta f} \quad , \qquad (7\text{-}6)$$

which is half the time period of the waveform. In this case, once the beam reaches a scan of $\theta = \pm 90°$, the beam continues to scan, but not in visible space. This results in a dead time in which there is no beam in real space.

On the other hand, when $d/\lambda = 0.5$, the time to scan real space is $t = 1/\Delta f$, which exactly matches the time period of the waveform. This case is illustrated in Fig. 7-15.

For $d/\lambda = 1.0$, the grating lobes are spaced at multiples of sin $\theta = \lambda/d = 1$, and the time to scan through real space is:

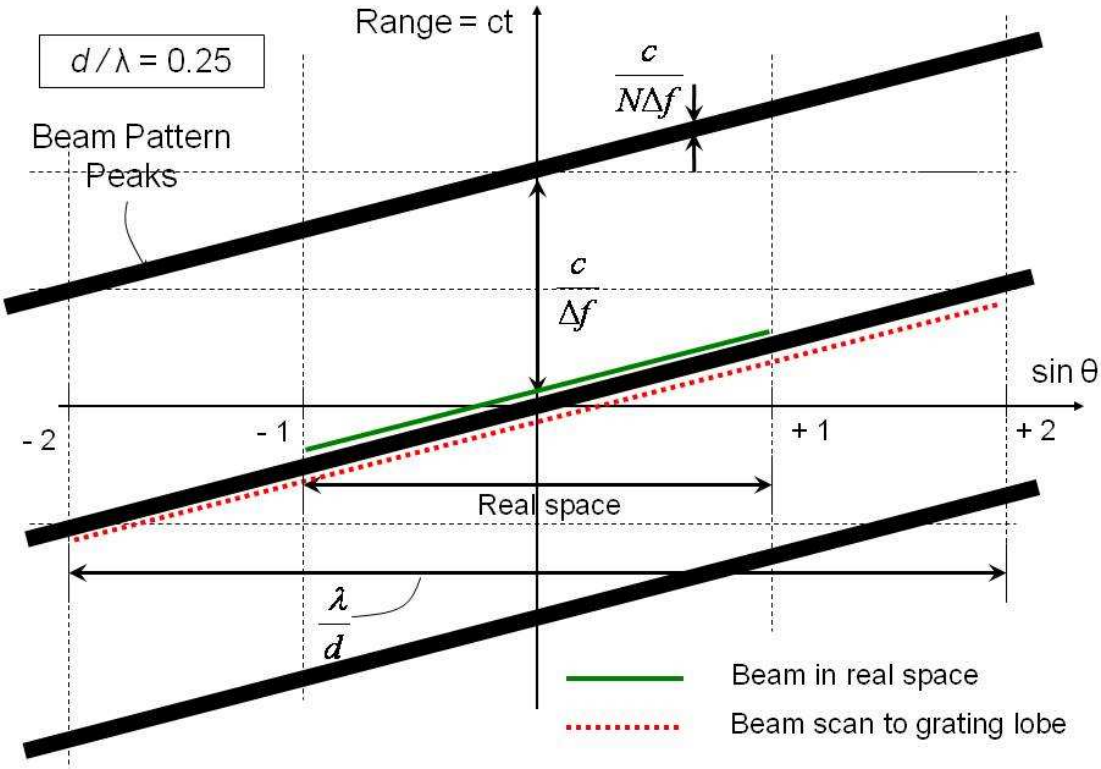

Fig. 7-14: Range-angle diagrams for $d/\lambda = 0.25$

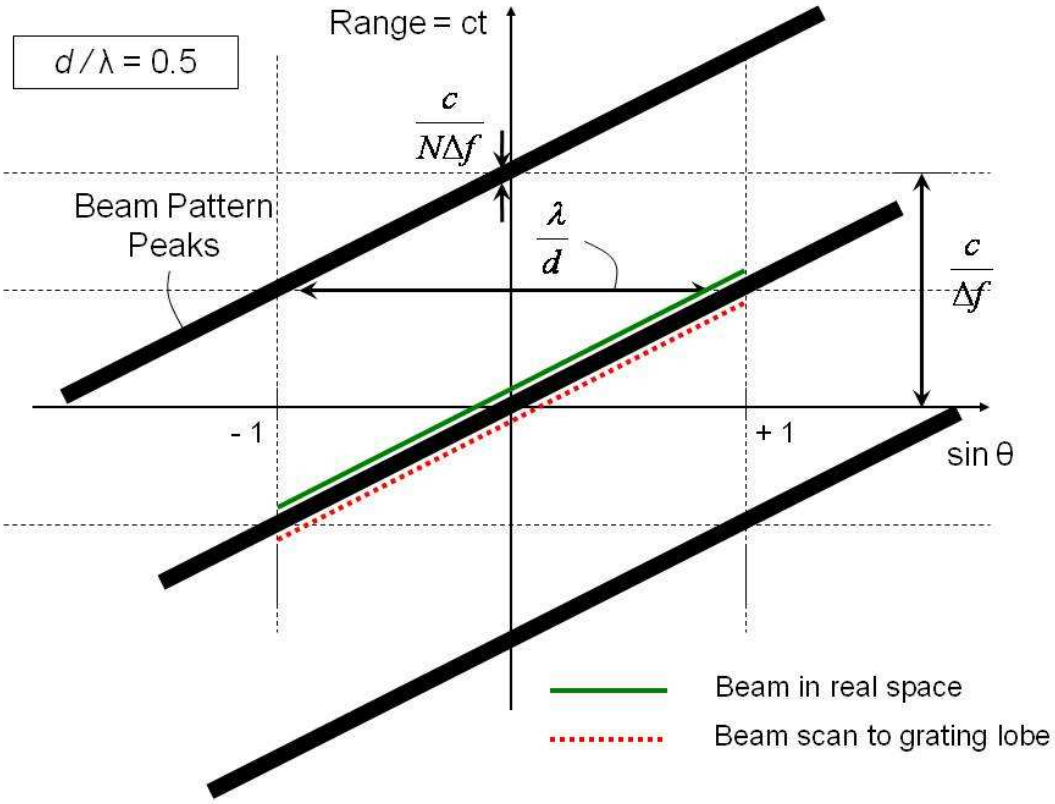

Fig. 7-15: Range-angle diagrams for $d/\lambda = 0.5$

$$\Delta t = \frac{-2(d/\lambda_0)}{\Delta f} = \frac{2}{\Delta f} \quad . \tag{7-7}$$

The wide spacing of elements therefore causes grating lobes to enter real space, resulting in a range periodicity being encountered before the beam has scanned an angle corresponding to real space. This is illustrated in Fig. 7-16.

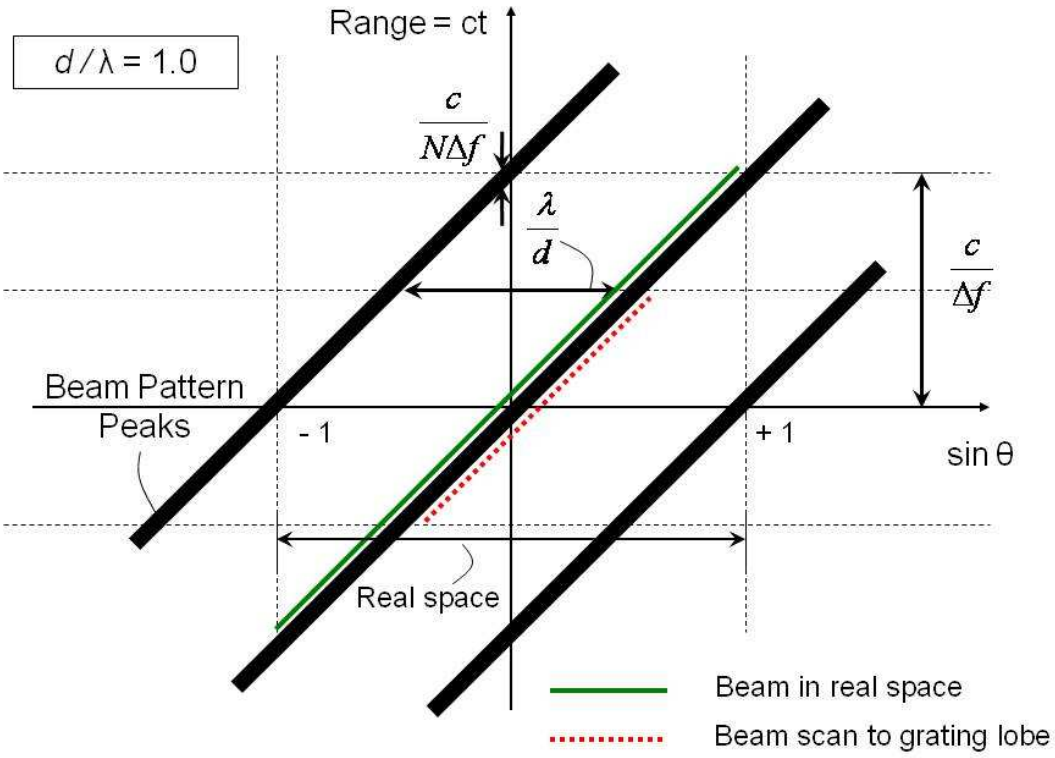

Fig. 7-16: Range-angle diagrams for $d/\lambda = 1.0$

In summary, the frequency diverse array beam pattern can be controlled by the transmit array configuration and the signal parameters. The slope of the beam in range-angle space can be controlled by the element spacing and the frequency offset. Grating lobes, and therefore the amount of time spent scanning in real space, is also governed by the element spacing. The periodicity of the beam in the range dimension can be controlled by the frequency offset, and the resolution of the beam in range is given by the size of the transmit array, the form of the transmitted signal, and the frequency offset.

7.5 Sources of Error

The measured data validated the theory well, especially considering numerous real world effects with potential to impact the results. Some of these sources of error include:

7.5.1 Multipath

The rooftop range was clearly not ideal, but the selection of test sites was dictated by available access to power, shelter, and associated test equipment. Figures 6-10 through 6-13 show significant potential sources of scattering in the vicinity of the transmit and receive antennas. These scattering sources include a large metal tower almost in direct line-of-sight between the transmitter and fixed receiver, additional antennas, roof vents, and portions of metal buildings that could act as corner reflector-type objects.

7.5.2 Transmit Channels

The performance characteristics for all transmit channels were not identical, even though the channels were constructed of similar components. This was due to typical component tolerance values for manufactured devices. For example, the element patterns for all radiating elements were not identical, and the input-output characteristics for the amplifiers used in all 5 spatial channels were also not identical. As seen in Fig. 7-17, the output of one amplifier was clearly below the other channels. This was compensated for by adjusting the amplitude and phase of all channels at the input to the antenna feed. The antenna feed was also constructed of cables of similar design and length. However, the outputs of the channels did drift over time due to typical oscillator and component stability, and care was needed to keep measurement times down or to periodically re-calibrate the channels periodically.

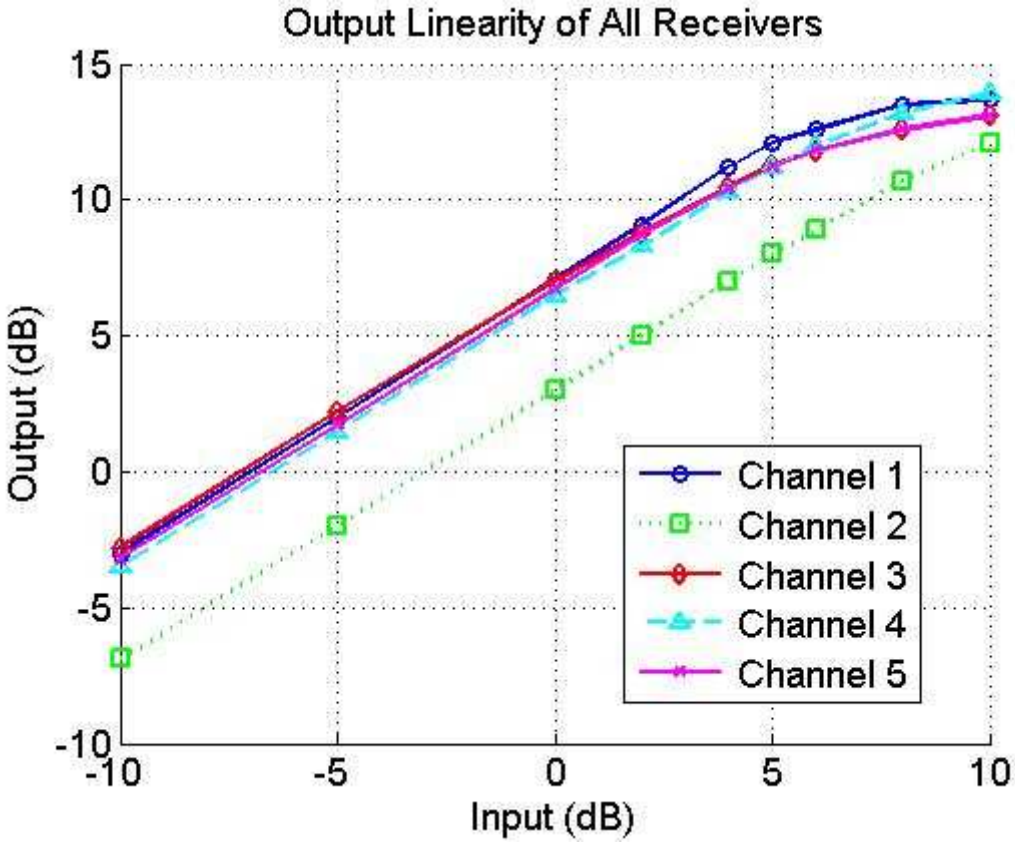

Fig. 7-17: Input-output characteristics for the amplifiers of all spatial channels

7.5.3 Receive Channels

The two receiver boards were constructed of similar components with typical manufacturing tolerance values, and the receivers were calibrated to a particular local oscillator input level. However, in practice a single LO was input simultaneously to both receive channels, so that neither channel was operating precisely at the design input level. However, the input levels were within approximately 1 dB of the design level.

Care was also taken to ensure that the cables from the antenna to the receiver for each channel were of similar electrical length. The delay over a length of cable is:

$$\tau = \frac{l}{c v_p} , \qquad (7\text{-}8)$$

where: l = length of cable

c = speed of propagation in free space

v_p = propagation factor

The propagation factor varies according to dielectric constant of the material of the cable, and is typically 0.66 for RG-214 coax of polyethylene dielectric. The delay over a 60 m length of cable is therefore approximately 303 ns. This delay does not have much of an impact for small Δf. For example, when Δf = 100 Hz, the period of the waveform is $1/\Delta f$ = 10 ms, and the delay due to the cable is about 0.003% of the waveform period. However, for the range variation experiments, where Δf = 2.5 MHz, the delay through the cable is nearly equal to the waveform period.

The lengths of cables from the antennas to the receiver channels were assembled from on-hand sections of stock components, and so therefore were not identical between channels. However, each section of cable was measured with a network analyzer to ensure that the cables on each receive channel were of similar electrical length, to within a few nanoseconds.

7.5.4 Processing

The data received by each channel were noisy signals modulated at a high frequency. Therefore, the signals were processed through a moving average window in order to estimate the location of the peak of each receive channel and the delay between channels. Slight variations of these estimated parameters were observed for different numbers of samples used in the filtering process.

7.5.5 Impact of Errors

The measurement and processing variations described in this section introduced some variation in the experimental results, but overall the sources of error did not affect the outcome of the experiments. The measured data agreed well with theoretical and simulated predictions.

7.6 Review of Assumptions

Several key assumptions were made during the theoretical development of the frequency diverse array, and it is worthwhile to recall these assumptions and discuss their implications.

7.6.1 Attenuation of the Signal

In (4-53) it was assumed that the attenuation constant, α, was zero. Also, in the plotting of (4-68), the decay of the electric field with range was ignored in order to emphasize the periodicity of the frequency diverse array pattern in range, angle, and time. In practice, the field will not propagate unabated, but the power in the transmitted signal will fall-off with range according to the inverse square law, and atmospheric effects will result in additional losses.

7.6.2 Uniform Weighting

In the development of (4-68), it was assumed that the weightings on all radiating elements were the same. This allowed the magnitude of the electric field to be computed in a simple closed form manner, resulting in a *sinc* function. In general, this is not required, and the electric field can be computed by brute force, or in some cases

also by closed form solution. The effect of non-uniform weighting would be similar to that for the conventional array, where the beam shape is altered to result in lower sidelobes, a broader mainbeam, and a loss in gain.

7.6.3 Element Patterns

The element patterns for all radiating sources were assumed to be identical in the summation of (4-54). In addition, the patterns' dependence on frequency was ignored. In practice, there will be some variation in these patterns due to manufacturing tolerances. Were the actual element patterns known, they could have been used to compute the electric field in a brute force manner. However, the effect of non-identical elements was reduced to some extent by the combination of multiple elements into a single spatial channel. This can be seen by the well-behaved pattern of Fig. 6-2. Also, the array column patterns and the element pattern for the centre element were measured over a frequency extent of 50 MHz. While the gain varied over that frequency extent by a couple of dB, the shape of the pattern in angle did not change appreciably, as illustrated in Fig. 7-18 for the centre column.

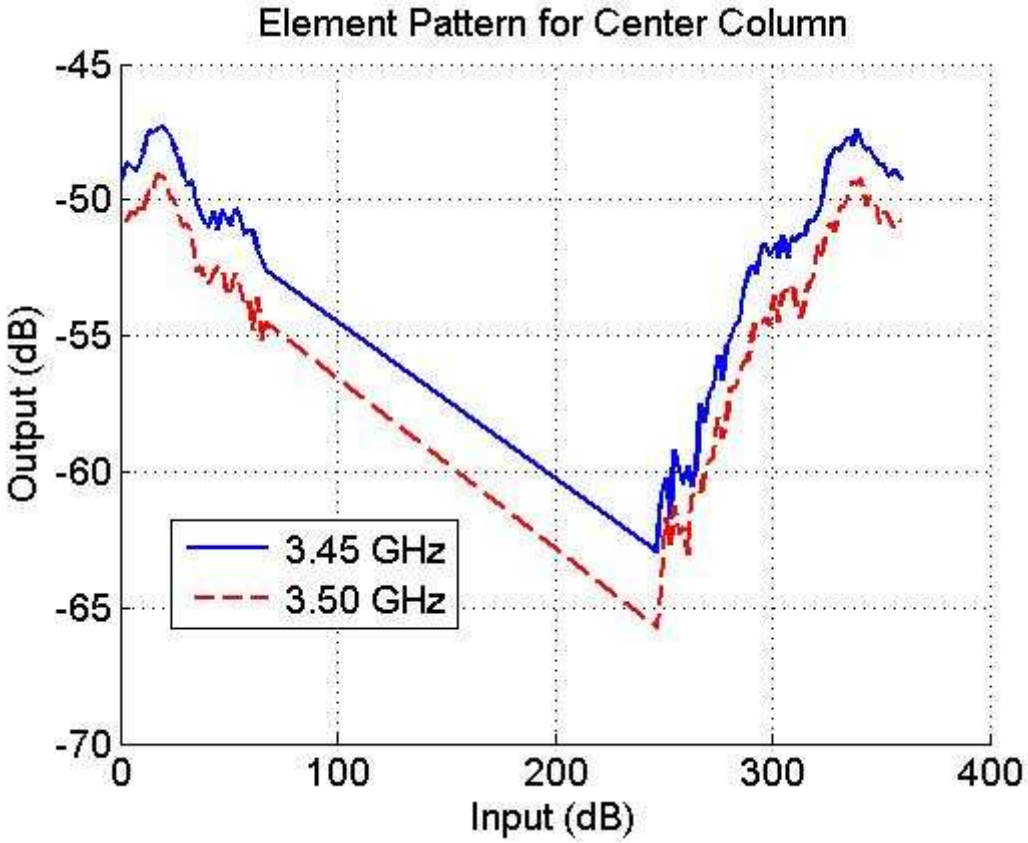

Fig. 7-18: Pattern of the centre column over 50 MHz

7.6.4 $f_0 >> n\Delta f$.

This is a fundamental assumption of the frequency diverse array. A common engineering rule of thumb is that this comparison operation implies two orders of magnitude difference in the quantities being compared. For a carrier frequency of 3.1 GHz and 5 spatial channels, this implies that Δf can be no more than about 6 MHz.

7.6.5 $R_0 >> nd \sin\theta$ **and** $t >> \frac{nd \sin\theta}{c}$**.**

These two conditions imply the same constraint, with $t = R_0/c$. The conditions imply that the range to a point in space must be much greater than the projected aperture length. This is generally true for points in the far-field of a typical array. However, this condition may not be true for widely spaced elements such as distributed systems with a wide baseline or for networked transmission systems.

Chapter 8

Conclusions and Future Work

8.1 Conclusions

This thesis describes a novel contribution for the design and control of antenna radiation patterns. This work is separate and distinct from previous contributions in this area, and has resulted in the award of two U.S. patents and one additional patent pending. In addition, the work performed under this research programme has generated significant interest within the radar community. The thesis developed the theory of the frequency diverse array, predicted its performance through simulation, and validated the theoretical and predicted performance through experimental measurements.

The frequency diverse array concept provides new dimensions of design freedom for beam forming and control. The approach considers the joint design of signals and antenna configuration to achieve unique beamforming characteristics. In the basic concept, a small incremental frequency shift is applied across spatial channels. This results in a radiation pattern that varies in angle with range. Moreover, the beam scans

in time without mechanical rotation or electronic phase shifters. This feature of the frequency diverse array pattern may result in an affordable scan option.

Another potential application for the frequency diverse array beam pattern is multipath mitigation. In addition to the direct path between the transmitter and receiver (communications) or transmitter-target-receiver (radar), transmitted signals often reflect off of natural and manmade objects, resulting in a dispersive received signal. The various signal components arrive from different ranges and angles, and it may be possible to suppress the unwanted reflections through a shaping of the beam pattern in range, angle, and time.

In large wideband arrays, the frequency diverse array concept may serve as an alternative to hardware-based true time delay techniques to compensate for pulse distortion effects of beam scan with frequency. In a similar manner, the frequency diverse array may have application to sonar, where the speed of propagation of transmitted signals results in a relatively wideband condition.

8.2 Extensions of the Work

This thesis discussed only the basic implementation of the frequency diverse array, which concerned continuous wave signals radiated from equally spaced identical elements. This concept can be extended to non-monochromatic waveforms.

8.2.1 Linear Frequency Modulation

In a linear frequency modulation (LFM) implementation, the frequency of each waveform varies linearly over the duration of a pulse. The transmitted waveform for each channel is identical, except for an element-to-element offset in the modulation starting frequency. Since the frequency offset is small compared to the modulation

bandwidth, there is considerable overlap in the frequencies used for all elements. In the narrowband case, the modulation bandwidth of each signal is on the order of tens of megahertz for typical radar frequencies, which is sufficient to support moving target indication (MTI) applications.

Fig. 8-1 illustrates modulation across spatial channels for an LFM implementation of a frequency diverse array. Signals received from all spatial channels are processed as in a conventional MTI application, and the frequency offset between channels provides range-dependent beamforming for flexible scanning and for multipath mitigation.

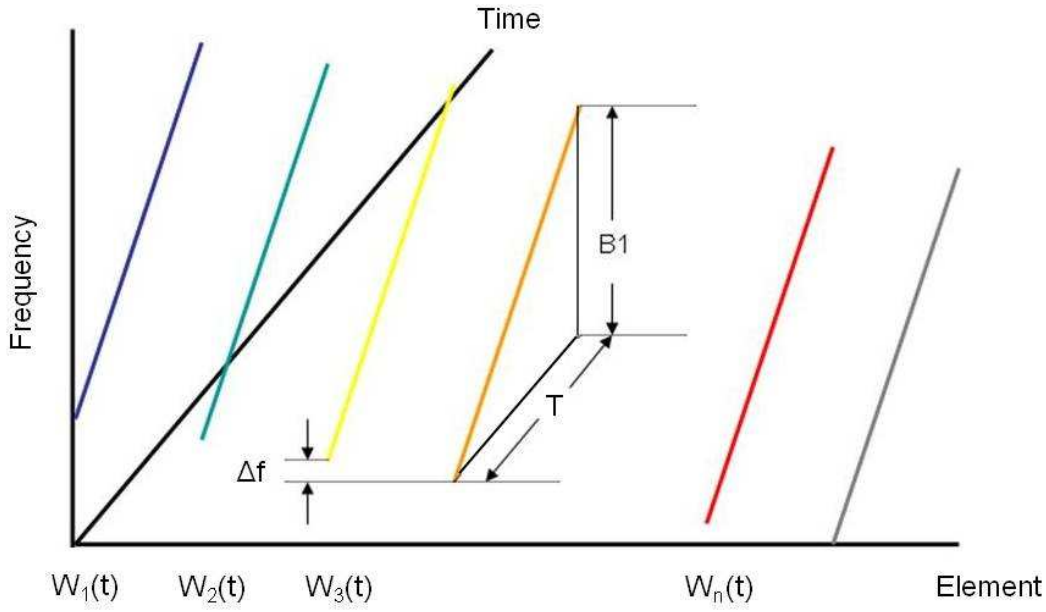

Fig. 8-1: LFM implementation of a frequency diverse array

A potential further extension may be implemented by utilizing contiguous and non-overlapping spectra on adjacent channels, as shown in Fig. 8-2. Using the contiguous bandwidth implementation, it may be possible to construct very large bandwidth signals, with each element radiating a non-overlapping segment of the entire frequency extent. Since all channels receive signals of each frequency, it may be possible to

construct N wideband receive signals of bandwidth NB, where N is the number of spatial channels and B is the bandwidth of each channel.

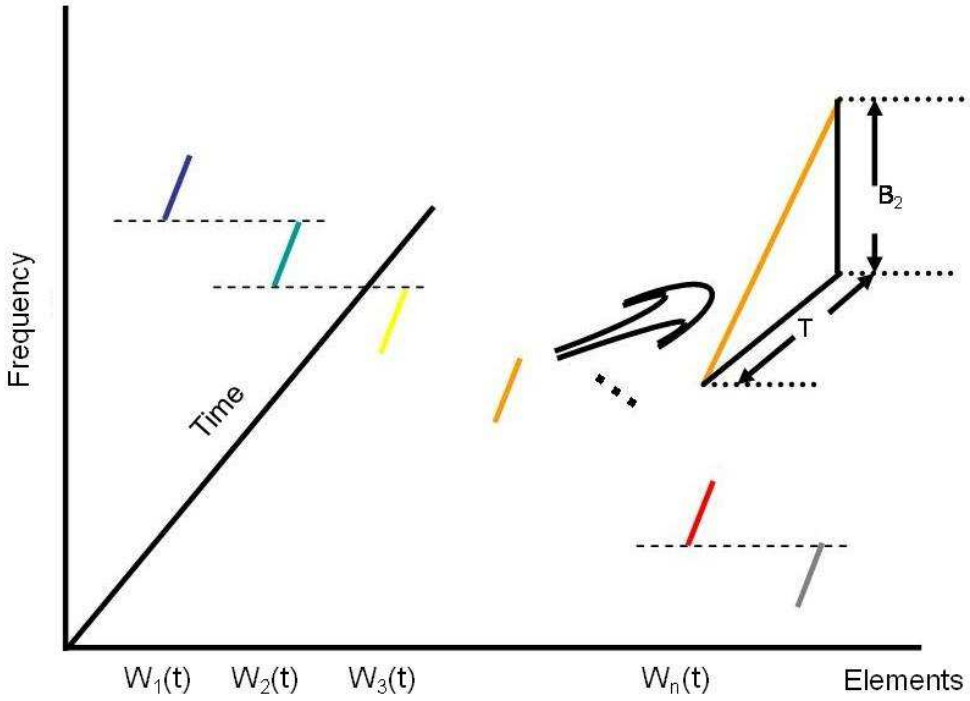

Fig. 8-2: Contiguous bandwidth implementation

8.2.2 Synthetic Aperture Radar

If each individual channel radiates a sufficiently wide-bandwidth signal, each spatial channel can act as a synthetic aperture radar (SAR). An architecture can therefore be proposed where the frequency diverse array serves as N SAR radars operating independently. Because the frequencies are non-overlapping, such an implementation has the potential to overcome the fundamental limitation of SAR, which is that small apertures are required for long coherent integration times and fine cross-range resolution, but which results in low gain on target.

In a typical SAR application, each element radiates a signal with a bandwidth on the order of hundreds of megahertz. This provides sufficient bandwidth for adequate range resolution for imaging purposes. At the same time, the cumulative bandwidth resulting from N elements (apertures) operating with non-overlapping frequencies provides much greater overall bandwidth for extremely high resolution SAR. The frequency diverse array implementation of SAR has the potential to place high gain on target while enabling a multitude of spotlight SARs to operate simultaneously, effectively resulting in stripmap and spotlight SAR modes at the same time.

8.2.3 Code Diversity

Besides linear frequency modulation, chirp diversity [104] may also be desired to manipulate the ambiguity diagram for rejection of interference or for target enhancement. Chirp diversity can easily be implemented within the framework of the generalized frequency diverse array. An example set of transmit signals for each channel is illustrated in Fig. 8-3.

Up- and down-chirp LFM signals provide some degree of orthogonality, but more elaborate coding schemes provide true orthogonality and may be required for some waveform diversity applications. Fig. 8-4 shows potential implementations of the frequency diverse array using random phase coded waveforms. Using advanced coding schemes, it may be possible to construct modes which enable ground moving target indication and synthetic aperture radar at the same time.

By exploiting multiple degrees of freedom, including space, time, frequency, and modulation, and by partitioning and combining the multi-dimensional space, it may be possible to construct waveforms which can support multiple missions at the same time. Potentially, traditional conflicts in timing and beam pointing for waveforms of different mission types can be avoided by parallel processing of data from multiple apertures

simultaneously, combined with range-dependent beamforming. Sophisticated code manipulation may also permit pulse-to-pulse phase modulation for ambiguity control and embedded communications. Fig. 8-5 illustrates the transmission and sorting of signals in multiple dimensions. The signals can potentially be sorted and processed for simultaneous synthetic aperture radar and ground moving target indication.

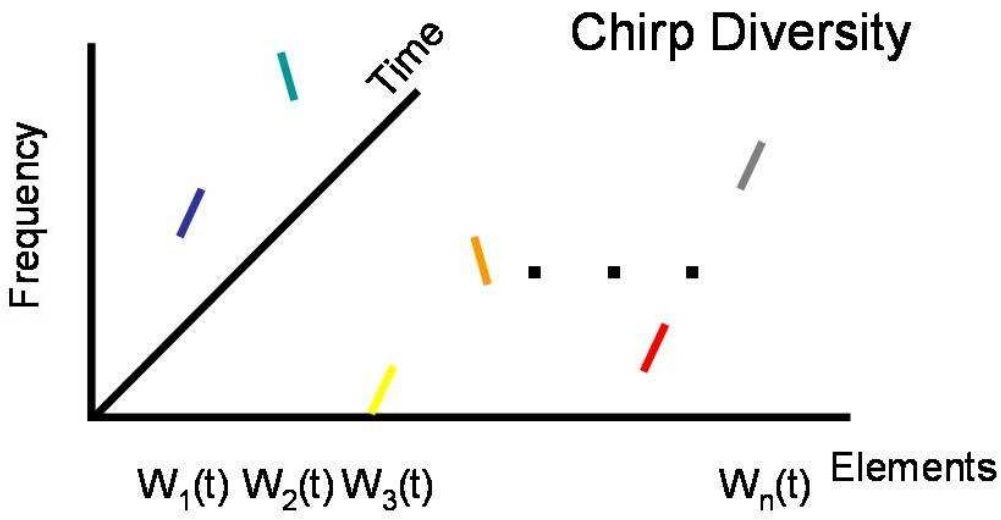

Fig. 8-3: Alternative implementations of the frequency diverse array

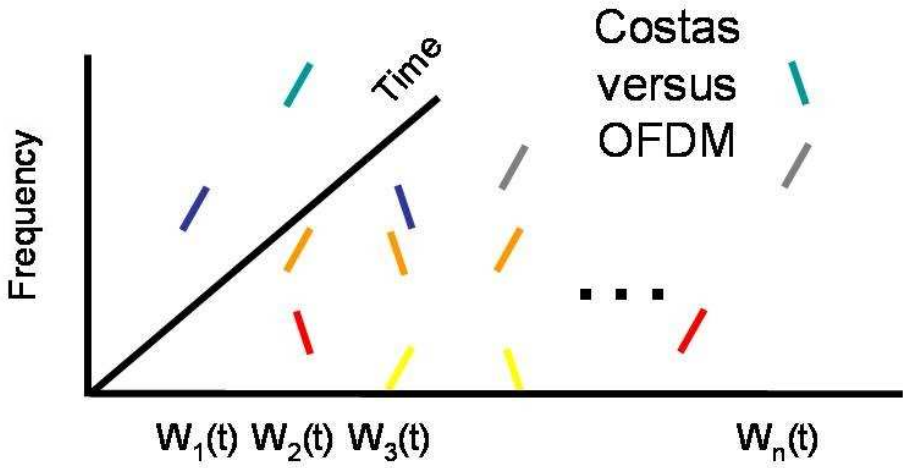

Fig. 8-4: Random phase coded waveform implementation for orthogonal signals

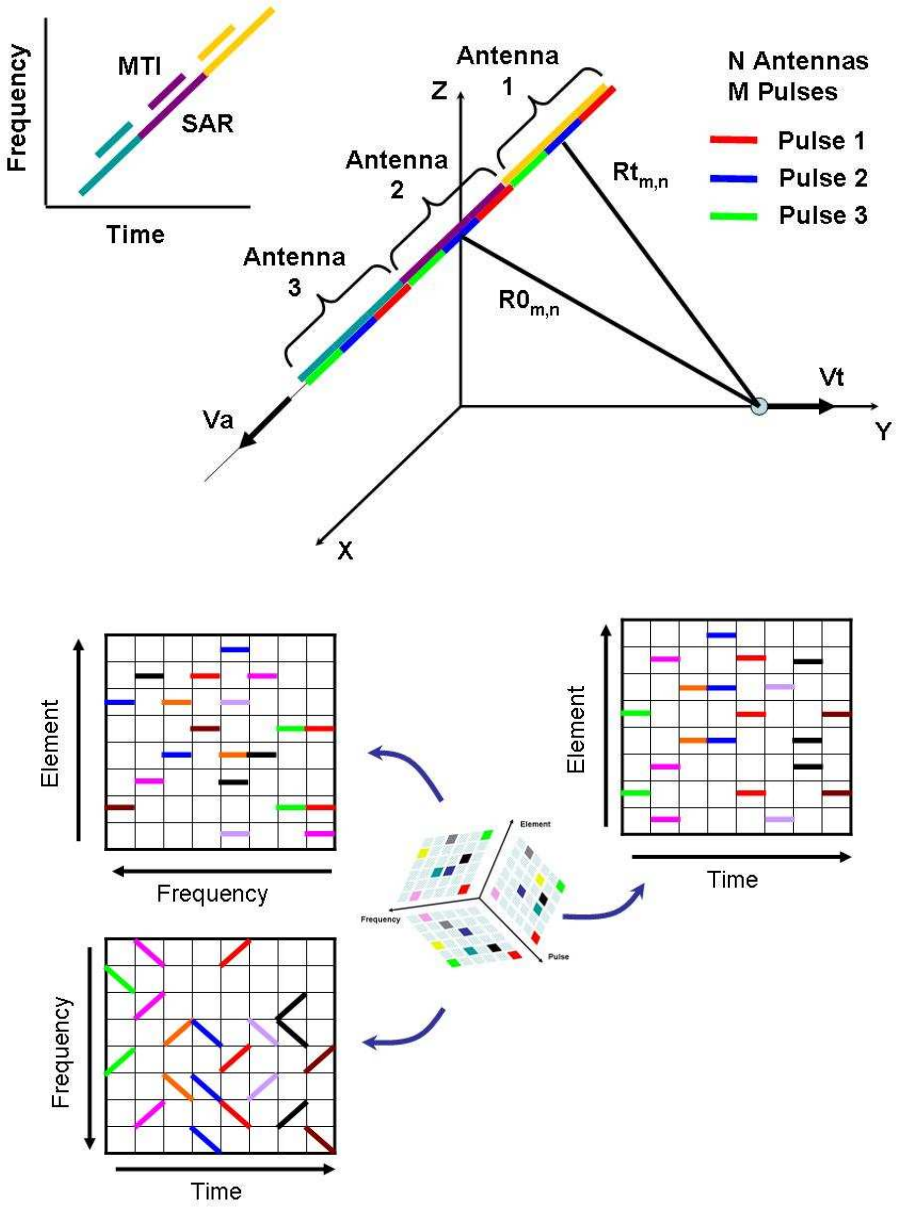

A

Fig. 8-5: Transmission and sorting of signals for simultaneous SAR and GMTI

8.3 Suggestions for Further Research

The basic implementation of the frequency diverse array was developed using the monochromatic assumption and equally spaced elements. As described in the previous section, many more fertile areas for exploration remain. In particular, the following is a partial list of additional promising research topics:

8.3.1 Amplitude Weighting

This research was primarily conducted utilizing a uniformly illuminated array. However, a weighted array was also constructed using Schelkunoff polynomials in order to demonstrate a frequency diverse array difference pattern.

Consider the N-element array of Figure 8-6. Similar to Section 3.1 the electric field for the conventional array can be written as:

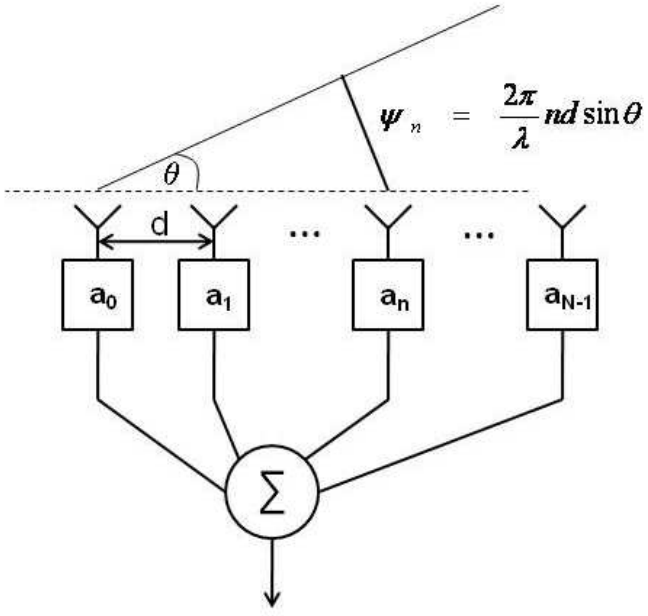

Figure 8-6: Weighted array

$$E = E_0 e^{j\omega t} \sum_{n=0}^{N-1} a_n e^{-jn\varphi}, \tag{8-1}$$

where: $$\varphi = \frac{2\pi}{\lambda} d \sin\theta. \tag{8-2}$$

Ignoring the carrier and letting

$$z = e^{-j\varphi}, \tag{8-3}$$

Equation (8-1) can be written as a polynomial:

$$E(z) = a_0 + a_1 z + a_2 z^2 + \cdots + a_{N-1} z^{N-1}, \text{ and} \tag{8-4}$$

$$E(z) = (z - z_1)(z - z_2)\cdots(z - z_{N-1}). \tag{8-5}$$

To place a single null at θ = 0, let $\theta_n = 0$ for all z_n:

$$z_n = z(\theta_n) = e^{-j\frac{2\pi}{\lambda} nd \sin\theta_n} = e^{j0} = 1. \tag{8-6}$$

For a 5-element array, the resulting polynomial is:

$$E(z) = (z-1)^4 \tag{8-7}$$

$$= 1 - 4z + 6z^2 - 4z^3 + z^4. \tag{8-8}$$

The weights to produce this difference pattern are therefore:

$$a_0 = 1 \quad (8\text{-}9)$$

$$a_1 = -4 \quad (8\text{-}10)$$

$$a_2 = 6 \quad (8\text{-}11)$$

$$a_3 = -4 \quad (8\text{-}12)$$

$$a_4 = 1. \quad (8\text{-}13)$$

A similar construction can be made for the frequency diverse array with

$$E = E_0 \, e^{j(\omega_0 t - k_0 R_0)} \sum_{n=0}^{N-1} a_n \, e^{-jn\varphi'} \,, \quad (8\text{-}14)$$

$$\varphi' = \Delta\omega t + k_0 d \sin\theta - \Delta k R_0 + \Delta k d \sin\theta \text{, and} \quad (8\text{-}15)$$

$$z = e^{-j\varphi'}. \quad (8\text{-}16)$$

The weights of (8-9) through (8-13) were applied to the frequency diverse array of Section 6.2.1, with Δf = 100 Hz, resulting in the close-range waveform of Figure 8-7. Notice that the difference pattern was produced with the periodicity of the frequency diverse array (period = 10 ms).

A difference pattern combined with the auto-scanning property of the frequency diverse array may be a useful feature for the rejection of multipath interference, and should be studied further. Other weightings can also be explored for spatial and time sidelobe control of the frequency diverse array pattern.

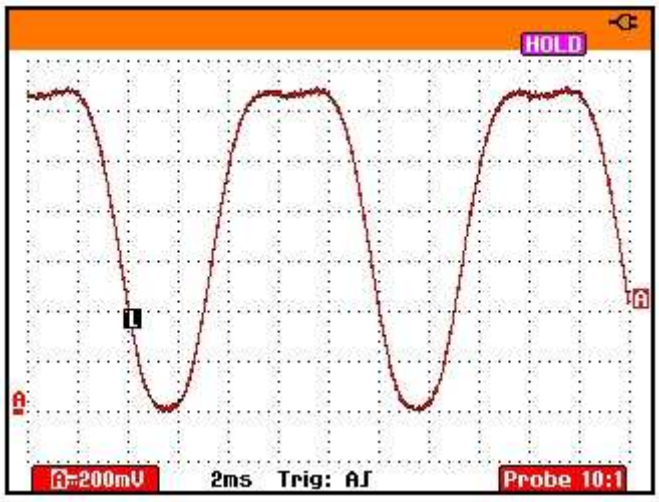

Figure 8-7: Close-range time waveform for FDA difference pattern, Δf = 100 Hz

8.3.2 Generalized Array Structure

This thesis concentrated on a frequency diverse array under the monochromatic assumption with constant frequency offset and equal element spacing. A number of generalizations of this concept are possible and should also be explored.

The traditional phased array has no frequency shift from element-to-element. In this thesis, a constant frequency offset was applied between elements. However, other implementations are also possible. The frequency offset can be allowed to vary as a function of time, using both linear and non-linear frequency modulations as shown in Figure 8-8. A time-varying frequency offset may further alter the structure of the frequency diverse array pattern and should be investigated.

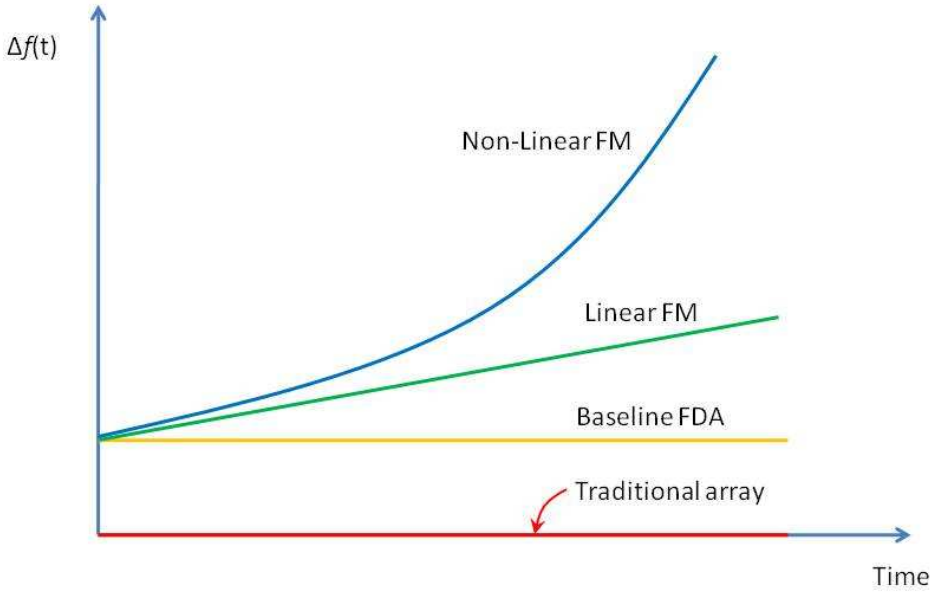

Figure 8-8: Time-varying frequency offset for ith element

Further control over the frequency diverse array pattern can be achieved through the use of non-linearly spaced elements. Sammartino and Baker [75] formed a version of the frequency diverse array called the wavelength array. Using non-linearly spaced elements, the wavelength array provides reduced dependence of range gain on angle gain, resulting in additional control of the radiated pattern.

In general, the basic waveform per element per unit time can be expressed as:

$$s_{ij} = A_{ij}\, \phi_{ij}\, f_{ij}\, e^{j\omega t}, \tag{8-17}$$

where:

A_{ij}	=	Amplitude modulation function
φ_{ij}	=	Phase modulation function
f_{ij}	=	Frequency modulation function
i	=	Element number
j	=	Pulse number.

The amplitude, phase, and frequency modulation functions can be combined to obtain:

$$s_{ij} = M_{ij} e^{j\omega t}, \quad (8\text{-}18)$$

where M_{ij} is the space-time modulation matrix. In general, M_{ij} is a function of amplitude, frequency, phase, time, and polarization.

The modulation in space (element) is conventionally a phase progression for beam steering. In time the modulation is typically LFM intra-pulse and phase modulation pulse-to-pulse. However, in general the modulation may be more flexible. Recall that (8-18) represents the basic waveform, or transmission chip, at each element per unit time. These can be constructed as elemental bases functions which can be summed and processed in various combinations as described in Section 8.2 such that the space-time waveform has a particular property. It may not be necessary for the bases functions to form a complete orthonormal set.

Channels with small frequency offset, highly overlapped spectra, moderate bandwidth, and linear frequency modulation chips may support moving target indication with frequency diverse array characteristics, such as auto-scanning and range-dependent beamforming. Pseudo random and orthogonal codes may enable a more generalized frequency diverse array architecture, enabling simultaneous multi-mission operation such as radar and communications or SAR simultaneous with GMTI.

Figure 8-9 illustrates potential transmission sequences for both conventional and frequency diverse array MTI and SAR functions. MTI requires relatively narrow bandwidth, while the SAR function requires much greater bandwidth for improved range resolution. The performance of MTI and SAR as a function of bandwidth is illustrated graphically in Figure 8-10. SAR performance improves with bandwidth,

while MTI performance degrades due to range and Doppler walk and super-resolution of targets.

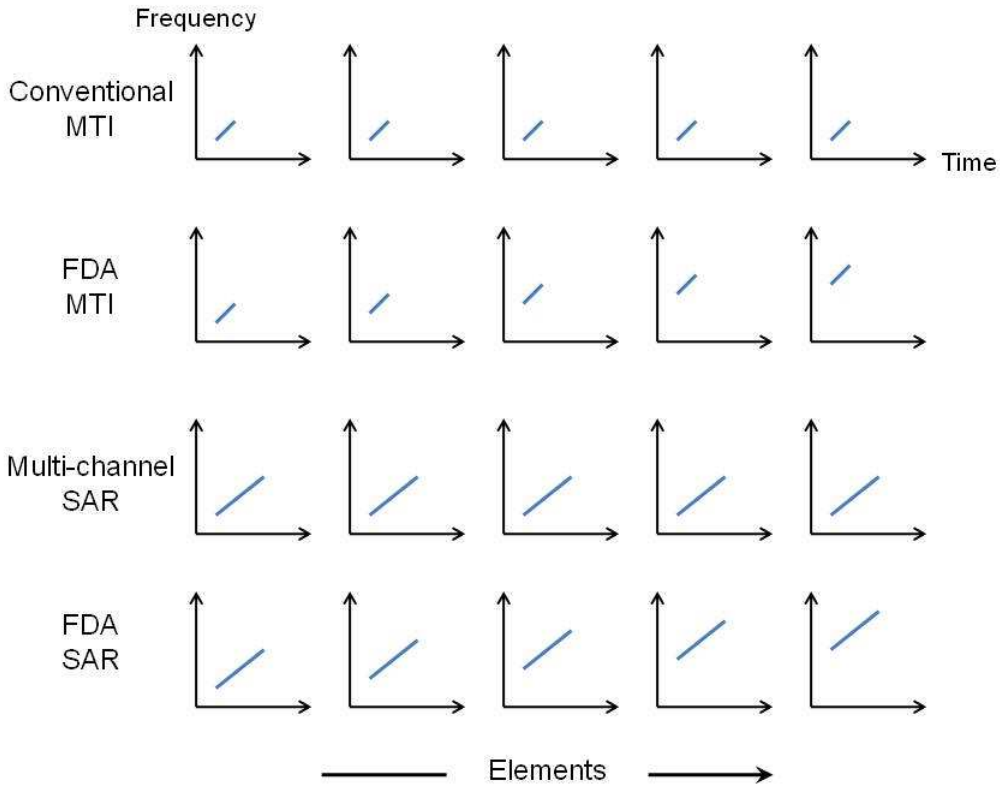

Figure 8-9: Transmission sequences for conventional and FDA MTI and SAR

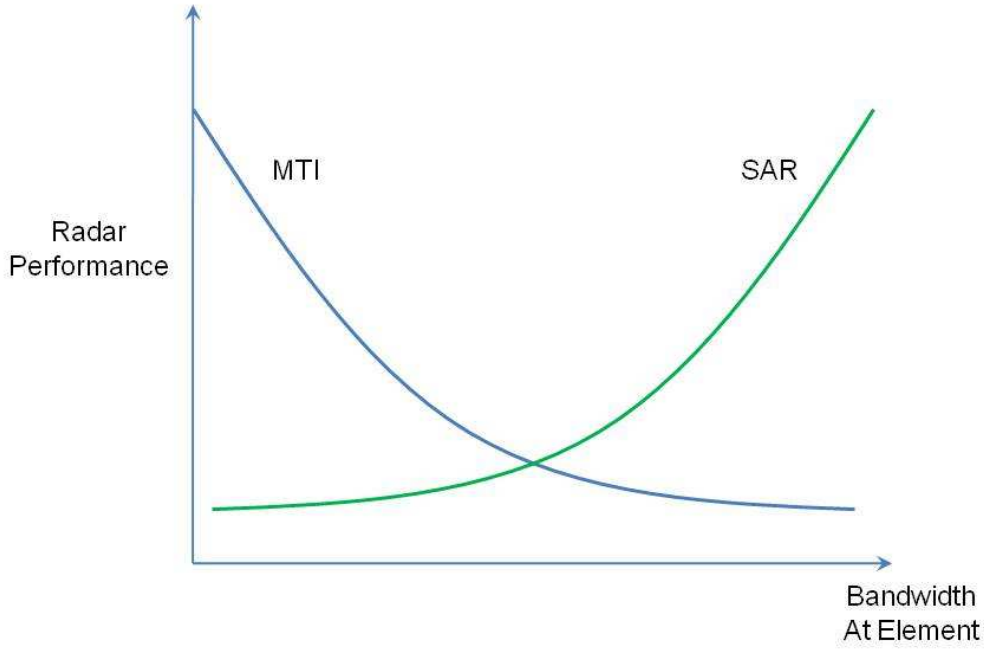

Figure 8-10: SAR and MTI performance as a function of bandwidth per element

Figure 8-11 illustrates a scheme to utilize both time-sequenced and simultaneous transmissions. The figure shows frequency as a function of time for two elements. For a portion of the transmission sequence both elements radiate simultaneously. This overlap produces a phased array effect.

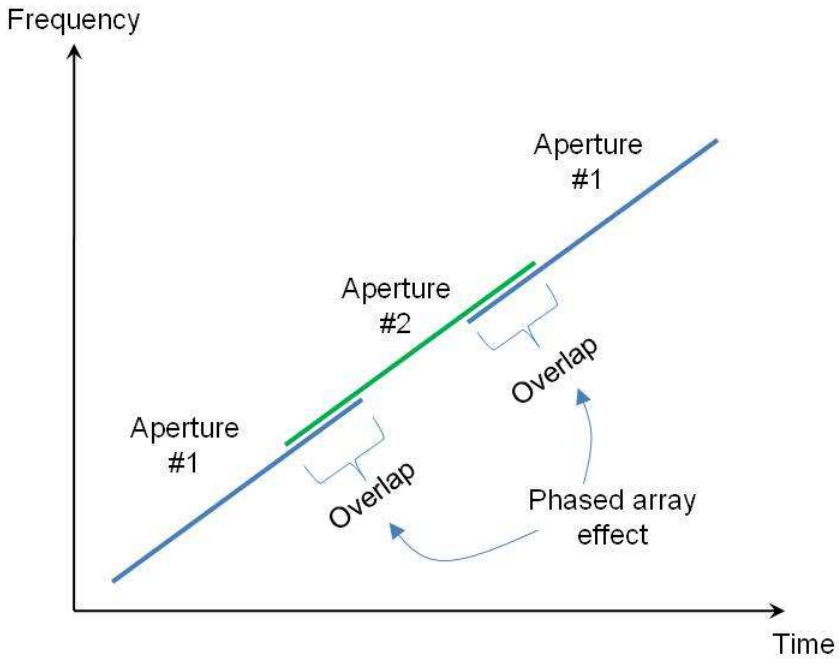

Figure 8-11: Overlapping transmissions producing both sequential and simultaneous modulation

A generalized frequency diverse array architecture, particularly for simultaneous multi-mission, multi-mode operation, will require schemes to select transmission chips and sort and process signals, both jointly and separately. The selection of the space-time modulation matrix must ensure stable beams in the radiation pattern. This is an exciting area for further investigation. Transmission selection schemes may include closed form algorithms, enumeration, or approaches such as genetic algorithms. The space-time transmission sequence should be investigated as a synthesis problem. Techniques for processing the complex transmitted waveforms should also be investigated. Interpolation, extrapolation, and pulse stitching techniques can be applied to contend with operation in a dense electromagnetic environment and electromagnetic interference. Pulse stitching and signal extrapolation are illustrated in Figures 8-12 and 8-13 respectively. Note that the basic frequency diverse array concept is a sparse frequency, thinned spectrum approach as depicted in Figure 4-5. Further work is also required in the development of optimal receivers for these transmission sequences.

Note that the configuration of the optimal receiver may vary as function of location due to properties of the frequency diverse array. The generalized architecture will also enable the use of space-time adaptive processing techniques to suppress interference and enhance target responses.

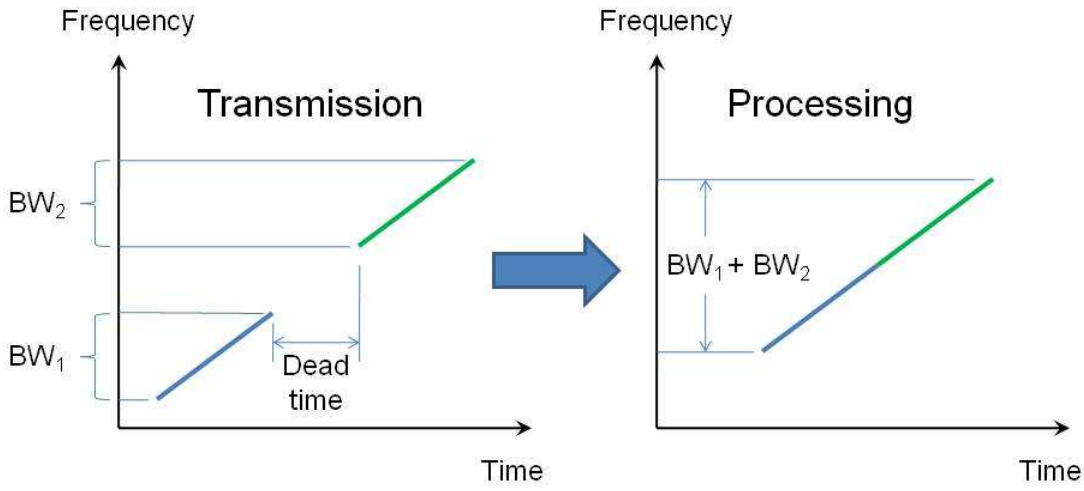

Figure 8-12: Pulse stitching

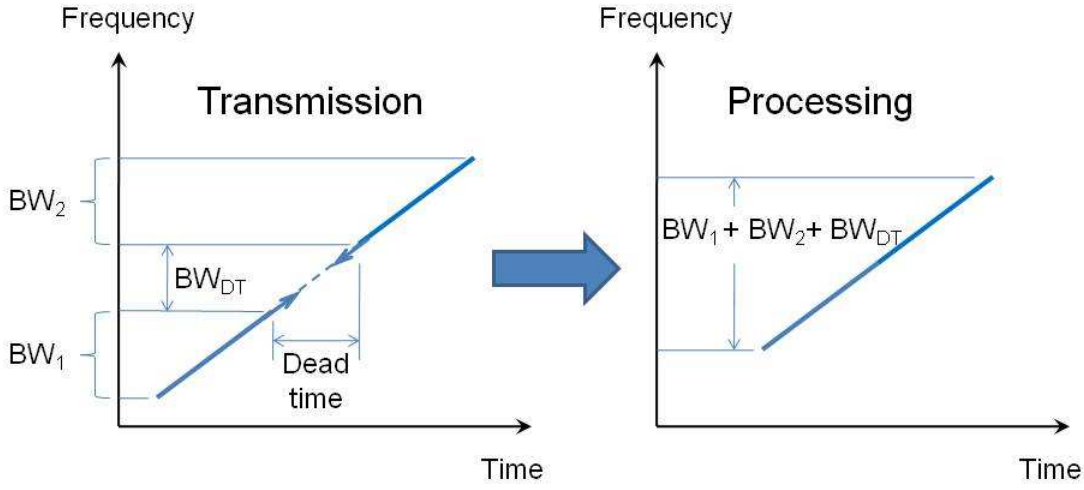

Figure 8-13: Extrapolation of transmitted signals

References

1. A.R. Kaye and D.A. George, “Transmission of multiplexed PAM signals over multiple channel and diversity systems”, *IEEE Trans. Comm.*, vol. 18, issue 5, pp. 520-526, Oct. 1970.
2. W. Van Etten, “An optimum linear receiver for multiple channel digital transmission systems “, *IEEE Trans. Comm.*, vol. 23, issue 8, pp. 828-834, Aug. 1975.
3. J.H. Winters, "Optimum combining in digital mobile radio with cochannel interference,*" IEEE J. Sel. Areas Comm.*, vol. 2, issue 4, pp. 528-539, Jul. 1984.
4. J.H. Winters, "Optimum combining in digital mobile radio with cochannel interference," *IEEE Trans. Veh. Tech.*, vol. 33, issue 3, pp. 144-155, Aug. 1984.
5. J.H. Winters, "On the capacity of radio communications systems with diversity in a Rayleigh fading environment," *IEEE J. Sel. Areas Comm.*, vol. 5, issue 5, pp. 871-878, Jun. 1987.
6. J.H. Winters, "Optimum combining for indoor radio systems with multiple users," *IEEE Trans. Comm.*, vol. 35, issue 11, pp. 1222-1230, Nov. 1987.
7. Gerard J. Foschini, "Layered space-time architecture for wireless communications in a fading environment when using multi-element antennas", *Bell Labs Technical Journal* 1 (2), pp. 41–59, Oct. 1996.

8. Gerard J. Foschini and Michael. J. Gans, "On limits of wireless communications in a fading environment when using multiple antennas", *Wireless Personal Communications* 6 (3): 311–335, Jan. 1998.
9. I. E. Telatar "Capacity of multi-antenna Gaussian channels". *European Trans. on Telecommunications* , 10, pp: 585-595, Nov. 1999.
10. E. Fishler, A. Haimovich, R. Blum, L. Ciminio, D. Chizhik, R. Valenzuela, "MIMO radar: An idea whose time has come", *Proc. 2004 IEEE Radar Conf.*, pp. 71-78, Philadelphia, PA, 26-29 April 2004.
11. F. Robey, S. Coutts, D. Weikle, J. McHarg, K. Cuomo, "MIMO radar theory and experimental results", *Proc. 38th Asilomar Conf. on Signals, Systems and Computers*, 2004.
12. Jian Li, "MIMO Radar - Diversity Means Superiority", Annual Report, Nov 2006 – Oct 2007, Grant No. N00014-07-1-0293, ADA47396525, Oct 2007. http://www.dtic.mil/cgi-bin/GetTRDoc?AD=ADA473965&Location=U2&doc=GetTRDoc.pdf, Accessed 27 Feb 2009.
13. Haidong Yan, Jun Li, and Guisheng Liao, "Multitarget Identification and Localization Using Bistatic MIMO Radar Systems", *EURASIP J. on Advances in Sig. Proc.*, vol. 8, issue 1, Art. No. 7, Jan. 2008.
14. P.K. Bondyopadhyay, "The first application of array antenna", *Proc. 2000 IEEE Intl. Conf. on Phased Array Systems and Technology*, pp. 29-32, 21-25 May 2000.
15. J. Mitchell, H.D. Griffiths, and I. Boyd, "Sir John Ambrose Fleming – His involvement in the development of wireless", Chap. 10 of History of Wireless, T. Sarkar et al. (eds.), Wiley Interscience, 2006.
16. M.I. Skolnik, Introduction to Radar Systems, 2nd Ed., McGraw-Hill Book Co., pp. 278-279, 1980.
17. M.I. Skolnik, "Survey of phased array accomplishments and requirements for navy ships", in Phased Array Antennas, A.A. Oliner and G.H. Knittel (eds.), Artech House, pp. 15-20, 1972.

18. T.S. Bird, "Going strong after 50 years: antenna R&D at the C SIRO division of radiophysics", *IEEE Ant. and Prop. Magazine*, vol. 35, issue 2, pp. 39-48, April 1993.
19. R.E. Franks, "Direction-Finding Antennas", Chap. 25 of Antenna Handbook: Theory, Applications, and Design, Y.T. Lo and S.W. Lee (ed.),Van Nostrand Reinhold Co, pp. 25-21 – 25-23, 1988.
20. T.A. Pauls, "Origins of sparse aperture imaging", *Proc. 2001 IEEE Aerospace Conf.*, Vol. 3, pp. 3/1421-3/1427, 10-17 March 2001.
21. J.S. Hey, The Evolution of Radio Astronomy, Science History Publications, 1973.
22. G.W. Swenson and N.C. Mathur, "The interferometer in radio astronomy", *Proc. IEEE*, vol. 56, issue 12, pp. 2114-2130, Dec. 1968.
23. L.C. Graham, "Synthetic interferometer radar for topographic mapping", *Proc. IEEE*, vol. 62, issue 6, pp. 763-768, June 1974.
24. J.D. O'Brien and D.N. Held, "Topographic mapping using a Ku-band airborne elevation interferometer", *Proc. IEEE 1992 Nat. Aero. & Elec. Conf.*, vol. 1, 18-22, pp. 244-249, May 1992.
25. E. Rodriguez and J.M. Martin, "Theory and design of interferometric synthetic aperture radars", *IEE Proc. F Radar and Sig. Proc.*, vol. 139, issue 2, pp. 147-159, April 1992.
26. P.A. Rosen, "Developments in repeat pass interferometric radar for Earth and planetary sciences", *Proc. IEEE 2004 Radar Conf.*, pp. 207-211, 26-29 April 2004.
27. H.D. Griffiths, C.J. Baker, A. Currie, R. Voles, R. Bullock, P.V. Brennan, "Aircraft-borne interferometric SAR for 3-D high resolution radar imaging", *IEE Colloquium on Radar and Microwave Imaging*, pp. 3/1 – 3/4.16, Nov. 1994.
28. P. Antonik, R. Bonneau, R. Brown, S. Ertan, V. Vannicola, D. Weiner, M. Wicks, "Bistatic radar denial/embedded communications via waveform diversity", *Proc. 2001 IEEE Radar Conf.*, pp. 41-45, 1-3 May 2001.
29. H.D. Griffiths, Bistatic denial using spatial-temporal coding, Final Technical Report, AFRL-SN-RS-TR-2001-28, March 2001.

30. H.D. Griffiths, M.C. Wicks, D. Weiner, R. Adve, P. Antonik, I. Fotinopoulos, "Denial of bistatic hosting by spatial-temporal waveform design", *IEE Proc. Radar, Sonar, and Nav*., vol. 152, issue 2, pp. 81-888, April 2005.
31. T.C. Cheston and J. Frank, "Array Antennas", Chap. 11 of Radar Handbook, M.I. Skolnik (ed.), McGraw-Hill, 1970.
32. J. Frank, "Bandwidth criteria for phased array antennas", in Phased Array Antennas, A.A. Oliner & G.H. Knittel, Artech House, pp. 243-253, 1972.
33. J.S. Ajoika & J.L. McFarland, "Beam Forming Feeds", Chap. 19 of Antenna Handbook: Theory, Applications, and Design, Y.T. Lo and S.W. Lee (eds.), Van Nostrand, pp. 19-7 – 19-8, 1988.
34. R. Tang, "Survey of Time Delay Beam Steering Techniques", in Phased Array Antennas, A.A. Oliner & G.H. Knittel, Artech House, pp. 254-260, 1972.
35. W.B. Adams, "The broad-band signal response of a phase-steered linear receiving array", *Proc. IEEE*, vol. 52, issue 1, p. 106, Jan 1964.
36. A.K. Agrawai, E. L. Williamson, J.G. Ferrante, "Design criteria for wideband active phased array antennas", *1997 Digest Ant. Prop. Soc. Intl. Symp*., vol. 2, pp. 714-717, 13-18 July 1997.
37. I.W. Hammer, "Frequency-scanned arrays", Chap. 13 of Radar Handbook, M.I. Skolnik (ed.), McGraw-Hill, 1970.
38. A.F. Stevenson, "Theory of slots in rectangular waveguides", *J. Appl. Phys*.,19, pp. 24-38, 1948.
39. J. Spradley, "A volumetric electrically scanned two-dimensional microwave antenna array", *IRE Intl. Conv. Rec*., vol. 6, pt. 1, pp. 204-212, Mar. 1958.
40. A. Ishimaru and H.-S. Tuan, "Theory of frequency scanning of antennas", *IRE Trans. Ant. and Prop*., pp. 144-150, March 1962.
41. K. Milne, "The combination of pulse compression with frequency scanning for three-dimensional radars", *J. Brit. IRE*, 28, (6), pp. 89-106, Aug. 1964.
42. G. Minkler and J. Minkler, CFAR: the principles of automatic radar detection in clutter, Magellan Book Co., Baltimore MD, 1990.

43. W.M. Siebert, “Some applications of detection theory to radar”, *IRE Natl. Conv. Rec.*, vol. 6, pt. 6, pp. 5-14, 1958.
44. S. Applebaum, “Adaptive arrays,” *IEEE Trans. Antennas and Propagation*, vol. 25, issue 5, pp. 585-598, Sep. 1976.
45. L. Brennan and I. Reed , “Theory of adaptive radar,” *IEEE Trans. Aerospace and Electronics Systems*, vol. AES-9, no. 2, pp. 237-252, Mar. 1973.
46. P. Antonik, H. Schuman, P. Li, W. Melvin, and M. Wicks, “Knowledge-Based Space-Time Adaptive Processing”, *Proc. 1997 National Radar Conference*, Syracuse NY, 1997.
47. C. T. Capraro, G. T. Capraro, D. D. Weiner, and M. C. Wicks, “Knowledge Based Map Space-Time Adaptive Processing (KBMapSTAP)”, *Proc. 2001 Intl. Conf. on Imaging Science, Systems, and Technology*, Las Vegas NV, 2001.
48. W. Baldygo, M. Wicks, R. Brown, P. Antonik, G. Capraro, and L. Hennington , “Artificial Intelligence Applications to Constant False Alarm Rate (CFAR) Processing,” *Proc. 1993 National Radar Conference*, Boston MA.
49. C. Morgan and L. Moyer, Knowledge Base Applications to Adaptive Space-Time Processing, Vol. IV: Knowledge-Based Tracking, USAF Res. Lab., Rome, NY Rep. AFRL-SN-RS-TR-2001-146 (IV), 2001, vol. IV.
50. C. Morgan and L. Moyer, Knowledge Base Applications to Adaptive Space-Time Processing, Vol. V: Knowledge-Based Tracker Rule Book, USAF Res. Lab., Rome, NY Rep. AFRL-SN-RS-TR-2001-146 (V), 2001, vol. V.
51. R. H. Dicke, “Object detection systems”, U.S. Patent No. 2,624,876, 6 Jan. 1953.
52. R. Manasse, “The use of pulse coding to discriminate against clutter,” M.I.T. Lincoln Lab., Lexington, MA, Group Rept. 312-12, June 1961.
53. S. Sussman, “Least-square synthesis of radar ambiguity functions, ” *IEEE Trans. Information Theory* vol. 8, issue 3, pp. 246-254, Apr. 1962.
54. L. J. Spafford, “Optimum radar receive waveforms in the presence of clutter,” M.S. thesis, Polytechnic Institute of Brooklyn, Brooklyn, N.Y., June 1965.

55. H. L. Van Trees, “Optimum signal design and processing for reverberation-limited environments, ” *IEEE Trans.Military Electronics,* vol. MIL-9, issues 3-4, pp. 212-229, Jul.-Oct. 1965.
56. M. Ares, “Optimum burst waveforms for detection of targets in uniform range-extended clutter”, *IEEE Trans. Aerospace and Elec. Sys*., vol. AES-3, pp. 138-141, Jan. 1967.
57. W. D. Rummier , “Clutter suppression by complex weighting of coherent pulse trains”, *IEEE Trans. Aerospace and Electronics Systems*, vol. AES-2, pp. 689-699, Nov. 1966.
58. D. DeLong and E. Hofstetter , “On the design of optimum radar waveforms for clutter rejection”, *IEEE Trans. Information Theory*, vol. 13, issue 3, pp. 454 – 463, Jul. 1967.
59. C. E. Cook and M. Bernfeld, Radar signals: an introduction to theory and application, New York, NY, Academic Press, 1967.
60. C. A. Stutt and L. J. Spafford , “A ‘best’ mismatched filter response for radar clutter discrimination”, *IEEE Trans. Information Theory*, vol. IT-14, no. 2, pp. 280–287, Mar. 1968.
61. T. K. Sarkar, M. C. Wicks, M. Salazar-Palma, and R. J. Bonneau, Smart Antennas. Hoboken, NJ; John Wiley & Sons, 2003, p. 57.
62. G. Ross et al, “Transient behaviour of microwave networks”, USAF Rome Air Dev. Ctr. Rept. TR-69-78, 1969.
63. C. Bennett, J. Delorenzo, and A. Auckenthaler, ”Integral equation approach to wideband inverse scattering,” USAF Rome Air Dev. Ctr. Rept. TR-70-177, 1970.
64. V. Martins and J. Van Meter, “Signal processing of impulse excited objects in space,” USAF Rome Air Dev. Ctr. Rept. TR-72-347, 1973.
65. P. Van Etten, “Temporal-Spatial Compression Antennas”, USAF Rome Air Dev. Ctr., Rome, NY Rep. RADC-TR-73-179, 1973.
66. P. Van Etten, “Polarization radar method and system,” U.S. Patent 4 053 882, October 11, 1977.

67. M. C. Wicks and P. V. Etten, “Orthogonally polarized quadraphase electromagnetic radiator”, U.S. Patent 5 068 671, November 26, 1991.
68. J. R. Guerci and P. Grieve, “Optimum matched illumination waveform design process”, U.S. Patent 5 121 125, June 9, 1992.
69. P. G. Grieve and J. R. Guerci, “Optimum matched illumination-reception radars”, U.S. Patent 5 175 552, December 29, 1992.
70. S.U. Pillai, H. S. Oh, D. C. Youla, and J. Guerci , “Optimum transmit-receiver design in the presence of signal-dependent interference and channel noise,” *IEEE Trans. Information Theory*, vol. 46, no. 2, pp. 577–584, Mar. 2000.
71. D. A. Garren, M. K. Osborn, A. C. Odom, J. S. Goldstein, S. U. Pillai, and J. Guerci, “Enhanced target detection and identification via optimized radar transmission pulse shape”, *Proc. Inst. Elect. Eng., Radar, Sonar, Navigation*, vol. 148, no. 3, pp. 130-138, Jun. 2001.
72. R. Adve, R. Schneible, R. McMillan, “Adaptive space/frequency processing for distributed aperture radars”, *Proc. 2003 IEEE Radar Conference*, pp. 160-164, 2003.
73. R. S. Adve, R. A. Schneible, G. Genello, P. Antonik, “Waveform-space-time adaptive processing for distributed aperture radars”, *Proc.2005 IEEE Intl. Radar Conference*, pp. 93-97, 2005.
74. P. F. Sammartino, C.J. Baker, and H.D. Griffiths, “A comparison of algorithms for MIMO and netted radar systems”, *Proc. 2nd International Waveform Diversity & Design Conference*, Lihue, HI, 2006.
75. P. F. Sammartino and C. Baker, “The frequency diverse bistatic system”, *Proc. 4th Intl. Waveform Diversity & Design Conf.*, Orlando, FL, 8-13 Feb. 2009.
76. M.C. Wicks, B. Himed, J.L.E. Bracken, H. Bascom, J. Clancy, “Ultra narrow band adaptive tomographic radar”, *Proc. IEEE 2005 1st Intl. Workshop on Computational Adv. In Multi-Sensor Adaptive Proc.*, pp. 36-39, 13-15 Dec. 2005.
77. IEEE Standard Radar Definitions, IEEE Std 686-2008, 26 March 2008.
78. G.E. Moore, “Cramming more components onto integrated circuits”, *Electronics*, vol. 38, no. 8, 19 April 1965.

79. R.R. Schaller, “Moore’s law: past, present and future”, *IEEE Spectrum*, Vol. 34, Issue 6, June 1997, pp. 52-59.
80. J.R. Powell, “The quantum limit to Moore’s Law”, *Proc. IEEE*, Vol. 96, Issue 8, Aug. 2008, pp. 1247-1248.
81. E. Sperling, “The next phase of Moore’s Law”, http://www.forbes.com/2008/06/09/ibm-moores-law-tech-cionetwork-cx_es_0609ibm.html, 9 June 2008, 1800 ET, accessed 4 Mar. 2009.
82. J. Osa, R. Castello, J. Radulovich, B. Gillcrist, C. Finocchiaro, “Distributed positioning, navigation, and timing (DPNT)”, *Proc. 2004 Position Loc. And Nav. Symp*., pp. 728-732, 26-29 April 2004.
83. P.T. Shaw, S. Peaslee, M.O. Ferguson, “Integrated and distributed position navigation and timing (PNT) data in shipboard environments”, *Proc. MTTS/IEEE TECHNO-OCEAN ’04*, vol. 2, pp. 796-801, 9-12 Nov. 2004.
84. P. Swerling, “Probability of detection of fluctuating targets”, *IRE Trans*., Vol. IT-6, April 1960, pp. 269-308.
85. M.I. Skolnik, Introduction to Radar Systems, 2nd Ed., McGraw-Hill Book Co., 1980.
86. J. Li and P. Stoica, MIMO Radar Signal Processing, John Wiley & Sons, 2008.
87. F. Daum & J. Huang, “MIMO radar: snake oil or good idea?”, *Proc. 4th Intl. Waveform Diversity & Design Conf*., Orlando, FL, 8-13 Feb. 2009.
88. P. Antonik, M. C. Wicks, H. D. Griffiths, C. J. Baker, “Frequency diverse array radars”, *Proc. 2006 IEEE Radar Conf*., Verona, NY, pp. 215-217, 24-27 April 2006.
89. P. Antonik, M. C. Wicks, H. D. Griffiths, C. J. Baker, “Multi-mission, multi-mode waveform diversity”, *Proc. 2006 IEEE Radar Conf*., Verona, NY, pp. 580-582, 24-27 April 2006.
90. M.C. Wicks and P. Antonik, “Frequency diverse array with independent modulation of frequency, amplitude, and phase”, U.S. Patent No. 7,319,427, January 15, 2008.

91. M.C. Wicks and P. Antonik, “Method and apparatus for a frequency diverse array”, U.S. Patent No. 7,511,665 B2, March 31, 2009.
92. P. Antonik and M.C. Wicks, “Method and apparatus for simultaneous synthetic aperture radar and moving target indication”, U.S. Patent Application 20080129584, June 5, 2008.
93. M. Secmen, S. Demir, A. Hizal, T. Eker, “Frequency diverse array antenna with periodic time modulated pattern in range and angle”, *Proc.2007 IEEE Radar Conf.*, pp. 427-430, 17-20 April 2007.
94. Jingjing Huang, Kin-Fai Tong, C. J. Baker, “Frequency diverse array with beam scanning feature”, *Proc. IEEE 2008 Ant. and Prop. Soc. Intl. Symp*., 5-11 July 2008, pp. 1-4.
95. T. Higgins and S. Blunt, “Analysis of range-angle coupled beamforming with frequency-diverse chirps”, *Proc. 4th Intl. Waveform Diversity & Design Conf*., Orlando, FL, 8-13 Feb. 2009.
96. Y.T. Lo, “Array Theory”, Chap. 11 of Antenna Handbook: Theory, Applications, and Design, Y.T. Lo and S.W. Lee (eds.), Van Nostrand, pp. 11-5 to 11-8, 1988.
97. P.M. Woodward, Probability and Information Theory, with Applications to Radar, Artech House, 1980.
98. R. C. Hansen, “Design Trades For Rotman Lenses”, *IEEE Trans. Antennas and Propagation*, Vol 39, No. 4, pp 464-472, Nov 1991.
99. H. J. Moody, “The systematic design of the butler matrix”, *IEEE Trans. Antennas Propag.*, 1964, AP-2, pp. 786–788.
100. A. Ishimaru and H.-S Tuan, “Frequency scanning antennas,” *Proc. IRE Intl. Conv. Rec.*, vol. 9, pt. 1, pp. 101-109, Mar. 1961.
101. J.S. Ajioka, “Frequency Scan Antennas,” Chap. 19 of Antenna Engineering Handbook, 3rd Ed., R. C. Johnson (ed.), McGraw-Hill, New York, 1993.
102. S. Drabowitch, A. Papiernik, H. Griffiths, J. Encinas, & Bradford L. Smith, Modern Antennas, Chapman & Hall, London, pp. 400-402, 1998.
103. M.J.N. Sibley, Optical Communications: Components and Systems, The MacMillan Press, Hampshire, UK, 1995.

104. V.C. Vannicola, T.B. Hale, M.C. Wicks, P. Antonik, “Ambiguity function analysis for the chirp diverse waveform”, *Record of the IEEE 2000 Intl. Radar Conf.*, pp. 666-671, 7-12 May 2000.